Engineered Crystal Systems for Erbium Quantum Hardware

THE UNIVERSITY OF
SYDNEY

Timothy Geoffrey Meadows Newman

Quantum Integration Laboratory

School of Physics

Faculty of Science

University of Sydney

A thesis submitted in fulfilment of the requirements for the degree of

Doctor of Philosophy

2026

Supervisor: Dr John G Bartholomew

Statement of Student Contribution

This is to certify that the content of this thesis is my own work. This thesis has not been submitted for any other degree or purpose.

I certify that the intellectual content of this thesis is the product of my own work, and that all assistance received in preparing this thesis, and all sources have been acknowledged.

The research reported in this thesis was supported by the award of a Research Training Program scholarship, and a Sydney Quantum Academy Supplementary Scholarship to the PhD Candidate.

Timothy Geoffrey Meadows Newman
March 13, 2026

Authorship Attribution Statement

The entirety of the work presented in this document is my own, with the exception of:

- The FTIR Data Presented in Chapter 6 comes from Mr Michael Moull at the University of Canterbury.
- The magnets which were built for the experiments described in Chapter 6 are made in our lab. These were designed by me, with input from Alice Jeffery and Matt Choi. The coils were wound by Alice and Lasse Sweetland.
- The magnetic field simulations in Chapter 5 are based on code originally written by JGB, adapted by Lasse Sweetland.
- All experiment-driving software was written by myself, with help from ALJ.
- The simulated rotation pattern code was initially written by ALJ, and later expanded by me.
- Our SNSPD was Fabricated by Dr Ian Berkman, the readout electronics I developed were based on a design by Prof Chunming Yin, during his postdoc at UNSW.
- Chapter 4 is partially adapted from a working manuscript of a review paper by TGMN, JGB, A/Prof Tian Zhong, and Dr Alan Dibos.
- Dr Luke Trainor wrote the code which drives the resonator cutting lathe, and developed the recipes for CaF_2 used in the Resonant Optics Lab.
- The SiN coupler described in Chapter 7 was fabricated at the University of Queensland by Dr Igor Marinkovic. Its design is based on components routinely made in the lab of Professor Warwick Bowen.
- During the preparation of the thesis, I have made use of LLM-based tools, specifically Claude Sonnet 4.5 for evaluating the structure, brevity, and flow of arguments presented. I have typed each character in this document, and take full responsibility for the content submitted.
- This manuscript was produced by me, with input and editing from a number of people to whom I am extremely grateful - Dr John G Bartholomew, Dr Miloš Rančić, Lasse Sweetland, Ben Field, Angela Liang, and John Newman.

For my dear parents,
to whom I owe my passion,
and everything else.

Acknowledgement of Country

I would like to acknowledge the Traditional Owners of the land upon which this work was conducted. Primarily, that is the Gadigal People of the Eora Nation. It is upon their Ancestral Lands that the University of Sydney rests. Some of this work was also conducted on Jagera, Turrbal and Yuin land. This thesis has also benefited greatly from work done on the lands of the Ngunnawal and Wurundjeri peoples.

I wish to formally recognise each of the nations mentioned here as the traditional owners of the lands and seas that we now know as Australia, and clearly state my support for ongoing efforts for constitutional recognition and Aboriginal sovereignty.

Ki ngā tāngata whenua o Te Waipounamu; ko Ngāi Tahu mā, tēnā koutou.
(To the people of the land of the South Island of New Zealand; the Ngāi Tahu and others, thank you.)

I also wish to pay respect to the many first peoples of Aotearoa - New Zealand, where a great deal of this work was also conducted. Some of the work of thesis was conducted in the following locations, in these institutions:
Ōtautahi - *(Christchurch)*, at Te Whare Wānanga o Waitaha - The University of Canterbury;
Ōtepoti - *(Dunedin)*, at Ōtākou Whakaihu Waka - University of Otago;
all with researchers from Te Whai Ao - *(The Dodd-Walls Centre for Photonic and Quantum Technologies)*.

I have benefited greatly as both a researcher, and a person from my two visits to the South Island, and wish to make particular note of the translations of the *Te Reo* names for these institutions. In the order presented above they are: ‘Waitaha House of Learning’, ‘A Place of Many Firsts,’ and ‘From the World of Light.’

May the genuine and enthusiastic engagement with first peoples that is set by our neighbours across *Te Moana-a-Rehua* (the Tasman Sea) continue to serve as a shining example, and an aspirational state for those of us living and working on the lands which are now known as Australia.

Abstract

As quantum information systems scale toward solving problems of societal utility, distributing entanglement over long distances is becoming an important challenge for the field. Rare-earth ions in solid-state hosts are a compelling hardware platform for quantum networking due to their exceptional $4f - 4f$ optical transitions, and long-lived spin transitions.

Erbium has optical and spin transitions which couple to photons in the Telecom-C band, making it compatible with fibre networks. Erbium atomic centres can be manufactured via doping or implantation into solid-state hosts, and have demonstrated high coherence and low spectral diffusion in a range of materials. However, erbium has a low optical dipole moment, leading to a low light-matter coupling strength. This limits the rate at which quantum entanglement may be distributed, or other operations performed within a network.

Despite decades of research, the mechanisms that affect Er^{3+} transitions remain poorly understood. Hosts are chosen for ions based on convention, convenience, and (well-informed) heuristics, since *ab initio* calculations of the properties of lanthanide $4f$ shell have historically been prohibitively difficult. This thesis addresses the challenge of this weak dipole through two complementary approaches; both of which constitute engineering the erbium-crystal system.

Firstly, we engineer the emitter itself, from the 'bottom up.' We seek an optimal crystalline environment for ions, which maintains their coherence but increases optical transition strength. To this end, we have characterised four Er^{3+} sites in CaF_2 to understand how the crystal field affects optical and spin properties. We identify sites with dipole moments as high as 1.63×10^{-32} C $\cdot$ m despite lifetimes in excess of 10 ms, and a maximum coherence time of 43.9 μs. This informs our next steps, both of selecting an optimal site for single ion addressing in calcium fluoride and our longer-term goal of designing sites for high dipole moments.

In the second approach, we engineer the crystal from the 'top down,' fabricating whispering gallery mode resonators in calcium fluoride to enhance the interaction of single Er^{3+} ions with light. I have fabricated five high quality factor optical resonators in both doped and undoped CaF_2, and commenced initial characterisation of these at room temperature. We have prototyped a waveguide coupler for operating these devices in a cryogenic environment with no free-space optical access.

The resulting engineered crystal system – a high dipole moment erbium site coupled to a high quality factor resonator – provides a path toward a competitive optical cooperativity architecture for single erbium ions in the solid state.

Acknowledgements

A PhD is a shared accomplishment. I'm grateful to everyone in our lab, the research community, and my personal life who has lent a hand, been there to talk, or otherwise made this experience so much more fun and less lonely than it could have been. I stand on the shoulders of those in my support network. I will try to do justice to their contributions, but there are many more than those listed here.

Above all, I thank Dr John Bartholomew for his guidance, his trust in me as the first student in our fledgling experimental effort, and his phenomenal dedication to me, to our group, and to science. John's passion for physics, technical expertise, and care for his students have defined the atmosphere of our group: one that values asking good questions, finding good answers, and doing so with respect for the technical and cultural contribution of each member.

JB, I've valued each one of our five-minute chats that turned into two hours, the ceaseless optimism with which you approach every day, and everything that you've taught me along the way. We've made it through one lockdown, two superfluid leaks, three house moves, four COVID cases, and not-quite-five of the most challenging and rewarding years of my life. As we've done so, my respect and admiration for you has only grown. I will always be grateful for this experience.

To Alice Jeffery, a diligent collaborator turned plucky and brilliant little sister. You are a constant source of laughter, warmth, and encouragement; always guided by curiosity and scientific rigour. Our time working together was always a joy. Thank you for making me a better scientist, and for putting up with a couple of years of bleep bloop music. Don't forget me when you're famous.

Lasse Sweetland, thank you for the calm manner with which you attack complex problems: generally with a wry smile and a shrug. I'm excited to see the upcoming progress as you gallop forth with these experiments. To Angela Liang, thank you for your enthusiasm, your positivity, and for being able to read my documentation. You're early on in your flashy-county career, but your approach is second to none. Justin Brown, thank you for your optimism, your operatic sighing, and for pulling me up when I get numbers wrong.

Dr Miloš Rančić, your whirlwind approach to getting things done is inspirational, if at times a little terrifying. I have greatly appreciated the dash of spice you have added to our lab, and sincerely wish we had more time together. Ben Field and Gargi Tyagi — my fellow PhD students. We've often run in parallel tracks, but it's been a pleasure to do so, and particularly nice to watch our work dovetail more and more as the years have gone on. You've been great office mates, collaborators, and friends.

Fergus, you are a deeply dedicated team member, may all of your dreams come true. Chintan, I hope we have the chance to work together again in the future, on an experiment or a sound system. Jackson, it's a pleasure to see you grilling on those Bragg Grating measurements. Aidan, I thank you for your tireless commitment to minimalist aesthetics. To the past members of QIL — thank you all for your contributions, your energy, ideas, and good humour.

Professor Mike Reid, Michael Moull, and Dr Jamin Martin, thank you for the crystal growth and modelling expertise, the FTIR data, and the music recommendations. To A/ Prof Jevon Longdell, thanks for the sails, meals, and for many insightful conversations over the years. Professor Sven Rogge, Dr Ian Berkman, Dr Ally 'Ali G' Goldingay, and the rest of the UNSW Er:Si team - thank you for the detectors, your expertise, and for science (and sourdough) discussions. Dr Igor Marinkovic, thank you for your enthusiasm for collaboration, and for the waveguides.

Professor Harald Schwefel, thank you for letting me loose in your lab for two weeks while the whole group was at conferences; that was both unconventional and deeply appreciated. Dr Luke Trainor, thank you for your generosity and patience. You led me from beginner to 'Good As' crystal machinist in a matter of days, rather than months. I always look forward to a chat with you. Thanks also to the rest of the Resonant Optics Lab team for the advice, encouragement, and your tolerance of my ambitious cutting schedules.

To my veritable army of proofreaders, including: Dr John Bartholomew, Professor Andrew Doherty, Angela Liang, Ben Field, Dr Miloš Rančić, Lasse Sweetland, Josephine Hall, and my eternally patient father, John Newman: Thank you all, I truly could not have done this without your contribution.

To our lab neighbours, Doctors all: Ting Rei Tan, Robert Wolf, Cyril Laplane, Xanthe Croot, Torsten Gaebel, and Steven Waddy — thank you for always being there to lend a tool, some expertise, or just a friendly ear. Thank you particularly to Professors Mike Biercuk and David Reilly, for inspiring me early on as an undergrad. To David I am particularly indebted, as it was his support that facilitated my transition into a quantum engineering researcher.

Thank you to USyd's 'Social Theorists,' particularly Dr Tom Smith for swims and moral support, Dr Dominic Williamson for fine dining, good conversation, and his office in my eleventh hour; Dr Angela Karanjai for many thoughtful discussions; and of course Professor Andrew Doherty for his tireless support of every physicist at Usyd. I am also grateful to Clare Birch, who is always ready to tear a document (or me) to shreds. I know it's nice on the West Coast, but come visit once in a while. We have jazz here too.

I have been particularly lucky to have a number of inspiring teachers throughout my schooling. Particular thanks have to go to my music teacher and friend Greg Howard, who sparked in me an interest in the physics of information science during a class on recording technology; and to my physics teacher Dr Andrew Haines, who inspired my interest in electronic instruments by introducing me to the theremin during Year 11 Physics. It is thanks to the both of you that these deeply connected endeavours have always provided a North Star in my life.

To my friends: Bill, Vee, Galit, Angus, Claudia, Peter, Eren, Griffin, Laura, Tom, Jack, Reg, Lewis, Cristina, Lucy, Vic, Kate, Shiv, Tess, Nick, Scott, Emma, Matt, and so many others — thank you for your support, for listening to me, and for simply being there when I needed it. Hubert and the campsite crew, thank you for dancing and cheering me on from afar. To Geraldine Kelly; your kindness, wit, and generosity have left an indelible mark on me.

To the Sydney music community - those who organise events, manage spaces, perform, attend, or contribute in any other way: Thank You. There is something truly unique about our little slice of the world, and I'm deeply grateful to be a part of it. From the Sydney Opera House to Sydney Steel Lane, the contribution you make to the culture of this city is invaluable.

To Josephine 'Jojo' Hall, thank you for your support through this challenging period of my life, supporting me and being there for me in every way. Your support, love and empathy has meant so much during this time. So too have all the meals in these last few weeks. I appreciate every discussion we have explaining our work to each other, sharing music and art together, cooking for each other, and swimming together. Thank you.

Finally to my family. My parents, John Newman and Julie Meadows — thank you for everything: for encouraging without forcing, for supporting without coddling, for enabling me to get to where I am. Also I hope you realised that dedication was a haiku! James, Stea, Evyenia and Basil — thank you for dinners, laughs, pizzas, and for letting me write while babysitting. To Nick and Mads — thank you for cheering me on, and for always having me stay in Aotearoa; and to Thomas, Josie and Otis — Uncle Tim will be around a fair bit more from now on.

Contents

"Nothing in life is to be feared, it is only to be understood. Now is the time to understand more, so that we may fear less."

Marie Skłodowska Curie

1

Introduction

Over the last two decades, quantum technologies have begun to emerge from experimental labs and are rapidly becoming the domain of the largest companies in the world. This has primarily been motivated by the potential of a fault-tolerant quantum computer, which could vastly outperform its classical counterparts for a range of problems [1]. A number of different architectures have been proposed, and initial proof-of-principle experiments have now grown to demonstrations of larger machines [2–4]. This interest in quantum hardware is also motivated by the potential of quantum technologies in other fields – including provably secure communication across networks [5], and advances in precision metrology that an improved understanding of quantum mechanics has already afforded us. This current moment in the field's history is known as the 'Second Quantum Revolution' [6].

The First Quantum Revolution was characterised by the demonstration and development of technologies that rely upon an understanding of the simplest quantum mechanical effect – wave particle duality – for their operation and development. Beginning to exploit wave-particle duality led to a number of new technologies including lasers, atomic clocks, magnetic resonance imaging (MRI), electron microscopes and optical lithography techniques. Over the latter half of the 20th Century, the development of these First Quantum Revolution devices led to the development of the massively interconnected information-technological landscape that we inhabit today.

By extension, Second Quantum Revolution technologies are those which take advantage of other quantum mechanical effects - specifically superposition and entanglement. The ability to generate a large entangled state of a large number of two-level quantum systems – *qubits* – which could also be individually controlled and read out is both a significant scientific goal and a foundational building block for a novel class of technologies [7]. This includes computers which can solve problems that classical computers could not [8], provably secure communication protocols [9, 10], and ultra-high-precision sensors of physical quantities such as magnetic and electric fields, mass, and gravity.

There are two algorithms whose speedup over their classical counterparts were large enough to motivate the quest for a large quantum machine: factoring large co-prime integers [11] and unstructured search through a database [12]. Tackling these problems at "commercially relevant" scales is as yet out of reach, requiring quantum computers orders of magnitude larger than current machines [13]. Whilst these facts may seem sobering relative to the levels of excitement generated by the potential of quantum hardware, there is an extraordinary amount of effort being put into scaling the field. A number of new algorithms have been uncovered with proven speed ups, including quantum walks and simulations of matter [14]. Further to this, research efforts in academic labs and companies are developing the hardware and techniques required for a scalable, fault tolerant quantum computer.

The field of study surrounding these efforts encompasses theory, experiments, design, numerical modelling and materials science, and is maturing into a novel entrant into the list of engineering disciplines – Quantum Engineering.

1.1 Linking Quantum Information Systems

As quantum computing and communication systems grow in qubit count (and physical size) towards ‘utility-scale’ machines [3, 4, 15, 16], one challenge which has emerged is that of distributing entanglement between quantum systems. Photon-mediated entanglement is relevant to developing quantum networks to connect quantum computers and distributed quantum sensors at distances up to hundreds of kilometres, traditionally called ‘long haul communication’. It is also increasingly relevant to the development of large-scale quantum computers, to locally connect sub-systems in a modular architecture [4, 17], or to improve and increase the number of connections between individual qubits in a monolithic architecture [18].

In the microwave regime, recent demonstrations have shown loophole-free bell tests using a microwave link between two superconducting qubits [19]. Whilst these results are impressive and suggest efficient means to distribute entanglement in a microwave-only architecture, such an approach is not suitable for long-haul quantum communication, since the link must be cryogenically cooled, requiring a bespoke cryogenic system [20, 21]. A number of small scale quantum networks have been demonstrated using fibre-optic links between atoms, or atom-like systems that emit photons entangled with the matter degrees of freedom [17, 22–24]. Each of these systems has a limited, relatively slow rate of entangled photon pair distribution — generally between 1-10 Hz. It is within the context of developing fibre-based quantum networks that our study of single erbium emitters is positioned.

1.2 Solid State Rare Earth Technologies

Rare-earth ions in solids are a compelling class of material system to link quantum information systems. They have excellent properties for quantum interfaces between light and matter, and prototype demonstrations of technologies such as quantum memories, repeaters, and transducers have been conducted [25–29]. In addition to ensemble-based technologies, single rare-earth ions also show promise as spin-photon interfaces for entanglement distribution [24, 30, 31]. Trivalent erbium (Er^{3+}) is of particular interest due to its compatibility with existing optical fibre technologies, since it has an optical transition which is in or near the infrared telecom-C band [32].

An ongoing challenge with all rare earths is that the optical (or infra-red) transitions of interest, the $4f \longleftrightarrow 4f$ transitions, have relatively small optical dipole moments, compared with other atom-like systems. To circumvent this ensembles are often used, to take advantage of the collectively enhanced ($\propto \sqrt{N}$ scaling) coupling strength between an atomic ensemble and light.

Making use of this scaling, rare-earth ion ensembles have enabled a number of technologies with impressive performance metrics, including quantum memories and transducers. Memories have demonstrated multi-mode storage with high efficiency (>60%) [33], coherence times ranging from seconds to hours [25, 34], and on-demand recall [35, 36]. Remote entanglement between pairs of ensemble-based memories has been demonstrated [37–39], with applications across long-term optical data storage, radio astronomy [40], and using REI spin ensembles as memories within a quantum computer [28]. Microwave-to-optical transduction using rare earth ensembles exploits the multi-level system of a rare-earth ion ensemble to couple to both optical and microwave fields. Demonstrations have used dilute crystals [41, 42], and more recently stoichiometric crystals – such as Er:LiYF$_4$, Er:GVO$_4$ and ErCl$_3$:6H$_2$O – utilise collective ferromagnetic or antiferromagnetic spin resonances for enhanced coupling [43–45].

However there are a number of challenges associated with realising a register of multiple qubits in an ensemble architecture [46, 47], leading to increased interest in enhanced interactions with single rare-earth ions [48]. The field of single rare-earth ion spectroscopy has moved rapidly over the last decade, from early demonstrations of incoherent detection [49] and subsequently state dependent readout [50, 51] to control of single rare-earth ions [52, 53]. Even more recently, spin-photon entanglement and multipartite entanglement with remote ions [24, 31] has been demonstrated, as well as local entanglement with spins in the host crystal [54, 55].

Along with this progress in 'traditional' rare-earth hosts, single ions have been read-out and controlled in a host of other materials including photonic nano-structures in silicon [56], nanocrystals [30], and thin films [57], revealing a promising path towards interfacing rare-earth technologies with scalable fabrication.

Each of the breakthroughs listed above (with the exception of [49], where a different optical transition was used) have been achieved by enhancing interactions with an emitter using a cavity [50, 51], and making use of the effects of cavity quantum electrodynamics.

1.3 Cavity Quantum Electrodynamics

Cavity quantum electrodynamics (cavity QED) describes the interactions between an emitter and the photonic mode of a resonator. It is the core theory of many quantum information technologies [58, 59]. Quantum networks are currently being prototyped using cavity QED with on a range of solid-state emitters, including vacancy centres in diamond [60, 61], defect centres in silicon [16], and rare-earth ions across different hosts [24, 38, 62, 63].

Interactions in cavity QED are governed by three key parameters: the loss rate from the atom, the loss rate from the cavity, and the strength of the interaction between the atom and cavity. This interaction strength, known as the coupling strength, is dependent on the cavity quality factor and mode volume, and the dipole moment of the target optical transition. The relative size of these parameters determines whether the given system is strongly coupled, with 'strong coupling' being the regime in which the interaction strength between the atom and cavity dominates all other rates [59, 64]. Efforts in the field of single rare-earth ions have historically targeted the fabrication of small, high quality factor cavities to enhance this interaction strength. An optical cavity with sufficiently high quality factor and small mode volume for single ion addressing is one focus of my experimental work.

1.4 Crystal Field Engineering

Another approach to enhancing the interaction between optical dipoles and light is to engineer the dipole moment of the atom itself by altering the crystalline environment in the immediate vicinity of the atom in a controlled manner. Increasing the optical dipole moment provides another degree of freedom with which to engineer the system's cavity QED parameters. The dipole moments of particular rare-earth ion species in different hosts have been measured, including investigation of complexes [65, 66], organic molecules [67] and some studies of the many crystal field environments (sites) that exist in a single crystal lattice [68]. That said, it is not clear whether the mechanism that enhances an ion's optical dipole moment will affect the favourable coherence properties of rare-earth ions. To the best of my knowledge, no systematic study of the effects of the crystal field on an ion's optical dipole and coherence properties has been undertaken. The bulk spectroscopy studies presented in this thesis represent the beginnings of the experimental component of such a study, with the theoretical components also being undertaken in our group.

1.5 The Work of this Thesis

This thesis investigates how to achieve stronger light–matter interaction between single erbium ions and confined optical modes, an essential step toward scalable, telecom-band quantum technologies. One central question in this field is whether static cooperativity ($C = 4g^2/(\kappa\gamma)$) can exceed unity for an individual Er^{3+} ion in a solid state environment where it can be tuned using electric fields. There are single rare-earth ion architectures that have achieved impressive 'rephased cooperativity' results, where coherence is maintained through rephasing schemes similar to dynamical decoupling [31, 54, 69]. However these approaches are based on nanophotonic cavities, so ions are necessarily very close to the surface. For this reason, the rare-earth ion host material is one in which the ion has no first-order sensitivity to electric fields.

We pursue two complementary strategies: engineering the electrostatic environment around the ion to optimise the transition dipole moment, and engineering the local density of states using a large (hundreds of μm diameter), high quality factor optical cavity.

Crystal field engineering for higher dipole moments. The first approach explores how crystal-field engineering can modify the 4f-level structure and optical coupling strength of erbium ions. By examining Er^{3+} in CaF_2 crystals – including both commercial and ion-implanted samples – I show how variations in the crystal field influence transition dipole moments and coherence. We use these studies to inform our decision on the ‘optimal site’ to explore single Er^{3+} behaviour in CaF_2. This work also contributes to a long term goal of identifying the optimal material conditions for high-coherence, high-dipole-moment Er^{3+} emitters, suitable for long term quantum photonics applications.

Whispering-gallery mode resonators for electromagnetic confinement. The second approach develops whispering-gallery-mode resonators (WGMRs) directly fabricated in erbium-doped CaF_2. Unlike nanophotonic cavities, WGMRs are large, ultra-high-Q devices with extremely narrow spectral modes. The fabrication process and device performance are discussed, defining a practical pathway towards high-cooperativity cavity QED in the telecom band.

The high dipole, stark sensitive sites and ultra-high Q devices will enable a suite of measurements and technical capabilities which are not otherwise possible in the other systems: their size enables interaction with ions that reside many optical wavelengths into the material, where the deleterious effects of the surface are mitigated. This geometry therefore permits access to ions in polar sites with non-zero Stark sensitivity, whilst maintaining coherence –a capability unique to this platform and impossible in surface-proximal systems. As erbium concentration is reduced, the narrow WGMR modes can selectively couple to ions closer to the centre of the inhomogeneous line, which we envision will further improve coherence properties of measured single ions.

1.6 Structure of This Document

Chapter Two is an introduction intended for a reader who is not already an expert in the field. I provide the context for the work, including a primer on quantum information, and motivate the hunt for a quantum light-matter interface to scale quantum machines. I outline the current challenges and limitations faced by a number of different quantum hardware platforms, and discuss the potential benefits of photonic links between (and within) quantum information systems. This chapter provides some of the background that motivates erbium ions in solids as a candidate system for quantum photonic technologies.

In **Chapter Three,** the focus shifts towards our implementation, building the theoretical background of the two methods that we are using to enhance interactions between erbium ions and optical fields. This chapter starts with a background on solid state spectroscopy of the rare earth ions, providing the necessary framework to understand erbium’s optical properties, and the spectroscopy techniques that we use to characterise it. I then introduce light-matter interactions, with a view towards high cooperativity interactions with rare earth ions. In this chapter, I detail our two methods of optical enhancement for erbium ions: crystal field engineering, and cavity enhancement in a high Q/V cavity, outlining the research questions that each seeks to answer.

Chapter Four provides a thorough review of the already existing work in the field on single rare-earth ions in nanophotonic cavities. I focus on the two pioneering works in the field, and discuss other efforts targeting single rare-earths. This chapter is adapted from a manuscript-in-progress.

In **Chapter Five**, I outline the experimental tools and techniques that I have developed over the course of this work. I focus on the current state of our bulk spectroscopy experimental setups, highlighting the hardware which I have developed or integrated to achieve high dynamic range switching, high efficiency collection of light, controllable magnetic field, and detection of small signals. I discuss design decisions based on the experiments that we have conducted, and our future plans. I provide characterisation results for the setup, including beam parameters, detection efficiency, magnetic field simulations, and temperature measurements based on thermal occupancy. I also outline the relevant experimental spectroscopic techniques of this work including inhomogeneous line surveys, hole-burning, and coherent transient (echo) measurements.

Chapter Six provides the details of the bulk spectroscopy experiments conducted so far. I present our work characterising the properties of four Er^{3+} sites in CaF_2, in both doped and implanted samples. I discuss our experimental results, ranging from a broad survey of Er^{3+}:CaF_2, to an in depth comparative study between 'native' sites and a manufactured erbium-oxygen complex. I investigate the site's effects on ion properties, motivated by selecting an Er^{3+} site for single ion experiments.

Chapter Seven focuses on whispering-gallery mode resonators. I present the theoretical framework for these devices, discuss their design and outline the challenges in working with them. I provide details on the devices which I have fabricated, and present our novel cryogenic coupling scheme for these resonators, contrasting it with other existing approaches. I discuss the initial results from our first prototypes, and outline the next steps for characterising our devices.

Chapter Eight will conclude this thesis with a summary of our results thus far, and the current state-of-play of our experiments. I provide my perspective on the possible next steps for the bulk spectroscopy and whispering-gallery-mode experiments, and discuss the long term potential of our system.

"Nature isn't classical, dammit,
and if you want to make a simulation of nature,
you'd better make it quantum mechanical.
And by golly it's a wonderful problem,
because it doesn't look so easy."

Richard Feynman

2

Background: Scaling Quantum Hardware with Photonics

Building large quantum information devices is a significant challenge, and a key motivator for a number of academic and industrial research efforts. In this chapter, I build the case for rare-earth ions, particularly erbium, for quantum photonic interconnects. It is intended as an introduction and descriptive overview of the field, intended for a non-expert reader. The aim is simply that this chapter will help to shed light on the technical context in which this package of work exists - motivating our study of a high-efficiency, telecom compatible quantum light-matter interface.

It starts with a brief introduction to quantum information science and the challenges associated with building large scale quantum information systems. I motivate both modularity and photonic interconnects as a path forward. I will close by discussing the open research questions associated with developing photonic interconnects, and arrive at single erbium ions as one of a number of promising paths forward. While the work of this thesis is not focused precisely on the architecture of a large quantum computer, our research is motivated by this effort. For further information, the reader is encouraged toward the references [7, 15, 17, 70–75].

2.1 Quantum Information Technologies

2.1.1 Bits and Qubits

In classical computing, information is represented by binary digits or ‘bits’. Bits are manipulated using logical operations to execute algorithms. Although bits are commonly described as ‘ones and zeroes’, this abstraction obscures the diverse physical implementations and underlying physics of computation. There is no one physical object which represents a bit. They can be stored, transmitted, or processed using various physical systems: voltage levels on a wire, charge states in flash memory, magnetisation on a disk, or positions of a switch.

Since 1947, classical computation has scaled via semiconductor transistors [76] which are fabricated in complementary metal-oxide-semiconductor (CMOS) processes. Very large scale integration (VLSI) [77] enabled scaling up to the billions of transistors per die that we see today. Long-distance communication was enabled by fibre-optic cables [78]. Each of these technologies has been enabled by a number of key technological advances, including lithography, fibre drawing, advanced packaging, simulation, splicing, and connectorisation.

Quantum bits, known as *qubits*, are the fundamental unit of information within a quantum computer [7]. Unlike a classical bit, which is confined to definite states `0` or `1`, a qubit is a quantum two-level system, which supports arbitrary linear combinations of these basis states, known as superposition states. This property arises because the state of a qubit is a vector in a two-dimensional Hilbert space, typically expressed as $|\psi\rangle = \alpha|0\rangle + \beta|1\rangle$, where α and β are complex amplitudes satisfying $|\alpha|^2 + |\beta|^2 = 1$.

The Bloch sphere, shown in Figure 2.1 is a common geometric representation of this state space, with its surface capturing the full continuum of qubit states, and providing geometric intuition for quantum gate operations. Superposition and entanglement allow qubits to carry richer information and enable the unique quantum phenomena that underpin quantum technologies.

Entanglement, a uniquely quantum correlation, further distinguishes qubits from their classical counterparts. When two or more qubits become entangled, the state of the system of qubits is no longer separable: the system may no longer be described as a product of the states of the individual qubits of which it is comprised. The state space spanned by a system of N entangled qubits expands exponentially to a 2^N dimensional state space [79]. This enables quantum advantages in computation, and entanglement distribution also provides the foundation for provably secure communication, and sensing with enhanced precision.

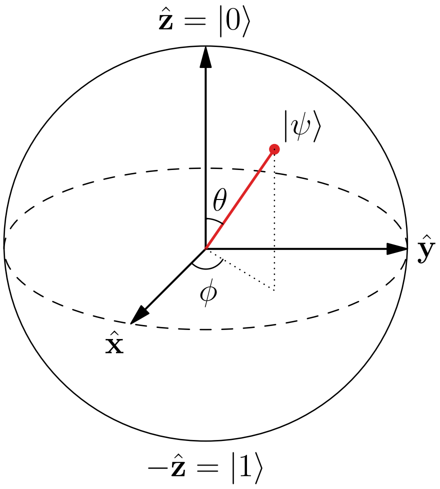

Figure 2.1: The Bloch Sphere representation of a quantum bit.

Similar to the bits of classical computing, there are a number of physical systems that are used to represent, hold, or operate upon quantum bits. An incomplete, but illustrative list of some physical systems that can be used to create qubits is provided in 2.1.7. These devices by design operate at the level of single excitations, be that one photon, one spin flip, the position of one electron, or some other quantity. As such, they are exquisitely sensitive to environmental noise, motivating the use of, for example: cryogenic systems to isolate solid-state realisations from thermal noise or ultra-high vacuum chambers to isolate single atoms or ions in traps.

Making use of the advantages offered by qubits requires overcoming their fragility, since quantum coherence can easily be lost through interactions with the environment. Maintaining long-lived coherence and precise control of qubit states thus remains one of the central engineering challenges for quantum systems on any physical platform.

2.1.2 Quantum Computing

Quantum computing uses arrays of qubits for computation, exploiting superposition and entanglement as a computational resource [7]. This enables a different set of logical operations to be performed than in classical computing. Algorithms exploiting superposition and entanglement can solve specific problems more efficiently (in number of logical operations) than classical computers. Notable examples include Shor's algorithm [11] for integer factorisation and Grover's algorithm [12] for unstructured search, both of which demonstrate quantum speedups.

The building blocks of such algorithms are quantum logic gates, which are unitary transformations that manipulate qubit states. Sequences of single- and two-qubit gates implement algorithms in much the same way that AND, OR, and NOT gates form the basis of classical logic circuits, but their reversible, linear nature reflects the underlying physics of the qubit system. The ability to perform reliable and precise quantum gate operations is central to building scalable quantum processors.

It is clear however that the goal of a Universal Quantum Computer is still relatively far away: The number of qubits required to factor an RSA 2048 encryption key (one of the most famous applications of Shor's algorithm) remains in the millions [80, 81], several orders of magnitude larger than the largest current demonstrated quantum processors, which demonstrate $\sim$1000 quantum bits [15]. Along with this, due to overheads imposed by error correction [82, 83], the number of physical qubits in a quantum computer is far greater than the number of logical qubits which may be used for any given computation. A good size reference for a machine deemed 'useful' by current standards would comprise between one thousand and one hundred thousand logical qubits – meaning up to 10^7 physical qubits in a machine [13]. The dimensions of such a machine are significant if made using current qubit technologies in terms of physical size and power consumption. Algorithm runtimes to perform some of the 'flagship calculations' of a quantum computer extend from days to tens of years. This motivates those in the field to look for new qubit architectures, improved algorithms, and methods of modularising a quantum computer.

2.1.3 Quantum Communication

Quantum communication exploits quantum effects to enable provably secure information transfer. Quantum key distribution (QKD) [5] ensures unconditional security by detecting eavesdropping through measurement disturbance, enabling encryption keys that cannot be intercepted without detection. Quantum random number generators (QRNGs) [84] leverage quantum measurement unpredictability to produce true randomness, essential for cryptographic protocols and secure communications. Both QKD and QRNG systems have transitioned from laboratory demonstrations to commercial deployment.

2.1.4 Quantum Sensing

The sensitivity that threatens the stability of quantum states also makes them powerful measurement devices. Quantum sensors take advantage of this for measurements of physical quantities at sensitivities beyond classical limits. Applications include GNSS-denied[1] navigation using magnetometry [85], improved medical imaging [86], and magnetic field sensing [87].

---

[1] Global Navigation Satellite System - colloquially "GPS"

2.1.5 What Makes a Good Qubit?

An ideal qubit is a quantum system in which two chosen states can be efficiently isolated, addressed, and measured. Effective gate operations must be available, including entanglement with other qubits for multi-qubit processing. The optimal qubit platform depends on context, applying the "horses for courses" maxim:

- Systems amenable to strong mutual interaction facilitate fast quantum logic and entangling gates.
- Qubits with weak interaction strengths—such as photons—are preferential for transport and long-distance communication.
- Long-lived systems with minimal environmental coupling are suited for memory and state storage.

2.1.6 The Loss-Di Vincenzo Criteria

The Loss-DiVincenzo criteria establish the fundamental requirements that any physical platform must satisfy to operate as a scalable quantum computer. These criteria are as follows:

1. A well-defined and scalable set of quantum bits (qubits).
2. The ability to initialise the state of these qubits with high fidelity.
3. Quantum coherence times significantly longer than gate operation times.
4. The capability to implement a universal set of quantum logic gates.
5. Reliable, individual measurement of each qubit.
6. (For quantum communication) The interconversion between stationary qubits and flying qubits.
7. (For quantum communication) Faithful transmission of flying qubits between specified locations.

The work of this thesis is focused on the final two criteria. The study of flying qubits, light-matter interfaces, and the efficient distribution of quantum information has led to the development of quantum networks as a unique field of study.

2.1.7 Physical Platforms for Quantum Computing

No single quantum platform has achieved a ‘CMOS-and-VLSI-like’ breakthrough, enabling million-qubit scalability. Instead, diverse physical systems – including superconducting circuits, trapped ions, solid-state spins, neutral atoms, defect centres, linear optical computation, and others – compete on distinct metrics: coherence, gate speed, scalability, and connectivity. Large-scale quantum computers require qubits with long coherence times, fast gates, efficient entanglement generation, and error-correction compatibility.

2.2 Building Large Scale Solid-State Quantum Systems

In the architecture of a large-scale quantum computer, inherent constraints arise along three principal axes: thermal management (heat), physical size (length), and the duration of operations (time). These considerations apply to all architectures - including ion traps, neutral atoms, superconducting circuits, solid-state spins and photonics. In this section I highlight the challenges associated with building large solid-state quantum information systems.

2.2.1 Physical Size and Latency

Dilution refrigerator dimensions impose limits on system footprint. Further, thermal contraction during cooldown introduces unpredictable changes in effective cable length, complicating synchronisation of signals [88–90]. While microwave cables can be phase-matched and calibrated using time-domain reflectometry (TDR), the number of cables - and hence measurements - required quickly exceeds practicality.

Further to this, as processors increase in size, loss may limit even the most efficient microwave waveguides. Standard materials for on-chip or PCB waveguides have losses in excess of 6 dB/m [91, 92], necessitating the move to bulk waveguides for efficient, long-distance qubit coupling [21].

This distribution introduces latency: even within a single dilution refrigerator, signal propagation delays are non-negligible relative to qubit coherence times. Qubit manipulations must be completed within durations that are short compared to decoherence times, motivating co-location of control electronics with qubits in the cryogenic environment. The ratio of gate operation time to coherence time provides a practical metric for assessing architectural viability.

2.2.2 Heat and Wiring Bottlenecks

Each microwave cable extending into a dilution refrigerator contributes a known heat load [75]. Even in the latest large-scale refrigerators, the practical upper limit is ∼1000 cables; exceeding this risks compromising the cooling efficiency. Specialised active cryogenic electronics, including fast routing switches, FPGAs, and logic circuits [74, 93] partially mitigate this bottleneck by enabling time-multiplexed qubit control [94]. However, these solutions shift the bottleneck to higher temperature stages (4 K) where greater cooling power is available. Between the 4K and millikelvin stages of cryostats, where most qubits operate, the permissible number of coaxial cables remains finite.

Beyond heat, electronic quantum systems face a wiring bottleneck described by Rent's rule [95, 96]: the number of external connections (pins) T to a logic block scales with internal components (gates) g as $T = t \cdot g^p$, where p (typically 0.5–0.8) characterises interconnection complexity. Current electrically controlled quantum systems have $p \sim 1$ (linear scaling: one control line per qubit), which is unsustainable. Achieving $p < 1$ through frequency multiplexing, cryogenic logic, or addressing architectures [97] is essential for scalability.

2.2.3 The Case for Optical Interconnects

Another approach to solving the wiring problem and reducing cryogenic heat loads is using optical-microwave conversion schemes [98–106]. Relevant to quantum technology are microwave (GHz frequency) to optical (hundreds of THz) transducers—especially those whose optical link is close to 200 THz (1.5 µm in wavelength).

The adoption of optical fibres has the potential to radically transform a number of the aforementioned scaling constraints. Fibres are low loss, especially in the telecom-C band, at 0.2 dB/km, and the available bandwidth at optical frequencies is much higher than that in the microwave. The thermal conductivity of a single-mode fibre is six orders of magnitude lower than that of a coaxial cable [107]. While there remains a thermal bridge between "hot" and "cold" stages, the minimised heat load from interconnect allows for an increased number of signal lines into a cryostat.

Furthermore, the thermal energy in the telecom C band is negligible at room temperature, enabling long distance communication in fibre at the single photon level. Since superconducting and spin qubits generally operate at microwave frequencies, they and their supporting infrastructure must be kept at temperatures below 1 K, such that their characteristic energy ($k_B T$) remains well below that of the photons that they couple to. In optical fibre at room temperature, this restriction is lifted, since $k_B T$ at 300 K is ∼6.25 THz. Consequently, long

Heat Load Due To Conduction

	Material	300 K → 4 K	4 K → mK stages
Coax [75, 108, 109]	BeCu / SS	11.6 mW	3.1 μW
	SS/SS	5.5 mW	1.8 μW
	NbTi/NbTi	-	1.1 μW
Loom [75, 108, 109]	BeCu	65 μW	59 nW
	Constantan	47 μW	21 nW
	NbTi	-	4.2 nW
Fibre	(Single Mode)	10 μW [110]	3 pW [107]

Table 2.1: The static heat load applied to various stages of a dilution fridge due to interconnects of different kinds.

haul quantum signal transmission is possible at these frequencies, and key optical components such as circulators, splitters, filters, and amplifiers can remain at room temperature. The primary cryogenic requirement is then reduced to qubits, and in some cases, single-photon detectors.

These considerations strongly motivate the pursuit of fibre-coupled optically active spin systems. Whether utilised as single-photon sources, qubits, transducers interfacing with microwave quantum hardware, or as the foundation for quantum memories (digital or analog), it is increasingly evident that scalable architectures for quantum computation cannot rely solely on coaxial cabling throughout the full temperature range from millikelvin to room temperature.

2.2.4 Manufacturing and Heterogeneous Integration

Scalable solid state quantum hardware demands repeatable, wafer-scale fabrication. Process design kits (PDKs) are being developed for superconducting qubits [111], semiconductor spin qubits [112], and cryogenic CMOS control circuits [74, 113], characterising material behaviour at low temperatures, enabling on-chip control that reduces wiring overhead [93]. Silicon integrated photonics leverages CMOS foundry infrastructure for high efficiency waveguides, resonators, and phase shifters [4]. However, integrating optically active impurities such as rare-earth ions [114] or colour centres [115] requires process modifications or post-fabrication implantation.

Alternative platforms trade scalability for performance. Thin-film lithium niobate (TFLN) enables electro-optic modulation; diamond and silicon carbide host defects but suffer limited wafer sizes; and crystalline materials including CaF_2, the material studied in this work, support ultra-high-Q resonators but require precision machining rather than lithography [116]. Hybrid approaches such as transfer printing [117] and heterogeneous bonding [118] sidestep foundry constraints but introduce alignment and yield challenges.

No single quantum platform excels in all metrics. Proposed heterogeneous architectures combine multiple qubit types via photonic interconnects, moving beyond today's "one-qubit-to-rule-them-all" approach [119]. Recent demonstrations have integrated colour centres with photonic waveguides [118], quantum dots with silicon nitride photonics [120], and used microwave-optical transducers to link superconducting qubits to telecom-band photonics [102, 121, 122]. Rare-earth ions – particularly erbium and ytterbium – naturally interface with fibre networks, positioning them as promising nodes in modular quantum systems [123, 124].

2.3 Connecting Quantum Information Systems

Scaling quantum computers beyond laboratory prototypes requires interconnecting distributed quantum hardware, both within physically (and in qubit number) large machines, and across large geographic distances. This challenge applies equally to warehouse-scale quantum computers integrating thousands of modules [4] as to intercity quantum networks enabling secure communication [22, 23, 125, 126].

Microwave links have enabled impressive demonstrations of networked superconducting qubits [19, 127], but temperature constraints limit their reach to tens of meters within bespoke cryogenic setups. Maintaining cryogenic temperatures along extended microwave paths is impractical for city-scale or continental networks. Instead, photonic links using room-temperature optical fibre enable quantum information transfer using infrastructure identical to classical telecommunications. This vision – cryogenic quantum modules connected via fibre at separations ranging from meters to tens of kilometres – motivates the focus of this work.

2.3.1 Quantum Networks and Repeaters

Quantum networking distributes entanglement via flying qubits over long distances, enabling secure communication, distributed computation, and entanglement sharing between remote nodes. A 'Quantum Internet' [9] is a proposed architecture in which individual nodes are linked by quantum channels that preserve coherence, generating and distributing entanglement without requiring local qubit interactions.

Photonic qubits couple weakly to environmental noise, making them ideal carriers of quantum information. Telecom-wavelength photons near 1550 nm (200 THz) enable low-loss (< 0.2 dB/km) transport over optical fibre, but cumulative loss still limits direct point-to-point entanglement to less than a few hundred km. Quantum repeaters are intermediate stations that can store, purify, and retransmit entanglement, extending this reach to continental and global scales [128, 129].

Ground-based repeaters could be realised using spin-photon interfaces with long coherence times, efficient optical coupling, and compatibility with one of the low-loss windows in fibre (such as the C- or O-band). Examples of systems that could be used for such interfaces include those based on cold atoms, trapped ions, and rare-earth-doped crystals [128, 130]. Amongst the rare-earths, erbium naturally satisfies these requirements: long-lived spin states store quantum information [34], while optical transitions at 1.5 µm couple directly to fibre infrastructure [131]. The convergence of scalable local processing and long-range quantum communication is expected to enable distributed quantum computing systems, forming the backbone of future secure computational and sensing networks.

2.3.2 Requirements for Quantum Network Nodes

A functional quantum network node must satisfy several stringent requirements [9, 62, 132]:

1. **High-fidelity qubit control:** The qubit must be initialised, manipulated, and measured with fidelities exceeding error-correction thresholds (typically $> 99\%$ for gates, $> 99.9\%$ for readout).
2. **Quantum memory:** The qubit or an auxiliary memory must store quantum information coherently during entanglement generation and distribution, with coherence times exceeding typical network latencies (milliseconds to seconds).
3. **Spin-photon interface:** A coherent light-matter interface must couple qubits to optical photons with high efficiency and indistinguishability, enabling entanglement distribution over fibre links.
4. **Auxiliary qubits and Bell-state measurement:** Multi-qubit gates and projective measurements enable entanglement swapping, purification, and error correction—essential for quantum repeater protocols.

Achieving these requirements simultaneously—particularly deterministic spin-photon coupling—motivates the cavity QED approaches discussed in Chapter 4.

2.3.3 Modular Quantum Computers

The toolkit of quantum networking could provide a path to larger scale quantum computers than are currently possible. Modular architectures for computation partition qubits across independent cryogenic modules connected by quantum interconnects. These architectures are now being pursued by efforts developing superconducting qubits, spin qubits, and linear optical quantum computers [4, 17, 18].

Optical fibres enable distribution of quantum states using room-temperature photonic links between modules without thermal bridges, avoiding the heat load and Rent's rule bottlenecks of coaxial wiring. Distributed quantum computing demonstrations using photonic interconnects between trapped-ion modules validate this approach [133], which is now being pursued by large quantum computing companies [18]. From the theoretical side, architectures based on low-density logical qubit encodings are being explored to reduce the ratio of physical to logical qubits, and increase the 'range' over which qubits can interact [134]. To scale a system to thousands of logical qubits, modularity is a significant advantage.

Fault-tolerant quantum computers will be capable of solving practical problems require millions of physical qubits, operating continuously for estimated run-times which ranging from days to months [13]. Monolithic architectures concentrating all qubits in a single cryostat face wiring and thermal bottlenecks, and could be vulnerable to failures. Classical high-performance computing already distributes computation across and nodes within data centres. Quantum computers will likely follow a similar trajectory.

2.4 Quantum Photonics

The preceding sections established the key advantages of optical interconnects for scalable quantum systems. This section addresses the photonic engineering challenges—loss budgets, fabrication, and coupling—that constrain real-world implementations.

2.4.1 Ultra Low-Loss Budgets

Classical photonic systems are widely used for long distance information transmission. These systems regularly tolerate significant losses which are accounted for with simple optical amplifiers. Due to the no-cloning theorem, this would be catastrophic for quantum systems. In telecommunications, 3 dB (decibels) of insertion loss, corresponding to 50% transmission, is routinely acceptable. Each decibel of loss reduces system performance exponentially, and so quantum networks and photonic quantum computers require high efficiency interconnects, exceeding 99% per link.

Achieving these targets requires careful loss budgeting across every component. Fibre-to-chip coupling is a dominant loss source, with best-in-class couplers achieving <0.5 dB. On-chip, waveguide losses stem from sidewall roughness (scattering), material absorption, and bend radius. State-of-the-art silicon nitride waveguides achieve <1 dB/m through atomic-layer-deposition smoothing and annealing [135], but foundry-compatible processes often exceed 5 dB/m of loss.

Cumulative loss budgets demand optimisation across the full photonic circuit: emitters → waveguides → couplers → fibres, and detectors. For a single-photon source with 90% collection efficiency, 1 dB waveguide loss, and 1 dB coupling loss, end-to-end transmission is ~71%. Each additional decibel cuts transmission by 20%, making low-loss platforms and high efficiency protocols essential for practical quantum photonics.

2.4.2 Desirable Traits for Photonic Quantum Interconnects

Summarising the key points of this chapter, we arrive at a number of desirable traits for photonic quantum interconnects:

- **Light-matter interface:** The interconnect converts ‘stationary’ to ‘flying’ qubits, be they spin, superconducting, or other types. A high Cooperativity $C > 1$ is required for entanglement distribution. Achieving this with weak emitters requires cavity enhancement.
- **Telecom-band compatibility:** Operation within fibre transmission windows (ideally in the C-band) enables long-distance links. Interconnects that do not operate directly in one of the telecom windows will require a frequency conversion scheme for long distance communication.
- **Efficient photon collection:** Purcell enhancement directs emission into the desired optical mode of the cavity, and strong cavity-interconnect coupling maximises end-to-end transmission efficiency.
- **Long coherence times:** Spin coherence (T_2) must exceed photon round-trip times in network links (milliseconds to seconds), enabling quantum memory for entanglement storage and synchronisation.
- **Scalable architecture:** Repeatable fabrication, wavelength tuning, and frequency multiplexing are necessary for multi-node networks. Platforms must balance performance with manufacturability.

2.4.3 Rare Earth Ions for Photonic Interconnects

Multiple physical platforms are being explored for photonic quantum interfaces, each offering distinct trade-offs in dipole strength, coherence, wavelength compatibility, and scalability. Rare earth ions in solids are a particularly compelling candidate system, and are the focus of this thesis. They possess narrow and coherent optical and spin transitions, owing in part to their shielded $4f$ shell [136].

Ytterbium operates at 980 nm, thus requires frequency conversion for fibre networks. Europium ions have exhibited extraordinarily long coherence times, in excess of ten hours [25], but operate at 580 nm.

Of the rare earths, erbium ions uniquely satisfy the requirements for long-distance quantum networks: telecom-band operation for compatibility with photonics and fibre, good optical and spin coherence, and a spin structure that leads to $\sim$GHz splitting in moderate magnetic fields.

2.5 Summary

Scalable quantum information systems demand optical interconnects to overcome the fundamental constraints of heat, wiring, and latency. Fibre-optic links enable modular architectures—whether distributed quantum computers, long-distance quantum networks, or hybrid qubit platforms—by transferring quantum states between cryogenic modules without thermal bridges or Rent's rule bottlenecks. However, quantum photonics imposes stringent requirements on engineered systems: sub-decibel loss budgets, telecom-band operation, and deterministic spin-photon coupling for efficient entanglement distribution.

Multiple physical platforms are being explored, including quantum dots, defect centres, trapped ions, and rare-earth ions. Erbium ions in the solid state uniquely satisfy the requirements for long-distance quantum networks: their optical transition couple directly to fibre infrastructure, they have demonstrated long-lived spin states ($T_2 \sim 10$ ms) which can provide quantum memory, and shielded $4f$ electrons resist decoherence. However, erbium's weakly allowed optical transition results in extremely weak dipole coupling ($\sim$10 ms radiative lifetime)—approximately 1000× weaker than quantum dots or defect centres. This weak interaction necessitates cavity enhancement for single ion technologies.

Cavity quantum electrodynamics addresses this limitation by confining photons in ultra-high-Q resonators ($Q > 10^8$), amplifying light-matter interaction via the Purcell effect. Achieving strong coupling ($C > 1$)—where a single ion deterministically emits and absorbs photons—requires host materials with intrinsic loss below ∼0.1 dB/cm and precise positioning of ions at cavity field maxima.

This thesis explores CaF_2 whispering-gallery mode resonators as platforms for high-cooperativity erbium spin-photon interfaces. Calcium fluoride (CaF_2) whispering-gallery mode resonators satisfy these constraints: ultra-low material loss enables $Q > 10^{10}$, and the crystalline lattice accommodates erbium doping while maintaining optical quality. We target high cooperativity interactions with ions deep in the bulk of the substrate material, far from the effects of the surface. Chapter 3 introduces the physics of erbium ions and the principles of cavity QED, providing the theoretical foundation for the experimental work that follows.

"The understanding of the precise nature of these lines is a matter of considerable interest to chemists and physicists . . . I have referred to the entire subject as a 'puzzle' as far as existing knowledge is concerned."

J H Van Vleck, October 1936

3

Light-Matter Interactions with Erbium Ions

This chapter will outline the theoretical framework for the key research question of my thesis: whether or not it is possible to achieve high optical cooperativity in a single Er^{3+} that retains its 'bulk-like' coherence properties. I will motivate the choice of whispering-gallery mode resonators in erbium-doped calcium fluoride for our experiments, first by focusing on ion and material properties, and then introducing the concepts of cavity quantum electrodynamics.

I begin by introducing the rare-earth ions as a candidate physical system to realise quantum light matter interfaces. The energy level structure of the rare-earth ions is outlined, including an identification of how the selection of ion, host, and site affect these properties. The specific properties of Er^{3+}:CaF_2 are discussed, motivating this material system for our crystal-field engineering study. I then provide the theoretical framework for coupling single emitters to optical cavities in a cavity quantum electrodynamics architecture. I highlight the importance of cooperativity, and finally will arrive at a description of the two methods of achieving high optical cooperativity that this thesis focuses on – engineered crystal field, and high Q/V resonators.

3.1 Solid State Spectroscopy of Rare Earth ions

Solid-state spectroscopy is a well-established field, dating back to before the development of the first laser. Optical centres of many kinds — single atoms, complexes, and defect centres for example — have been examined in a range of materials: bulk monocrystals, nanoparticles and powders, and glasses. Optical centres which possess a spin degree of freedom are a promising route towards building quantum network devices and demonstrations - notably light-matter interfaces [9].

Rare-earth ions in solid state hosts are a particularly interesting subclass of solid-state emitters. When in their 3^+ ionisation state in solids, they have narrow $4f \longleftrightarrow 4f$ transitions, which are only slightly perturbed by their host, leading to similar transition frequencies no matter which solid they are in. Depending on the ion and isotope species, rare-earth ions can have both electron and nuclear spin degrees of freedom, which yields optical access to processes with very long T_1 and T_2 [34, 51].

Rare-earth ions have been studied extensively in a number of hosts, with key technologies such as the Nd^{3+}:$Y_3Al_5O_{12}$ laser emerging from the field. They have proven performance for quantum applications in the single instance and ensemble regimes [26, 30, 52, 53, 137, 138], as well as for classical photonics as filters and references [139, 140]. That said, the precise connection between optical transition dipole moments and their nanoscopic environment is not yet well understood [141].

The optical linewidths of the $4f \longleftrightarrow 4f$ transitions of the rare earths are some of the narrowest in the solid state. In Y_2SiO_5, a linewidth of 73 Hz has been measured [142]. One reason for their particularly narrow homogeneous linewidths is that the $4f$ electrons - which comprise the the ions' valence shell - sit inside a number of completely filled electron shells. This provides a layer of electrostatic shielding, putting the $4f$ shell into a structure akin to a Faraday Cage. This leads to the $4f$ electrons being partially decoupled from perturbations in the local electrostatic environment, which produces the aforementioned effects of small perturbations on optical transitions, no matter the host.

However these electric dipole transitions are relatively weak. In a free-ion, the $4f \longleftrightarrow 4f$ electric dipole transitions are forbidden by selection rules - it is only the presence of a crystal field that breaks parity conservation, by mixing $4f^N$ wavefunctions with components from higher orbitals. This leads to mixed-parity $4f$ wavefunctions, and thus weakly allows electric dipole transitions [141, 143]. This means that transition photon rates remain relatively slow in crystal fields (often on the order of hundreds of Hz).

The relative weakness of transitions leads to long optical and spin-state lifetimes: $4f \longleftrightarrow 4f$ transitions with excited state lifetimes on the order tens of milliseconds [144, 145] have been observed. Electron and nuclear spin degrees of freedom are also present, with nuclear spins having lifetimes measured in units of hours or days [51].

The weak optical dipole moment – generally less than 1×10^{-28} C· m [143] – can be compensated for by simply increasing the strength of the optical field. Increasing optical power and decreasing beam size both come with their sets of engineering challenges. Increased power may not be appropriate for the measurement setup or for the application. An alternative to simply increasing optical power or decreasing beam size is to increase the strength of the optical field using an optical cavity [146–148]. An optical cavity modifies the local density of available optical modes into which the ion can emit, enhancing the interaction between the rare-earth ion optical transition and light.

3.1.1 Introducing the Rare Earths

The rare-earth ions, also known as the lanthanides, span across the periodic table from lanthanum to lutetium (La to Lu), and the set also includes yttrium and scandium (Y and Sc). They have been of considerable interest to spectroscopists for many decades, since they were noted to have narrow and coherent linewidths no matter which host they were doped into[136]. These optical transitions give access to optically addressable electronic and nuclear spin states, making lanthanides uniquely suited for quantum technology applications. In the specific case of Er^{3+}, the ground state to lowest excited state transition occurs reliably at or near 1.5μm, close to the current minimum optical loss in fibre (about 0.2 dB/km). This section will formally introduce rare-earth ion spectroscopy, discussing the physical properties that lead to these remarkable properties and outlining their energy level structure, with a particular focus on erbium.

When ionised in solids, the lanthanides generally take on the 3^+ charge state, so their electronic configuration is described by $[\mathrm{Xe}]4f^n$ - where n ranges from 0 to 14 as the $4f$ shell fills. In the case of Er^{3+}, our species of interest, atom lose 2 electrons from the $5s$ and one from the $4f$ shell [143]. This partially filled $4f$ shell – the valence shell – has its radial distribution mostly inside the $5s$ and $5p$ shells. Figure 3.1 shows the radial probability density functions of the $4f$, $5s$, and $5p$ shells in Gd^+.

The $4f$ electron shell's radial distribution also leads to a phenomenon known as the lanthanide contraction. This is a decrease in atomic (and hence ionic) radii as atomic number increases across the lanthanide series, counter to the trend in other atomic species. This occurs because

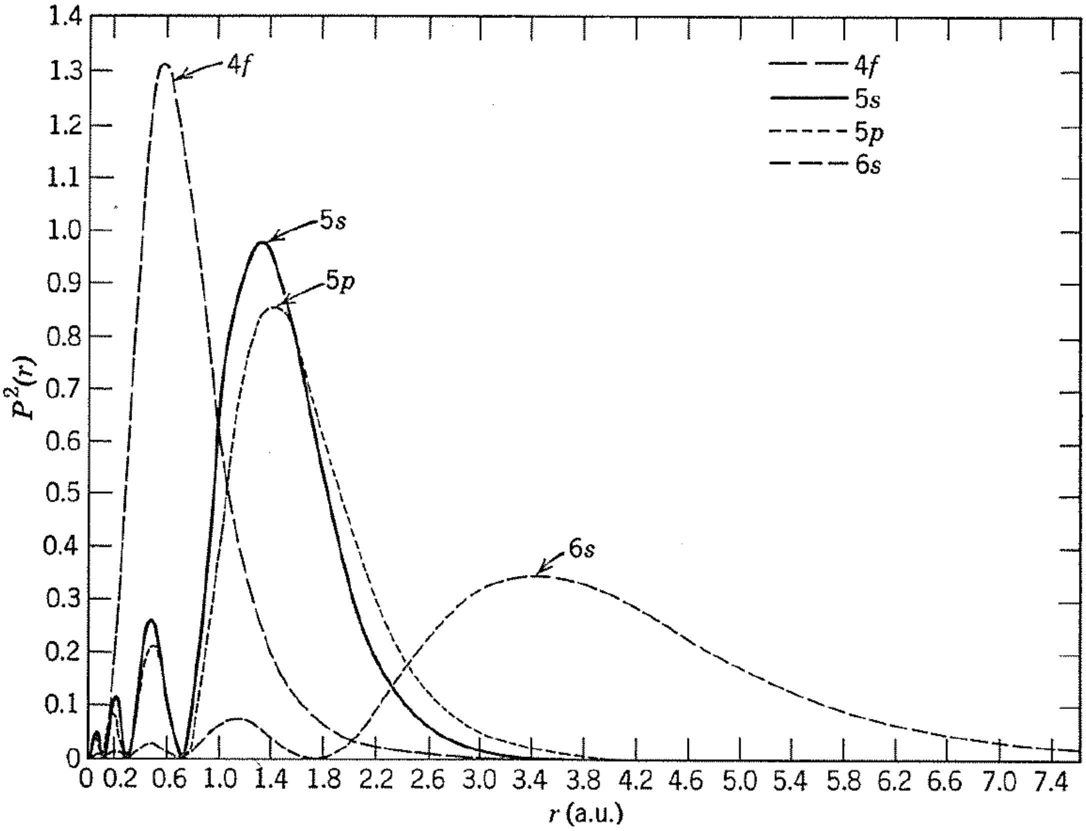

Figure 3.1: The radial probability distribution ($P^2(r)$) of the $4f, 5s, 5p, and 6s$ wavefunctions of Gd$^+$. Reproduced from [149].The $5s^2 5p^6$ shells surrounding the $4f$ shell - leading to shielding for its electronic states and transitions.

the inner $4f$ electrons of the lanthanides do not effectively shield the outer valence electrons from the increasing positive nuclear charge. As a result, outer electrons are pulled closer to the nucleus, leading to a 20% decrease in atomic (ionic) radius across the series [150].

3.1.2 The $4f$-shell Hamiltonian

The rare-earth ion transitions which are most commonly used for quantum information applications are the $4f \longleftrightarrow 4f$ transitions [152]. While these transitions are extremely narrow and characteristically have a long excited state lifetimes, it should be noted that many other optical transitions exist in the rare-earth ions. The $4f$-$5d$ transition is considerably broader, higher in energy, and has a shorter lifetime than the $4f \longleftrightarrow 4f$ transition. These have been used in the past as a method of speeding up optical detection of single rare-earth ions [49].

The linewidths of spin transitions of electrons within the valence shell may also be very narrow. Where $4f \longleftrightarrow 4f$ transitions can be thought of as ways to arrange electrons within the 14 available positions in the valence shell. Spin states correspond to the various values

Atomic number	Element	Electron configuration RE^{3+}	Ground state RE^{3+}	Ionic radius RE^{3+} (pm)
21	Sc	$3d^0$	$^1S_0$	87
39	Y	$4d^0$	$^1S_0$	101.9
57	La	$4f^05s^25p^6$	$^1S_0$	116.0
58	Ce	$4f^15s^25p^6$	$^2F_{5/2}$	114.3
59	Pr	$4f^25s^25p^6$	$^3H_4$	112.6
60	Nd	$4f^35s^25p^6$	$^4I_{9/2}$	110.9
61	Pm	$4f^45s^25p^6$	$^5I_4$	109.3
62	Sm	$4f^55s^25p^6$	$^6H_{5/2}$	107.9
63	Eu	$4f^65s^25p^6$	$^7F_0$	106.6
64	Gd	$4f^75s^25p^6$	$^8S_{7/2}$	105.3
65	Tb	$4f^85s^25p^6$	$^7F_6$	104.0
66	Dy	$4f^95s^25p^6$	$^6H_{15/2}$	102.7
67	Ho	$4f^{10}5s^25p^6$	$^5I_8$	101.5
68	Er	$4f^{11}5s^25p^6$	$^4I_{15/2}$	100.4
69	Tm	$4f^{12}5s^25p^6$	$^3H_6$	99.4
70	Yb	$4f^{13}5s^25p^6$	$^2F_{7/2}$	98.5
71	Lu	$4f^{14}5s^25p^6$	$^1S_0$	97.7

Table 3.1: Electronic configurations, ground states, and ionic radii of trivalent lanthanides [150, 151].

of total electron angular momentum that such arrangements can have, many of which are degenerate for cases where the ion is not in a magnetic field.

3.1.3 Host-dependent properties

In the case of a ‘free’ rare-earth ion, without the effects of the crystalline environment, the $4f \longleftrightarrow 4f$ electric dipole transitions are parity-forbidden. It is only via the ion’s placement into the electrostatic potential of a solid-state host that these electric dipole transitions become weakly allowed, via an increase in the admixture of wavefunctions of opposite parity, such as the $5d$ energy states into the otherwise "pure" $4f^N$ wavefunction [136]. Precise knowledge of the crystal field is critically important to understanding the properties of rare-earth ion energy levels and transition properties.

While the optical transitions of a given rare-earth ion are always relatively close in frequency, site- and material-specific crystal field properties do affect energy levels and states, and hence transition frequencies and rates. For example, the work presented in this thesis shows Er^{3+} excited state lifetimes ranging from >30 ms in cubic (O_h) sites to close to 11 ms in C_{3v} sites in CaF_2, compared to 9 ms in the C_1 site of Y_2SiO_5 [145], and even shorter in higher index materials such as silicon [153]. This link between crystal field parameters and dipole moments is central to this work. Some work has been conducted, particularly studying the optical properties of Nd:YVO_4 [141], but no generalised model yet exists.

Site symmetry also governs magnetic response: the g-tensor is anisotropic and depends on point group symmetry, as explored in Chapter 6 through magnetic field rotation studies. The field of study concerned with modelling and understanding these crystalline interactions is called crystal-field theory - and the enthusiastic reader is directed to Chapters One and Two of [143] for a thorough treatment.

The remarkable similitude that these ions have no matter which host they sit in is well captured by the famous 'Dieke Diagram' (Figure 3.2). This plot summarises the atomic-like multiplets arising from electron-electron interactions and spin-orbit coupling in lanthanides doped into LaF_3. The differences due to the host environment in dipole moment, magnetic sensitivity, and energy level structure are all many orders of magnitude smaller than the energy scales expressed in the Dieke Diagram, and can be treated as subsequent perturbations to the free-ion Hamiltonian. These are outlined in the following sections.

3.1.4 Electronic Energy Levels

In this section, I will outline the order and energy scales of perturbations to the rare-earth ion energy levels, starting with the intrinsic terms (ion properties), and following with extrinsic terms (those that vary with applied magnetic or electric fields - the variables we can control in an experiment). The Hamiltonian generally takes the form [143]:

$$\hat{\mathcal{H}} = \hat{\mathcal{H}}_{\mathrm{FI}} + \hat{\mathcal{H}}_{\mathrm{CF}} + \hat{\mathcal{H}}_{eZ} + [\hat{\mathcal{H}}_{nZ} + \hat{\mathcal{H}}_{\mathrm{HF}} + \hat{\mathcal{H}}_{\mathrm{Q}}] \tag{3.1}$$

where $\mathcal{H}_{\mathcal{FI}}$ is the Free-Ion Hamiltonian, $\mathcal{H}_{\mathrm{CF}}$ represents the Crystal-Field Hamiltonian, $\mathcal{H}_{eZ}$ the Electronic Zeeman Hamiltonian, $\mathcal{H}_{nZ}$ the Nuclear Zeeman Hamiltonian, $\mathcal{H}_{\mathrm{HF}}$ represents the Hyperfine Hamiltonian, and finally $\mathcal{H}_{\mathrm{Q}}$, the Quadrupole Hamiltonian. The last three terms (Nuclear Zeeman, Hyperfine and Quadrupole) are only relevant to isotopes with nuclear spin - in the case of erbium, this is only ^{167}Er, with a nuclear spin of $I = 7/2$. Each of these terms is placed in order of their energy scale in the above equation: the free-ion energy levels are generally spaced by optical energies (~200 THz in the case of Er^{3+}), crystal field splittings are generally on the order of ~1-10 THz. Quadrupole splittings are on the order 10s of MHz, and hyperfine splittings can vary: Kramers ions can have large splittings (GHz for Yb and Er [124, 155]), while non-Kramers ions have small hyperfine terms (Eu and Pr in the 10s-100s of MHz [65]). The field dependent Zeeman terms range from 60-200 GHz/T for electronic

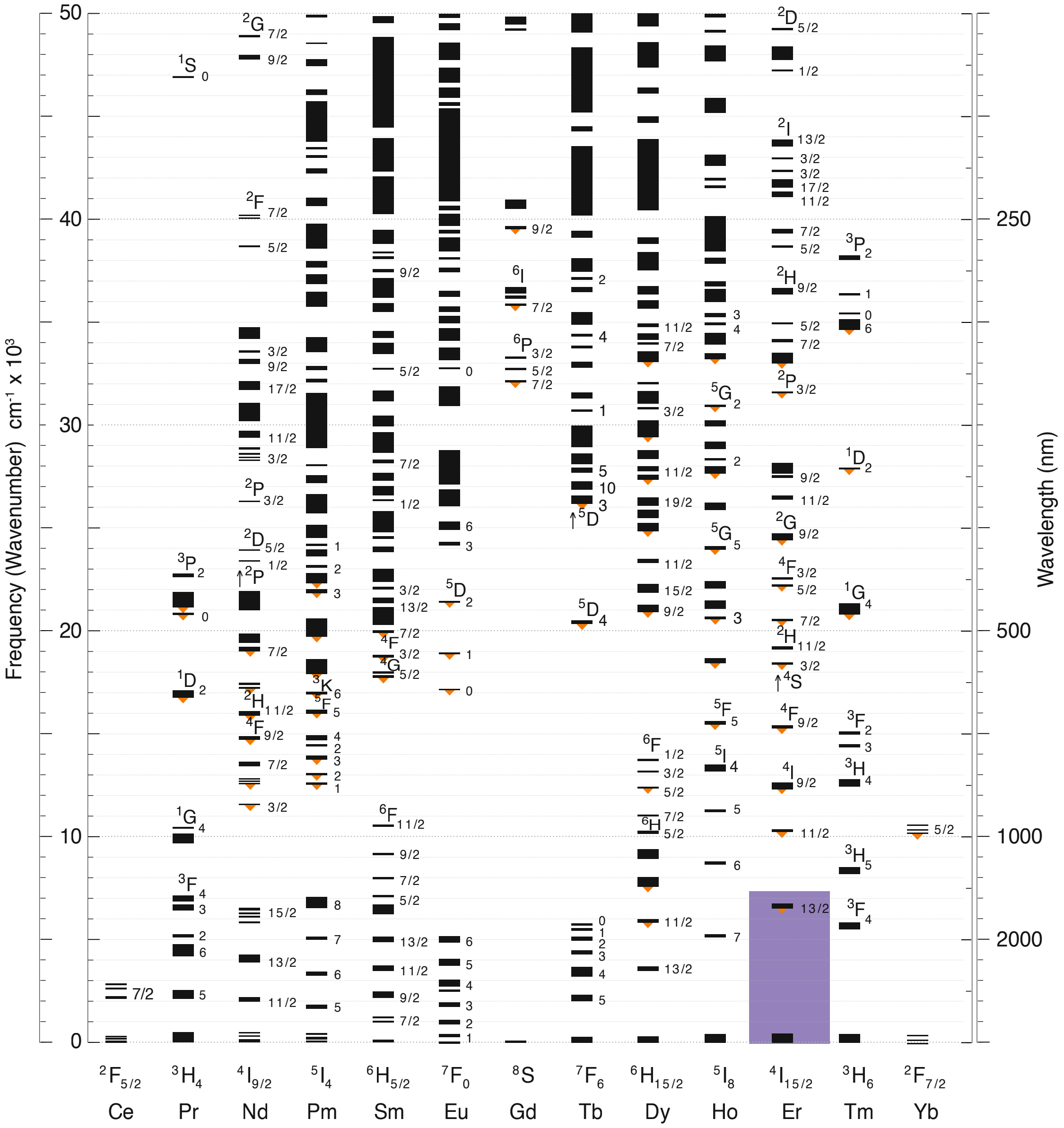

Figure 3.2: The Dieke Diagram - adapted from a version supplied by R.L Ahlefedlt, originally adapted from [154]. This diagram shows the $4f$ electronic energy levels of trivalent rare-earth ions in LaF_3, based on the free-ion and crystal-field Hamiltonian terms. The purple shaded region highlights the Er^{3+} transition which is explored in this work, the $^4I_{15/2} \longleftrightarrow {}^4I_{13/2}$ optical transitions, that are all close to 1550 nm (200 THz, or in wavenumbers 6500 cm^{-1}). Orange arrows highlight excited state levels with radiative decay.

Zeeman, and 10s of MHz/T in the case of Nuclear Zeeman terms. These energy scales are shown in Figure 3.4

Intrinsic Effects

The following *intrinsic* effects are energy level splittings that are always present in the rare-earth ion system, presented in order of energy scale.

Free Ion Hamiltonian

The free ion Hamiltonian captures intra-$4f$ shell interactions, with contributions from kinetic/potential energy ($\hat{\mathcal{H}}_0$), electron-electron Coulomb repulsion ($\hat{\mathcal{H}}_c$), and spin-orbit coupling ($\hat{\mathcal{H}}_{s.o.}$). The Coulomb term splits the $4f^N$ configuration into ${}^{2S+1}L$ states (where $S = \sum_i s_i$ and $L = \sum_i l_i$ are the total spin and orbital angular momentum operators), while spin-orbit coupling further splits these into ${}^{2S+1}L_J$ manifolds with $2J+1$ levels each (where J is the total angular momentum, taking values $|L-S|$ to $L+S$). These manifolds—visible in the Dieke diagram (Figure 3.2)—are separated by optical energies (200 THz for Er^{3+}).

The Crystal Field

When an ion is introduced into a crystal, the electrostatic potential of its environment—the crystal field—splits each J manifold into crystal field (or Stark) levels with characteristic splittings on the order of ∼1-10 THz, though can be as low as tens of GHz [124]. The number and degeneracy of these levels depends on the point group symmetry of the ion site. Using the formalism described by Wybourne [149], the crystal field Hamiltonian takes the form:

$$\hat{\mathcal{H}}_{CF} = \sum_{i}^{N} \sum_{k,q} B_q^k \hat{C}_q^{(k)}(i) \tag{3.2}$$

where $\hat{C}_q^k$ are Racah spherical tensor operators and B_q^k describes the strength of electric field components acting on the ion. The point group symmetry of the site (e.g., C$_{3v}$, C$_{4v}$) governs selection rules and the ion's response to applied fields—for example, a C$_{3v}$ site exhibits identical behaviour under 120° rotations about its symmetry axis.

For Kramers ions (those with odd $4f$ electron count), each J level splits into electronic doublets that remain degenerate at zero magnetic field. In higher symmetry sites, some degeneracy persists even for non-Kramers ions. Crystal field levels are labelled with Γ_i according to their irreducible representations, providing shorthand for predicting selection rules between levels [143, 156]. Extensive crystal field modelling is beyond the scope of this work but is detailed in [157, 158].

Magnetic Hyperfine Splitting

For isotopes with non-zero nuclear spin, the hyperfine interaction between nuclear and electronic magnetic moments produces splittings that vary per ion, between tens of MHz to a few GHz [159–164]. For Kramers ions such as ^{167}Er, this takes the form:

$$\hat{\mathcal{H}}_{HF} = \hat{I} \cdot A \cdot \hat{S} \tag{3.3}$$

where A is the hyperfine tensor, $\hat{I}$ is the nuclear spin operator, and $\hat{S}$ is an effective spin-half operator for the electronic angular momentum.

Nuclear Quadrupole Splitting

The nuclear quadrupole term arises from two contributions: genuine quadrupolar coupling between the electric field gradient and the nuclear quadrupole moment, and the second-order hyperfine (pseudo-quadrupole) interaction [143]. These combine into an effective quadrupole tensor:

$$\hat{\mathcal{H}}_{Q} = \hat{I} \cdot Q \cdot \hat{I} \tag{3.4}$$

where Q contains both contributions. Quadrupole splittings are typically on the order of hundreds of kHz to a few MHz [165].

Field-Dependent Terms

The following terms in the Hamiltonian depend on the strength and direction of an applied magnetic field:

Electronic Zeeman Effect

The Electronic Zeeman Hamiltonian describes the interaction between the electrons of the $4f$ shell and an applied field. It is given by

$$\hat{\mathcal{H}}_{eZ} = \mu_B B \cdot (\hat{L} + g_s \hat{S}) \tag{3.5}$$

where B is the applied magnetic field, g_s is electron spin g factor, and $\hat{L}$ and $\hat{S}$ are the electronic and spin angular momentum operators, respectively. In the case of Er^{3+}, the energy splitting of spin states is $\mathcal{O}(1 - 100)$ GHz/T, and can be anisotropic.

Experimentally, this leads to the splitting of one optical transition at zero field into four distinct lines at finite field. Each of the ground and excited state split into a ‘spin-up’ and ‘spin-down’ level (shown in Figure 3.3). The relative intensities of these lines depend on transition selection rules and the population occupying each of the spin states, which is primarily governed by the temperature of the spins.

This motivates studies of rare-earths in magnetic fields in excess of 100 mT, and at low temperatures (below 1K). This ensures that the only thermally occupied state is the lowest energy spin state of the system.[1]

At high fields or when crystal field levels are closely spaced, nonlinear effects such as quadratic Zeeman splitting may become significant [143].

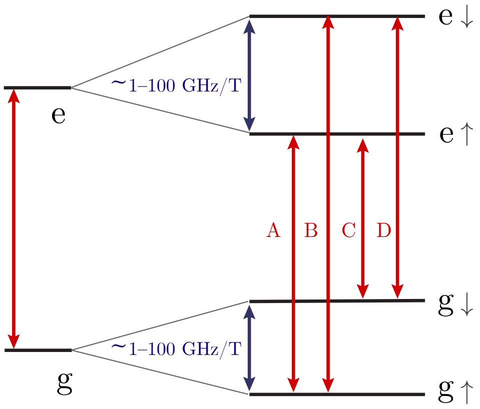

Figure 3.3: A cartoon image of an Er^{3+} optical transition splitting into four visible lines in the presence of a magnetic field. The scale of splittings is accurate for erbium sites, though these vary depending on host, site, and magnetic field. **Blue** transitions are addressable with microwave electronics, while **red** transitions are addressable with lasers.

Nuclear Zeeman Effect

For rare-earth ions with nuclear spin, such as ^{167}Er, a Nuclear Zeeman term must also be added to the Hamiltonian. Similar in form to the Electronic Zeeman term, but vastly smaller in energy scale, this describes an interaction between the magnetic dipole of the nucleus of an ion and an applied magnetic field. It is given by:

$$\hat{\mathcal{H}}_{nZ} = -g_n \mu_N B \cdot \hat{I} \tag{3.6}$$

where $g_n = \frac{\mu}{\mu_N I}$ is the nuclear spin g-factor, μ_N is the nuclear magneton and $\hat{I}$ is the nuclear spin angular momentum operator. A tabulated list of magnetic moments μ for all ions is available in reference [166].

---

[1] A useful heuristic to convert between energy scales and temperatures is that 1 Kelvin is approximately 20 GHz. This means that for temperatures below 1K, spin-states split by >20GHz will start to predominantly thermalise into the ground state, at a rate given by Boltzmann.

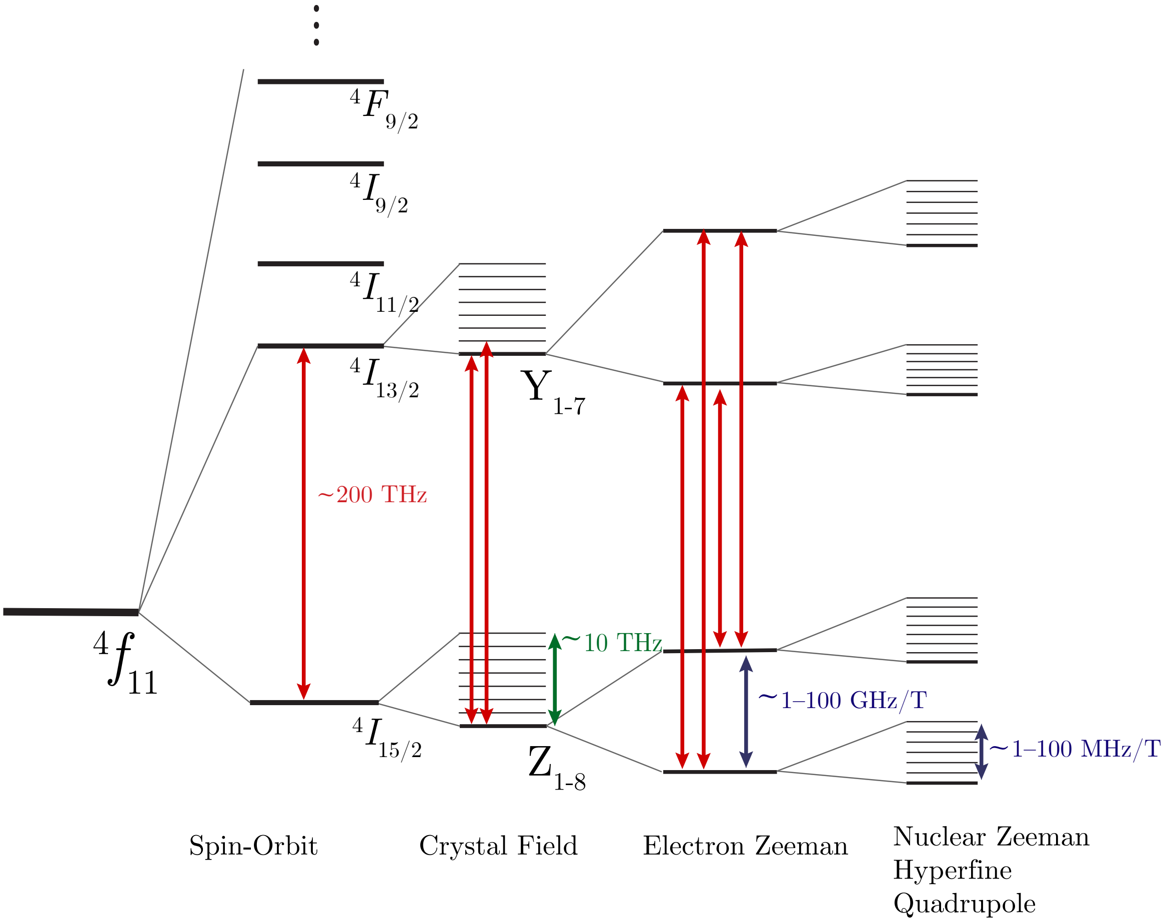

Figure 3.4: The Energy Levels of Er^{3+}in various crystal hosts, showing the hierarchy of splittings from the $4f$ shell down to nuclear Transitions which can be addressed using our laser are highlighted in **red**. It is important to note that we can address $Z_1 \longleftrightarrow Y_1$ and $Z_1 \longleftrightarrow Y_2$ transitions for all sites of interest, however we can not address every one of the higher $Z_1 \longleftrightarrow Y_i$ transitions, since their frequencies become too high (wavelengths too short) for our laser system. Transitions that can be addressed with microwave electronics are shown in **blue**. Note that these can also be addressed using modulated optical pulses – such as Raman Heterodyne, optically detected magnetic resonance (ODMR), or other forms of two-photon spectroscopy. **Green** transitions (in the few THz) are not directly accessible with one laser.

Additional Interactions

Stark Effect
In polar sites, energy levels exhibit first-order sensitivity to applied electric fields. DC Stark shifts enable tuning of optical transition frequencies by tens of MHz for fields of 100 V/mm [167], while AC Stark effects from optical fields can produce similar splittings [168]. This sensitivity has enabled demonstrations of deterministic ion addressing in nanophotonic cavities [57, 169, 170]. Stark sensitivity - and hence electrical tunability - is an advantage of the C_{3v} symmetry sites examined in this work for future single-ion experiments.

Spin-Spin Interactions
Interactions between neighbouring electronic and nuclear spins (superhyperfine coupling) can create additional spectral structure - whose scale depends on the species and magnitude of the nearby spin [171]. While this can contribute to spectral diffusion and decoherence, as discussed in Section 3.1.7, these spin-spin interactions can also serve as a resource. A number of demonstrations have shown intentional coupling to spins near to single rare earth ions [54, 55], and the use of ions in 'satellite lines' for computation in stoichiometric rare-earth crystals has been proposed [172].

3.1.5 Spin-Hamiltonian Modelling

The tensor-and operator based formalism presented in the previous sections hints at the methods of modelling the energy levels of rare-earth ions which are commonly used in the field - a parameterised 'Spin Hamiltonian' model for rare-earth ion sites of interest can be developed from spectroscopic investigations, and used to predict or explain other experimentally observed behaviour. For excellent examples of the genre, see [52, 124, 159, 173, 174], and calculations extended from such studies in [160, 164].

It is important to note that the tensors including g, Q, and A may not have the same principle axes - so careful attention must be paid when modelling these systems, applying rotations to each of the respective tensors to bring them into a common co-ordinate system.

3.1.6 Transition Properties of Rare-Earth Ions

Up until this point, we have examined the energy level structure of the rare-earth ions – deriving a Hamiltonian whose eigenvalues are the allowable spin states of a rare-earth ion system, and described mechanisms that broaden or shift those energy levels. The following section examines these transitions closely, noting the timescales of lifetimes and coherence times for rare-earth excited states, what governs selection rules for these transitions, and which mechanisms lead to decoherence in rare-earth ion systems. This section examines transition dynamics, characteristic timescales, and the factors governing coherence for optical and spin degrees of freedom.

Optical Transitions

Optical transitions between crystal field levels of different J manifolds (e.g., ${}^4I_{15/2} \leftrightarrow {}^4I_{13/2}$ in Er^{3+}) exhibit excited state lifetimes T_1 ranging from hundreds of microseconds to tens of milliseconds, depending on the ion and host. These lifetimes are long for optical transitions, reflecting the parity-forbidden nature of $4f \leftrightarrow 4f$ electric dipole transitions – the transitions are only weakly allowed by the admixture of opposite-parity states through the crystal field.

Optical coherence times T_2^{opt} are typically microseconds to tens of microseconds in dilute bulk crystals at low temperature, limited primarily by spectral diffusion from spin bath fluctuations. Applied magnetic fields can extend coherence by reducing sensitivity to magnetic noise. In some cases where the entire nearby spin environment can be polarised, this can extend to hundreds of µs [44].

Electron Spin Transitions

For Kramers ions at a non-zero magnetic field, electronic spin transitions are present. These exhibit different dynamics to optical transitions. Direct phonon processes dominate relaxation at low temperature, with rates scaling approximately linearly with temperature below ~10 K.

Electronic spin coherence times T_2^{spin} can reach milliseconds in isotopically purified or nuclear-spin-free hosts, limited by fluctuations in the local magnetic field from nearby electronic and nuclear spins [52, 175]. Dynamical decoupling sequences can extend effective coherence by refocusing low-frequency field fluctuations [176–178].

Nuclear Spin Transitions

For isotopes with non-zero nuclear spin, such as ${}^{167}\mathrm{Er}$ ($I = 7/2$), the nuclear spin degree of freedom can also be accessed. The weak magnetic moment of the nucleus and its isolation from phonon coupling lead to exceptional coherence properties. Nuclear spin T_1 times can exceed hours to days [179, 180].

Nuclear spin coherence times T_2^{nuc} are also considerably longer than the other degrees of freedom. Values in excess of ten hours for ${}^{151}\mathrm{Eu}^{3+}$:$\mathrm{Y_2SiO_5}$at 1.4 K [25], and over a second for Er^{3+}:$\mathrm{Y_2SiO_5}$[34]. These remarkable properties position nuclear rare-earth ion spins as quantum memories, accessible through the optical transition for initialisation and readout while remaining largely decoupled from environmental noise during storage.

This hierarchy of timescales—optical (μs), electronic spin (ms), nuclear spin (hours)—enables sophisticated multi-level quantum information processing schemes, suitable for Quantum Networks, particularly when considering the requirements for quantum networks discussed in Section 2.3.2, and the desirable traits for photonic interconnects outlined in Section 2.4.2. Optical transitions provide fast gates and network connectivity, electronic spins serve as working qubits, and nuclear spins act as long-lived memory, all within a single physical system [9, 46, 181].

Other Transitions

Transitions between crystal field levels within one J manifold are at THz frequencies (1–20 THz) and in general have very short excited state lifetimes. These transitions are generally less technologically useful, as non-radiative multi-phonon decay dominates in most systems, leading to loss of coherence.

3.1.7 Homogeneous Broadening and Decoherence

Thus far we have examined an idealised case – a single ion in a known site in a static, defect-free crystal lattice. This is of course fictitious - however all is not lost.

The interactions of single (and ensembles of) rare-earth ions with their host environments are well-understood, and in some cases, the broadening or splitting of spectral features is of benefit when designing quantum hardware based on rare-earth ions. It is worth noting too that many of the effects described herein can be modelled using the same perturbative approach as described in Section 3.1.4.

Homogeneous Broadening

Homogeneous broadening describes the linewidth of a single ion. It can be calculated from the optical excited state lifetime T_1 and dephasing rate:

$$\Gamma_h = \frac{1}{2\pi T_1} + \Gamma_\phi \tag{3.7}$$

where Γ_ϕ is the dephasing rate – which is caused by other dynamic processes in the host, such as electric and magnetic noise. As noted above, rare-earth ion lifetimes can often be long (T_1^{opt} on the order of 10 ms [143]), and so these homogeneous linewidths can be relatively small (Γ_h as low as 10s of Hz).

This being said, the finding the pure dephasing rate is challenging, and a more 'experimentally common' approach is to calculate this after having measured an excited state lifetime T_1 and a homogeneous linewidth from a coherence time T_2 – a much easier quantity to measure in a lab. Homogeneous linewidth and T_2 are related by:

$$\Gamma_h = \frac{1}{\pi\, T_2} \tag{3.8}$$

T_2 directly captures the effects of all decoherence mechanisms - including spin flips and spectral diffusion.

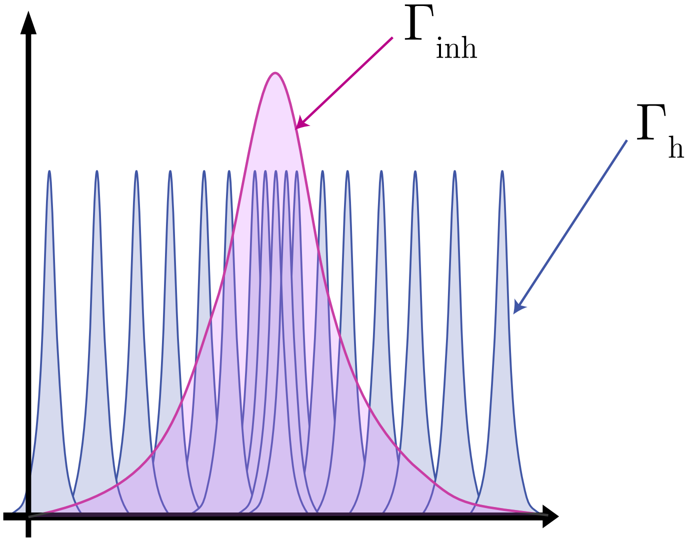

Figure 3.5: The inhomogeneous linewidth of an ensemble of emitters Γ_{inh} is comprised of many homogeneous lines Γ_h. Adapted from figures originally in [182]

The mechanisms that produce broadening in the frequency domain also produce decoherence in the time domain. Understanding these mechanisms is essential for designing quantum devices and motivates the architectural choices explored in this thesis. I describe a number of these here:

Phonon-Induced Decoherence

Coupling between electronic states and lattice phonons introduces both temperature-dependent broadening and pure dephasing. Direct single-phonon processes dominate at low temperatures, with decoherence rates scaling approximately linearly with temperature below ∼10 K [26]. At higher temperatures, two-phonon Raman and Orbach processes become significant, introducing stronger temperature dependence. The effectiveness of the $5s$ and $5p$ shell screening means phonon coupling to the $4f$ electrons remains relatively weak compared to other solid-state emitters, enabling optical coherence times exceeding microseconds even at liquid helium temperatures [51].

Spectral Diffusion

Spectral diffusion—the slow, stochastic wandering of transition frequencies—arises from fluctuations in the local environment. Sources can include spin flips from neighbouring electronic and nuclear spins, charge fluctuations of nearby defects, and strain field dynamics [183]. In rare earth ensembles, spectral diffusion typically dominates over phonon processes in determining optical coherence, with characteristic timescales ranging from microseconds to milliseconds depending on material purity and ion concentration [26]. Instantaneous spectral diffusion—where optical excitation of the ensemble itself perturbs the local field—can be mitigated through careful experimental design and low ion concentrations [184].

Surface-Induced Decoherence

Ions located within an optical wavelength of material surfaces are more likely to experience increased decoherence, when compared to those deep in the bulk. It has been shown that a well-prepared surface produces no excess broadening nor spectral diffusion mechanisms for Pr:YSO [65], however near-surface ions are more likely to be exposed to increased charge noise from dangling bonds and adsorbates. Along with this, surface ions experience enhanced phonon coupling due to modified acoustic modes near boundaries, and strain from surface damage. This is particularly relevant for ions in polar (and hence electric field sensitive) sites in nanophotonic devices [50].

This surface sensitivity highlights a trade-off in cavity QED architectures for rare earth ions: achieving strong interactions with small cavities leads to the loss of bulk-like coherence properties. The whispering-gallery mode resonator approach explored in this thesis addresses this tension by achieving high quality factors in large mode volumes, enabling placement of ions many wavelengths from surfaces while maintaining sufficient Q/V for enhanced light-matter interaction.

Material Quality and Ion Environment

Crystal quality profoundly affects coherence. Inhomogeneous strain from dislocations and defects broadens spectral distributions and drives spectral diffusion [183]. Dopant and impurity concentrations determine spin bath strength, while isotopic composition affects magnetic noise [171]. Single ion efforts have targeted host crystals composed of nuclei with zero spin where possible [185]. Hosts of non-zero spin (e.g., ^{19}F in CaF$_2$) interact with rare-earth ions via the superhyperfine interaction [186, 187]. Trivalent rare earths can also substitute for aliovalent atoms in their host. This charge must be compensated, and the mechanism of that compensation can produce site-dependent crystal field variations and local strain, affecting both optical properties and coherence [68, 143, 156, 157, 188]. Our investigations of the sites in calcium fluoride examine this closely.

3.1.8 Inhomogeneous Broadening

In the case of an ensemble of rare-earth ions, each individual ion has a a linewidth equal to Γ_h. However the central frequencies of these lines are placed following a distribution known as the inhomogeneous linewidth. Due to the large number of ions in even the most dilute of samples, this takes the form of a continuum, which is generally several orders of magnitude larger than the homogeneous linewidth, as shown in Figure 3.5.

This linewidth depends not only on the host crystal's constituents, but the specific sample: ion concentration, proximity of ions to the surface, defects, inclusions and grain boundaries in the lattice affect the inhomogeneous line, or add satellite structure to the line [43, 172]. Experimental configuration may also affect inhomogeneous linewidth: strain and inhomogeneous magnetic fields are often common features of cryogenic measurement of dielectric crystals.

In the case of Er^{3+}in crystals with a low concentration of defects or other impurities, the profile of the inhomogeneous line is a Voigt Profile with a linewidth anywhere between 10s of MHz (Er^{3+}:Y$_2$SiO$_5$bulk crystals [139]) and 10s of GHz (nanoparticle samples [30, 189]).

As such, there is no 'one single' mathematical description of inhomogeneous broadening, but there are models for different regimes of some of the above parameters. For samples with dilute concentration of rare-earth ions, a low concentration of uncharged defects will yield a Lorentzian inhomogeneous line. As the concentration of charges increased, this is convolved with a Gaussian distribution, until at a sufficiently high concentration the line shape is simply a Gaussian [183].

3.1.9 Refractive Index Corrections to Transition Rates

The relationship between intrinsic dipole moment and measured transition rates contains a refractive index dependency that must be considered when making comparisons between hosts. The Einstein A coefficient scales as $A_{21} \propto n^5$, where n is the refractive index, while measured absorption coefficients scale as $\alpha \propto n$ [190, 191]. These dependencies arise from the local field correction and mode density in dielectrics – photons couple differently to the same dipole, depending on the surrounding medium. The interested reader is directed towards [190, 191], and M.F. Reid's Chapter in [143].

We use the same framework as Reid, with the implication being that the *intrinsic* electric dipole moment μ of an atomic transition is independent of refractive index. This means that transitions in ions in lower-index materials, may "be stronger than they appear" when comparing radiative rates with those in higher index materials. As an example, considering two optical transitions in $\mathrm{CaF_2}$ ($n \approx 1.43$) and $\mathrm{Y_2SiO_5}$ ($n \approx 1.8$): a factor of ∼2 in the measured lifetimes could arise purely from the $(1.8/1.43)^3 \approx 2$ refractive index scaling, obscuring the differences in dipole moment μ without some consideration. For cavity QED applications, this consideration becomes essential.

3.1.10 Transition Selection Rules and Polarisation Sensitivity

Transition selection rules in rare-earth ions arise from symmetry properties of electronic states and operators, dictating allowed optical and spin transitions. Polarisation sensitivity manifests as mode and polarisation selectivity of optical and spin transitions, governed by crystal field symmetry and dipole orientation. Knowledge and control of experimental parameters, including σ, π, and wave-vector components, is critical for resolving transitions and maximising signal contrast. Recent high-resolution studies confirm the nuanced nature of dipole orientations, providing practical guidance for experimental design in erbium-doped systems [68, 124].

3.1.11 Branching Ratios

The lifetimes observed for rare-earth optical transitions are generally considerably shorter than what would be expected from a direct calculation of spontaneous emission for a given dipole moment. The expected excited state lifetime from a transition with dipole moment μ is:

$$T_{\text{spon}} = \frac{8\pi^2 n \chi_L}{3\epsilon_0 \hbar \lambda^3}\mu^2 \tag{3.9}$$

where χ_L is the local field correction factor, and ϵ_0 the permittivity of free space. The reason for this is that emission from an excited state does not pass directly to the ground state: there may be intermediate states to which an excited state is (radiatively or non-radiatively) coupled. Using the calculated value for T_{spon} and direct measurements $\mathrm{T_1}$ lifetimes from fluorescence, branching ratios can be evaluated:

$$\Upsilon = \frac{T_1}{T_{\text{spon}}} \tag{3.10}$$

Branching ratios are important for high efficiency, cyclic transitions with rare-earth ion emitters, however it should be noted that once an emitter is placed inside a cavity, the enhanced optical transition can greatly modify the 'bulk' branching ratio [52, 137].

3.1.12 Erbium

Among the rare earth ions, erbium (Er^{3+}) is the experimental focus of this work a number of reasons. Most notably, its lowest-energy $4f \longleftrightarrow 4f$ optical transition occurs near 1550 nm in the near-infrared, coinciding with the global minimum attenuation in optical fibre [192]. This makes erbium uniquely suited for integration into long-distance quantum networks, with architectures demonstrating entanglement distribution over distances exceeding 10 km [193].

Erbium is a Kramers ion with an odd number of $4f$ electrons, granting it a spin degree of freedom in magnetic fields. Typical electronic spin sensitivities lie in the range of 60–100 GHz/T, resulting in optical transition Zeeman splittings from zero up to 200 GHz/T depending on field, host, and site. This spin sensitivity facilitates effective magnetic tuning and coherent spin control in quantum devices.

Erbium's excited state lifetimes range from a few milliseconds to tens of milliseconds depending on the host environment, with longer lifetimes observed in high-symmetry sites. Corresponding optical coherence times (T_2) reach tens of microseconds at cryogenic temperatures, limited primarily by interactions with spins in the host. Among naturally abundant erbium isotopes, ^{167}Er (with nuclear spin $I = 7/2$) offers access to hyperfine structures ideal for long-lived quantum memory states [34, 160, 194].

3.1.13 Summary

This section has introduced the spectroscopic properties of rare-earth ions in crystalline hosts, with a focus on dilute crystals doped with Er^{3+}. The transition properties were discussed, including expected timescales for optical and spin lifetime and coherence times. Mechanisms of broadening and decoherence were discussed, including homogeneous and inhomogeneous broadening, and the considerations when working close to the surface of even the cleanest crystals. Finally, the focus was shifted toward erbium, highlighting the technologically relevant properties of the Er^{3+} optical and spin transitions.

Whilst this section provided the theoretical background for our work on Er^{3+} sites in whispering-gallery mode resonators in CaF_2, it is hoped that it will be of utility to a novice in the field who is hoping to understand the physics underneath the spectra they may be looking at.

3.2 Crystalline Rare Earth Hosts

Having established erbium as the rare earth of choice for telecom-compatible quantum interfaces, the next question is: which host material? This section motivates the use of calcium fluoride (CaF_2) as a host for erbium, examining how material properties—crystallographic structure, optical quality, and spin environment—shape ion performance. I first outline general considerations for selecting rare earth hosts, contrast CaF_2 with other prominent materials in the field, and conclude with specific advantages that make CaF_2 a platform well-suited for the crystal field engineering studies central to this thesis.

3.2.1 Host Material Considerations

The choice of host material profoundly affects rare earth ion properties through multiple factors. Site symmetry, determined by the host crystal structure and charge compensation mechanism, governs the crystal field and hence the ion's transition dipole moment and Stark sensitivity. Spin environment—the density and species of nuclear and electronic spins in the host—determines spectral diffusion rates and sets a practical limit on coherence times. Material quality and the maturity of high purity growth processes may affect optical loss, the availability of high-purity samples, and reproducibility of sample qualities.

Optical properties of the host impose practical constraints. Low optical absorption and scatter are essential for high-Q resonators, while refractive index affects mode confinement in photonic structures and compatibility with waveguide integration. For cavity QED applications, the ability to fabricate high-quality optical devices from the host material is not a requirement, but may be desirable. The relative maturity of growth and fabrication processes can vary widely: some hosts (such as Y_2SiO_5) benefit from decades of optimisation for laser gain media, while others remain challenging to produce at scale.

The ideal host would combine low nuclear spin concentration (minimising magnetic noise), mature growth and processing techniques, excellent optical quality for resonator fabrication, and crystal field sites that enhance erbium's optical dipole moment while preserving coherence. It seems still that the field is yet to find a host that satisfies all criteria perfectly. Material selection necessarily involves trade-offs based on application priorities.

3.2.2 Established Rare Earth Hosts

Yttrium Orthosilicate

Yttrium orthosilicate (Y_2SiO_5) has emerged as the workhorse material for rare earth quantum technologies, with extensive characterisation across temperature, magnetic field, and frequency for multiple rare earth species [26, 194]. Its structure provides two distinct yttrium sites, both with C_1 symmetry, which splits all crystal field levels into singlets and enables first-order Stark sensitivity, but complicates characterisation of spin hamiltonian and crystal field tensors. A precise, 3 dimensional magnetic field alignment is required to determine the orientation-dependent g, A, and Q tensors. Y_2SiO_5 offers good optical quality [195]. Commercial availability and decades of characterisation make Y_2SiO_5 valuable for protocol development and benchmarking measurements.

Y_2SiO_5 has been the material upon which a number of impressive rare-earth ion spectroscopy results are based, including the aforementioned 73 Hz optical homogeneous line [142], one of the first direct detection of single ions [50], quantum memory prototypes [28], and transduction protocols [42]. That said, in the context of out work, there are a number of key downsides:

There are only two sites in Y_2SiO_5 both with similar symmetry (C_1), and no known method of controllably adjusting ion population in either of these sites. We seek to perform a comparative study between a large number of different sites, and control site occupancy [156, 157]. The low symmetry of these sites also means they are challenging to model [160]. Although optical resonators have been manufactured directly in Y_2SiO_5 the crystal is higher loss than CaF_2 leading to limited Q factors [196], and considerably harder making fabrication challenging. Finally, Y_2SiO_5 is a rare-earth crystal (based on yttrium), and so contains a relatively high background of other rare-earth ions.

For single-ion applications, thin-film growth of Y_2SiO_5 remains unestablished. Recent demonstrations have instead transferred silicon photonic layers onto polished Y_2SiO_5 substrates [31, 170], or integrated bulk samples into optical cavities [197]. These hybrid approaches preserve bulk Y_2SiO_5 properties while enabling some degree of nanophotonic integration.

Yttrium Orthovanadate

Yttrium orthovanadate (YVO_4) is an alternative to Y_2SiO_5 that has a higher site symmetry (D_{2d}), leading to no Stark sensitivity for rare-earth ion dopants. Like Y_2SiO_5, YVO_4 is a rare-earth-based host, with yttrium providing both the lattice structure and an inevitable background of paramagnetic impurities. High-quality crystals can be grown and processed, and the material has seen use in nanophotonic demonstrations. The vanadium nuclear spins

(^{51}V with $I = 5/2$ at $\sim$ 100% natural abundance) can serve as a resource rather than purely a source of decoherence [54].

Calcium Tungstate

Calcium tungstate ($CaWO_4$) has recently emerged as an alternative to rare-earth-rich hosts. Unlike Y_2SiO_5 or YVO_4, $CaWO_4$ contains no electron spins in its natural isotopic composition, and both calcium and tungsten predominantly are zero nuclear spin, offering a quiet magnetic environment. High-quality crystals can be grown with low optical loss, and a low enough microwave loss tangent that it can host superconducting microwave circuits [137, 198]. There are a number of different crystalline environments (rare-earth ion sites) in calcium tungstate, each with slight variations in crystal field parameters [68].

3.2.3 Calcium Fluoride

Calcium fluoride offers multiple erbium sites with distinct symmetries and crystal fields, allowing direct comparison of how local environment sets lifetime, coherence, and dipole orientation in the telecom transition. It is a well-understood crystal system, and host for lanthanide (and actinide) dopants, with generations of EPR [188, 199, 200] and laser spectroscopy conducted [156, 201, 202].

From a material perspective, CaF_2 is a highly developed optical-grade crystal with well-understood growth and post-growth treatments such as annealing, enabling controllable manipulation of the population of Er^{3+}ions in each site [156–158, 202, 203]. It possesses an exceptionally wide photonic band-gap ($\sim$12 eV), which ensures ultra-low intrinsic optical absorption losses across a broad spectral range ($\alpha = 10^{-8} m^{-1}$ at 1550nm). CaF_2 also has both low dispersion and birefringence. Due to these favourable properties, low loss optics and high quality factor optical resonators are regularly made from CaF_2.

The crystal's softness facilitates precise machining and surface polishing – enabling ductile machining using a single-point diamond turning lathe [204, 205]. This enables fabrication of whispering-gallery mode resonators (WGMRs) with ultra-high quality factors (Q $> 10^9$) [206–208].

For targeting a scalable photonic architecture, thin-film growth and photonic fabrication are desirable. The calcium fluoride lattice is known to match with silicon [209–211], but poorly with silicon nitride [212] and silicon carbide. Calcium fluoride thin films doped with Er^{3+} have been studied [211]. Studies into thin-film growth of CaF_2 onto silicon open up avenues for devloping architectures around a photonic 'backplane'. THis could include high quality photonic resonators defined in the silicon, or in the dielectric itself [213], and extremely high quality interfaces between the two materials, a limitation in many heterogeneous architectures [31].

Moreover, CaF_2 has been shown to exhibit resistance to implantation damage [211], supporting applications involving ion implantation. Using techniques that are well-established from the donor spin community [214], one could deterministically implant erbium ions with high precision, without severely degrading the crystal's optical properties. In chapter 6, I discuss our lab's initial efforts in this direction.

When compared to alternatives like magnesium fluoride (MgF_2),CaF_2 presents a marginally more favourable refractive index (∼1.43 in CaF_2 versus ∼1.38 for MgF_2) for enhancing optical confinement. This slightly higher index also increases the ease of coupling efficiently to guided modes such as waveguides and tapered fibres. These guided modes are most often made in materials with high bulk index (Si has n ∼3.48 at 1550nm), in which a low-loss waveguide is tapered to a lower *effective* refractive index.

As discussed in 3.1.6, the Einstein A coefficient of an ion in a material scales as $A_{21} \propto n^5$, while the absorption coefficient scales as $\alpha \propto n^3$. Other commonly-studied rare-earth ion hosts have higher indices, including dielectrics such as $CaWO_4$ (1.9), YVO_4 (2), and TiO_2 (2.61), along with crystalline Si (3.5). As an example, this implies that a dipole in CaF_2will have an Einstein coefficient A_{21} as much as two orders of magnitude smaller than an otherwise identical dipole in Si, and α about 15 times less.

Additionally, the low concentration of background rare-earth impurities and absence of heavy metal ions in CaF_2 reduces magnetic noise and electronic perturbations, leading to a comparatively cleaner rare-earth ion spectral environment. Other single rare-earth ion programs have historically focused on materials such including YVO_4 and Y_2SiO_5, in which the rare-earth ion substitutes for yttrium, causing minimal strain. This comes with the downside that in these materials there will always be a background doping of rare-earth ions, due to the challenges of separating them. I note that the host crystals used in Refs. [52, 54], and [198] were nominally undoped.

Finally. the nuclear spin environment in CaF_2 must be addressed. While other studies of single rare-earth ions have deliberately avoided nuclear spins [185], our studies are focused on a material with a significant nuclear spin background from F^- ions (∼ 100 % spin 1/2) This is primarily determined by the fluorine isotopes (spin-1/2), creating a relatively simple and manageable spin bath. Techniques such as dynamic decoupling and precision RF driving are applicable here to extend optical and spin coherence times [187]. Beyond this, we envision using the nuclear spin bath as a resource - comparable to recent works [54, 55].

3.3 Erbium in Calcium Fluoride

Calcium fluoride has a bi-cubic structure, denoted by space group Fm$\overline{3}$m. The crystal structure of CaF_2 is face-centred cubic. The primitive (though not a unit cell) is a face-centred cubic lattice of F^- ions, with every second cage of this lattice populated by a Ca^{2+}, as shown in Figure 3.6 [215].

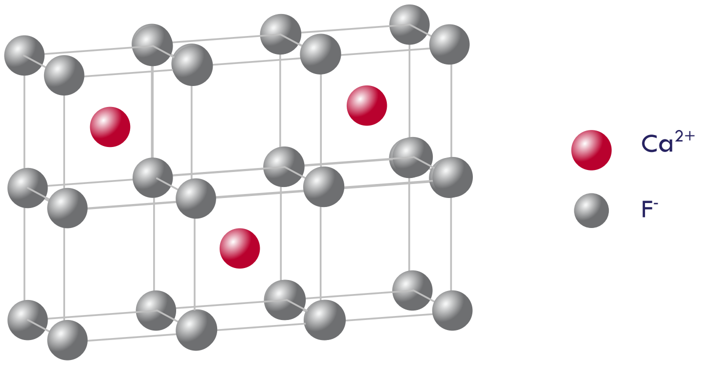

Figure 3.6: The calcium fluoride crystal structure can be depicted as a bi-cubic lattice: a regular array of fluorine atoms with a calcium in every other void

There are multiple different ways in which a rare-earth ion can be incorporated into the calcium fluoride lattice, but we will only treat those where the Er^{3+} ion has substituted in for a Ca^{2+} [201, 215, 216]. In these substitutional sites, an Er^{3+} ion replaces a Ca^{2+} ion. Given the erbium ions substitute into the lattice in place of a Ca^{2+} cation, some form of charge compensation is required to maintain overall charge neutrality. There are a number of different mechanisms by which this commonly occurs, leading to a crystallographically distinct sites [156]. Each site as its own unique crystal field Hamiltonian H_{CF} for the ion, governed by the location of the rare-earth ion and the extra compensating negative charge (if there is one). [217–220]

These sites are labelled by the point group symmetry of their local environment, and the species of atoms surrounding it [156, 157, 188, 215, 221, 222]. It is also possible to increase erbium population in some of these sites, or create erbium-oxygen complexes via annealing processes in a controlled atmosphere [156, 157].

Each site has its own local electrostatic and nuclear spin environments around the rare-earth ion, and some of these sites share symmetry properties. These in turn will affect the ion's optical and spin properties, including energy levels, transition strengths and linewidths, as well as how the ion will respond to incident electric and magnetic fields. A useful feature to remember is that axial sites which share a symmetry axis will respond to magnetic fields similarly – i.e. the same number of lines will split, however with gradients unique to each site. This is useful for interpreting rotation pattern data. The sites relevant to our study are shown in Figure 3.7, and characterised extensively in Chapter 6.

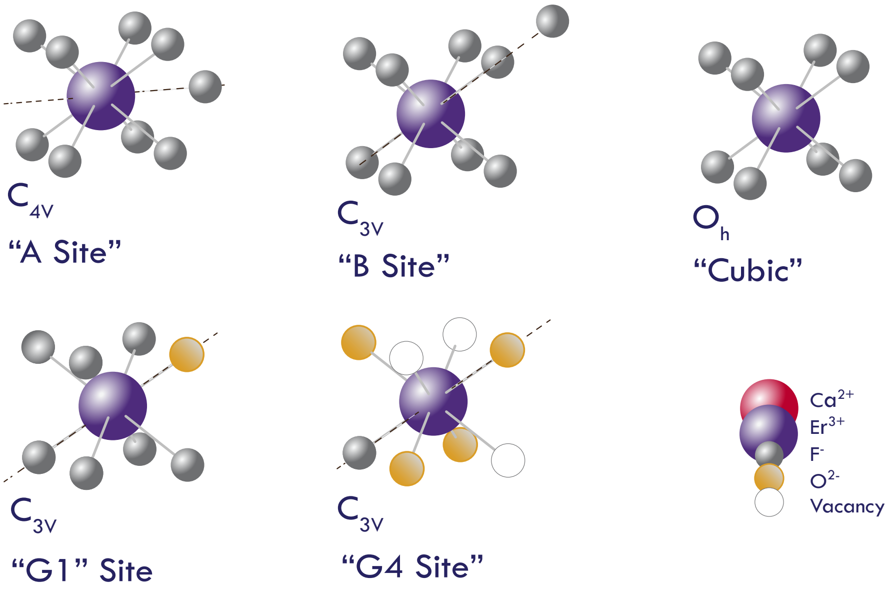

Figure 3.7: Indicative diagram showing five of the Er^{3+}sites in CaF_2. It is most likely that an Er^{3+} will replace a Ca^{2+}, requiring charge compensation. The most common site in untreated, doped calcium fluoride is the 'A site' in which a fluorine compensates the excess charge of the Er^{3+} ion, by occupying an interstitial site in the <100> direction. The 'B Site' is similar, however the interstitial fluorine ion sits in the <111> direction. A near-cubic site, with unknown, remote charge compensation is also seen - this is discussed in **Chapter Six**. The final two sites are oxygen-compensated: the G1 (in which a single O^{2-} replaces a fluorine ion in the Er^{3+} unit cell, and the G4, in which 4 O^{2-} ions, and four vacancies surround the Er^{3+}. These sites are each shown here with their point group symmetry presented, and their symmetry axis highlighted. Sites first characterised in EPR measurements [188, 199], and studied optically in site selective spectroscopy [66, 156, 202].

- **Remote Charge Compensation:** if the site's local excess of charge is not compensated locally, this excess of charge may be taken up remotely by a source of negative charge which does not affect the site symmetry. This could be a far-away interstitial anion such as fluorine, or a roving free radical [188]. This produces a cubic site of O_h symmetry.
- **Interstitial Fluoride:** a calcium cation may be replaced in the lattice by a F^- ion,

leading to one of four different sites (all shown in Figure 3.7). In the case where this F^- replaces a neighboring Ca^{2+}, a tetragonal (C_{4v}), trigonal (C_{3v}), or rhombohedric (C_{2v}) site is formed depending on whether the neighbouring unit cell shares a face, vertex, or edge (the $< 100 >$, $< 111 >$, and $< 110 >$ directions) respectively. In the (less likely) case where an F^- replaces a Ca^{2+} and an Er^{3+} fills an empty octahedral hole, a (C_{4v}) site is also produced [223].

- **Oxygen Compensation - the G Centres:** Charge compensation can also occur through one or more proximal O^{2-} ions [156, 188, 199]. Of particular interest is the G1 site, in which a single O^{2-} replaces an F^- in the lattice adjacent to the Er^{3+}. This oxygen substitution creates a significant perturbation to the local crystal field.

  Studies of high-dipole-moment transitions in Nd:YVO_4 suggest that oxygen's predominantly covalent (rather than ionic) bonding character may enhance rare-earth dipole moments by modifying admixture from the $5d$ and higher shells [141]. This hypothesis is supported by measurements of the G1 site in Eu:CaF_2, which exhibits an electric dipole transition moment approximately three times larger than in typical rare-earth hosts [65]. These oxygen-compensated sites represent a compelling starting point in the search for optimal environments for Er^{3+} quantum technologies.

Erbium centres in CaF have been investigated using EPR [188] and to some extent optically [66, 156, 209, 218], however limited studies on optical coherence have been conducted, and no single-ion properties have been measured in this system. This is an excellent candidate system in which to investigate the link between crystal field perturbations and optical properties.

3.4 Cavity Quantum Electrodynamics

To address single erbium ions in calcium fluoride we employ high-Q whispering-gallery resonators to enhance interactions between the atoms and light. Cavity quantum electrodynamics (cavity QED) provides the theoretical framework to understand these interactions. This section outlines the key principles of cavity QED, highlighting the importance of coupling, loss rates, and dipole moments. I will outline the implications of some of the different regimes of cavity QED, introduce the concept of *cooperativity*, and describe the implications of these figures-of-merit in single rare-earth ion cavity QED systems.

Cavity quantum electrodynamics – the study of coupling atom-like systems to discrete photon modes – is a field of significant importance to developing quantum information technologies. Single ions in traps or solids, solid-state defects, and superconducting quantum electronics are all described by the cavity QED formalism. The dynamics of single emitter and cavity systems are governed by the Jaynes-Cummings Hamiltonian

$$\hat{\mathcal{H}} = \hbar\omega_a \frac{\hat{\sigma_z}}{2} + \hbar\omega_c \hat{a}^\dagger \hat{a} + i\hbar[g(\mathbf{r})\hat{a}\hat{\sigma_-} - g(\mathbf{r})\hat{a}^\dagger \hat{\sigma_+}] \tag{3.11}$$

where ω_c and ω_a are the cavity and atom resonant frequencies, $\hat{a}^\dagger$ and $\hat{a}$ are the creation and annihilation operators for photons in the cavity, and $\hat{\sigma}$ denotes various operators for the atom. The final term, $g(\mathbf{r})$ is the the interaction strength between the emitter and a local light field. For the specific case of an electric dipole transition, this can be calculated by:

$$g(r) = \sqrt{\frac{\mu^2 \omega_c}{2\hbar\varepsilon_0\varepsilon_r(\boldsymbol{r})V_m}} \tag{3.12}$$

or

$$g(r) = \frac{\mu}{n(\boldsymbol{r})}\sqrt{\frac{\omega_c}{2\varepsilon_0\hbar V_m}} \tag{3.13}$$

Where μ is the transition dipole moment, ε_0 represent the permittivity of free space and $\varepsilon_r(\boldsymbol{r})$ the position dependent permittivity respectively,and we have assumed the ion is located at an antinode of the cavity field. V_m is the mode volume of the photonic mode of interest, given by:

$$V_m = \frac{\int \varepsilon|E(r)|^2 dV}{max[\varepsilon(r)|E(r)|^2]} \tag{3.14}$$

A Cavity QED system is generally characterised by three quantities: g, the coupling between the atom-like system and the photonic mode defined above; γ, an ion-and-host specific property that quantifies the direct loss rate out of the atom, and κ, the loss rate out of the photonic resonator, which depends on the resonator quality factor.

The atomic loss rate, given by γ is equal to the single ion linewidth, known as the homogeneous linewidth. The cavity loss rate κ is given by:

$$\kappa = \frac{\omega_c}{Q} \tag{3.15}$$

The relative sizes of these three quantities govern the dynamics of the system - and the relative utility of the system for various Quantum Information applications.

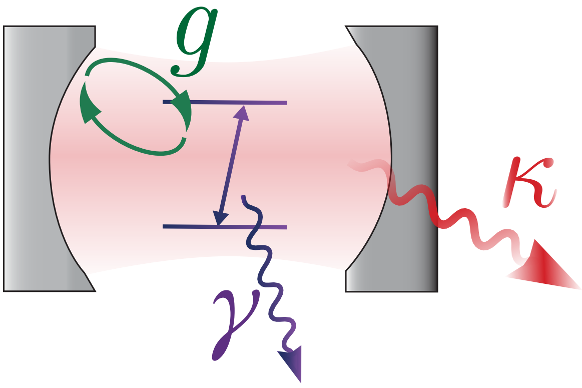

Figure 3.8: A schematic of the cavity QED system: a two-level atom sits in a cavity with which it is in resonance. The atom has intrinsic loss γ, defined by its dipole moment / radiative lifetime. The cavity has loss rate κ, defined by its quality factor. These two systems interact with coupling rate g

3.4.1 Purcell Enhancement

Increasing coupling between the atomic system and the photonic mode is important for two reasons. Firstly, researchers seek higher rates of photon emission, given the emission of a rare-earth ion in free space may only be on the order of a few tens to a few hundreds of photons per second. This enhancement of an emitter's rate of photon emission is given by the *Purcell Factor* [224].

$$F_P = \Upsilon\, \frac{3}{4\pi^2}(\frac{\lambda_{free}}{n})^3 \frac{Q}{V_m} \tag{3.16}$$

Where λ_{free} is the free space (vacuum) wavelength of the transition of interest, n is the refractive index of the surrounding dielectric, Υ is the branching ratio of the transition of interest, and Q is the quality factor of the resonator mode. The Purcell Factor can also be rewritten as:

$$F_P = \Upsilon\, \frac{4g^2}{\kappa\Gamma} \tag{3.17}$$

where Γ is the free-space decay rate of the atom, as distinct from γ, the single ion linewidth (generally measured from coherence times). Either form of this equation may be used, and when characterising an experimental system this factor is quickly attained by measuring the ratio of free-space to cavity-coupled (Purcell Enhanced) lifetime $T_{1,free}/T_{1,P}$. The majority of current single-rare-earth-ion schemes rely upon the phenomenon of Purcell Enhancement, since the reduced lifetime effectively 'brightens' an otherwise 'dim' emitter.

Intuitively (and accurately), a high Purcell factor is sought after, however the key goal of cavity QED systems is not simply 'brighter emitters.' Stronger coupling between an atom and a cavity mode enables more quantum-coherent interactions between ions and electric fields. Depending on the strength of the coupling, the dynamics of the atom-cavity system may be significantly modified when compared with either element in isolation.

3.4.2 The Coupling Regimes of Cavity QED

The relative sizes of g, κ, γ, ω_c, and ω_p all define which coupling regime an emitter-cavity system is in. This section will provide a brief, non-exhaustive treatment of some of the regimes that a Cavity-QED system can be in:

When $g << \kappa, \gamma$, and ω, the system is said to be in the **Weak Coupling** regime. In general, the cavity and ion will be unimpacted by each other: the cavity will not prevent the emission of a photon from the atom, but their interaction may modify the emsission rate, through Purcell Enhancement. In terms of understanding their dynamics, the Rotating-Wave Approximation remains valid and so the system is still well described by the Jaynes-Cummings Hamiltonian [225].

When κ,$\gamma << g$, but $g << \omega$, the system is said to be in the **Strong Coupling Regime**. In this regime it is possible for a single excitation to be absorbed and re-emitted by the emitter and cavity and back again, in a *Rabi Oscillation.* In the strong coupling regime, the cavity mode will split into a pair of polaritons, leading to a splitting of the spectral peak of the cavity when probed. The strong coupling is the basis of a number of second-quantum-revolution technologies, including superconducting qubits [58], atomic qubits[226], and network nodes [9, 24].

In the regime of increasing g, where the coupling constant starts to compete with either the resonant or driving frequencies of the cavity, the Rotating-Wave Approximation starts to break down, and the Jaynes-Cummings Hamiltonian no longer holds. Beyond this, the **Ultrastrong**, and **Deep Strong Coupling** regimes occur as $g >= \omega$. This regime remains a subject of considerable theoretical interest, and has only recently been reached experimentally [227].

The regime in which many solid-state quantum networking demonstrations operate is known as the **'Bad Cavity Limit'** [148] – in which $\kappa >> g > \Gamma$. In this regime, photons leave the cavity quickly, via emission which is often tailored toward a specific mode, such as a waveguide. This is useful for network demonstrations, since atomic emission is 'funnelled' directly into a quantum channel.

The bad cavity regime is technologically relevant when considering ultra-low-threshold lasers and single photon sources. For rare-earth ion systems, all experimental realisations are in this regime.

3.4.3 Cooperativity

All cavity QED systems experience dissipation through cavity photon loss (κ) and atomic dephasing (Γ). The cooperativity C quantifies the ratio of coherent to incoherent processes in the system, representing how many times an excitation can be coherently exchanged between atom and cavity before being lost to dissipation. For architectures operating in the bad cavity regime, cooperativity is a particularly useful figure of merit, given by:

$$C = \frac{4g^2}{\kappa\Gamma} \tag{3.18}$$

This quantity can be thought of as a measure of the impact that a single emitter has on the cavity mode (and vice versa) [228]. High cooperativity enables access to a number of different regimes in which some components of the above Hamiltonian may no longer hold. Extending the discussion of the 'Bad Cavity' regime, one can split this domain into two categories: those with $C < 1$, and those with $C > 1$. When $C > 1$, one has access to a number of different quantum information operations, mediated by coherent atom-cavity interactions: spin-spin coupling via the photonic cavity mode [229], perfect absorption of photons [230], and deterministic interactions with (and between) photons [64, 231].

Expressing cooperativity in terms of material and engineering parameters shows paths towards higher values: Using the forms of g and κ derived earlier, the cooperativity depends on the dielectric permittivity ε_r, the atomic loss rate Γ, and the transition dipole moment μ, along with two key engineering parameters—the quality factor Q and mode volume V_m:

$$C = 2\frac{\mu^2}{\varepsilon_0\varepsilon_r\hbar\Gamma}\frac{Q}{V_m} \tag{3.19}$$

This expression motivates considerable research effort in single rare-earth ion systems: a high cooperativity architecture requires a high Q/V ratio. Unsurprisingly, the architectures yielding the fastest progress toward higher cooperativity with rare-earth ions are based on nanophotonics.

3.4.4 Implications for Rare Earth Ions

Rare earth ions possess transition dipole moments approximately 10^3 times smaller than other solid-state emitters such as NV^- centres in diamond [232]. This weak oscillator strength makes reaching the strong coupling regime ($g > \kappa, \Gamma$) at the single-ion level challenging with current cavity technology. However, rare-earth ion systems can operate productively in the bad cavity limit ($\kappa > g > \Gamma$) while still achieving high cooperativity, the regime most relevant for quantum networking applications.

The small dipole moment of rare-earth ions represents a significant challenge for achieving high cooperativity in cavity QED systems. While the coherent coupling rate $g \propto \mu$ and radiative decay rate $\Gamma \propto \mu^2$ both depend on dipole moment, the cooperativity $C = 4g^2/(\kappa\Gamma)$ would appear insensitive to μ if optical coherence were lifetime-limited. However, rare-earth ions in bulk crystals exhibit coherence times T_2 far shorter than their radiative lifetimes T_1, limited instead by spectral diffusion and spin bath dynamics. In this regime, increasing the dipole moment directly enhances cooperativity: stronger coupling ($g^2 \propto \mu^2$) improves the coherent interaction rate while the dephasing rate Γ remains dominated by environmental noise rather than radiative decay. This motivates the crystal-field engineering approach explored in this thesis: by identifying sites with enhanced dipole moments, we can increase g without proportionally degrading coherence. Additionally, rare-earth $4f \longleftrightarrow 4f$ transitions exhibit high radiative branching ratios, meaning Purcell enhancement more efficiently couples emission into cavity modes without competing non-radiative decay channels that affect other solid-state emitters.

These properties suggest that high-cooperativity single-ion cavity QED with rare earths is achievable through two complementary strategies:

- Engineering high-Q/V_m photonic cavities
- Optimising the crystal-field environments to maximise transition strengths while preserving coherence.

This thesis explores both approaches, with particular focus on erbium as a promising candidate for cavity-enhanced quantum networking due to its telecom-band optical transition and established material platforms.

3.5 Engineered Crystal Systems

3.5.1 Approach I: Crystal Field Engineering for Higher dipole moments

The optical transition dipole moment of a rare-earth ion is determined by the admixture of opposite parity wavefunctions into the 4f shell, which depends on the local crystal field environment. By understanding the mechanisms that govern this admixture, we can move beyond the limitations of naturally occurring crystal sites and work toward engineering optimal environments for single erbium ions. This thesis investigates crystal-field engineering as a route to simultaneously enhance dipole moments while preserving the coherence properties that make rare-earth ions attractive quantum emitters.

We study erbium in calcium fluoride through two complementary approaches: naturally incorporated Er^{3+} sites in annealed doped crystals (grown at the University of Canterbury), and co-implanted Er^{3+} and oxygen in commercially available CaF_2. The naturally incorporated sites serve as a baseline for understanding intrinsic Er^{3+} behaviour in the fluoride lattice, including the effects of the fluorine spin bath on coherence, and the relationship between the site and its optical properties. Our most recent addition to this study is on implanted samples of ultra-pure calcium fluoride. These address a number of technological questions, notably these two: Firstly, can we create designer Er^{3+}-O^{2-} charge compensation complexes – or other engineered sites with desirable properties – through ion implantation alone? Secondly, we choose calcium fluoride beacuse we believe it to be a ‘clean slate’ – there should be no background Er^{3+} in the CaF_2 lattice. Is this truly the case? Positive outcomes in both these questions would enable precise spatial positioning of emitters in photonic devices while controlling their local environment.

3.5.2 Approach II: High Q/V Resonators

While nanophotonic cavities achieve strong light-matter coupling through sub-wavelength mode volumes, they necessarily place ions within nanometres of surfaces – an environment where surface-induced decoherence mechanisms can degrade the exceptional coherence properties of rare-earth ions. This thesis investigates whispering-gallery mode resonators as a platform for addressing single erbium ions.

We envision that whispering-gallery mode resonators could maintain Q/V_m ratios comparable to nanophotonic approaches, but with quality factors exceeding 10^9 and mode volumes on the order of $(10^3 - 10^4)\lambda^3$ (one limit to how high one might push Q is that the cavity should remain broader than the ion linewidth). Furthermore, these resonators couple to ions located many microns from any surface, at least an order of magnitude further than any current architecure [24, 31]. We target the long optical and spin coherence times characteristic of bulk crystals while still achieving sufficient Purcell enhancement for single-ion detection. Success would establish whether bulk coherence times are achievable in cavity-coupled systems and demonstrate an alternative pathway toward high-cooperativity quantum networking nodes. The challenge lies in fabricating ultra-high-Q resonators from rare-earth-doped crystals while maintaining surface quality and in efficiently coupling light into and out of high-finesse cavity modes.

Another benefit of far-from-surface ions is the possibility of dynamic spectral control: without the coherence-limiting effects of nearby interfaces, Er^{3+} ions in polar sites can be tuned via the DC Stark shift. This enables a long-term architecture in which applied electric fields shift individual ions in and out of resonance with their cavity mode [57, 167, 233] or modulate exchange interactions between nearby ions. Such switchable coupling would enable programmable quantum networks where individual nodes are selectively activated or isolated on demand.

3.6 Summary

In this chapter I have outlined the theoretical concepts required to assess a cavity QED architecture based on single rare-earth ions. I have motivated our choice of CaF_2 as a host material based on its low refractive index, uniform spin bath, low rare-earth ion background, and optical transparency at telecom wavelengths, as well as the ability to machine high Q factor resonators in it. Importantly, I introduced calcium fluoride as the host for our initial studies of 'crystal-field engineering,' using deterministic approaches to alter the erbium site, and hence its properties.

The principles of cavity quantum electrodynamics provide a framework for understanding how optical resonators enhance light-matter interactions through the Purcell effect and, at higher coupling strengths, enable quantum information operations. I have outlined that achieving high cooperativity ($C \gg 1$) requires a high ratio of quality factor to mode volume ratio (${}^{Q}\!/_{V}$). We pursue a high ${}^{Q}\!/_{V}$ ratio via the ultra-high quality factors accessible in whispering-gallery mode resonators, with a view to preserving bulk-like coherence in ions that are far from the surface in their large mode volumes.

"Architecture is the learned game, correct and magnificent,
of forms assembled in the light."

Le Corbusier

4

Cavity QED with Single Rare-Earth Ions

The key elements of this thesis have now been introduced: quantum technologies, rare-earth ions, and cavity quantum electrodynamics. Before moving the discussion directly to my experiments and results, it is important to highlight the scientific context from which this project emerges. At the time that this work started, there were a small number of experimental efforts around the world focusing on single rare-earth ions, only two of whom had achieved high fidelity readout of single rare-earth ion spins [52, 53]. This has grown, with well over ten groups now examining rare-earth ions in a number of different materials and architectures. Each of these has their own opportunities and challenges.

In this chapter, I review the current state of single rare-earth ion cavity QED. I outline the two pioneering approaches to single ion control and readout, and present a survey of other single ion research. I discusses the trade-offs in each implementation, and highlight open questions in the field. Finally, I present our approach in this context – using whispering-gallery mode resonators in Er^{3+}:CaF_2, to address ions in polar sites, far from surfaces in a material with a low background of rare-earth ion dopants.

4.1 Considerations for Single Ion Devices

Cavity enhanced experiments with rare-earth ions have historically focused on ensemble experiments to demonstrate strong collective coupling. Ensemble efforts continue, exploring memories[28, 138] and coherent transduction [29, 42], leveraging ensembles to overcome the relatively weak dipole moment of rare-earth ions.

The focus of this work is on single ions to enable scalable, optically addressable spin qubits for quantum network nodes. While achieving strong coupling for a single ion remains challenging, it is not essential for scalable quantum networks. In the strong coupling regime, the coupling strength g exceeds both cavity decay κ and ion decoherence γ, requiring ultra-high quality factor cavities with minimal mode volume. A more pertinent figure-of-merit is the cooperativity, discussed in 3.4, which quantifies the ratio of coherent processes to loss rates in a cavity QED system.

Material parameters require careful consideration, including ion and host choice, dopant density, coherence and spectral diffusion properties, and surface effects. Architectural factors such as repeatable fabrication, tuning capabilities, and long-term scalability are also critical.

4.1.1 Choice of Ion and Host

Selecting the optimal ion-host system is crucial for achieving good ion-cavity coupling and long coherence. This choice hinges on maximising the ion-cavity coupling strength, and subsequently the cooperativity, which depends on both material intrinsic properties and device architecture.

Rare-earth optical transitions are parity forbidden in free ions, but become weakly allowed in crystalline hosts due to crystal field interactions. The ion species determines the wavelength of the transition, and the extent to which the transition is allowed determines its dipole moment. Prior experimental efforts have explored ions such as Nd, with its relatively high dipole moment [51], and ^{171}Yb, which has zero-field spin structure [52], but the over-arching goal remains: high optical dipole moments will help to achieve the strongest coupling and best coherence times possible within practical fabrication constraints.

One concern when choosing an ion/host pair is the wavelength of emission from the $4f \longleftrightarrow 4f$ transitions. All rare-earth ions (except Ce) have $4f \longleftrightarrow 4f$ transitions, however some are incompatible with the bandgaps of various photonic materials: erbium's telecom-band emission makes it well suited for silicon photonics and fibre optic systems, while ytterbium suffers from absorption losses in silicon. Shorter wavelength ions, such as praseodymium and europium are incompatible with silicon, but may remain compatible with hosts with larger photonic bandgaps, including SiC.

When choosing ion, a significant consideration is the choice between Kramers and non-Kramers ions: Kramers ions such as erbium have unpaired electrons, leading to a half-integer total spin which splits in the presence of a magnetic field – and hence, an optically addressable spin degree of freedom. Non-Kramers ions have electronic singlet ground states, and generally operate at shorter wavelengths. In both cases, a nuclear spin degree of freedom can further split energy levels.

The optical properties of the host material also affect performance. The refractive index influences the optical lifetime, leading to longer optical T_1 in lower-index materials [190]. Optical loss affects the achievable Q of resonators, if they are to be fabricated directly in the host.

The composition of the host is a significant factor for coherence, and hence cavity QED performance. Hosts with abundant nuclear spins lead to environment with significant magnetic noise, which will limit coherence times. Furthermore, hosts which are based on rare-earth ions themselves (for example YVO_4 and Y_2SiO_5) will host a background of other rare-earth ions. The difficulty of completely separating rare earth species results in tens of parts per billion of each rare-earth still in the host. An ideal host would be a ‘clean slate,’ with no background rare-earth ions.

Finally on scalability: some hosts have proven, well-established fabrication in large-scale foundries, while others do not. Should efforts focus on bringing rare-earth ions to hosts with mature fabrication infrastructure, or on developing advanced fabrication techniques for proven rare-earth hosts?

4.1.2 Ion Concentrations

Achieving single-ion occupation of an optical cavity mode via doping poses significant challenge, since extremely low doping concentrations would be required. A doping level of 0.5 parts per trillion still leads to $\sim 10^{13}$ atoms per cm^3 (10 per μm^3) [49]. Nanophotonic resonators have mode volumes $\sim$0.1-10 μm^3, so would have between 1 and 100 ions per device, even in this extremely dilute doping concentration.

Many leading demonstrations employ yttrium based host crystals. As discussed in the previous chapter, these have a natural background of rare-earth impurities which are a source of noise. In nanophotonic resonators, this level is of order 100 ions per device [52]. For this reason, early studies focused on ions spectrally shifted several linewidths away from the centre of the inhomogeneous line [51]. Whilst excellent coherence properties have been measured, the frequencies at which these ions appear are consistent with significant strain in the host. It remains unclear whether coherence properties may be improved by studying single ions closer to the central peak.

Ion implantation offers several advantages as an alternative. It enables controlled placement of ions in optical mode antinodes, although some hosts may be affected by damage. Some substrates are annealed to reduce defect density. With low enough fluence, once can achieve deterministic implantation of only one ion per device. Implantation aligns well with foundry fabrication processes: high-quality films can be grown, and photonics patterned before ions are implanted in a final step [114].

4.1.3 Photonic Cavities

It is not immediately obvious which type of photonic cavity is best for single ion cavity QED. What is clear however, is that a high quality factor to mode volume ratio (Q/V) is required to maximise coupling between ions and light. A desire for long term scalability would lean towards cavities that can be made with standard lithography techniques. Smaller cavities lead to ions closer to surfaces, whilst larger cavities risk having a mode volume too large to achieve high cooperativity. Cavities could be made electro-optically tunable - by using the χ^2 nonlinearity of a material like $LiNbO_3$, for example [57, 169] - or piezomechanically tunable [234].

4.2 Initial Experimental Realisations

The first experiments demonstrating single rare-earth ions coupled to nanophotonic cavities were published in 2018, led by the Thompson group at Princeton University [50] and the Faraon group at Caltech [51]. These works built on decades of high-resolution rare-earth ion spectroscopy, and the initial experimental realisations of incoherent single ion detection [49]. The key distinction of the efforts in [50] and [51] was the integration of nanophotonic resonators directly with rare-earth ion materials, enabling enhanced light-matter interactions.

The Thompson group at Princeton pursued an approach using silicon photonics, coupling to rare-earth ions embedded in a substrate via evanescent fields. By contrast, the Faraon group at Caltech fabricated nanophotonic resonators directly within the rare-earth ion host crystal using focused ion beam (FIB) milling. The following sections will detail these complementary approaches and then briefly summarise other leading implementations in the field. These nanophotonic platforms share common features and constraints: mode volumes are small for enhancing coupling, but available quality factors (Q) are limited by fabrication quality. Ions are within 100 nm of surfaces in these nanofabricated devices, which can impact coherence. Depending on the nature of the point group symmetry of the ion's site, this impact can be significant: polar sites have non-zero stark sensitivity and are increasingly sensitive to the electric field at the surface.

In the following two sections, I present these two differing approaches in detail. I then conclude by summarising the current state-of-the-art and other leading implementations in the field of cavity-coupled single rare-earth ions .

4.2.1 Heterogeneous integration

The first successful approach to single ion detection, readout and coherent control in a cavity was realised in a heterogeneous integration architecture, developed in the Thompson lab at Princeton University. This section examines the experimental path from initial single-ion detection to quantum control, highlighting key achievements across multiple material platforms. While the focus remained on erbium and single-ion physics, the group explored a range of host materials to optimise device performance. Their work began in Y_2SiO_5 and eventually moved to a number of hosts including MgO and $CaWO_4$. This was informed by the results of a broad materials survey [185]. The experimental platform has now demonstrated spin-photon entanglement [31] and high indistinguishability as a single photon source [137], two fundamental milestones toward future quantum networks and repeaters.

The Architecture

In their architecture, a layer of silicon photonics is fabricated on a silicon wafer and transferred onto a rare-earth ion doped substrate using a stamping technique described in the Supplementary Material of [50]. The mode of the photonic resonator has an evanescent field that penetrates tens of nanometers into the host crystal (generally a dielectric) of choice, and can be used to address ions which are resonant with this cavity.

The stamping technique involves fabricating a complete layer of silicon photonics directly on a wafer of crystalline silicon, then extracting this and transplanting it onto a rare-earth ion doped substrate. The photonic devices – consisting of an on-and-off-chip coupler, waveguides, and a photonic crystal resonator – are all defined using electron-beam lithography, top-down reactive ion etching, and the underlying oxide layer is undercut with hydrofluoric acid. The transfer stamping technique is done using a PDMS stamp in a wafer bonder, which has been coated in a small layer of polypropylene carbonate (PPC), which adheres to the surface of the silicon photonic chip.

Devices are bonded directly onto the rare-earth-doped substrate of interest. This allows silicon photonic resonators to be fabricated reliably and repeatably in a controlled process, which can be iterated upon independent of the dielectric crystal substrate that it is bonded to.

The photonic crystal cavities in these types of devices have achieved quality factors of $Q \sim 2 \times 10^5$, corresponding to a cavity linewidth (FWHM) on the order of 8 pm (1 GHz), and a mode volume of $\sim 1\ (\lambda/n)^3$. The initial published results with devices achieving single-ion addressing did so with a Purcell Factor approaching 650, but a much lower single-ion cooperativity due to spectral diffusion. Precise quantification of the single ion linewidth on relevant timescales wasn't performed. More recent experimental realisations have moderately higher Purcell factors but greatly improved single ion cooperativity values near 1 [31].

The response of the cavity can be tuned via gas condensation tuning. The device is tuned by depositing a thin layer of N_2 ice onto the surface of the silicon photonic layer – which modifies the effective refractive index of the cavity mode. Using this technique, the cavity's resonance can be redshifted by up to about 1THz, with accuracy in the order of 100MHz, achieved by depositing a thicker layer than required, then removing using ablative laser pulses, of the order of a few hundred μW [50]. This precise and highly sensitive tuning scheme is one which is employed by many groups working on cryogenic applications of photonic resonators, however is highly sensitive to experimental parameter changes, including cryostat vacuums.

This approach has enabled researchers to leverage the scalability of silicon fabrication methods. The short fabrication timeline has meant that fabricating, and iterating upon the designs of a large number of devices on a single wafer is possible. This leads to a shorter loop of iterating and redesigning, and means that it is possible to build out device statistics for both the cavities and the implanted crystal of choice. That said, there are a number of engineering requirements that must be considered in such a system – many of these will affect the system parameters such as which ion may be used, the concentration of ions in the host crystal, and the ability of these devices to integrate into larger modules or systems within a quantum network prototype.

Firstly, the rare-earth species must have a $4f - 4f$ optical transition whose energy is below the bandgap of the photonic layer, and the photonic device layer must have a refractive index above that of the ion host substrate to achieve mode confinement. Silicon devices therefore must target erbium as their rare-earth ion of interest, with even ytterbium's optical transition at ∼980 nm being above silicon's bandgap energy. Devices built in this architecture must always target erbium ions, unless a change of photonic substrate is employed. By contrast, the Faraon group's experimental architecture allows addressing of Nd and Yb, each generally having a higher optical transition dipole moment than Er [235]. A similar device geometry has been demonstrated using GaAs [236] and GaP [118] photonic crystal cavities stamped on diamond to explore NIR defect based emitters within the diamond substrate. A similar approach could be used for the visible and NIR-active rare earth ions embedded in bulk host crystals, using these, or other photonic materials (such as SiC and SiN) with photonic bandgaps higher than silicon.

Whilst erbium ions may not have the strongest optical dipole of the rare earths, their transition frequency is in or near the telecom-C band, and so they are well-suited for long-haul quantum communication. Given this restriction to Er^{3+}, the Thompson device architecture has been used to address Er^{3+} ions in a number of different dielectric hosts, using the evanescent field of specificaly designed silicon photonic cavities [137, 237].

Ions in the substrate couple directly to the evanescent field of the cavity. The electric field magnitude at the Si-substrate surface is approximately 60% of the value that it is in the centre of the Si layer, and decreases exponentially from the surface [117, 238, 239]. Therefore for the ions of interest, the cavity mode is at its strongest at the surface of the host crystal. This leads to a system in which the only ions that can be addressed with high cooperativity in these devices are *by design* close to the surface of their host crystal – and with that, closer to sources of noise.

Y_2SiO_5 samples for the initial work had an Er concentration of about 200 ppb. Based on the concentration of ions in the host crystal the device dimensions, and the field strength profile of the photonic crystal resonator, one expects an estimate of ∼20 Er^{3+}within the active portion of the dielectric [117].

Early work in Y_2SiO_5 encountered Stark sensitivity due to the C_1 site symmetry, leading to spectral instability from electric field fluctuations [53]. The group subsequently transitioned to $CaWO_4$, where the ions occupy inversion-symmetric sites with nominally zero first-order Stark sensitivity, improving coherence. There is a tradeoff incurred here however: using a site with nominally no sensitivity to electric field removes a degree of freedom which can otherwise be used to tune ions in and out of resonance with the cavity [233].

The early published results using this device architecture also highlighted the group's ability to perform microwave experiments [117], given a stripline was also incorporated close to the optical resonator, enabling the group to deliver ESR pulses to ions in the substrate too. A rapid pace of iteration is possible, due to the natively modular architecture that the group has employed, where each individual subsystem – the microwave circuit, the angle polished fibre, the photonic layer, the crystalline substrate, and even the doping concentration – could

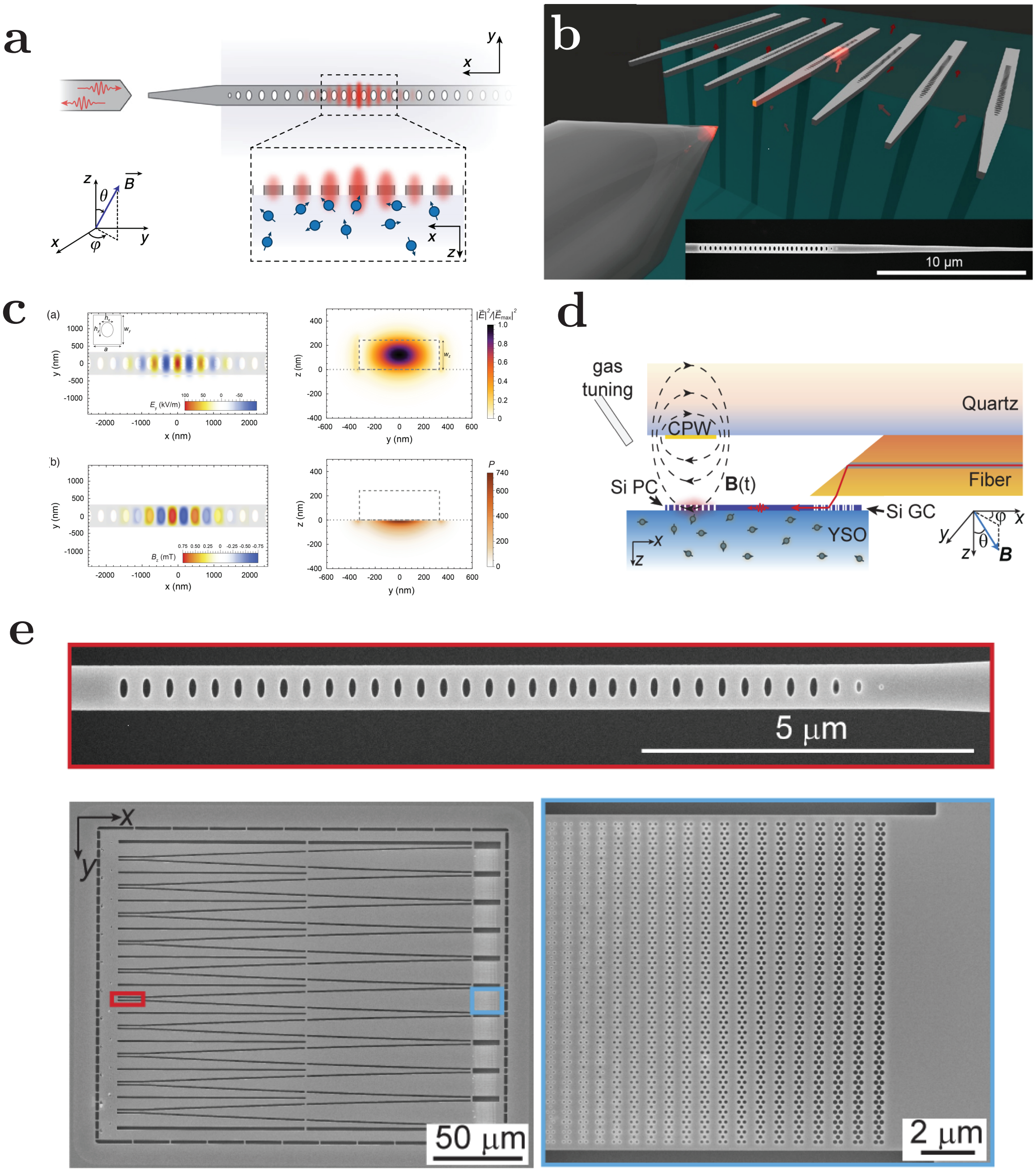

Figure 4.1: Thompson Lab Devices. **(a, b)** Experimental concept for [50, 53]. **(c)** Simulated mode of the devices used in [50]. **(d)** Novel coupling concept – an angle polished fibre is positioned over a grating coupler shown in **(e)**, blue inset. **(e)** Second-generation devices used in [137]: Red inset shows the novel waveguide resonator, lower left inset shows an array of these, each connected to a grating coupler on one chip.

be individually investigated without a complete redesign of the rest of the system.

Experimental Achievements in the Thompson Architecture

Since the initial experiments, the Thompson group has achieved a series of significant results using the silicon photonics architecture described above. The first major demonstration was a telecom-wavelength single-photon source in 2018, realised with erbium ions in YSO [50]. This work established the viability of the silicon photonics platform for single-ion addressing. Subsequent achievements included parallel single-shot measurement capabilities and optical quantum non-demolition (QND) measurement of a single ion qubit, advancing toward deterministic qubit readout [53]. Also in the original Y_2SiO_5 host, a single nearby spin in the lattice (most likely a hydrogen nucleus) was controlled, using the erbium ion as a bus [55].

Some of the group's early results employing these devices were a part of a survey of a significant number of materials with low nuclear-spin backgrounds. The group examined a number of hosts both computationally and experimentally, seeking those in which erbium ions would naturally have their longest possible coherence times [131, 185]. Within this package of work, the Thompson group narrowed the search for their preferred ion and host crystal pairing, and has subsequently published significant results using erbium doped Y_2SiO_5 [50, 55], $CaWO_4$ [137], and MgO [237].

A particularly impressive result demonstrated indistinguishable photons from single erbium ions, confirmed via Hong-Ou-Mandel interference measurements after propagation through 36 km of optical fiber [137]. This experiment, conducted in $CaWO_4$, validated the platform's compatibility with long-distance quantum communication infrastructure. The demonstration of spin-photon entanglement [31] represents one of the essential building blocks for quantum repeaters and networked quantum systems.

In parallel to these flagship results, the group has conducted materials-focused studies to identify optimal host crystals. A large-scale computational survey sought spin-free host materials to minimise magnetic noise [185], and initial experiments were conducted on a number of different host materials [240]. Experimental work in Y_2SiO_5 explored coupling between erbium ions and nearby single nuclear spins [55], while investigations in MgO, in which Er^{3+}only occupies a site of cubic symmetry, examined the effects of enhancing a purely magnetic dipole transition [237].

4.2.2 Monolithic devices

Running in parallel to the Thompson group, the group of Andrei Faraon at Caltech were also targeting single rare-earth ions in nanophotonic structures. This section examines their experimental path to initial single-ion detection and beyond, highlighting key achievements in their experimental architecture, Yb^{3+}:YVO_4. Their approach can be described as 'monolithic' or 'homogeneous' – whereby the nanophotonic resonators that couple to rare-earth ions are fabricated directly in the host crystal. For the single ion work, these are made in YVO_4, by contrast to the Thompson group who examine a number of sites. The Faraon group were however, able to examine a number of different rare-earth ions in their work, specifically Nd, Yb[1].

The Architecture

Similarly to the Princeton group, one key challenge to overcome was how to achieve vertical photonic mode confinement in materials without well established, high-quality thin films. The Faraon group were able to successfully achieve the necessary mode confinement through focused-ion-beam (FIB) milling. FIB milling had previously proved successful in creating nanophotonic resonators in diamond thin films [241] prior to the development of large-scale reactive-ion etching methods that are now widely used [242].

FIB is used in the Faraon lab to release suspended triangular nanobeam waveguides from the bulk substrate by two milling passes from equal angles on opposite sides of the nanobeam. This is combined with a lattice of rectangular sub-wavelength grooves, leading to the distinctive 'toblerone' one-dimensional photonic crystal resonators [235], distinct from the previously demonstrated 'air-hole' photonic crystal cavities upon which these are based [241]. The triangular nanobeam resonators are of the order of 15λ long, and 0.9λ wide, with light is coupled into and out of the nanobeam using total internal reflection from 45° cuts [235]. This opened up a versatile micro-machining pathway for the group to work with a range of bulk crystalline host materials without requiring thin films.

There were a number of key outcomes from this - firstly the quality factors of the resonators were up to an order of magnitude greater than previous work [235]. The group's typical resonator Q factors are 2-4×10^4, with some devices recording up to 7×10^4 [123]. The contributing limits to resonator Q include imprecise geometries and surface roughness, the reflectivity of the mirrors, and other less controllable properties. The highest Q devices are

---

[1] The group also works with other hosts including Y_2SiO_5, and other ions including Er, for ensemble-based experiments.

those fabricated for longer wavelengths; for example to interface with erbium ions at resonance wavelengths around 1530 nm [124].

The mode volume of these resonators approaches 0.05 $\mu\text{m}^3 = 0.5\ \lambda/n^3$, close to the limit for conventional dielectric photonic crystal cavities. Given the rare-earth ion background concentration in this host, even nominally undoped samples contained ∼100 Yb^{3+} ions. Resonator modes are tuned in a manner similar to those in the Thompson architecture, with deposition of argon or nitrogen modifying the effective index of the mode. However in the Faraon architecture, the modes can be moved by up to 10nm (approximately 4 THz).

Ref [235] demonstrated the ability to fabricate these structures for $\lambda = 605$ nm to $\lambda = 1536$ nm making it possible to consider coupling to the $4f^N \leftrightarrow 4f^N$ transitions of interest across the lanthanide series. For their single ion work, the Faraon group has focused on the 883 nm transition of Nd^{3+} and 985 nm transition of Yb^{3+} in yttrium vanadate (YVO_4).

The ion beam milling process involves a number of tool passes, with pauses to image and/or rotate the workpiece. This process relies upon a number of manual intervention steps – as distinct from one single planar electron-beam or photo-lithography step. There is a clear barrier to scaling, without advances similar to the large-scale lithographic and reactive ion etching techniques which have been developed for materials such as diamond [115], LiNbO_3 [243], or more recently BaTiO_3 [4].

In YVO_4, rare-earth ions occupy non-polar D_{2d} sites, eliminating sensitivity to electric fields to first order, and providing improved spectral stability compared to non-polar sites. The high refractive index of YVO_4 ($n \sim 2$ at 980nm) enables strong optical confinement within the nanobeam structure, contributing to the high quality factors achieved.

Experimental Achievements in the Faraon Architecture

This section will highlight the key results on single ion addressing and control enabled by these nanobeam devices in the Faraon group. The first landmark achievement was the detection and addressing of individual rare-earth ions in nanophotonic cavities [51]. Zhong and coauthors performed single-ion spectroscopy and measured optical coherence times for Nd ions in nanobeam cavities.

Notably, the device used for this work was initially designed for ensemble experiments and had dopant concentrations significantly above later-generation devices - 50 ppm, compared with later devices that should have < 100 ppb. The implications of this are not negligible – the ions in question, one way or another, have optical transition frequencies that are statistically many orders of magnitude less likely than the vast majority of ions in the YVO_4 host. These

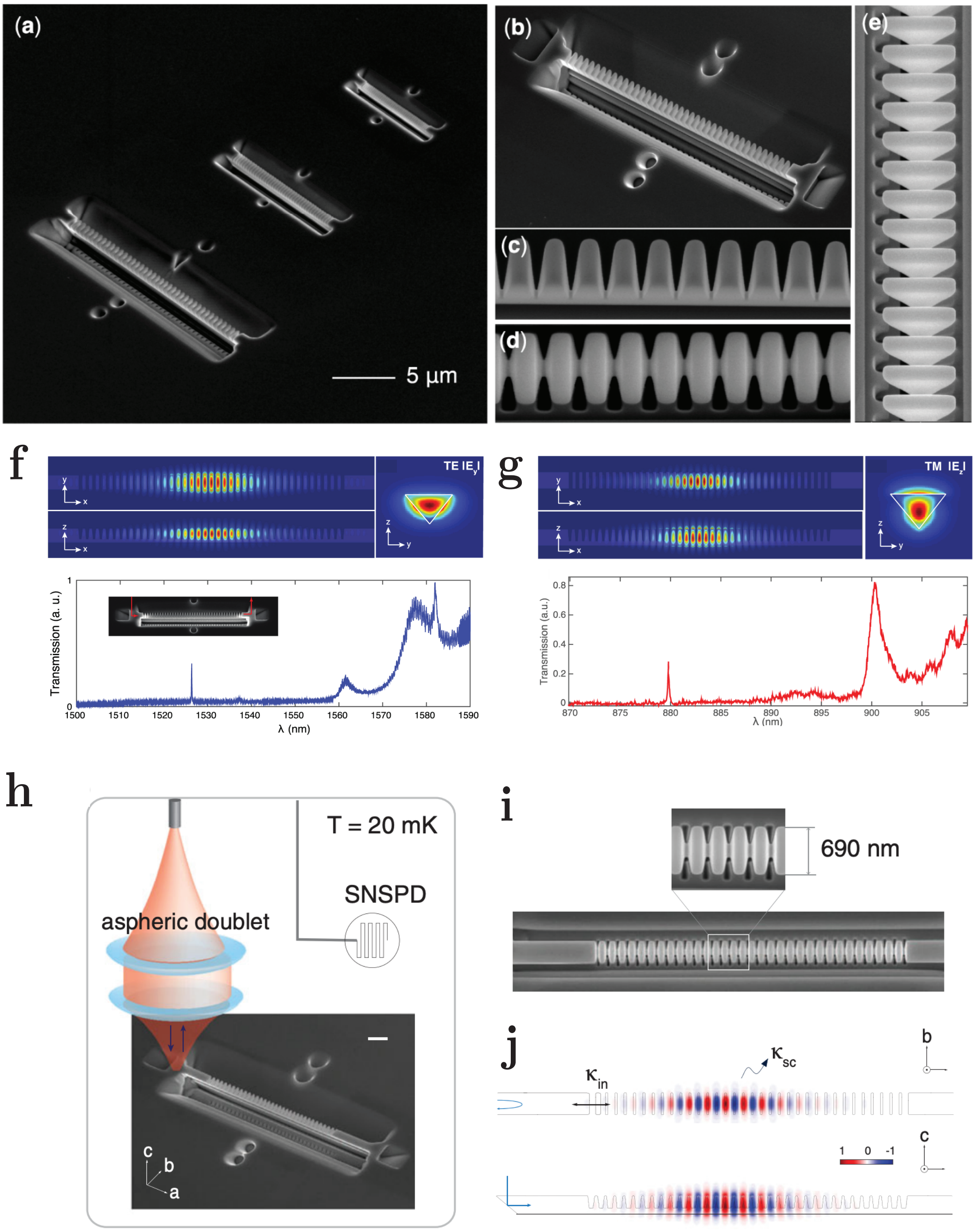

Figure 4.2: Faraon lab devices **(a-e)** Scanning electron micrograph (SEM) images of nanophotonic resonators made in the Faraon lab. **(f-g)** simulated photonic modes of the devices described in [235] showing narrow peaks intended to target Er (f), and Nd (g). **(h-j)** Experimental concept and details from [52].

ions are most likely in significantly strained sites.

Subsequent work employed significantly lower dopant concentrations to address ions closer to the inhomogeneous line centre. The ytterbium ions studied in the first spin-state-selective readout experiments [52] were sourced from nominally undoped crystals with trace rare-earth concentrations in the tens to hundreds of parts per billion range.

More recent achievements include entanglement with the nearby vanadium nuclear spins [54] for use as a nearby register of qubits, and most recently, tripartite entanglement [24], advancing toward modular quantum network prototypes.

While these devices have been integral to a number of experiments on the Faraon group's path toward single rare-earth ion detection [51], readout, and control [52], they have also been used for a number of other experiments. These include a nanophotonic AFC implementation [244], microwave-optical transduction [101], and a number of studies of the properties of various rare-earth ions in YVO_4 and Y_2SiO_5 using ensemble measurements [168, 245–247]. Particularly notable are recent efforts with $Er^{3+}$to develop efficient, telecom-C band quantum transduction schemes [41].

4.2.3 Direct Comparison of the Two Architectures

Cavity QED Parameters – A Table

Table:

Approach	**Host**	**Ion**	Q	$\mathbf{V}_m$	$T^*_{2,opt}$ (μs)	$\mathbf{F}_P$	**C**	Cit.
Heterogeneous	Y_2SiO_5	Er	6×10^4	$<1\ \lambda^3$	3.3	700	1.8×10^{-3}	[53, 55]
Heterogeneous	$CaWO_4$	Er	1.6×10^5	$<1\ \lambda^3$	2.1	850	> 1	[31, 137]
Monolithic	YVO_4	Nd	3.9×10^3	$0.056\ \mu m^3$	4.0	111	3.9	[51]
Monolithic	YVO_4	Yb	1×10^4	$0.095 \mu m^3$, $1\lambda^3$	4.1	116	3*	[24, 52, 54]

Table 4.1: Summary of the Cavity QED parameters measured in experiments at the Faraon and Thompson labs. * indicates that the cooperativity measured is a 'rephased' cooperativity through a scheme described in [132]

Similarities and Differences

While both the Thompson and Faraon groups pioneered single rare-earth ion detection and control using nanophotonic cavities, their approaches diverged in several key aspects.

The Thompson group focused exclusively on erbium ions due to silicon photonics bandgap constraints, embracing erbium's telecom-band compatibility for long-haul quantum communication. In contrast, the Faraon group prioritised ions with the highest optical dipole moments, targeting neodymium and ytterbium for single ion experiments. This flexibility stemmed from their monolithic fabrication approach, which enabled resonator creation directly within a host with a higher band-gap than silicon.

Both architectures prioritised minimising mode volume V_m over maximising quality factor Q, however the spatial distribution of ions within the mode differs significantly. There are more strongly, and more weakly coupled ions in both devices.

In the Faraon architecture, ions are distributed throughout the entire nanobeam structure ($\sim$100 nm from the nearest surface). The main coupling region is the spatial antinode of that mode, in the centre of the triangular peak.

In the Thompson heterogeneous approach, the strongest coupling is near the Si/dielectric interface, with coupling dropping off exponentially away from the interface. This means that only ions within a few nanometers of the silicon-substrate interface experience sufficient evanescent field strength for high cooperativity.

This geometric constraint has two implications – firstly that the ions must inherently reside closer to surfaces, potentially increasing sensitivity to surface-induced decoherence effects, whilst in the Faraon case, the mode is strongest near the centre of the triangular nanobeam, so ions may experience reduced surface perturbations. Secondly, the 'active' portion of the mode is smaller in the Thompson architecture – meaning that a single resonator can be used to address a smaller number of atoms in potentially more densely doped samples. This is beneficial, since each architecture could easily be hampered by frequency crowding of atoms.

Neither group initially settled on a single host material. The Faraon group explored Y_2SiO_5 and YVO_4 experimentally [51, 52, 54, 235], while the Thompson group examined many candidate hosts before experimentally investigating Y_2SiO_5 and MgO, before eventually moving toward $CaWO_4$ [53, 137, 237]. Both have achieved coupling between single rare-earth ions and nearby nuclear spins in the lattice, demonstrating pathways toward spin-based quantum memories and registers.

It is worth mentioning that the Faraon group has also explored heterogeneous integration. In work by Wu and colleagues [248], a gallium arsenide (GaAs) photonic crystal cavity was transferred onto ytterbium-doped YVO_4. This approach leveraged GaAs's broader transparency window compared to silicon, enabling coupling to ytterbium ions at 985 nm – a wavelength above silicon's bandgap. The demonstration validated the versatility of heterogeneous integration while retaining the advantages of working with bulk rare-earth-doped crystals.

The Thompson approach offers the flexibility to transfer silicon photonic structures onto any substrate, while the Faraon approach fabricates resonators directly within the host material itself, providing flexibility in choice of ion.

Both approaches face collection efficiency challenges arising from on- and off-chip coupling losses. The Thompson group's stamping technique offers potential scalability to a parallelised, larger scale fabrication process. By contrast, the Faraon group's serial FIB milling process currently limits throughput. Neither approach is presently compatible with 'industrial-scale' fabrication, though both represent significant steps toward manufacturable quantum hardware.

Both groups use non-polar rare-earth ion sites, to eliminate sensitivity to electric fields to first order [117], which is beneficial in architectures where ions are within 1 λ of the surface. That said, this limits the ability to use electric fields to tune and select ions. The Thompson group's progression from Y_2SiO_5 to $CaWO_4$ highlights this trade-off: Stark-insensitive non polar sites improve coherence but sacrifice fast electrical tuning capabilities. Both architectures therefore use gas condensation tuning or similar methods to bring cavities into resonance with specific ion transitions, rather than ions in and out of resonance with cavities.

Both implementations – as well as current microwave studies of single erbium ions [179, 198] – work with nominally undoped crystals of YVO_4, $CaWO_4$, and Y_2SiO_5, operating at ion concentrations of approximately 10 ppb or lower.

A compelling question remains regarding the interplay between ion density, mode volume, and spectral resolution. In the both architectures, the number of ions within the mode volume is determined by the host doping and resonator dimensions, offering limited control over ion number due to lack of doping control in the limit of low concentration. Both groups have demonstrated exquisite sensitivity to individual atoms, but future scalability may require engineered control over ion placement at maxima of the resonator mode, or the ability to tune individual ions in and out of resonance with the cavity.

Unexplored Parameter Space

Both the Faraon and Thompson approaches optimise for minimal mode volume, accepting quality factors limited by fabrication precision. This is one approach to increase Purcell enhancement, but constrains cavity linewidths to ∼GHz. Whether ultra-high quality factors ($Q > 10^7$) can compensate for larger mode volumes to reach $C > 10$ in these architectures remains to be seen.

Both geometries position ions near surfaces by design. Thompson's evanescent coupling requires ions within nanometers of the silicon-substrate interface, while Faraon's nanobeams position ions within ∼100 nm of etched surfaces. Whether surface proximity limits optical and spin coherence, or whether other mechanisms (spectral diffusion, charge noise, magnetic environment) dominate, cannot be completely determined from these experiments, however there is evidence to suggest that the main dephasing mechanism in the Thompson experiments is electric [69]. No architecture has demonstrated single-ion coupling with ions positioned micrometers from the surface.

These constraints motivate an alternative approach - which I explore in my work: ultra-high Q cavities (targeting $Q > 10^8$) with larger mode volumes, to position ions far from surfaces. This will isolate the impact of material environment on coherence and coupling strength. This regime of the parameter space – which cannot be examined in nanophotonic architectures – forms the basis of the work presented in subsequent chapters.

4.3 Other Research Efforts Targeting Single Rare-Earth Ions

While the Thompson and Faraon groups pioneered the first demonstrations of single rare-earth ion detection and control in nanophotonic cavities, the field has expanded rapidly since 2018. A diverse array of experimental platforms has emerged, focusing on a number of distinct architectures and techniques to address complementary challenges in rare-earth ion quantum technology. These efforts span fibre-based Fabry-Perot cavities, direct implants into integrated photonics in silicon, and thin-film fabrication in other photonic materials including lithium niobate and titanium dioxide. Recently, the development of single microwave photon detectors (SMPDs) [249] has opened these single-ion experiments to the microwave domain too. This section surveys key experimental approaches beyond the pioneering Princeton and Caltech architectures, highlighting their unique contributions and how they complement the broader landscape of single rare-earth ion research. It is an indicative, but by no means exhaustive list.

4.3.1 Direct Implantation into Photonic Structures

One approach to single ion addressing that has seen remarkable success is to directly implant erbium ions into foundry-compatible materials. Researchers fabricate photonics, and directly implant rare-earth ions into the finished device. This strategy is being pursued by the Reiserer group at the Technical University of Munich / Max Planck Institute for Quantum Optics in Garching, Germany [56, 114], and the Rogge group at UNSW, Sydney [153, 175].

Direct implantation offers several advantages. It leverages the mature fabrication ecosystem of silicon photonics while avoiding the complexities of heterogeneous transfer, or FIB milling of dielectric crystals. Importantly, ion placement can be deterministically controlled through masked implantation [214] or focused ion beams, potentially enabling precise positioning within the mode of a photonic structure. Silicon hosts may also be isotopically enriched prior to fabrication [250], or during implantation [251, 252].

The Reiserer group has demonstrated single-shot optical readout of implanted erbium ions in silicon photonic crystal cavities [56], validating this approach for single-ion quantum information processing. They have also explored implantation into commercial silicon waveguides [114], demonstrating Er^{3+} compatibility with commercially available devices.

For those investigating single ions in semiconductors, the importance of site characterisation cannot be overstated. Silicon is a complex crystal, and there are a large number of Er^{3+} sites - each with their own coherence time, dipole moment, and site symmetry. The Rogge group has pursued site identification and characterisation using an in-house developed excitation and detection schemes, and has identified long optical and spin coherence times [153, 253, 254], while recently also moving to investigations of Er^{3+} in silicon carbide [255]. The Reiserer group has produced a thorough characterisation of a number of sites in a rotating magnetic field [173]. Other challenges include managing implantation-induced damage, achieving sufficient annealing to restore optical coherence, and understanding the local environment around the sites of interest.

4.3.2 Fibre-mirror Cavities

An alternative architecture that has shown promise for accessing the single-ion regime employs compact Fabry-Pérot cavities formed between a precisely machined fibre facet and a planar mirror on a substrate [27, 30, 256]. The fibre mirror is typically fabricated using CO_2 laser ablation to create a concave profile, then coated with a distributed Bragg reflector consisting of alternating dielectric layers. These custom mirrors are commercially available and can be tailored to specific reflectance profiles and wavelength ranges. This approach offers a few key advantages, notably compatibility with a wide range of rare-earth-doped materials, including thin films, nanoparticles, and precisely thinned bulk crystals. The substrate mirror can incorporate rare-earth-doped samples in various forms, providing flexibility in material selection and preparation.

Multiple groups have pursued fiber-mirror cavities for rare-earth ion physics. The Hunger group [27] and de Riedmatten group [30] have both demonstrated cavity-enhanced spectroscopy of rare-earth ensembles and single ions in this geometry. Initial demonstrations in 2018 by Casabone et al [257] demonstrated a finesses of 1000, in a cavity 2 µm long. The Reiserer group extended this approach to couple single erbium nuclear spins in fibre-mirror cavities [258]. In this geometry they have also investigated europium-erbium co-doped Y_2SiO_5 membranes - a system that could allow for long-lived storage in an ion which is not coupled to the mode of the resonator [197].

While fibre-mirror cavities typically have larger mode volumes than nanophotonic structures, their ease of integration with diverse materials make them attractive for exploring new ion-host combinations and for applications prioritising experimental flexibility over maximal cooperativity. The primary challenge in working with these devices is connected to one of their key advantages: the non-monolithic nature of the structure leads to a highly tunable cavity mode that can be placed precisely over a sample of interest - a nanocrystal, or a portion of a bulk sample. The downside of this is that stabilising the optical mode of the cavity is challenging [259].

4.3.3 Planar DBR Cavities

Planar distributed Bragg reflector (DBR) cavities fabricated on wafers offer another approach to cavity-enhanced rare-earth spectroscopy. Alternating dielectric layers form high-reflectivity mirrors with a rare-earth-doped layer positioned between them. The Zhong and Awschalom groups at the University of Chicago have explored this architecture with materials such as TiO_2 thin films and ceramics such as Y_2O_3 [260–263]. This geometry enables wafer-scale fabrication, top-illumination setups, and straightforward integration with electrical or mechanical tuning. While mode volumes are typically larger than nanophotonic structures (similar to the fibre-mirror cavities), compatibility with thin-film deposition and standard nanofabrication makes this approach attractive for material exploration and device arrays.

4.3.4 Thin-Film and Waveguide Platforms

Thin-film photonic platforms such as lithium niobate ($LiNbO_3$) offer alternatives to silicon for rare-earth integration. These materials can be fabricated using techniques like smart-cut and are compatible with standard nanofabrication processes. A number of groups have pursued erbium integration into thin-film $LiNbO_3$ devices [167], and flip-chip bonding of $Er{:}Y_2SiO_5$ to thin-film lithium niobate, using flip-chip bonding [170].

Related efforts have explored other waveguide geometries and materials. NTT has investigated CeO_2 and other oxide-based waveguides [264], while the Tittel group has investigated $Ti{:}Tm{:}LiNbO_3$waveguides [265]. The USTC group has pursued Type-II waveguides for rare-earth ion integration [266]. These diverse approaches highlight the expanding materials toolkit for single rare-earth quantum photonics beyond traditional platforms.

4.3.5 Non-Nanophotonic Resonators

An alternative to nanophotonic architectures involves whispering-gallery mode resonators (WGMRs) fabricated directly in bulk rare-earth-doped crystals. The Longdell and Sellars groups have pursued this approach, fabricating WGMRs in materials such praseodymium and erbium-doped yttrium orthosilicate (Pr: Y_2SiO_5, and Er:Y_2SiO_5) [196, 267]. These resonators sacrifice the ultra-small mode volumes of nanophotonic devices in favour of significantly larger quality factors and ions positioned far from surfaces—often many optical wavelengths into the bulk crystal. This geometry potentially provides access to ions with properties more closely resembling those measured in bulk ensemble experiments, minimising surface-induced decoherence effects. The trade-off is that larger mode volumes reduce single-ion cooperativity compared to nanophotonic approaches, though exceptionally high Q values can partially compensate. The work presented in this thesis follows this philosophy, employing WGMRs fabricated in erbium-doped calcium fluoride (Er^{3+}:CaF_2) to explore single-ion physics in a regime where ions are far from the surface.

4.4 Open Questions in Single Rare-Earth Ion Cavity QED

There has been significant progress in single rare-earth ion cavity QED over the past decade and the field has matured considerably, with key prototypes of quantum networking nodes demonstrated. That said, there remain challenges to these systems serving as practical quantum network nodes or processors. This section examines the technical hurdles facing the field and the opportunities that may overcome them.

First, can ‘static’ cooperativity exceed $C > 1$, which is required for long term, scalable quantum network nodes based on rare-earth ions? Beyond this, could cooperativity *far exceed* unity, to enable dispersive readout [268]? Are ultra-high quality factor cavities ($Q > 10^9$) a viable path towards high C despite their mode volumes, or is minimising V_m the only way?

Second, what limits single-ion optical coupling strength? Can crystal field engineering be used to systematically enhance oscillator strengths beyond current demonstrations, while maintaining coherence?

Third, both the Thompson and Faraon architectures position ions within ∼100 nm of surfaces, by design. Does surface proximity present an ultimate coherence limit, or do other mechanisms (spectral diffusion, charge noise, magnetic environment) dominate? Testing ions positioned micrometers from surfaces in bulk-like environments remains unexplored.

Finally, is a ‘clean slate’ possible? A material which had zero rare earth background in the host would be ideal. With this, the material would ideally have a clean local spin environment - that is, devoid of both electronic and nuclear spins. In the absence of such a host, a predictable, and controllable spin bath may suffice [44, 171, 187].

4.4.1 Toward High Cooperativity

Achieving strong coupling between single rare-earth ions and optical modes remains challenging. This would enable dispersive readout, where ion states are distinguished through cavity transmission or reflection without spontaneous emission. This would require ions to be in the strong coupling regime, where $g > \kappa, \gamma$, a significant challenge. A more modest goal would be for $C = 4g^2/(\kappa\gamma) \gg 1$.

Increasing Coupling Via High Q/V Cavities

Nanophotonic cavities with small mode volumes offer large coupling, since $g \propto 1/\sqrt{V_m}$, but have fabrication-limited quality factors, and ions face decoherence from surfaces. Surface roughness limits constrain achievable Q factors. Photonic crystal cavities and FIB-milled nanobeams are both currently limited to $\sim 10^8$. Pushing beyond these limits requires improved fabrication or alternative cavity geometries, and ions would still be in relatively close proximity to the surface of their host.

High-Q micro-scale cavities offer an alternative. Whispering-gallery mode resonators in bulk rare-earth-doped crystals achieve $Q > 10^9$ routinely, with considerably higher values recorded in unique experiments [206, 207]. The trade-off with these devices are their larger mode volumes. It is then a reasonable avenue to explore these devices, to learn whether high Q/V_m may be achieved with these ultra-high-Q approaches, especially with ions that have increased dipole moments. This is our approach,

Increasing Coupling Via Higher Dipole Moments

As discussed, the approach taken by the Faraon group was to work with an ion with the highest dipole moment possible, in a site with no first order sensitivity to electric field - the D_{2d} Nd:YVO_4 site was chosen for initial demonstrations for this reason.

A less-explored approach is to engineer the crystal to deliberately increase the optical dipole moment. This is our approach. In the specific case of CaF_2, the ‘G1’ oxygen complex has been noted to have a dipole moment three times larger than the highest oscillator strengths among known europium sites [65, 148]. This factor of three becomes close to an order of magnitude in both Purcell Factor and Cooperativity, due to the $\propto \mu^2$ scaling of these parameters. Therefore we ask: is it possible to intentionally increase the erbium optical dipole moment? If so, what are the levers of control that we have access to to perform this?

An ideal host would enhance the optical dipole moment of an ion, enabling efficient optical access, while maintaining coherence. Further, this would not reduce the optical coherence properties required to achieve high cooperativity.

Ab Initio calculations of rare-earth ion properties are challenging, especially for low symmetry systems such as Y_2SiO_5 [160]. For higher symmetry sites, crystal field models, fitted from experiments, have been extremely successful in predicting some properties of ions, including posarisation sensitivity and hyperfine splittings [269]. By characterising the electronic structure of ions in sites with well-known crystal fields, the link between site properties and dipole moment could be examined.

4.4.2 Ion Density

Isolating single ions remains challenging due to doping density limits. A diffraction-limited spot ($\sim 1\ \mu\text{m}^3$) in 10 ppb Er:Y_2SiO_5 contains $> 10^3$ ions. Lower concentrations encounter uncontrolled background contamination in nominally undoped crystals. This suggests that seeking a 'blank slate' material, especially in the more commonly used hosts may not be possible.

Two approaches address this issue. Nanophotonic cavities with mode volumes near $(\lambda/n)^3$ combined with spectral selection can isolate individual ions, as demonstrated by the Thompson and Faraon groups. Alternatively, ion implantation using focused ion beams could enable deterministic placement with nanometre precision [114, 214].

Another strategy to the ion density issue accepts multiple ions per cavity as a feature rather than a limitation. Frequency-multiplexed architectures could address tens or hundreds of spectrally resolved ions per device, increasing capacity. This would require advances in fast tuning of ions, and multi-ion control protocols. These would benefit significantly from these ions being electrically tunable via the Stark interaction [167, 233].

4.4.3 Tuning Mechanisms and Dynamic Ion Selection

Matching ion transitions (kHz-MHz linewidth) to cavity resonances (10s of MHz-GHz) within inhomogeneous distributions spanning hundreds of GHz requires precise tuning mechanisms, especially in the case of many ions being addressed in a single cavity.

Several approaches exist with different trade-offs. First the cavity may be tuned. Gas condensation of cavities tuning offers large ranges ($\sim$ THz) but operates slowly. Electro-optic tuning in materials like lithium niobate enables rapid (sub-microsecond) adjustment via the Pockels effect, however rare-earth ions in these materials generally occupy Stark-sensitive sites, meaning the atom is tuned in parallel with the cavity.

Secondly, the ions themselves may be tuned. Magnetic field tuning of ions is common but generally slow. It is challenging to predictably select one of a number of ions in a cavity unless their properties (such as coupling to the cavity mode) differ [270]. AC Stark shifts using off-resonant drives provide reversible tuning without structural modification, though dressing fields lead to heating, and hence decoherence. DC Stark tuning of ions favours polar sites, as distinct from recent work seeking non polar sites for improved coherence [137]. The trade-off is clear: Stark-insensitive sites minimise decoherence but sacrifice dynamic tunability needed for multi-ion registers and frequency-multiplexed networks.

4.5 Our Testbed Architecture In Context

Here I summarise the experimental architecture we are building, describing how we intend to approach the open questions posed in 4.4. This is a testbed, rather than an attempt at creating a scalable photonic platform on a first pass. Our architecture is intended for studying the link between rare-earth ion properties and their host, developing control and readout schemes for many interacting ions in one cavity, and performing remote entanglement experiments.

Of the rare-earth ions, we choose Er^{3+}, for direct compatibility with fibre. The possibility in the long term of using the nuclear spin resource of $^{167}\mathrm{Er}$ for operation as a high-spin qudit [271, 272] is also a long term consideration.

We choose CaF_2, for its low optical loss, well-characterised growth, and that it can be machined into high Q crystalline resonators. Further, we choose a non rare-earth material, seeking a ‘clean slate’ free of nearby rare-earth ion dopants.

Calcium fluoride has multiple crystal sites, which we can use for our initial crystal field engineering studies. We can deterministically populate sites, enabling robust comparisons regarding the impact of crystal fields on both coherence and dipole moment. We approach the creation of these sites through two means: doped growth/annealing, and direct implantation. The former of these is well understood, while the latter represents an avenue for novel research on precise creation of complexes.

Of the sites available to us in Er^{3+}:CaF_2 we choose polar sites for single-ion work. These will have first-order electric field sensitivity, such that emitters can be tuned dynamically in and out of resonance with the cavity. In the long term, we envision modulating the Purcell Enhancement of an individual ion at a rate governed by how fast we can tune a voltage. This is analogous to the manner in which a fibre-mirror cavity may tune Purcell enhancement at bandwidths in the hundreds of kHz by adjusting the position of mirrors [259].

Finally, we choose whispering-gallery-mode resonators for exceedingly high Q factors that can be achieved. We focus on achieving very high quality factors, accepting larger mode volumes where necessary. Using whispering-gallery mode resonators fabricated directly into the CaF_2 host, we aim to address single ions positioned far from the surface, yet well-coupled to an optical mode.

4.6 Summary and Outlook

In this chapter, I have outlined the pioneering single rare-earth ion experimental efforts, describing each nanophotonic architecture and discussing the current state of the art experiments from each effort. I highlighted the scientific and technical milestones toward building scalable quantum network nodes achieved in both labs, notably tripartite [24] and spin-photon entanglement [31], and discussed the future for each effort. I have also discussed other state-of-the-art of single rare-earth ion experiments, showcasing some of the many impressive results that have emerged in this field in the years since our project started, including single ion qubit readout in silicon [56], lithium niobate [57, 167], and nanoparticles in fibre-mirror cavities [30].

Every experimental system has its own unique benefits and challenges, and our system is no exception to this. I highlighted the potential benefits that we hope to see in our testbed architecture, where we hope to address single ions far from the surface, in polar sites in CaF_2. This would enable fast tuning of ions with long coherence times relative to a cavity with a high Purcell Factor.

Nanophotonic implementations have established the feasibility of single rare-earth ion hardware. The challenge is transforming demonstrations into practical technologies, which will come via a number of paths, including increasing coupling between ions and optical fields and developing schemes for fast-tuning of ions relative to their cavity. These challenges are addressed through judicious choice of host material, ion, site, cavity parameters, dopant density, and control schemes. The following chapters present our lab's initial work towards a specific corner of this parameter space.

"Good design is as little design as possible."

Dieter Rams

5

Experimental Tools and Techniques

Most of the outputs from experimental quantum technology labs appears as publications in which researchers test theory with experimental results, demonstrate novel phenomena, or benchmark implementations against each other. However, a significant amount of effort – often the bulk of an experimentalist's work life – lies in creating the tools that make those experiments possible. In young labs this is especially true, since each setup establishes standards and conventions from scratch.

The purpose of this chapter is to provide the reader with an understanding of how (and why) we have constructed our experimental tool kit, whilst remaining focused on how we use these tools to characterise Er^{3+} sites for quantum technology applications.

I detail the current state of the hardware that has enabled the scientific work of this thesis, describing the key components in our high spectral resolution, high sensitivity, low temperature spectroscopy setup. I quote performance metrics where possible, through characterised figures of merit, and discuss the physics constraints and engineering requirements that drive our design choices. Following this, I describe our approach to measuring linewidths, lifetimes, coherence times, and spectral diffusion.

5.1 Cryogenic Hardware

This section will detail the experimental apparatus that enables the spectroscopy presented in this thesis. It comprises: sample thermalization in a dilution refrigerator, fibre-based optical delivery, orthogonal superconducting electromagnets, single-photon detection, and high-speed, high dynamic range optical switching.

5.1.1 Bluefors LD250 Dilution Refrigerator

All optical spectroscopy experiments are performed in our lab's Bluefors LD250 dilution refrigerator, often loaded multiple experiments running in parallel. The cryostat has an unloaded base temperature <7 mK. After integration of the apparatus required for these and other experiments, the base temperature rose to $\sim$50 mK.

Optical fibres are routed in and out of the cryostat to enable light delivery and collection - each fibre enters the fridge as part of a bundle of four, passing through an NPT 1/4" feedthrough. UT-086 coaxial cables run through the fridge, with two lines dedicated to superconducting nanowire single-photon detector (SNSPD) readout, and others reserved for microwave experiments. Superconducting magnets are oriented to allow for static magnetic field control during measurements. The system includes Attocube DC wiring for nanopositioners and additional DC lines supplying a number of cryogenic HEMT amplifiers. Heaters on the still ($\sim$5–15 mW) and mixing chamber optimize ^{3}He flow and temperature control.

The challenge when designing experiments in the constrained environment of a dilution refrigerator is to balance low temperatures, flexible wiring, and magnetic field control, while providing a reliable platform for high-sensitivity measurements. There are extensive resources on the operation and management of heat loads in dry dilution refrigerators – the interested reader is directed to [75, 108, 273, 274] and [275] for further information. I will address some of the considerations of operating a cryostat in the context of our research effort.

Each stage of the refrigerator has zero cooling power at its base temperature, and a different 'capacity curve' – i.e. Stage Temperature vs Dissipated power. Every change one makes in a cryostat – installing a new superconducting magnet, adding coaxial cables, and so on – will affect this cooling curve, since each connection that one makes between plates delivers some amount of heat – a static thermal load – to lower plates.

Thus, hardware changes must be carefully managed to support the required experimental wiring and components whilst still maintaining temperatures cold enough to observe desired physical phenomena – in our case, spin polarisation and superconductivity. SNSPDs and bias tees mount at the cold plate (100 mK), while higher-dissipation amplifiers operate on the 4 K flange or the still plate (0.9 K). Table 5.1 summarises cooling budgets per stage.

Name of Stage	**Base Temp (K)**	**Approx. Cooling Power (at Temperature)**	**Notes / Purpose**
Mixing Chamber	0.007	390 μW (100mK)	As cold as possible, quantum devices
Cold Plate	0.100		SNSPDs, bias tees, microwave circulators
Still Plate	0.9	25 mW (1 K)	Low power consumption amplifiers
4 K Flange	2.8	2 W (4 K)	High power consumption amplifiers, HTS magnet leads
50 K Flange	45	$\sim$10W (50 K)	non SC magnet leads

Table 5.1: Cooling power at each stage of our Bluefors LD250

In our case, component placement within the fridge is optimised to minimise thermal load on the mixing chamber stage, such that the ultimate sample temperature of the $\mathrm{Er^{3+}{:}CaF_2}$ samples we examined could be minimised. The Still plate is where experiments that may dissipate significant power are placed. Note too that the Still Plate temperature quoted in table 5.1 is measured with the ‘Still Heater’ on – this stage can be cooled to <700 mK if required.

5.1.2 Sample Mounting

$\mathrm{Er^{3+}{:}CaF_2}$ samples were held in copper mounts (transmission) or epoxied to mirrors (reflection). Samples were thermally anchored to the MXC using oxygen-free copper (OFC Grade C10100), thermally conductive braid, or copper tape where needed. Although the mirror-bonded configuration has lower thermal conductivity, spin temperature measurements via Zeeman spectroscopy [42, 182] estimate sample temperatures <200 mK.

5.1.3 Light Delivery and Collection

Delivering optical signals efficiently into dilution refrigerators is a common challenge in quantum information science. Two approaches dominate: free-space beams through optical windows, or guided modes in optical fibres.

Free-space techniques offer flexibility but introduce vibration sensitivity, or require expensive cryogenic objectives for efficient collection. Optical windows bypass radiation shields, allowing stray photons to reach superconducting components, causing issues for SNSPDs and other superconducting microwave electronics. Fibre coupling avoids these challenges: no windows, minimal static heat load, and compatibility with room-temperature optical components.

We use fibre-based optical access throughout to avoid thermal radiation through windows and maintain compatibility with superconducting microwave circuits [75].

Transmission and Reflection Spectroscopy Setups

Early surveys used Thorlabs PAF-X-2-C U-Benches for bulk spectroscopy with a custom holder. These fibre-to-fibre benches can be aligned to >80% coupling efficiency with no sample in the path, and we have achieved in excess of 50% with an appropriately prepared sample (above 75 % if the collection fibre is multi-mode). When cooled, their single-mode to single-mode coupling is between 5 and 20%. These are still in use in our lab, however their beam waist is limited to 0.38 mm and the lens cell is magnetic, leading to a ∼0.7–2 mT field at beam centre.

Cryogenic limitations, and the unknown dipole moment and coherence properties of Er^{3+} in CaF_2 motivated a tight beam focus for coherent spectroscopy, discussed in Section 6.4.3. To reduce the beam waist, I have developed a compact optical system based on Thorlabs 16mm cage, and custom copper mounts compatible with our magnets (Figure 5.1). These can be configured either in transmission, or reflection as shown in Figure 5.1.

A short focal-length lens (Thorlabs C220TMD-C, C660TME-C, C151TMD-C, or C710TMD-C) couples single-mode fibre light into free-space, either collimated or focused onto a mirror in the magnet bore. The C710TMD-C (1.5 mm focal length) setup achieves >50% room-temperature coupling, ∼20% cold, and an estimated beam waist <300 μm – smaller than the U-Bench's 380 μm.

In each system, the fibre launch is between 1 and 2 focal lengths from the lens - producing a beam which varies from collimated (perfect collimation occurs at $1f$ from the lens, a significant challenge) to focusing at a known distance (at $2f$ from the lens, the focus is also $2f$ from the lens). Thread pitches and other mechanical parameters are well known, and so an initial alignment can be accurate to within 100µm. That said, for our experiments, these are set up via careful tuning, optimising for reflected power rather than painstakingly measuring every distance.

Given the mechanical restrictions of the Thorlabs Fibre Launches (SM05FCA2 in our case), the facet of a fibre ferrule will always be 1.5 mm away from the surface. This limits how close a lens can be to a fibre, and affected collimation and focusing ability in our initial versions of this setup. To mitigate this, we carefully modify our fibre launches. A pocket no greater than 8mm diameter is milled out, no deeper than 2.5mm. This enables lenses in their mounts to advance the whole way to the fibre facet.

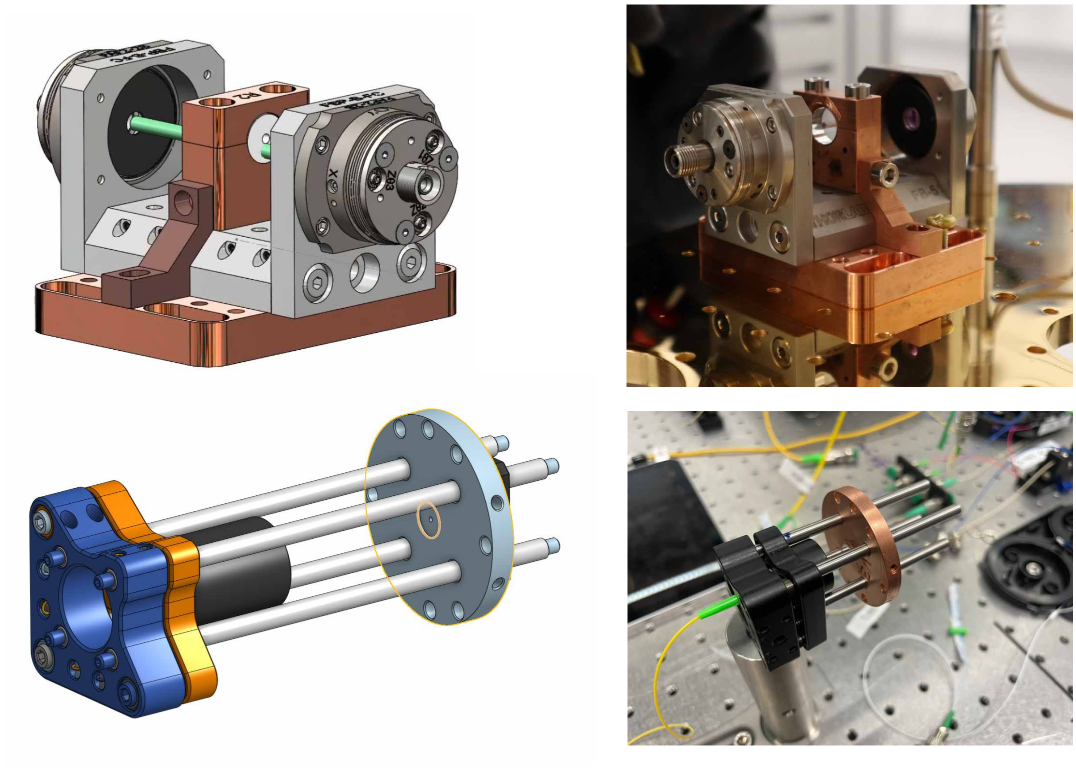

Figure 5.1: Iterations of our Cold Optics setups: Custom copper sample mounts and thermal links were made to hold samples in a Thorlabs ‘U-Bench’ (Fiberports are PAF-X-2-C). Shown in green is the 2mm waist of the beam from our older PAF-X-11-C. Later iterations of our experimental setup are based on Thorlabs’s 16mm cage system (shown at lower left). A modified (milled out to enable a closer distance between fibre tip and lens) SM05FCA2 is colocated in a short lens tube with a lens, enabling a very short working distance for single-lens reflection setups. The round sample holder is designed for integration in our custom superconducting magnet.

Confocal Microscopy

A confocal microscope uses a pinhole matched to the focal spot, greatly improving signal-to-noise versus wide-field microscopy, and is ideal for isolating small ensembles or even single ions in solid hosts. Accurate spatial filtering allows for the investigation of stress profiles, inhomogeneous broadening, and optical coherence near crystal surfaces and interfaces. Given the long-term goals of Er^{3+} integration in solid-state photonics, such studies are important at the materials characterisation (pre-device) stage.

Confocal microscopes enable sub-micron axial resolution - limited by $0.76\lambda/(n - \sqrt{n^2 - \mathrm{NA}^2}$. They also offer precise optical sectioning, allowing fluorescence to be detected from thin layers deep within bulk crystals while rejecting background from out-of-focus ions. This makes it possible to study the impact of stress, surface damage, and miniaturisation on local line shapes – essential information for quantum hardware in the long term [65]. High-NA lenses also provide efficient collection due to large solid angle.

Recently, a confocal microscope has been designed in collaboration with Ms Angela Liang. An extensive characterisation of this will be presented in her honours thesis.

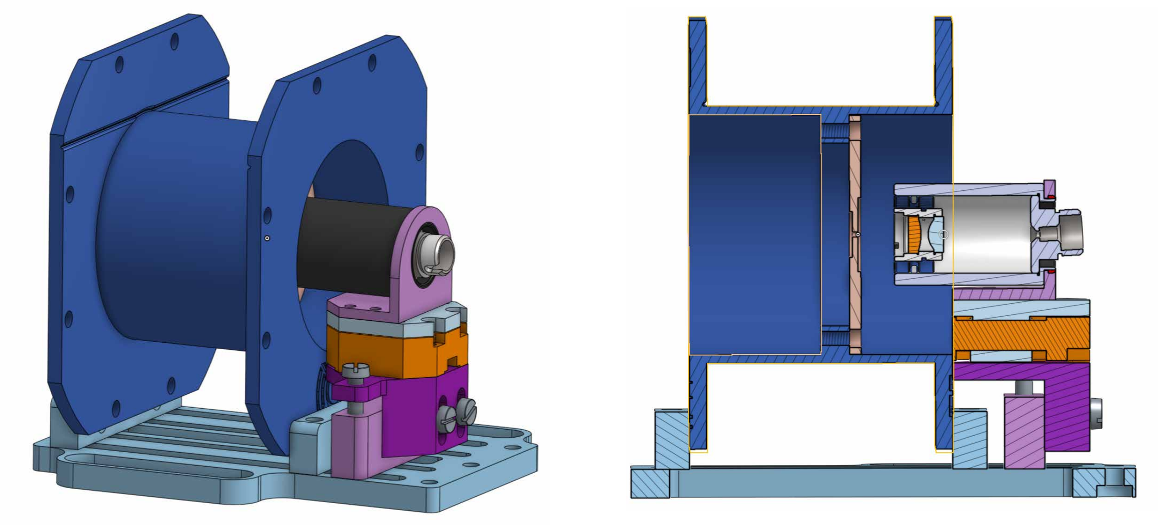

Figure 5.2: Isometric view and section of our one-axis, magnet-enabled confocal microscope. The next iteration will provision a second nanopositioner, enabling control over both depth and one linear position. This allows us to examine an area larger than a single diffraction limited spot.

In our experiments, the confocal pinhole is the mode of a single mode fibre - placed in an SM05FCA2 fibre launch. A doublet lens (Thorlabs C230C260P-C) is used to achieve a high numerical aperture, focusing the excitation beam to diffraction limited spot close to 3 mm from the lens. The lens is moved toward and away from the sample using an x-axis nanopositioner (Attocube ANPx101 [276]), tuning the position of the focus relative to the surface of the sample. The next iteration of this assembly will include a second nanopositioner, enabling control over depth and one linear direction. This allows us to examine an area larger than a single diffraction limited spot. That being said, given our known implantation depth and fluence, we expect that there will be $> 10^3$ Er^{3+} atoms in a diffraction-limited spot in the samples we are currently working with.

5.1.4 Superconducting Electromagnets

A significant infrastructure development at the beginning of the work of this thesis was designing, modelling, and fabricating superconducting electromagnets for optical spectroscopy studies. They have both been acknowledged already, however a special mention must go to Ms Alice Jeffery and Mr Lasse Sweetland, who both have contributed significantly to this work: Alice during the initial design of our first magnets and development of the winding procedure, and Lasse when it was time to add a second axis to our magnet system.

One key difference between other spins and Er^{3+} centres is that erbium tends to have a considerably higher gyromagnetic ratio than other spins - with a spin state sensitivity up to 200 GHz/T, as discussed in Section 3.1.4, meaning that relatively low fields are all that is required to separate Er^{3+} spin states by $\sim$GHz. This means that at the < 100 mK temperatures of our dilution refrigerator, it is possible to separate out spin states at low field such that all but the lowest spin state is occupied[1]. Thus, our initial single axis magnets were designed for comfortable operation up to $\sim$1 T (approximately 1000 turns of NbTi wire, on a 50mm-long former).

The anisotropy of the g-tensors in Er^{3+} necessitate multi-axis field control. This motivated the design of a split-pair magnet, with a higher number of turns than the original solenoid. Figures 5.3–5.4 show single- and two-axis configurations. This is designed for operation up to $\sim$0.3 T. A third axis is in preparation, for other materials with lower symmetry.

All magnets are wound around copper formers, using NbTi superconducting wire, Kapton insulation, and layer-by-layer loctite bonding. Magnets are driven by Kepco BOP-125-MG supplies (American Magnetics 4Q06125PS [277]) via AMI430 controllers. Room-temperature Hall-probe characterisation confirmed numerically predicted field strengths and homogeneity. Homogeneity across the optical beam and sample depth is shown in Figure 5.4.

5.2 Optical Excitation and Detection

5.2.1 Optical Excitation

For all spectroscopic studies described in the subsequent chapters, the excitation source was a Toptica CTL 1500 – a continuously tunable, external cavity diode laser, with instantaneous linewidth 100 kHz [278]. This laser enables direct addressing of the optical transitions between the Z_1 and Y_x crystal field multiplets, of any of the erbium sites of interest in CaF_2, described in Chapter 6, and many free-spectral ranges of our resonators as described in Chapter 7. This laser has a peak output power of about 40 mW into fibre, though after passing through the optical switching and modulation apparatus described in Section 5.2.2 below, excitation powers into the cryostat rarely exceed $\sim$2 mW.

---

[1] There are other reasons to operate at high field – if seeking large electronic spin-state splittings, to use nuclear spin states of ^{167}Er as a resource [34, 43], however these are beyond the scope of my initial investigations.

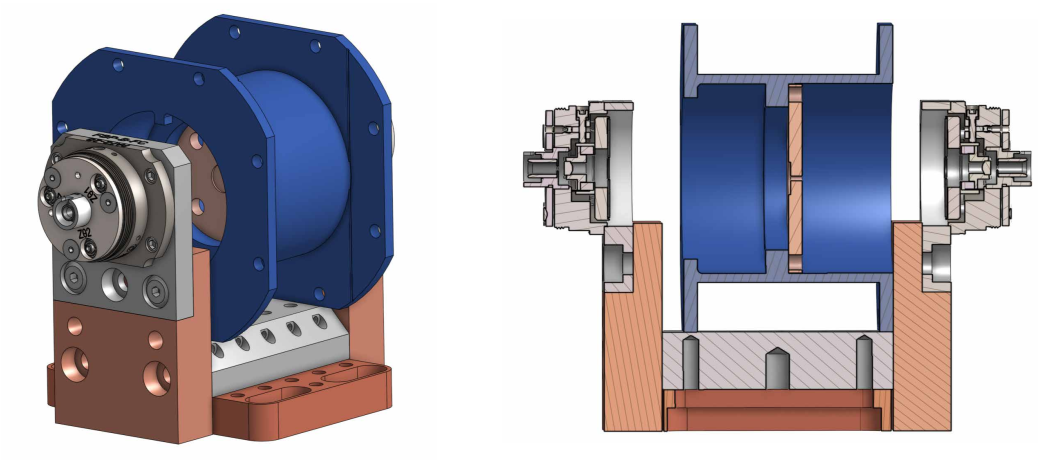

Figure 5.3: U bench spectroscopy setup with a single axis magnet (former only modeled). Note the magnet is not modelled - see photos in Figure 5.4. This is the setup used for magnetic sensitivity measurements described in in [182].

For broad spectroscopic surveys, we scan the laser using its internal motor, mapping all absorption features in our samples. For inhomogeneous line surveys, the laser's piezoelectric actuator scans 35 GHz in 50 ms – fast enough to avoid significant optical pumping, slow enough for photodiode readout.

The laser's internal wavelength reference is accurate down to < 1 GHz, however spectral features in rare-earth ion spectroscopy can often be considerably narrower than that. For this reason, we reference our laser to a wavemeter [279].

5.2.2 Optical Switching Apparatus

Of critical importance when performing coherent spectroscopy measurements, including Hahn, Rabi, and Ramsey echoes is the ability to gate light with a sufficiently high dynamic range to prevent 'stray' light passing through the setup in periods when the excitation signal is off, since such signals would lead to a high background of counts on our single photon detectors. For this reason, we have assembled a switching system with high dynamic range, by placing multiple gating/switching elements in series. This of course comes with the tradeoff of increased insertion loss.

For other studies including hole-burning and inhomogeneous line surveys, the ability to impart small (tens to hundreds of MHz) frequency shifts on an optical excitation signal is useful too. For our experiments, both of these functions are served by a series of switches and acousto-optic modulators.

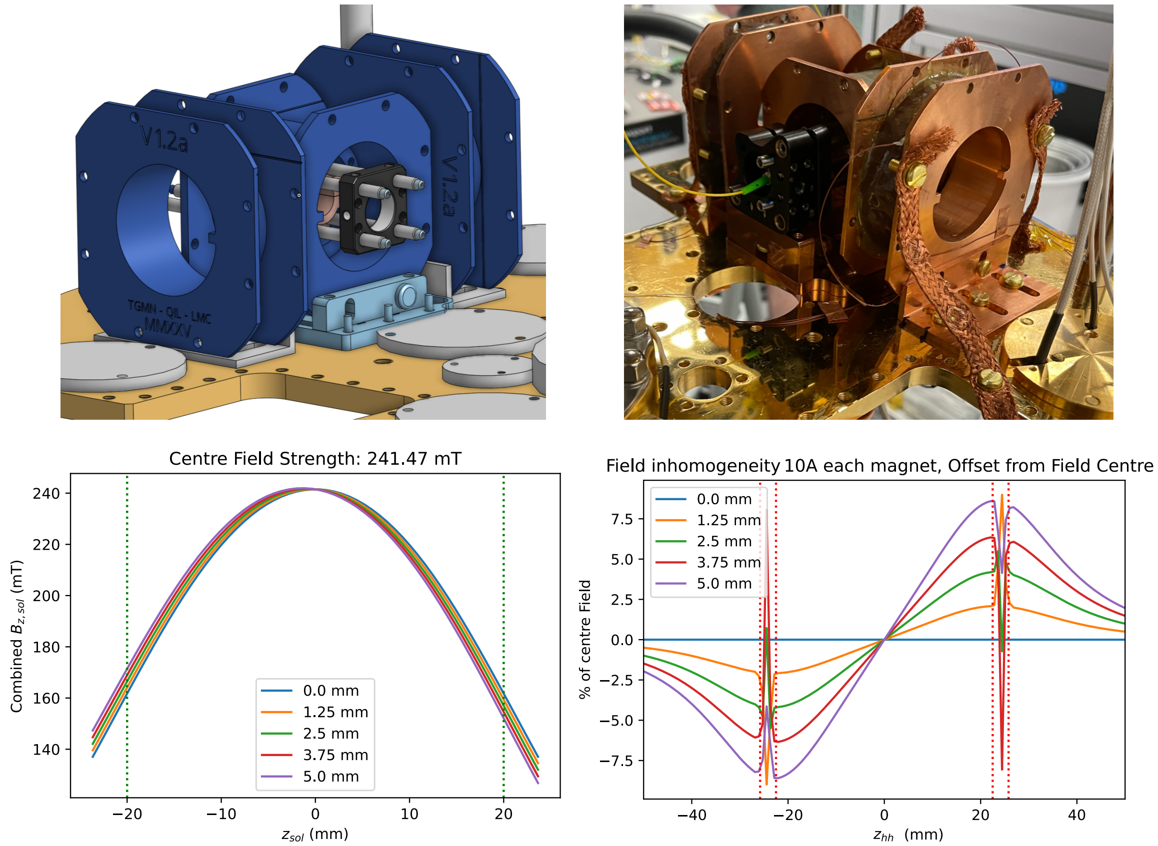

Figure 5.4: Two-axis superconducting magnet system - 1 T solenoid field and ∼300 mT side field - with two reflection-type optical spectroscopy setups embedded in its centre. Field strength and homogeneity (with both magnets at 10A current for simplicity), shown both as a function of the position along the solenoid axis (lower left), and the split-coil axis (lower right). These are calculated at a number of offsets from the beam, highlighting off-centre components. Green dashed lines show the extent of the solenoid former, while red dashed lines show the inner and outer diameters of the coils themselves.

The spectroscopy setup which was used for most of the experiments described in this thesis is shown in figure 5.5. The fibre path is mostly based around a pair of Boston Applied Technology (BATi) 1x2 optical switches (Model FOS-1200-1300) [280], capable of switching with ∼20 dB on-off ratio at ∼MHz repetition rates. These are configured "face to face" (shown in Figure 5.5) so as to allow a high efficiency throughput of light in both the excitation and collection paths of our experiments, switchable on a $\sim \mu$s timescale. The first switch – configured as a 1x2 – provides a high power local oscillator for optical heterodyne detection. The final 2x1 switch can be thought of as a low loss circulator, offering $<$ 1.5 dB of insertion loss in both directions, and having the added benefits of higher extinction when 'off.'

Between the two 1x2 switches are a pair of Brimrose technology acousto-optic modulators (one TEM-200-50-10-1535-2FP-SM and one TEM-200-18-30-1535-2FP-SM) [281] which are configured for high dynamic range switching: They are driven by a 200 MHz tones from an RF signal generator (Windfreak SynthHD), which are switched by a pair of microwave TTL Switches (Mini Circuits ZASWA-2-50DRA+) and amplified to 2 W (33 dBm) by an RF-Bay MPA-10-33. This yields approximately 4 dB of insertion loss in their 'On' state, and in excess of 50 dB extinction in their 'Off' state in this configuration. The whole setup is summarised in Table 5.2).

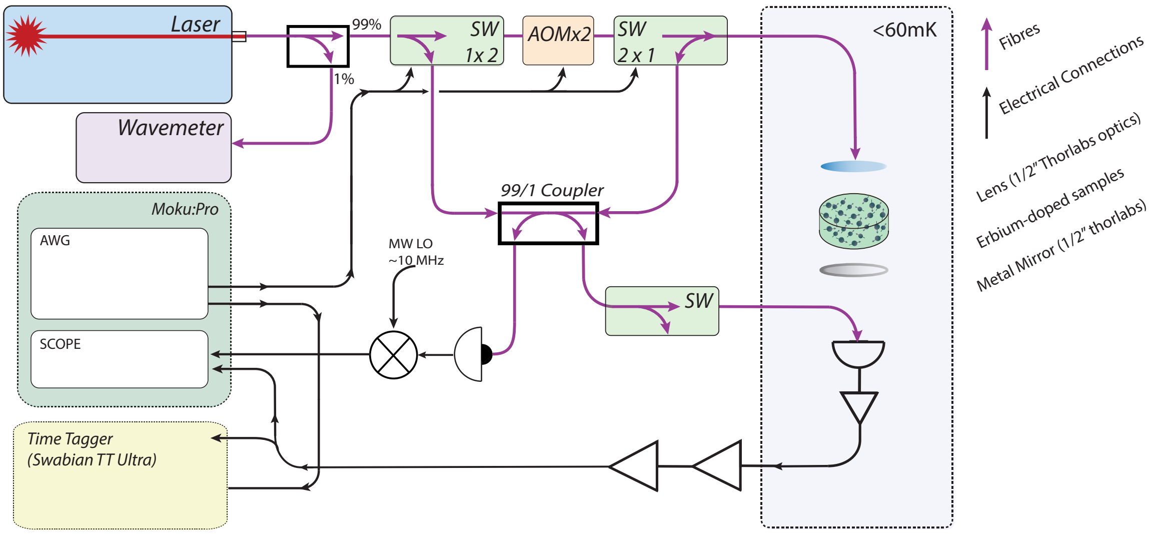

Figure 5.5: High Dynamic Range Spectroscopy Setup A schematic of the room temperature electronic and optical components of our experimental apparatus. For simplicity, some components are not shown: This includes microwave oscillators (Windfreak SynthHD), amplifiers (RF-Bay MPA-10-33), and switches (Minicircuits ZASWA-2-50DRA+)used to drive and gate AOMs, and the High Voltage driver for the BATi FOS switches.

The system of free-space optics described in section 5.1.3 has a typical insertion loss of around 12 dB. That said, we have conducted experiments with as much as 30 dB return loss when using our SNSPDs: the main variable which this affects is the integration time. In some transmission geometries have reduced this to <6 dB by using a multi-mode fibre on the collection path. This is much more efficient for absorption measurements, but may limit the utility of the signal after that, since echo detection schemes in our lab require single-mode fibre elements. Directly coupling a multimode to a single mode fibre incurs a $>$ 10 dB loss, due to the mode-field diameter mismatch of the two fibres. Despite tha a multi-single mode interface was used in [282] to successfully detect low-field echoes in Er^{3+}:Y_2SiO_5.

After light leaves the sample and cryostat, it is either sent directly into a coupler (Thorlabs

TN1550R1A2) for heterodyne detection on a Newport Fast Photodiode (1611FC-AC), or to a bank of optical switches used to gate the light to our SNSPD system. These three Agiltron switches (NanoSpeed NSSW 1x2) [283] are configured in series to achieve $>$ 140 dB of isolation to protect our SNSPD from reflected pulses, and can switch on at a rate faster than 100ns. Combined with the excitation-side AOMs and BATi switches, total laser-to-SNSPD isolation exceeds 330 dB (reduced to ~275 dB after removing Agiltron 3 for improved insertion loss).

5.2.3 On-Off Ratio of the Entire High Dynamic Range system

Component	**Insertion Loss (dB)**	**On-Off Ratio (dB)**	**Notes**
BATi FOS 1	~0.75	17.67	Second path IL: $<$ 1 dB
AOM 1	4	61.38	
AOM 2	4	62.85	
BATi FOS 2	~0.75	23.82	Second path IL: $<$ 1 dB
Total at Sample:	**~12**	**165.72**	
Cryo-optics (typical)	12-16	–	When 'well aligned' (>30%) at Room Temp.
Agiltron 1	1	43.61	Second path unused
Agiltron 2	1	51.09	as above
Agiltron 3	1	55.86	Eventually removed from setup
Min. Loss Laser to SNSPD		**~54**	
Max. Loss Laser to SNSPD		**$>$ 330**	Reduced to ~275 by removal of Agiltron 3.

Table 5.2: On-Off ratios, and insertion loss of each individual component in the spectroscopy setup, measured at 1518nm. Similar numbers (within 0.5dB) were attained when measuring at 1536nm. Note that the quoted insertion loss figures include the APC fibre connections to these components - splicing fibre connections could reduce these numbers further.

5.2.4 Heterodyne Detection

Coherent optical signals (e.g., photon echoes) often fall below direct detection sensitivity. Heterodyne detection effectively amplifies weak signals by beating them against a strong local oscillator (LO), at a different frequency to the detected signal. The beat between the LO and the signal is then read out.

A dual-heterodyne scheme was used for our first echo detection, with a slightly modified optical setup to that shown in Figure 5.5. The returned echo beats against an optical local oscillator (LO) at 200 MHz (combined via non-polarising beam-splitter, detected on a Newport 1611FC-AC photodiode [284]). This optical beat is then electrically mixed down to 13 MHz using an RF mixer and another (electrical) LO at 213MHz, producing a final IF signal within our oscilloscope's bandwidth while maintaining high signal-to-noise.

5.2.5 SNSPD and Readout Electronics

Superconducting Nanowire Single Photon Detectors

Superconducting nanowire single-photon detectors (SNSPDs) [285] are among the most sensitive near-infrared detectors. A superconducting nanowire biased just below its critical current transitions to a resistive state after absorbing a photon above the superconducting gap energy. This increase in resistance produces a measurable voltage pulse.

Detectors used here were fabricated by collaborators in Professor Sven Rogge's group (UNSW) using 20 nm tungsten silicide (WSi) films in a cavity-enhanced optical stack optimised for 1550 nm [153]. The stack comprises Si substrate, SiO_2 (240 nm), Al mirror (80 nm), WSi film (20 nm), and capping layers (SiO_2 240 nm, SiN_x 220 nm) with half-wavelength spacing between Al mirrors for resonant absorption enhancement.

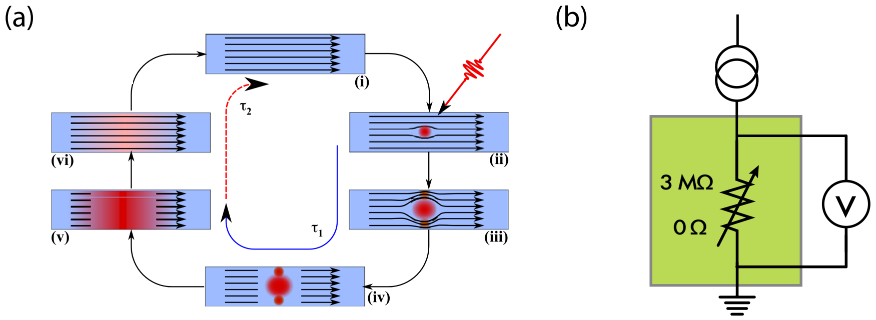

Figure 5.6: **(a)** The working principle of the SNSPD detection cycle, reproduced from [286]. A superconducting wire (i) ish hit by an incident photon (ii). This induces a resistive hotspot (iii) which grows and drives the whole wire normal (iv, v). The system remains non-superconducting until (vi,i), at a rate governed by the electrical circuit it is embedded in and thermal properties of the device. **(b)** An electrical circuit diagram highlighting the conceptual simplicity of the detection scheme. The SNSPD can be modeled as a two-state resistor, across which a voltage drop is measured. The challenge is performing this measurement fast, without affecting the device, in a cryogenic environment.

Readout Electronics, Operating principle, and Characterisation

Depending on the application and architecture in question, some of the electronic devices may be placed in the confines of the cryostat with the SNSPD, necessitating careful electronic design. Figure 5.7 shows our SNSPD readout circuit.

A bias-tee directs DC current (typically 5–6 μA) through the SNSPD via a 10 kΩ series resistor. It consists of a capacitive arm, hereafter known as the output, and two resistive arms. When the SNSPD switches resistive ($\sim$2 MΩ), current is shunted through a $\sim$250 Ω resistor, creating a voltage transient at the output, which is capacitively coupled to a home-built cryogenic amplifier.

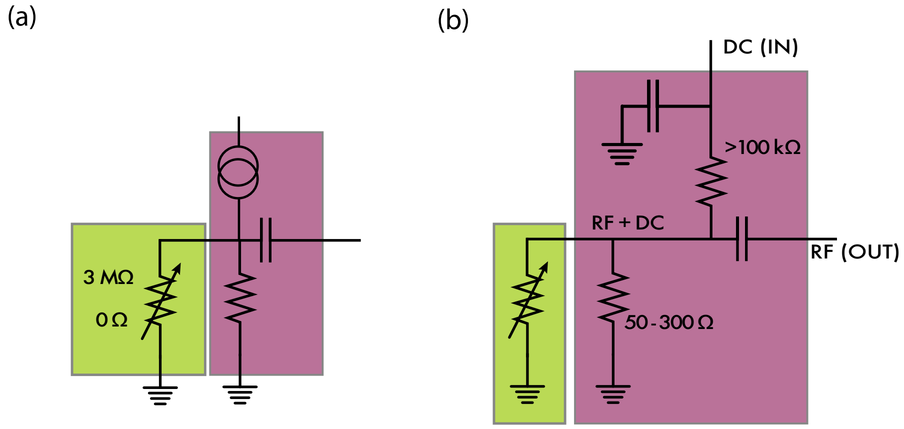

Figure 5.7: SNSPD Bias-tee circuit, showing DC bias, shunt path, and AC output coupling

The cryogenic amplifier uses a Skyworks SKY65050-372LF GaAs pHEMT transistor with NP0 capacitors and thin-film resistors for cryogenic stability [287]. Operating between the 4 K and still plate (0.9 K), it provides $\sim$6 dB gain while dissipating $<$5 mW. Alternative commercial amplifiers (e.g., Mini-Circuits ZX60-P103LN+) offer higher gain but consume $\sim$100 mW, requiring more thorough 4 K stage mounting.

Amplified pulses pass through two room-temperature RF amplifiers (Mini-Circuits ZFL-500LN+) and a 10 MHz high-pass filter (to reject building RF interference). Signals are split to a Rigol 1202Z oscilloscope (time-domain monitoring) and Swabian Instruments Time Tagger Ultra (photon counting, correlation measurements).

Operating Principle and Characterisation

A precision voltage source (Stahl DAC, graciously on loan from the Quantum Nanoscience Laboratory) supplies 700–900 mV through a variable decade box ($\sim$130 Ω at room temperature) and the bias-tee's 10 kΩ resistor, biasing the SNSPD at $<$6 μA. Operating parameters are tuned based on dark count rate, detection efficiency, and environmental noise[2].

---

[2] The numbers provided here are approximate because they may change, depending on experimental requirements including integration time, efficiency, and dark count rate... or the perennial grounding issue our

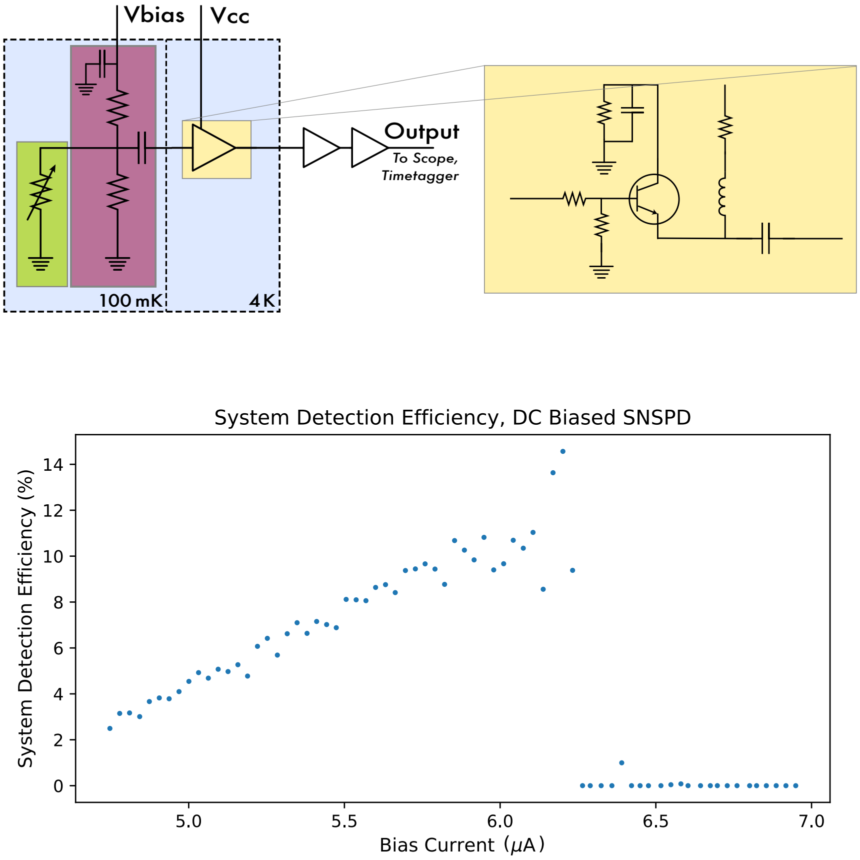

Figure 5.8: Top: A full circuit diagram of the SNSPD system, with inset (yellow) showing the schematic of the HEMT amplifier circuit. **Bottom:** the system detection efficiency of the detector usied in this work.

During the periods of time when the SNSPD is superconducting, current flows straight to ground. The moment this superconductivity is broken, the SNSPD's resistance switches to ∼2 MΩ, and therefore the current passes instead through R$_s$, the shunt resistance. This shunt resistance and the pre-amplifier capacitance create an effective R-C circuit, which along with the thermalisation and cooling dyanmics of the SNSPD itself govern the timing of the electrical pulse that is read out in the lab.

This signal passes through the cold amplifier described above, to two room temperature RF Amplifiers (Mini-Circuits ZFL-500LN+) and a high-pass filter designed with a cutoff at ∼10MHz (chosen for the purpose of cutting out interfering signals from a nearby proximity card reader on a lab door). After this, the signal is divided and sent to an oscilloscope

---

building faces.

(Rigol 1202Z) for real-time monitoring of the time-domain signal, and a time tagger (Swabian Instruments Time Tagger Ultra) for counting and histograms.

System Detection Efficiency

The highest measured system detection efficiencies in our system are ~20-30 %. There are a number of reasons for this being lower than expected, including four fibre interfaces between the reference signal and our detector, and a sample of Er^{3+}:Si (used for a parallel research effort in our lab) which is placed directly on top of the SNSPD itself, in a configuration similar to that described in [153]. We note that this sample likely has effects upon our maximum detection efficiency - both through reflections and absorption, and by moving the fibre ferrule further from the detector and so changing the overall mode shape of arriving photons.

5.3 Spectroscopy Techniques

This section will outline the main experimental techniques used throughout the work of this thesis to characterise Er^{3+} in CaF_2, and benchmark its performance against other hosts. A more thorough introduction to the rare-earth ions and their energy level structure can be found in section 3.1.4. In parallel with our experimental setup becoming increasingly sensitive to small signals, I have focused on optimising these techniques for increasingly dilute samples of Er^{3+} doped materials at dilution refrigerator temperatures: we seek single-ion sensitivity in the long term.

In our experiments there exists a natural tension: the restricted cooling power of a dilution refrigerator leads to strict limits on the amount of optical power that can be deposited into a sample. Because of this, both the power of pulses and the duty cycle of our experiments must be limited accordingly. At the same time, the low optical dipole moment of the rare-earth ions leads to a natural desire to increase input power. For this reason, the goal of our experimental platform has always been to maintain a high collection efficiency from the sample in the cryostat, and develop ‘switching and sweeping’ infrastructure with low insertion loss.

Each experimental technique covered in the following section yields results for essential parameters when assessing the performance of specific Er^{3+} sites for quantum technologies, including oscillator strengths, population distributions, and coherence properties.

5.3.1 Transmission/Absorption Based Spectroscopy Techniques

Absorption spectroscopy measurements in lanthanide doped samples are used to measure inhomogeneous linewidths and absorption coefficients of rare-earth ions in solids. Depending on the time resolution of the detection chain, the timing with which the optical signal can be swept or gated, the optical depth of the sample, and the collection efficiency, various parameters may be measured. Transmission and absorption measurements can be used to probe excited state lifetimes (T_1), and provide a means of bounding the homogeneous linewidth from above, as well as the oscillator strength, provided the concentration, optical power, sample and beam geometry are well known.

Absorption Spectroscopy

A tunable laser scans through the inhomogeneous line of rare-earth ions in a cryogenic sample. There exist a number of excellent texts on extracting parameters from absorption spectra [143, 190, 288]. I provide a brief overview of the theory here. Absorbed light reduces transmission, following the Beer–Lambert law:

$$I(z) = I_0 \exp(-\alpha(\nu) z), \quad \alpha(\nu) = N\sigma(\nu), \tag{5.1}$$

where N is the ion density and $\sigma(\nu)$ is the absorption cross-section. The cross-section relates to the transition dipole moment μ via:

$$\sigma(\nu) = \frac{\pi}{3\epsilon_0 \hbar c} |\mu|^2 g(\nu), \tag{5.2}$$

with $g(\nu)$ the normalized lineshape. The homogeneous linewidth is:

$$\Gamma_{\text{hom}} = \frac{1}{\pi T_2}, \quad \frac{1}{T_2} = \frac{1}{2T_1} + \frac{1}{T_\phi}. \tag{5.3}$$

Extracting μ requires knowledge of beam geometry, optical power, sample length, and ion concentration. Oscillator strengths f can be calculated from dipole moments and compared with absorption measurements to validate models [157, 158]. Precise T_1 measurements from fluorescence (Section 5.3.2) enable cross-validation.

Accurate modeling of the absorption spectrum thus requires simultaneous consideration of these relaxation processes, dipole strengths, laser intensity, and sample geometry, in order to reliably extract physical parameters such as oscillator strengths and coherence properties relevant to quantum information science.

For absorption measurements, observable quantities are related to oscillator strengths. Recall that the oscillator strength may be calculated from the dipole moment of an ion by the following relationship:

$$\begin{aligned} f_{FI,q} &= f^{\text{ED}}_{FI,q} + f^{\text{MD}}_{FI,q} \\ &= \frac{2m\omega_{FI}}{\hbar e^2} \frac{1}{g_I} \left(\frac{\chi_{\text{L}}}{n} S^{\text{ED}}_{FI,q} + n S^{\text{MD}}_{FI,q} \right). \end{aligned} \tag{5.4}$$

These expressions include the degeneracy of the initial state, g_I, the refractive index, n, and the local electric field correction. Here we assume the Lorentz or virtual cavity model correction given by

$$\chi_{\mathrm{L}} = \left(\frac{n^2+2}{3}\right)^2 . \tag{5.5}$$

Precise knowledge of T_1 from time-resolved fluorescence, as described in section 5.3.2 will also allow an independent test of absorption-derived parameters using these fundamental relations.

Zeeman Spectroscopy

Performing these scans with the sample in a magnetic field adds another degree of freedom to these experiments. Spin states will split in an applied field, and each optical transition will therefore split into four branches (denoted 'lower'/'upper' to 'lower'/'upper'), as shown in Figure 3.3.

This enables measurements of magnetic sensitivity of optical transitions, which can be combined either EPR [221] or Raman Heterodyne [289] methods to distinguish between ground and excited state sensitivity, and extract g tensors. See ref [182] for information on how this has been conducted in our experimental platform, yielding a measurement of the Er^{3+}:CaF_2 G1 site's excited state g tensor.

Hole-burning Spectroscopy

Spectral hole-burning is a technique which is commonly used in rare earth spectroscopy [171, 179, 290]. It is made possible due to the long optical and spin lifetimes ($T_{1,opt}$ and $T_{1,spin}$ respectively) of the lanthanides, and the fact that the inhomogeneous linewidth of an ensemble of ions is often many orders of magnitude larger than the homogeneous linewidth of a single ion at low temperatures.

The laser is held at a specific frequency within the inhomogeneous line of an ensemble of rare earth ions for an amount of time that is long compared to the Rabi frequency. As this excitation signal continuously drives a given transition from a specific ground state. When an ion is optically excited and subsequently decays, it returns to one of a number of states, with probabilities given by the Branching Ratio. This creates a spectral 'hole' at the original laser frequency – shown in Figure 5.9 – which can then be observed by scanning the laser through the inhomogeneous line as per section 5.2.1. The depth and persistence of the hole depends on the relative populations of the various ground state sub-levels and the rates of relaxation between them. A spectral 'hole' will form.

This hole is a narrow region of increased transparency, comprised of a sub-ensemble of ions, each with an optical transition frequency close to the burn frequency. The lifetime and width of the hole give an upper bound on the linewidth, and a lower bound on the coherence properties of a single atom in that sub-ensemble. This method also hints at a general feature of rare-earth ion spectroscopy: selecting smaller and smaller sub-ensembles from dense ensembles helps to inform bounds on single-ion properties.

Measurements of holes provide a method of measuring the non-integer branching ratio of any transition from an excited state back to the ground state from which the ions were excited. Due to this, it is possible to 'burn into' structure aside from simple optical or electron spin structure, and nuclear spin structure from the ion of interest or nearby ions in the lattice [139, 290–292].

Typically these holes decay in a multi-exponential manner, with the typical ordering of timescales for rare earth spins being very short - ∼100s of ps or less - for crystal-field levels, ∼100s of μs-ms for optical lifetimes, ∼10s of ms for electron spin lifetimes, and ∼seconds and above for nuclear spin structure [65]. In some extreme cases, holes can live for anywhere between minutes and months [179]. In our doped CaF_2 samples, we have recorded lifetimes of spectral holes in some conditions up to ∼10 hours [182], confirming the presence of ^{167}Er in our samples.[3]

When a hole is created, an 'anti-hole' will also appear in another part of the spectrum - an area of increased absorption. As ions decay into ground state sub-levels that were initially less populated, this creates increased absorption – an "anti-hole" – at frequencies slightly offset from the original burning frequency. The spectral positions and relative intensities of holes and anti-holes can provide detailed information about the level structure and the branching ratios of the optical transition. These dynamics are governed by precisely what structure has been 'burned into.' If the hole is probing electron spin, the anti-hole will appear in one of the Zeeman-split inhomogeneous lines (up to a few GHz away depending on field strength), but if the hole is caused by nuclear spin structure, the anti-hole will appear much closer to the hole.

---

[3] Running experiments of this nature is challenging, as arbitrary waveform generators, TTL sources, and other experimental hardware is not usually suited to microsecond precision pulsing and sequence generation for times in excess of tens of seconds. To perform these experiments, the entire experiment stack was bypassed and the optical shutter on the front panel of our CTL1500 was used. This also makes for a nice story to describe shuttering the laser, going home, and coming back to the lab the next morning to find last night's hole still present.

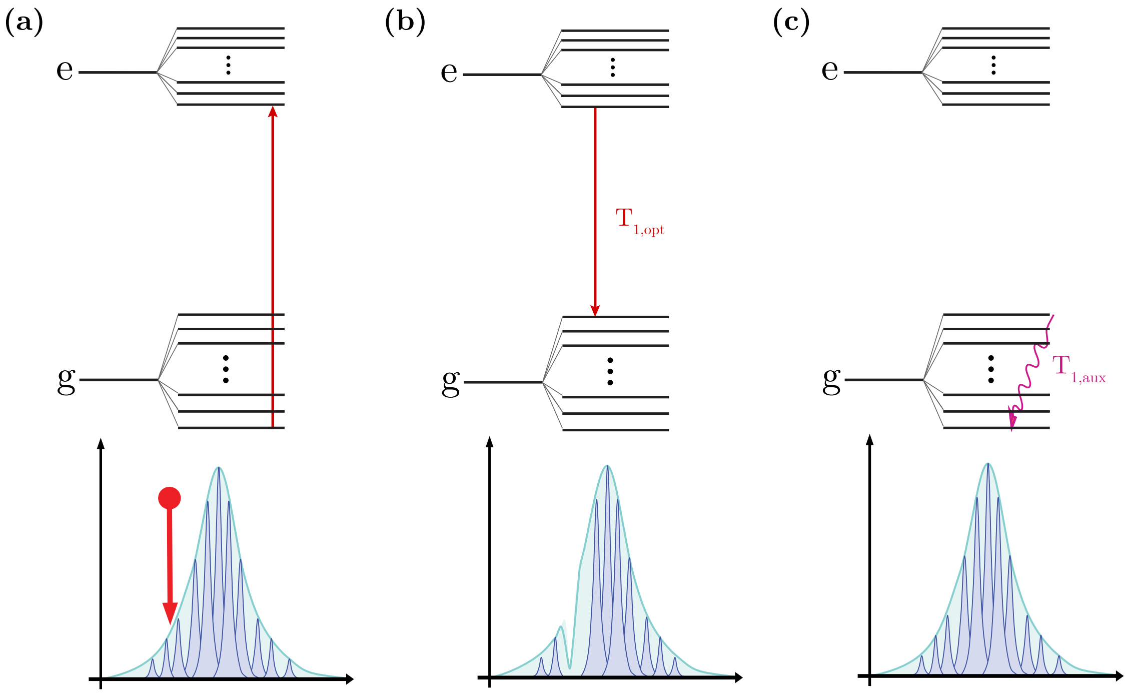

Figure 5.9: Schematic representation of spectral hole-burning: **(a)**Holding the laser frequency (red arrow) at a specific frequency somewhere within the inhomogeneous line drives population into the excited state. **(b)** As the population relaxes back down to the ground state (over $T_{1,opt}$, some portion of the ions will relax into a different ground state to the one that they initially left from (here depicted as a generic auxiliary level). This opens a region of increased transmission – a spectral 'hole' in the spectrum. **(c)** The hole fills in on a timescale which is governed by the lifetime of whichever auxiliary state the population has relaxed to. This auxiliary state could be due to electron or nuclear spin, super-hyperfine interactions with other nearby spins, crystal field levels, or other splittings. Adapted from [182]

As detailed in Section 3.1.4, a comprehensive energy level diagram for rare-earth ions in crystalline hosts must account for multiple types of auxiliary levels: electronic crystal field levels, electron and nuclear spin sub-levels, and in some cases super-hyperfine structure from interactions with neighbouring nuclear spins. The timescales for relaxation between these various levels span many orders of magnitude, from picoseconds for crystal field relaxation to seconds or longer for nuclear spin processes.

5.3.2 Fluorescence spectroscopy

Resonant Photoluminescence

Resonant photoluminescence excitation (PLE) spectroscopy provides a highly sensitive method for probing the optical properties of rare-earth ions with high time and frequency resolution.

In this technique, a narrow-linewidth tunable laser is scanned across the inhomogeneous absorption profile of the rare-earth transition. While it is pulsed, a detector (in our case an SNSPD as described in Section 5.6) monitors the fluorescence intensity.

As the laser crosses the optical transition frequency of an erbium ensemble, those ions are excited (from $Z_1 \longleftrightarrow Y_1$, for example) and subsequently relax to the ground state manifold (from $Y_1 \rightarrow Z_x$) emitting photons. That fluorescence is read out using our SNSPD. This approach is particularly valuable for studying rare-earth ions in dilute samples when compared with direct absorption measurements. This is because PLE can achieve much higher sensitivity since it relies on fluorescence – a positive signal – rather than absorption – which leads to measuring small negative changes in transmitted intensity, and hence poor signal-to-noise ratios.

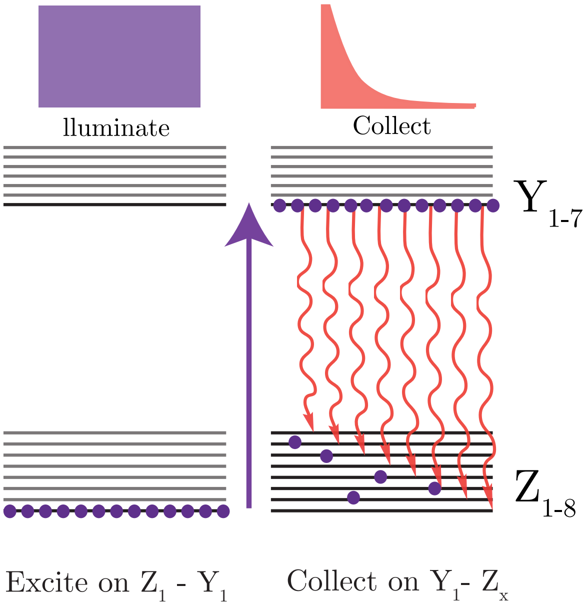

Figure 5.10: Incoherent excitation pulse and fluorescence decay. A long (∼ms) pulse is used to incoherently excite a population from the ground Z_1 to an excited (Y_1 or Y_2) state. The laser is then gated and the path to the SNSPD turned on, providing a measurement of optical excited staate lifetimes.

For Er^{3+}:CaF_2 systems, resonant PLE enables detailed characterisation of site-specific properties. Different crystallographic sites exhibit slightly different transition frequencies due to variations in the local crystal field environment. By monitoring the fluorescence as a function of excitation frequency, it is possible to identify and characterise the spectral features of erbium sites in our crystal. The fluorescence lifetime and spectral characteristics provide additional information about excited state properties – including the frequency and lifetime of other crystal-field levels (Y_2 and up), and with filtering of excitation pulses, the branching ratio – and can be used to identify sites with particularly favourable properties for quantum applications.

Finally, it is important to note the recent development in our lab of a cryogenic confocal microscope, a collaboration between myself and Ms Angela Liang. This enables depth-sensitive studies, and importantly enables spectroscopy on samples of much lower concentration. We have recently started acquiring data on implanted, rather than doped Er^{3+}:CaF_2, to assess ion properties after implantation. The first outputs from this work are presented in Chapter 6.

5.3.3 Coherent Spectroscopy

Photon echo spectroscopy is a nonlinear optical technique that probes dynamics, coherence, and dephasing in quantum systems using sequences of timed laser pulses. In rare-earth ion systems, photon echoes can be used to probe optical coherence, dipole moment, and spectral diffusion properties [145]. Photon echoes are directly analogous to spin echoes from NMR. We perform Rabi, Ramsey, and Hahn experiments: a pulse sequence is used to manipulate the state of an ensemble, and as parameters of this sequence are varied, we measure properties such as relaxation, coherence, and phase memory times.

These techniques are sometimes known as ‘coherent spectroscopy’ as they have rely on phase-coherent emission from an ensemble of atoms. An ensemble of atoms (optical dipoles) emitting a phase coherent echo together is directly analogous to a phased-array antenna [293], a tool used in radar and communications engineering to steer beams. The phase on each emitter in this case, however, is whatever phase of the light pulse each atom ‘picked up’ during the initial excitation pulse, due to its transition frequency and location in the ensemble. For this reason, this emission is best collected in the transmissiom geometry, described in section 5.1.3.

Two-Pulse (Hahn) Echoes

We perform Hahn echoes by applying two timed pulses — a $\pi/2$ pulse followed by a π pulse — to ions. Originally developed for nuclear magnetic resonance, this two-pulse sequence has been extensively adapted for optical coherence studies in solid-state systems. The first pulse creates coherence among quantum states, which dephase due to inhomogeneities in the atoms transition frequency. The second (rephasing) pulse reverses the dephasing, leading to a coherent burst known as the echo. This technique allows accurate determination of coherence times (T_2).

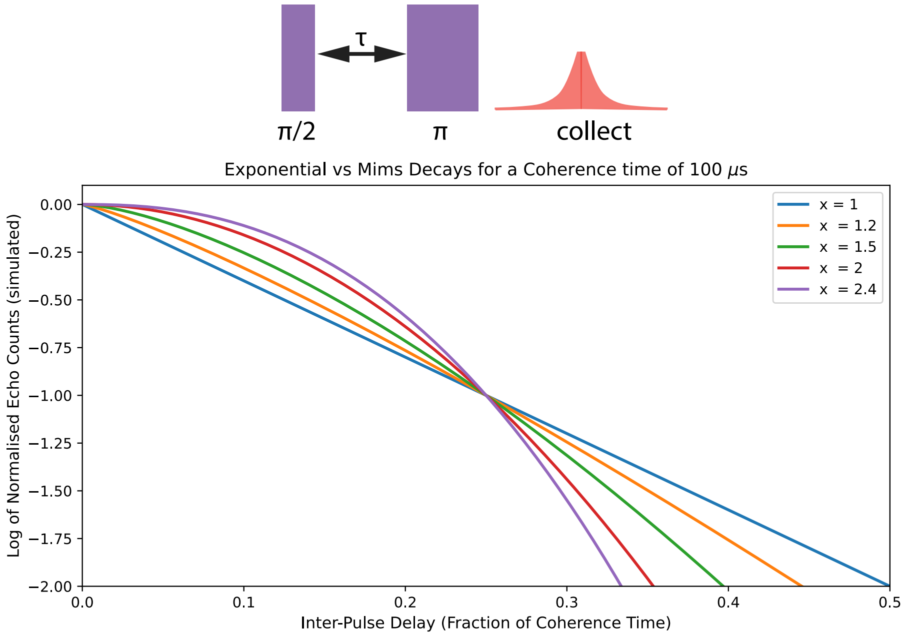

Figure 5.11: Hahn Echoes. The sequence (top) and simulated output of a Hahn Echo experiment (bottom). The different curves show the response of systems with various 'Mims' exponent x. We use the model of nonexponential decay provided in [294].

In the context of Er^{3+}:CaF_2 systems, Hahn echoes provide direct access to the coherence time T_2 — or analogously the single ion homogeneous linewidth Γ_h, by measuring the echo amplitude (or intensity) as a function of the inter-pulse delay τ. This measurement provides an understanding of the fundamental limits on coherence in these systems, and helps to identify the dominant decoherence mechanisms. Unlike absorption linewidth measurements, whose results are coupled to inhomogeneous broadening, echo techniques can isolate the homogeneous contribution and provide insight into decoherence mechanisms. The decay of the Hahn echo signal is often consistent with a simple exponential decay, with time constant proportional to the coherence time T_2.

However in the case of rare-earth ions (especially in hosts with nuclear spin, like fluorides), the decay often follows a nonexponential decay, as described by Mims in 1967 [295], identified by Macfarlane in 1991 [294]. This non-exponential profile that reflects the complex environment of the ions, and provides a new timescale, T_M — the phase memory time. The echo amplitude decay curve takes the form:

$$I(\tau) = I_0 e^{-(4\tau/T_m)^x} \tag{5.6}$$

where I, I_0 are the intensity and a reference intensity of the echo, τ is the inter-pulse spacing, T_m is the Phase Memory time and x is the 'Mims Exponent'. This exponent takes values between 1 and 2.4, depending on the dynamics of the system: $x = 1$ corresponds to a straight exponential decay, while $x = 2.4$ describes the most extreme case [296].

As is shown in Figure 5.11, the ‘Mims-type’ decay of an ensemble in a crystal is an improvement on exponential decay coherence at short times relative to the overall lifetime, but worse over longer timescales. This can be thought of as due to cascading effects. This decay is a useful metric to examine when considering dynamical decoupling pulses for long-lived quantum memories [176].

Interactions with environmental spins (both electronic and nuclear), spectral diffusion processes, and instantaneous spectral diffusion all contribute to the observed decoherence dynamics. By analysing the echo decay, the Mims exponent, and the dependence on temperature and magnetic field, it is possible to identify and quantify various decoherence mechanisms.

Rabi Oscillation Measurements

Rabi oscillations occur when a system is subjected to a continuous resonant field, causing populations to oscillate between quantum states. Measuring and controlling these oscillations helps characterise transition strengths and coherence. In photon echo experiments, Rabi-like pulses set the stage for induced coherence and timing of echo formation.

These oscillations provide direct access to the coupling strength between the optical field and the atomic transition, encoded in the Rabi frequency $\Omega = \mu E/\hbar$, where μ is the transition dipole moment and E is the electric field amplitude. For rare-earth ion systems, Rabi oscillation measurements are essential for characterizing the electric dipole properties of different sites and optimizing pulse sequences for quantum control applications.

The observation of Rabi oscillations requires that the coherence time T_2 significantly exceed the Rabi period π/Ω. In particular Er^{3+}:CaF_2 systems operating at cryogenic temperatures, Rabi oscillations can be observed over more than one full cycle, as shown in Chapter 6. This allows us to determine the transition dipole moment, providing a means to calibrate pulse areas for more complex quantum control sequences, and in consort with absorption measurements, provide an estimate on precisely how many atoms are in a given spectral feature.

Three Pulse Echoes

We use three-pulse echoes to study dynamic processes in rare-earth systems, including spectral diffusion - the long-term ‘wandering’ of the transition frequency of an ion. Three-pulse echo

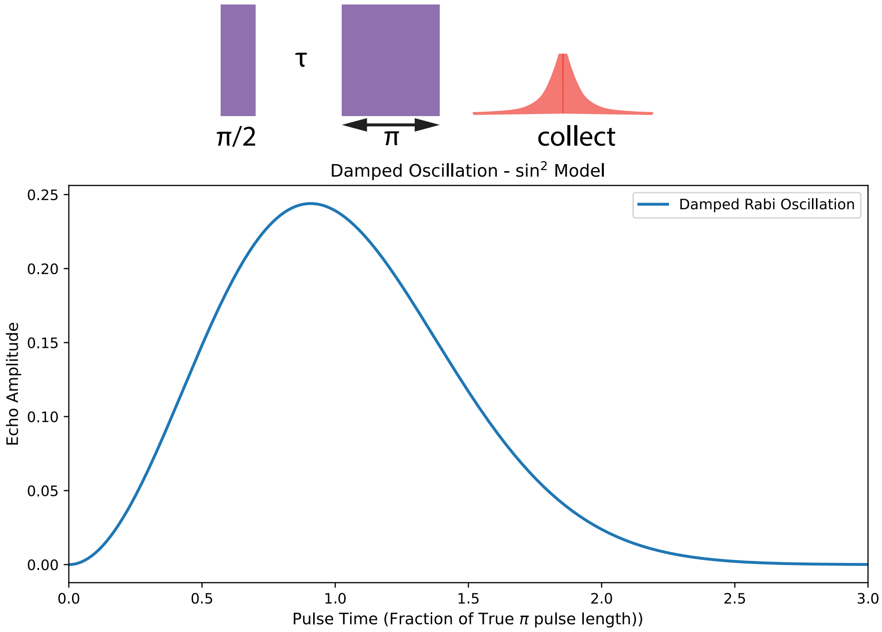

Figure 5.12: Rabi Oscillation. Pulse sequence (top) and a ‘cartoon’ of a trace of a Rabi experiment. This trace follows a $\sin^2$ curve, which tracks the characteristic ‘Rabi Flop,’ then is damped immediately afterwards. In some rare-earth ion systems with sufficiently high dipole moment, a second peak can be seen [65].

sequences are an extension of the original Hahn Echo technique, in which the rephasing π pulse is split into $\pi/2$ pulses. The second and third pulses of this echo are separated by a period of free evolution – often much longer than the coherence time.

The basic three pulse echo sequence consists of three separated $\pi/2$ pulses - with a variable delay between the second and third. Unlike Hahn echoes, which refocus inhomogeneous broadening, the three pulse echo signal is sensitive to transition frequency variations, since the second pulse maps all of the ensemble coherence onto ground and excited state population (see figure 5.13). To model spectral diffusion, we use Bottger’s model from [297]:

$$\Gamma_{\text{eff}}(T_W) = \Gamma_0 + \frac{1}{2}\Gamma_{\text{SD}}[1 - \exp\{-RT_W\}] \tag{5.7}$$

where T_w is the inter-pulse delay between pulses 2 and 3, $\Gamma_{\text{eff}}, \Gamma_0$ are a reference and current homogeneous linewidth, Γ_{SD} is the spectrally diffused linewidth, and R is the diffusion rate. If using a ‘Mims-type’ phase memory time, care must be taken when calculating linewidths - a good estimate of the pure dephasing homogeneous linewidth is $\Gamma_H = 1\ /\pi\ T_M$.

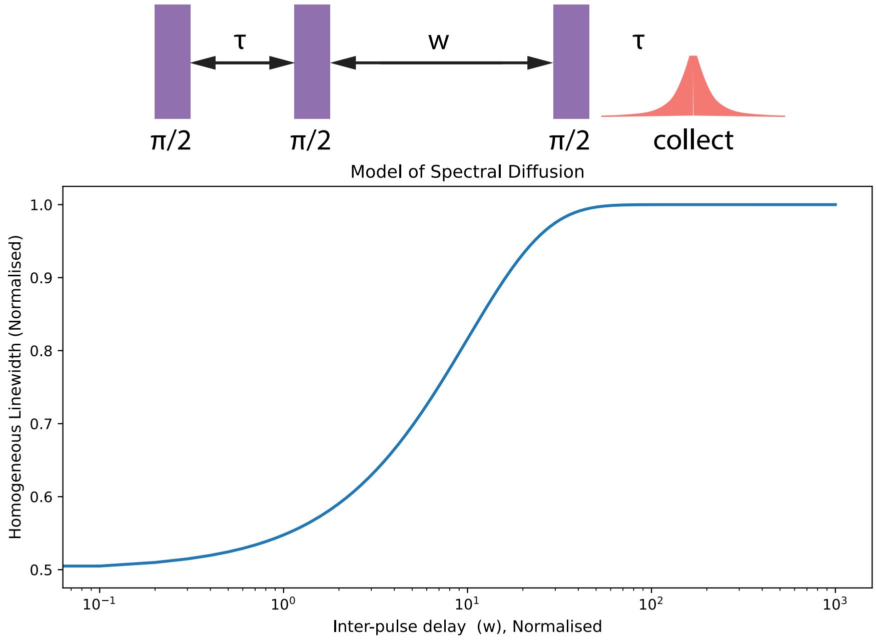

Figure 5.13: Three Pulse Echoes Pulse sequence (top) and a spectral diffusion model (bottom) showing the results of a three-pulse echo experiment. These experiments are conducted like a nested series of Hahn echoes: at each 'wait time' w, the inter-pulse delay between the first two pulses τ is varied to produce a T_2 or T_m. Homogeneous linewidths are calculated based on these fitted times, and a plot of linewidth vs delay (shown at bottom) is produced.

Echo Readout

The emitted photon echoes are detected one of two ways – and occasionally we work with these simultaneously. First and foremost, the SNSPD system described in Section 5.6 is used. A well-defined signal is sent to a time tagger, triggering starts and histograms are taken. The second method is the 'double heterodyne' approach, which was described in Section 5.2.4.

5.3.4 The Role of Magnetic Fields

Known, controlled magnetic fields are critically important, serving three essential functions in our rare-earth spectroscopy experiments. They enable the extraction of ground and excited state g-tensors that characterise the magnetic response of erbium sites. We use these tensors to model and identify field-insensitive zero first-order-zeeman (ZEFOZ) points, for coherent quantum operations. Second, at cryogenic temperatures where Zeeman splitting exceeds thermal energy ($\mu_B g B \gg k_B$ T), the Boltzmann-distributed populations across ground state sub-levels provide a direct optical thermometer through absorption intensity ratios. Third, sufficiently strong fields (B $>$ 100 mT at T $<$ 100 mK) start to polarise nearby paramagnetic spins, suppressing spectral diffusion and decoherence by "freezing out" spin-flip processes with other Er^{3+} ions, or other impurities that otherwise dominate inhomogeneous broadening and dephasing dynamics.

5.3.5 Temperature Studies

Variable-temperature measurements enable characterisation of temperature-dependent broadening and decoherence mechanisms. Heaters on the mixing chamber and still plate (Section 5.1) provide controlled sample heating, and less controlled measurements can be taken during cryostat cooldown or warm-up. Temperature-dependent T_2 measurements distinguish phonon-mediated decoherence processes. We use thermal population distributions to enable site assignment fo individual spectral lines via relative intensities at elevated temperatures [182].

5.4 Conclusion

This chapter has described the experimental apparatus and spectroscopic techniques that enable the spectroscopy presented in this thesis. The infrastructure developed represents a high-resolution, high-sensitivity platform, optimised for studying dilute rare-earth ion ensembles at sub-kelvin temperatures. As our measurements move toward resonators which target single ions, these tools and techniques will be well suited to the requirements of such sensitive experiments.

Hardware capabilities: Our Bluefors LD250 dilution refrigerator maintains sample temperatures <200 mK, verified through Zeeman thermometry. Fibre-based optical delivery achieves 5–40% cold coupling efficiency, depending on geometry, with custom 16 mm cage mounts providing <300 μm beam waists for coherent spectroscopy. Two-axis superconducting magnets deliver up to 1.4 T (solenoid) and 300 mT (transverse) with field homogeneity sufficient for ~1 mm^3 sample volumes. SNSPDs provide 20–30% system detection efficiency for fluorescence and echo measurements. High dynamic range optical switching (>300 dB laser-to-detector isolation) enables sub-microsecond gating for photon echo experiments.

Spectroscopic techniques: We have developed schemes for absorption and fluorescence measurements to characterise site-specific properties including inhomogeneous linewidths, excited state lifetimes (T_1), and magnetic field sensitivities (g-tensors). Spectral hole-burning has been used to provide upper bounds on homogeneous linewidths and probes auxiliary level structure (electron and nuclear spin states). Coherent transient methods, including Two-pulse (Hahn) echoe, Rabi oscillations, and three-pulse sequences directly measure coherence times (T_2, T_m), transition dipole moments, and spectral diffusion.

This toolkit enables the comprehensive Er^{3+}:CaF_2 site characterisation presented in Chapter 6, where we identify sites with excited state lifetimes exceeding 30 ms and transition dipole moments up to 2×10^{-32} Cm. Chapter 7 describes the fabrication and steps toward characterisation of whispering-gallery mode resonators fabricated from the same material, and our ongoing work to couple light to them in the confines of a dilution refrigerator.

"The consequence of the small dipole moment of rare-earth-ion transitions is that achieving ion-cavity interactions sufficient to realise the condition $g > \kappa$ is experimentally challenging"

Dr John Bartholomew, in Appendix C of his PhD Thesis

6

Spectroscopy of erbium sites in calcium fluoride

This chapter presents a detailed spectroscopic characterisation of the optical properties of four Er^{3+} sites in CaF_2. Using the spectroscopy system described in Chapter 5, I have started to explore the relationship between rare-earth ion sites and their quantum properties, using Er^{3+}:CaF_2 as a testbed system. We use these data to develop an understanding of the effects that lead to decoherence and spectral diffusion in this material. In the long term, these data inform our site engineering work, in which we examine precisely what controlled perturbations we could make to the crystal field to increase optical dipole moment.

We can also assess which of these sites is best suited for experiments at the single ion level in CaF_2 whispering-gallery mode resonators. For the resonator experiments we seek high cooperativity interactions between our atoms and light, and thus require a site with both a high optical dipole moment and sufficient coherence to enter the regime of lifetime limited coherence with a Purcell-enhanced single ion.

6.1 Summary of Experiments Conducted

I have measured inhomogeneous linewidths in both the $Z_1 \longleftrightarrow Y_1$ and $Z_1 \longleftrightarrow Y_2$ transitions for four of the Er^{3+}:CaF_2 sites, via transmission (absorption) and fluorescence spectroscopy, and studied the effects of temperature on the G1 site inhomogeneous line. Also using fluorescence, I have measured the optical excited state lifetime, placing upper bounds on dipole moments for these transitions. This informs the optimal choice of site for our single ion investigations, and provides heuristics to follow for our long-term goal of creating 'designer sites' with engineered crystal fields.

I have extracted excited state g tensors for a number of energy levels of interest from absorption and fluorescence studies in a rotating magnetic field. This study also was used to determine the precise crystal orientation relative to our magnetic field and optical beam. The g tensor also quantifies magnetic field sensitivity in our sites, and so provides insight into the optimal orientations of site, optical resonator mode, and field to maximise optical coherence with carefully chosen magnetic field direction [142]. Recent work using a confocal microscope developed by Ms Angela Liang on an ion-implanted CaF_2 sample provides promising hints for future single-ion device fabrication. Preliminary results indicate that inhomogeneous linewidths of pristine erbium sites remain largely unaffected by the implantation process itself, preserving spectral quality. Ongoing investigations aim to determine whether Er^{3+}–O^{2-} complexes can be created through implantation followed by inert-atmosphere annealing, via co-implantation, or whether oxygen-rich annealing is always required. These findings will define the first steps towards scalable pathways for deterministic ion placement in future cavity QED architectures.

The first estimate of the homogeneous linewidth of the G1 site comes from hole-burning spectroscopy. These data were taken during the work of [182], providing an independent lower bound on the coherence time through a homogeneous linewidth measurement.

I have also directly measured the coherence, dipole moment and spectral difusion properties of some of our sites, through photon echo spectroscopy following the Hahn, Rabi, and 3 Pulse schemes described in Chapter 5. I have improved the bounds on dipole moment and coherence time for three of the sites of interest (the G1, Cubic, and B sites), while photon echoes were not observed in the A site. Coherence times in the G1 and B sites were also measured as a function of rotating magnetic field, evaluating a low magnetic sensitivity direction for single-ion work in the dense nuclear spin bath of CaF_2. I have measured the effects of temperature on the homogeneous linewidth, and spectral diffusion of the G1 and B sites over timescales up to 1 ms.

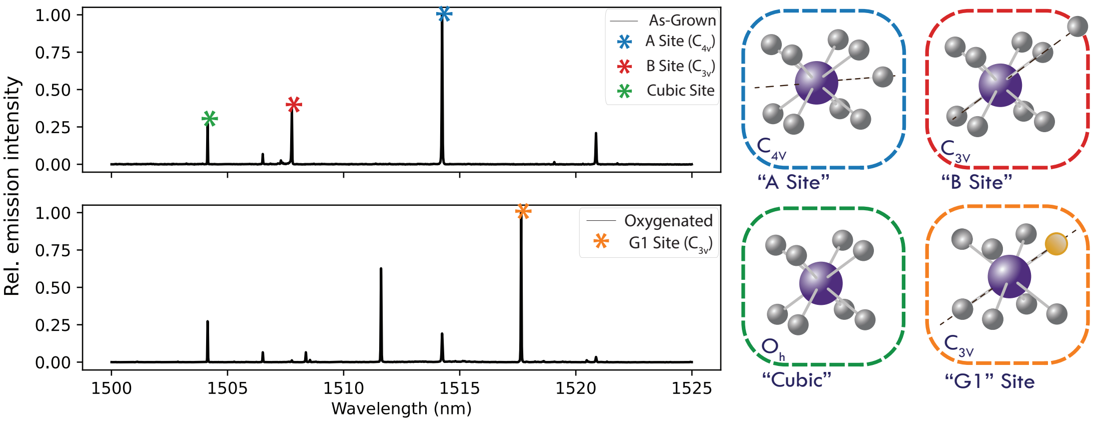

Figure 6.1: Broad spectroscopic survey and the four most prominent spectral features from the sites of interest in this work. Spectrum originally taken during [157]

6.2 Site summary

Recall from Section 3.3 that there are a number of crystallographically distinct sites that Er^{3+} can occupy in CaF_2. We study four of these in depth - known as 'A', 'B', 'Cubic,' and the 'G1' site. The ions in each site comprise a spectrally distinct ensemble of erbium: each of these ensembles has a $^4I_{15/2} \longleftrightarrow {}^4I_{13/2}$ optical transition with an inhomogeneous linewidth of the order of ~0.1-1 GHz, and these are easily resolved in frequency (for example, the G1 optical frequency is 197.468 THz, whilst the B site has its optical transition at 199.858 THz, some 2000 inhomogeneous linewidths away).

Whilst they are all optically separated from each other, these subensembles of erbium are also distinct from each other in terms of their spin. Their gyromagentic tensors g, are all distinct from each other (though the 'shape' of these tensors will be the same for sites of the same symmetry).

The sites we have studied in detail in our annealed Er:CaF2 sample are described in Table 6.1 below and are shown in Figures 6.1 and 6.3.

The study of these multiple crystalline environments provides access to a rich system – a 'spectroscopist's playground.' Each Er^{3+} site behaves as its own distinct ensemble of atoms, with their own site symmetry, their own dipole moment, their own g tensor, and their own coherence properties. A high-level summary of each of our sites is provided below:

A Site The 'A' Site - in which Er^{3+}'s extra charge is compensated by an interstitial fluorine entering the lattice in the [100] direction, is the most prominent peak in the non-annealed crystals. The site has C_{4v} symmetry. The highly visible line is actually the $Z_1 \longleftrightarrow Y_2$ line,

Site	Common name	Symmetry	Charge compensation
O_h	'Cubic'	O_h (cubic)	remote
$C_{4v}(F^-)$	'A Site'	C_{4v} (tetrahedral)	F^-, $\langle 100 \rangle$ direction
$C_{3v}(F^-)$	'B Site'	C_{3v} (trigonal)	F^-, $\langle 111 \rangle$ direction
$C_{3v}(O^{2-})$	'G1' Site	C_{3v} (trigonal)	O^{2-}, $\langle 111 \rangle$ direction

Table 6.1: Dominant erbium sites in our calcium fluoride samples. Note that while the 'G1' is produced predominantly by annealing in an oxygen-rich environment, it still occurs in small numbers for non-annealed crystals.

which is close to an order of magnitude larger in absorption and fluorescence than the $Z_1 \longleftrightarrow Y_1$. No evidence yet has been seen of coherent transients (echoes) in these spectral features.

B site In the 'B' Site, the charge is compensated by an interstitial fluorine entering the lattice in the [111] direction, leading to C_{3v} symmetry. The transition frequencies of $Z_1 \longleftrightarrow Y_1$ and $Z_1 \longleftrightarrow Y_2$ of this site are considerably higher (lower wavelength) than the other charge-compensated sites. In our fluorescence measurements in Figure 6.3, both of these emission lines are of similar prominence.

Cubic There is also a cubic site (O_h symmetry), in which the charge compensation mechanism is not well understood. A remote charge compensation scheme is suspected [156]. Both the $Z_1 \longleftrightarrow Y_1$ and $Z_1 \longleftrightarrow Y_2$ lines are within 3 nm (475 GHz) of each other, indicating that Y_1 and Y_2 crystal field levels are closer to each other than in other sites. Close interrogation of the inhomogeneous line reveals three tightly spaced peaks at zero field, and distinct satellite structure. This could be due to the isotope shift [298], as our samples are natural abundance Er^{3+}. Since this site is *cubic* its g tensor reduces to a diagonal: the idenntity matrix multiplied by 1/3 of an effective scalar g [188]. We use this for a calibration of the relative strength of orthogonal pairs of magnets.

G1 The G1 site is an oxygen-compensated site where an oxygen ion replaces a nearest-neighbour fluorine for charge compensation. This yields a C_{3v} symmetry. The $Z_1 \longleftrightarrow Y_1$ transition and $Z_1 \longleftrightarrow Y_2$ transition have both been studied in this work, with the $Z_1 \longleftrightarrow Y_1$ peak more prominent in FTIR and fluorescence scans. I have focused on the $Z_1 \longleftrightarrow Y_1$ for coherent spectroscopy. In other lanthanides, notably Eu:CaF_2 [65] the G1 site has an anomalously strong dipole moment, however the mechanisms which cause this increase in optical activity are not well understood. We use these studies in parallel with current crystal field modelling [157] to assess whether Er^{3+}benefits from the same enhancement, and if so, to better understand its mechanism.

Another view of this system is as an optically addressable Er^{3+} spin system with 'tunable properties' - including some that are normally immutable. Using Er^{3+}:CaF_2 in this context, we develop a system for spectroscopy of Er^{3+} in which we have control over:

- **Local electrostatic environment:** the charge and location of the charge balancing ion produces a different Crystal Field Hamiltonian.
- **Site symmetry:** Some sites have the same symmetry, which can be useful for making direct comparisons.
- **Immediate spin environment:** When compared to the cubic site, the G1 occupying erbium atoms see one less nuclear spin in the immediate neighbourhood of the Er^{3+}on average. In the case of the A and B sites, there is one more.

As well as the controls that solid-state spectroscopists are used to:

- **Magnetic field:** Field strength and direction are defined in a plane by our orthogonal coil pairs.
- **Spin population:** Via temperature and field strength.
- **Coupling to optical fields:** using optical resonators in the long term, but now by using timed pulses.

6.3 Bulk Calcium Fluoride Samples

6.3.1 Doped Crystals, Grown at University of Canterbury

The Er^{3+}:CaF_2 crystals used in this study were grown using the vertical Bridgman technique at The University of Canterbury crystal growth facility. Considerable detail on the facillity and methods has been provided in [157, 194, 220]. High-purity CaF_2 powder (99.99%) was mixed with ErF powder to achieve the desired erbium concentrations. The starting materials are loaded into iridium crucibles and sealed under vacuum, and lead fluoride added to prevent oxidation during growth. Because the details of the segregation coefficient during growth are not known, concentration across a boule is not easy to predict. Our quoted concentrations in a given sample of Er^{3+}:CaF_2 are therefore nominal.

In the growth process, the crucible is lowered through an inductive furnace at a rate slow enough to ensure complete crystallisation. Typical lowering times range from 24-96 hours, with a cooldown period of up to 48 hours after complete lowering. Post-growth oxygen annealing was performed to reduce unwanted defects, and introduce oxygen into the lattice for creation of G1 complexes. Samples were annealed in flowing oxygen atmosphere at temperatures between 600–900°C for durations of 12-24 hours. In [157], annealing conditions were varied to study their effect on site formation. Over the course of this work, we have benefited from a number of growths - each by Mr Michael Moull during the work of [157]. The growths from which we have samples are tabulated in Table 6.2.

Crystal Batch	Molar Conc. (Nominal %)	Growth Temp (°C)	Lowering Time (hours)
Older Growths	0.01	1450	24
MM8	0.001	1450	48
MM9	0.001	1450	96

Table 6.2: Crystal growth parameters for different batches of Er:CaF_2 samples grown at The University of Canterbury for this work.

The grown crystal boules are not strictly oriented, so some care is required to identify the crystallographic axes. Boules are either cleaved to produce faces of the dominant cleavage plane (the [111] plane), or cut using a diamond circular saw (along the [100] plane). Selected samples were annealed in an oxygen atmosphere to promote the formation of oxygen-compensated erbium sites, following the procedure described by Moull [157]. The annealing process varied between samples, with different temperature profiles and hold times employed.

For older growths (pre MM8), annealed samples were wrapped in aluminium foil and placed inside an annealing furnace. The temperature was raised at 1°C/min to 850°C, held at maximum temperature for 24 hours, and then lowered to room temperature at 1°C/min. Samples from growths MM8 and MM9 followed a modified annealing protocol. These samples were wrapped in aluminium foil and placed inside the oven. The temperature was raised at 1°C/min to 850°C, held at maximum temperature for 5 hours, and then lowered to room temperature at 1°C/min.

Samples break stochastically during the cleaving process, making it difficult to trace their origin within the boule. Only the oriented disk samples had documented positions within the original crystal growth. In some cases, it is possible to retrospectively identify the approximate locations of some off-cuts within the original boule by inspection of their shape. Samples close to the perimeter of the boule provide clues via their appearance too: The top and bottom regions of the crystal often exhibit visually distinct characteristics, with the bottom portion typically having a conical shape resulting from the growth process.

6.3.2 Implanted High Purity Samples

In addition to the crystals grown in collaboration with Mr Michael Moull and Prof. Mike Reid, a separate set of calcium fluoride samples was obtained commercially from Fairfield Crystal Technology, New Milford CT. Both were Excimer Grade CaF_2, fine-ground discs measuring 4 mm x 2 mm. The sample studied in this work has its optical axis parallel to the $\langle 111\rangle$ direction, with a $\langle 100\rangle$ sample reserved for future work.

These samples were ion-implanted with erbium and oxygen to a target concentration of approximately 50 ppm relative to calcium ($\sim 1 \times 10^{18}$ cm^{-3}), centred around a depth of 2µm from the surface. Implantation was performed at the Australian Heavy Ion Implantation Facility, using 8 MeV $^{170}Er^{+}$ at 7.5×10^{13} cm^{-2}, followed by 1.5 MeV $^{16}O^{+}$ at 2.7×10^{13} cm^{-2} and 2.0 MeV $^{16}O^{+}$ at 3.3×10^{13} cm^{-2}. Simulated implantation profiles for 8 MeV Er and 1.75 MeV O showed good spatial overlap between erbium and oxygen distributions.

These commercially prepared crystals provide a comparison to the in-house-grown material and serve as a controlled test of the properties of implanted erbium in CaF_2. Aside from the comparison between native Er^{3+} sites, the goal of this implantation study is to assess whether it is possible to create Er^{3+}-O^{2-} complexes, or other designer Er^{3+} sites, using implantation alone.

6.3.3 Summary Table of Samples

Sample	**Growth No.**	**Conc. (ppm)**	**Treatment**	**Orientation**	**Dimensions**
A	MM6	100	No anneal	unknown	10 mm diam. ∼3 mm
B	MM6	100	24hrs	$\sim\langle 100\rangle$- see [182]	10 mm diam. ∼3 mm
C	MM8	10	No anneal	$\langle 111\rangle$	irregular-octahedral, ∼2.5 mm thick
D	MM8	10	5 hrs	$\langle 111\rangle$	irregular-octahedral, ∼2.5 mm thick
E1	Fairfield	50 @ 2 µm depth	none	$\langle 100\rangle$	4 mm diam. x 2 mm
E2	Fairfield	50 @ 2 µm depth	none	$\langle 111\rangle$	4 mm diam. x 2 mm

Table 6.3: Samples used in our bulk spectroscopy surveys. Crystals labeled ‘MM’ are from the University of Canterbury [157]. Concentrations are nominal, based on the best measurement possible of growth reactants. Concentration may also vary across the boule. Samples E1 and E2 are commercial, excimer grade CaF_2, implanted by Shao Qi Lim at the Heavy Ion Accelerator at the Australian National University.

6.3.4 Sample Preparation and Mounting

For optical measurements, sample preparation varied depending on the experimental requirements and the samples received. Those obtained from the University of Canterbury collaborators received minimal polishing from the source laboratory, with only a quick polish performed when samples were transferred between institutions. These samples were then optically prepared – using SiC abrasive they were cleaned both dry, and when wetted with deionised water. The samples which were studied over the course of this thesis are detailed in Table 6.3.

For cryogenic measurements, samples were mounted using several configurations depending on the experimental requirements. Samples were thermally anchored to the appropriate temperature stage of the cryostat to ensure thermal equilibrium during measurements. Some samples were glued directly to mirrors for reflection geometry measurements, while others were mounted in free-space transmission configuration with the laser beam passing directly through the sample, as described in Chapter 5

6.3.5 A Note on Orientation

Given the cubic CaF_2 lattice and the axial nature of three of our sites, there are multiple orientations of site available relative to crystal axes. Depending on the site, there are either one (Cubic), three (A Site), or four (B and G1 Sites) individually oriented sub-ensembles in these sites, shown in Figure 6.2. These are degenerate at zero magnetic field, however split at different rates depending on their orientation to the magnetic field. - a deeper treatment of these sites is provided in [202]. The ideal sample is one in which the experimentalist knows precisely the orientation of crystal axes before the spectroscopy starts, however this is often challenging. Throughout the analysis of this chapter I will outline how we have precisely determined our crystal orientation, and which sub-ensemble(s) we are addressing.

6.3.6 A Note On Concentration

Knowing exact concentration of erbium ions in the crystal following annealing requires a suite of additional measurements. Knowing precise site occupancy, and yield when annealing to create oxygen complexes, is important for understanding the annealing process in the long term. Our experiments provide a means of improving estimates on site occupation when compared with FTIR spectroscopy. The FTIR results on the 5-hour annealed samples (MM8 and MM9) show that the peak absorption strengths of the C4v (A site) and G1 lines are comparable, however one can not make direct comparisons about site concentration using FTIR due to resolution limits. Even with high resolution absorption studies, dipole moments may vary between sites.

There is more erbium in the crystal than than in the sites identified here: there exist pair and cluster sites, along with other single ion sites (such as the G4 oxygen complex), and

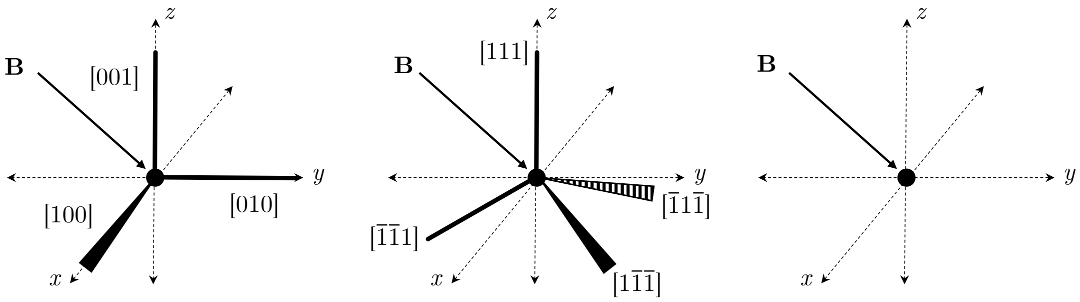

Figure 6.2: Indicative diagrams of the magnetically inequivalent orientations of our sites under an applied magnetic field, **B**. The labels [100], etc, show the direction which each orientation points relative to the original reference frame of the crystal. The C_{4v} site (A), at left, has its principal axes in common with the crystal's cubic system. The C_{3v} sites (B and G1) have their principal axes through the major diagonals fo the cubic crystal system, and as such there are four, tetrahedrally arranged, directions. The cubic site, at right, has no directional preference. Adapted from a figure originally produced in [182]

some ions will become optically inactive. Without independent measurements of site-specific absorption cross-sections, peak height comparisons provide only a qualitative indication of relative abundance. One of the capabilities this work enables is a more precise estimate on number of Er^{3+} in the G1 site in our samples.

Based on the spectral features in Figure 6.1 (observed in the University of Canterbury FTIR), a conservative estimate suggests that the G1 site concentration reaches at most approximately one-third of the original erbium dopant concentration in the annealed samples from MM8 and MM9. However, this estimate is highly uncertain and should be treated as an order-of-magnitude approximation only. Samples annealed for 24 hours (pre MM8) exhibited significantly higher G1 conversion compared to the 5-hour annealed samples (MM8 and MM9), suggesting that conversion efficiency from C4v to G1 sites is strongly dependent on annealing duration at maximum temperature. The longer annealing time appears to facilitate more complete oxygen incorporation and subsequent site conversion.

6.4 Detailed Experimental Results

This section summarises the key experiments from our systematic investigation was carried out to characterise the spectroscopic and coherence properties of these four sites in Er^{3+}:CaF_2, in doped and implanted samples.

6.4.1 Incoherent Spectroscopy

To identify optically active Er^{3+} sites within the CaF_2 host, we carried out a wide-ranging spectroscopy study, using PLE to find emission. Prior to SNSPD integration, this was conducted in transmission too, for details see [182]. These data are used as a verification of the FTIR data provided to us by the Canterbury crystal growth lab shown in Figure 6.1.

This survey revealed distinct absorption lines, some of which are indicative of the four sites of interest in our survey. The four most prominent features are the same as those in the UC FTIR data. These linewidths and peak positions provided a preliminary map for subsequent targeted investigations.

We also use these spectra as a comparison to the theoretical crystal-field models developed by Reid and Moull, available in [158], since the sensitivity and frequency (and time) resolution of our system is higher than the FTIR. This allows us to resolve $Z_1 \longleftrightarrow Y_1$ and $Z_1 \longleftrightarrow Y_2$ transitions in the four sites of interest. We also note that in our setup, we can still resolve fluorescence from G1 sites in a sample in which they have not been intentionally created.

Our fluorescence measurements are ultimately limited by our laser linewidth of 150 kHz [278], compared to the FTIR's 0.1 cm^{-1}, or approximately 3 GHz. In the broad survey shown in Figure 6.3, we apply a dither signal to our laser, broadening our resolution to 350 MHz. This is still considerably narrower than the FTIR results, and likely accounts of the relative prominence in the (otherwise smaller) cubic emission lines around 1504.6 and 1507 nm

Also notable in these spectra is the difference between oxygenated (annealed) and unoxygenated (non-annealed) samples. Firstly, the non-annealed Sample "A" yielded stronger fluorescence signals, likely due to experiment-specific factors (geometry, surface quality, mounting) rather than intrinsic site differences. Also, in our data we note that G1 fluorescence appears even in the as-grown Sample A, confirming that some Er^{3+}:O^{2-} complex formation occurs during growth from residual oxygen. While the signal is weaker than in deliberately annealed samples, this demonstrates that "background" G1 populations exist in our UC-grown samples, and complete elimination would require rigorously oxygen-free growth conditions. Finally, non-annealed samples consistently exhibit broader inhomogeneous lines. This is addressed in detail in Section 6.5.

Fluorescence Measurements

Lifetimes: From the survey shown in Figure 6.3, time-resolved fluorescence from each site was measured, allowing an excited-state lifetime (T_1) measurement for each Y_1 and Y_2 level of our sites of interest. Following pulsed excitation, we recorded photon arrivals using our

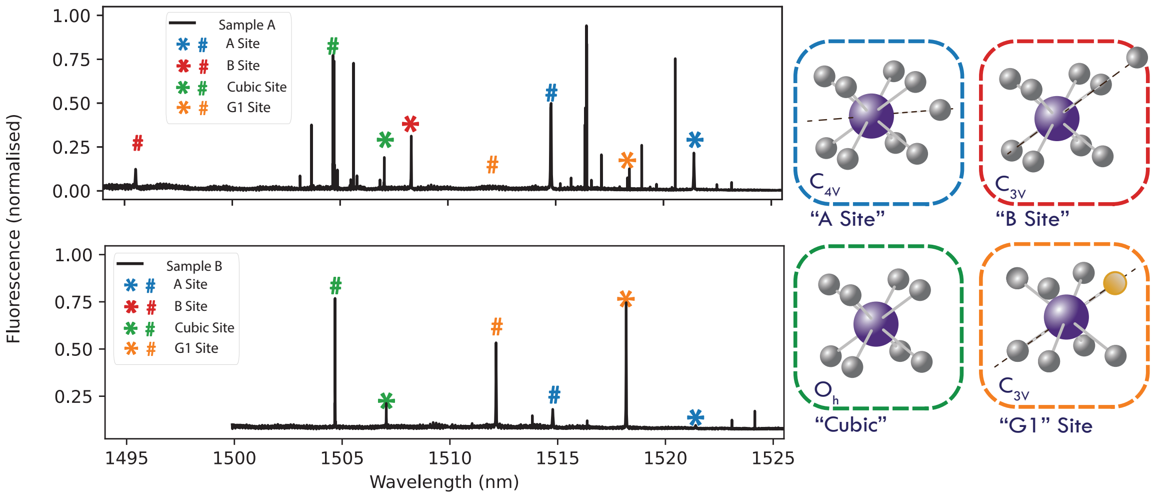

Figure 6.3: Wide scan spectroscopic survey of Sample A (as-grown) and Sample B (annealed), taken in our dilution fridge at T $<$ 100 mK. $Z_1 \longleftrightarrow Y_1$ transitions are denoted with $*$, while # shows a $Z_1 \longleftrightarrow Y_2$ transition, for each of our four sites of interest. We note a number of bright features in Sample A's trace. These bright features are not seen in any of our absorption studies, and their fluorescence decay does not follow an 'erbium-like' pattern. Therefore we say that they are most likely attributed to quenching behaviour of our SNSPD.

SNSPD and time tagger. The resulting decay curves provide radiative lifetimes, providing insight into the influence of local environment variations on the Er^{3+} dipole moment.

The fluorescence lifetime data provides insight into branching ratios of emission from different crystal field levels. The Y_2 excited state lifetimes are generally slightly longer than Y_1 for the Cubic, B, and G1 sites, suggesting fast non-radiative decay from $Y_2 \rightarrow Y_1$ dominates over direct $Y_2 \rightarrow Z_1$ emission. The A site presents the only exception, with $T_1(Y_2)$ slightly shorter than $T_1(Y_1)$, though this most likely reflects the higher signal-to-noise in the Y_2 transition rather than a true difference in decay pathways, and is still consistent with our fast, non-radiative decay hypothesis.

Upper Bound on Dipole Moments: The measured excited state lifetimes place upper bounds on the optical transition dipole moments for the $Z_1 \longleftrightarrow Y_1$ transitions. The spontaneous emission rate (Einstein A coefficient) for an electric dipole transition in a medium is given by:

$$A = \frac{1}{\tau_{\text{rad}}} = \frac{2\pi e^2}{\varepsilon_0 m_e c} \times \chi_L^2 \times \frac{n^2}{\lambda^3} \times f_{ij} \tag{6.1}$$

where e is the electron charge, m_e is the electron mass, n $=$ 1.43 is the refractive index of

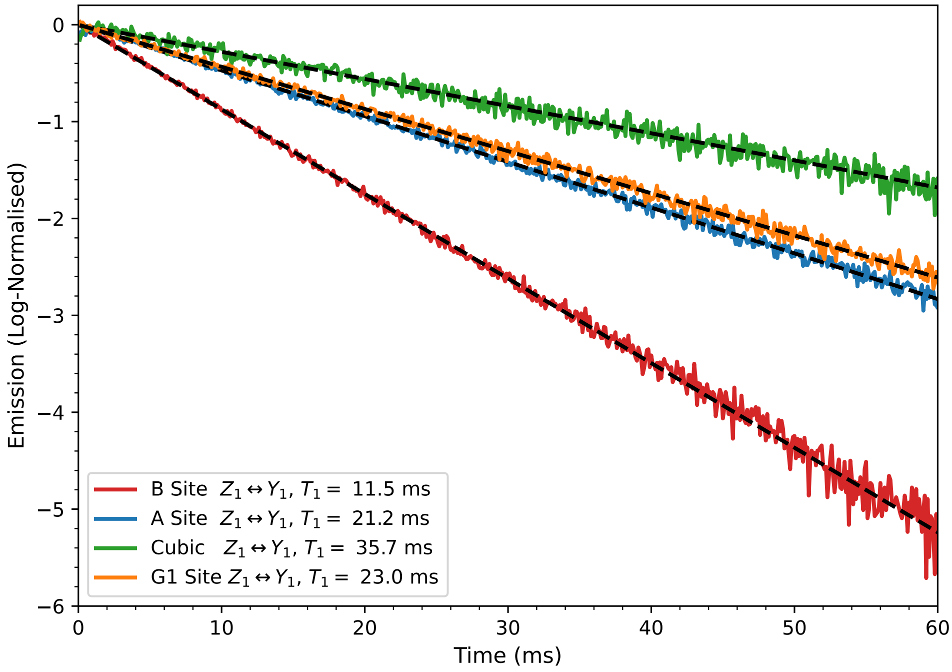

Figure 6.4: Fluorescence, and associated exponential fits for the $Z_1 \leftrightarrow Y_1$ transitions in our samples of Er^{3+}:CaF_2, Cubic, A, and B site lifetimes from Sample A, and G1 are from Sample B. These were via fluorescence using an SNSPD and readout techniques described in Section 5.3.2. The Y_2 excited state lifetimes are also provided in Table 6.4. These are not plotted, since they are indistinguishable from the Y_1 at these scales. This suggests a fast, non-radiative decay from Y_2 to Y_1, given the difference in lifetimes is within the experimental margins of error of our fitted lifetimes.

CaF_2 λ is the transition wavelength, and f_{ij} is the oscillator strength. χ_L is the local field correction: there are two models commonly used for this correction - the so-called Real and Virtual cavity models. The Real Cavity model [228] is given by:

$$\chi_L^{(R)} = \frac{3n^2}{2n^2+1} \tag{6.2}$$

While the virtual cavity model is

$$\chi_L^{(V)} = \frac{n^2+2}{3} \tag{6.3}$$

We employ the Real Cavity model in this work - as it has been shown to be suitable for rare-earth ions in substitional sites [51]. For an electric dipole, the oscillator strength relates to the dipole moment through:

$$\mu = \sqrt{\frac{f_{ij}\hbar e^2}{2m_e\omega}} \tag{6.4}$$

Since the measured T_1 may include non-radiative processes, we have $T_1 \leq \tau_{rad}$, yielding upper bounds on dipole moment μ. With our assumptions that the transition is solely electric dipole and approximating our measured $T_1 = \tau_{rad}$, we find these upper bounds, summarised in Table 6.4.

Label	Transition	f(THz)	λ	T_1(ms)	μ ($\times 10^{-32}$ C·m)
Cubic	$Z_1 - Y_1$	198.928	1507.00	35.7	2.8
Cubic	$Z_1 - Y_2$	199.241	1504.60	36.1	
'A'	$Z_1 - Y_1$	197.049	1521.13	21.2	3.9
'A'	$Z_1 - Y_2$	197.912	1514.70	20.8	
'B'	$Z_1 - Y_1$	198.762	1508.29	11.5	4.9
'B'	$Z_1 - Y_2$	200.460	1495.51	11.6	
'G1'	$Z_1 - Y_1$	197.469	1518.18	23.0	3.7
'G1'	$Z_1 - Y_2$	198.257	1512.14	23.4	

Table 6.4: Summary of parameters from T_1 measurements: Wavelength and excited state lifetime are presented for all transitions of interest. Dipole moments and oscillator strengths are calculated for Y_1 excited state lifetimes only. μ is calculated assuming a solely electric dipole transition.

However, it is important to note that the optical transitions we target are *not* solely electric nor magnetic dipole. In fact while the cubic site's transition is predominantly magnetic dipole [237], analysis from Moull [157] has shown the G1 has significant contributions from both. These estimates are high. We refine our bounds through direct measurements of Rabi oscillations, presented in Section 6.4.3.

Inhomogeneous Linewidths

I have performed a detailed analysis of the inhomogeneous line broadening for each site. In early experiments, this was conducted in absorption. Later experiments in our dilute samples were predominantly performed using fluorescence measurements.

Initial Absorption Measurements: Absorption measurements of the four most prominent infrared transition of the Er:CaF$_2$ sample were made in transmission using a Toptica CTL laser, and detected on a PDA20CS2 Thorlabs switchable gain detector. These are shown in Figure 6.5.

Given our samples are of various concentrations and have undergone different annealing processes, inhomogeneous linewidths provide some insight into the quality of the crystalline environment. One observation from the data in Figure 6.5 is that the A site has a broader

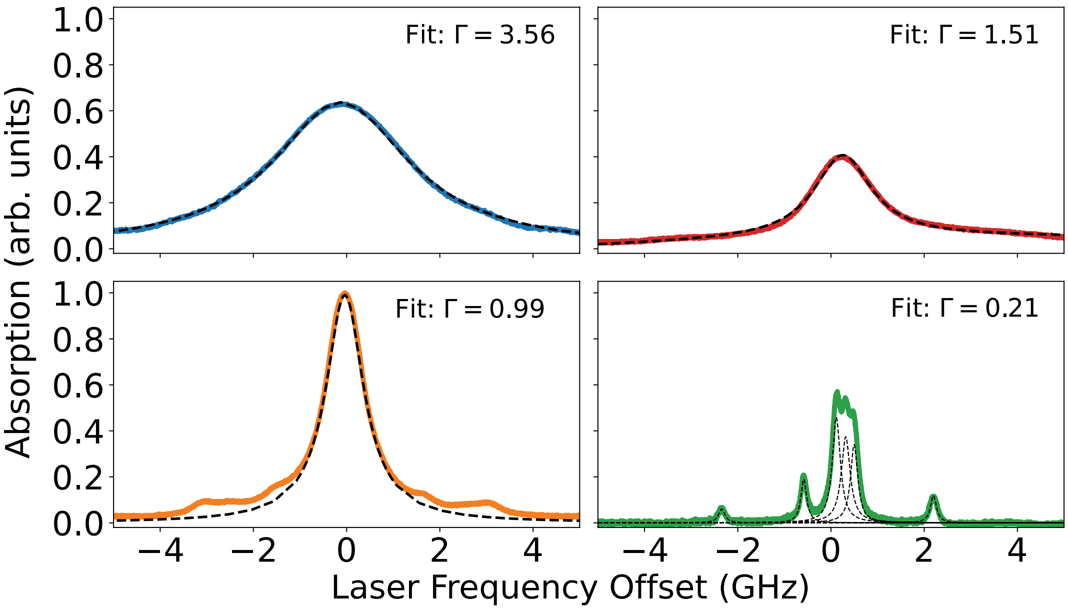

Figure 6.5: Inhomogeneous lines, taken in absorption, of the most prominent spectral features in our samples: A Site $Z_1 \leftrightarrow Y_2$ (blue), B site $Z_1 \leftrightarrow Y_1$ (red), G1 $Z_1 \leftrightarrow Y_1$ (orange), and Cubic $Z_1 \leftrightarrow Y_2$ (green) sites in Er^{3+}:CaF_2. A and B site spectra were taken in Sample A (unoxygenated), whilst the G1 and Cubic spectra were taken in the annealed sample. Fitted linewidths provided in the figure: A site (Z1-Y2) 3.56 GHz, B site 1.51 GHz, G1 0.99 GHz, and Cubic (Z1-Y2) 0.21 GHz

inhomogeneous line in sample A than the G1 does in sample B. One possible explanation for this excess broadening then is that the annealing process removes defects, narrowing the inhomogeneous line.

Across Various Samples: We have studied linewidths of the same line across a number of samples. As our samples have progressed towards more and more dilute, and our experimental platform evolves towards coherent measurements of progressively smaller ensembles, this has become easier in fluorescence than absorption. Our system is sensitive enough to read out the ‘stray’ G1 sites which are generated in a standard – not annealed – growth. Consistent with our hypothesis on the relative broadening of the A and B sites, the linewidth of the G1 $Z_1 \longleftrightarrow Y_1$ line in a sample in which those sites were not intentionally created is *broader* than that in an annealed sample. This is shown in Figure 6.6.

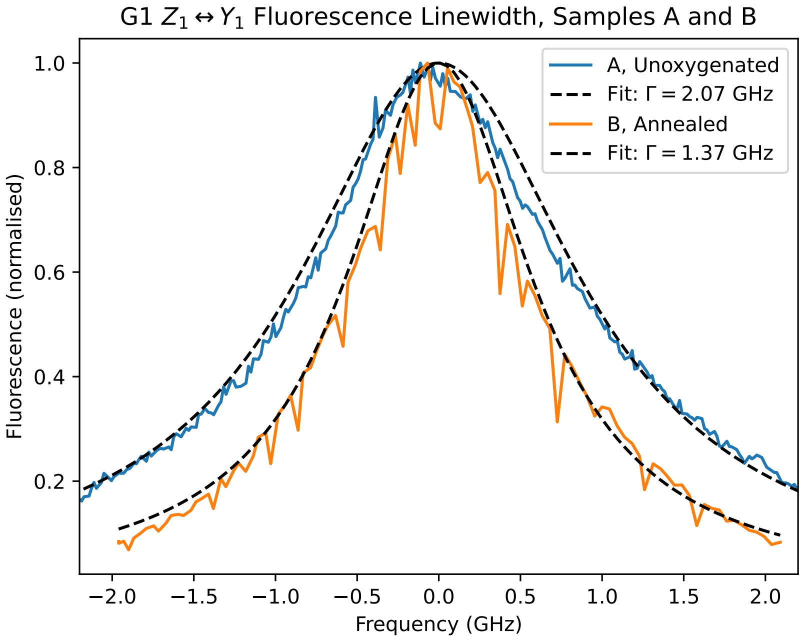

Figure 6.6: The inhomogeneous line of the G1 site in samples A and B, measured in fluorescence using our SNSPD. Data are each normalised to their own maximum count rate.

In Implanted Samples: As we progress towards photonic devices coupled to single Er^{3+} ions fabricated directly in CaF_2 it will become prohibitively difficult to grow doped samples with sufficiently low ion density, especially in the larger mode volumes of whispering-gallery mode resonators. A long-term solution to this problem is to fabricate photonic devices in ultra pure bulk (or thin film) CaF_2 and implant erbium post hoc, similar to the approach taken by parallel groups who work in Er:Si [114, 254], or other atomic systems in Si [214].

Thus, assuming we want to work with the G1, we ask: do we need to use a doped, annealed crystal to create the sites we seek in Er^{3+}:CaF_2? Would it be possible to implant Er^{3+}, alongside O^{2-} to create our own G1 centres? The initial data shown in Figure 6.7 show our first studies of a sample implanted with ^{170}Er and ^{16}O, our $\langle 100 \rangle$-aligned, implanted sample

In Figure 6.7, we see fluorescence from every site in this sample except the G1. Each line has an inhomogeneous linewidth comparable to its linewidth in a doped crystal, and optical excited state lifetimes are equal within error bounds. Similar to the initial FTIR data, the A site's $Z_1 \longleftrightarrow Y_2$ transition is the largest feature in these data. This could be owing to its optimised dipole direction (the excitation beam is perpendicular to the dipole), or the A site is simply the most common site for erbium occupation in the lattice.

We have not yet observed G1 sites in these samples, which could be caused by a number of

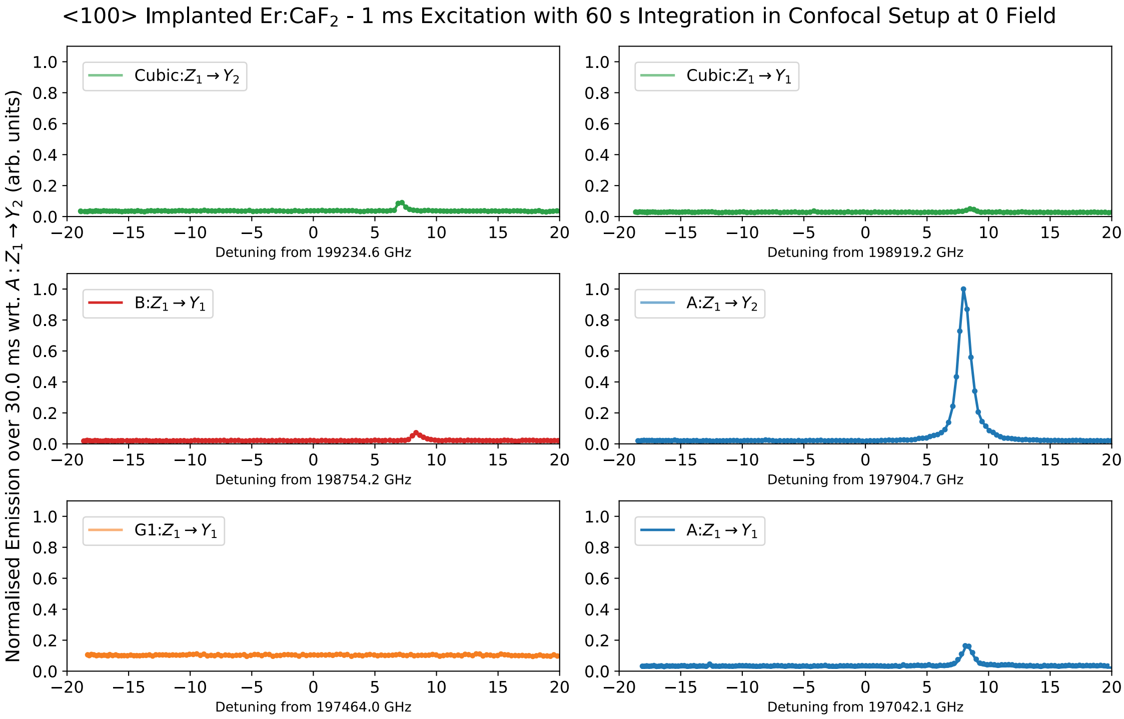

Figure 6.7: Preliminary data, courtesy of Ms Angela Liang. Fluorescence measured in our commercially acquired pure CaF$_2$ samples, implanted with erbium and oxygen. We measure fluorescence around the zero-field transition frequencies of each of our sites of interest. We see evidence of Er^{3+}population in each site, with the exception of the G1.Data are normalised to the largest spectral feature in the dataset – the emission from the A site Z1-Y2 transition.

effects. Firstly, the alignment of G1 dipoles to the light is not optimised for absorption in this orientation (the <111> axis makes an angle of 45 degrees with the light), and secondly we have not yet annealed this sample. The next step will be to anneal above 800° C, such that implanted O and Er ions are mobile enough to move in the lattice.

Temperature Dependence: The G1 inhomogeneous linewidth was measured - in transmission, in Sample B - with increasing temperature at zero field. The trend shown in Figure 6.8 shows the linewidth not exceeding 4 GHz, even at a temperature of 50 K. Above 100 K, absorption depth decreased to the point where the line was no longer visible. Using methods detailed in [180], it is possible to estimate the effective Debye temperature, highlighting when coherence will be phonon-limited.

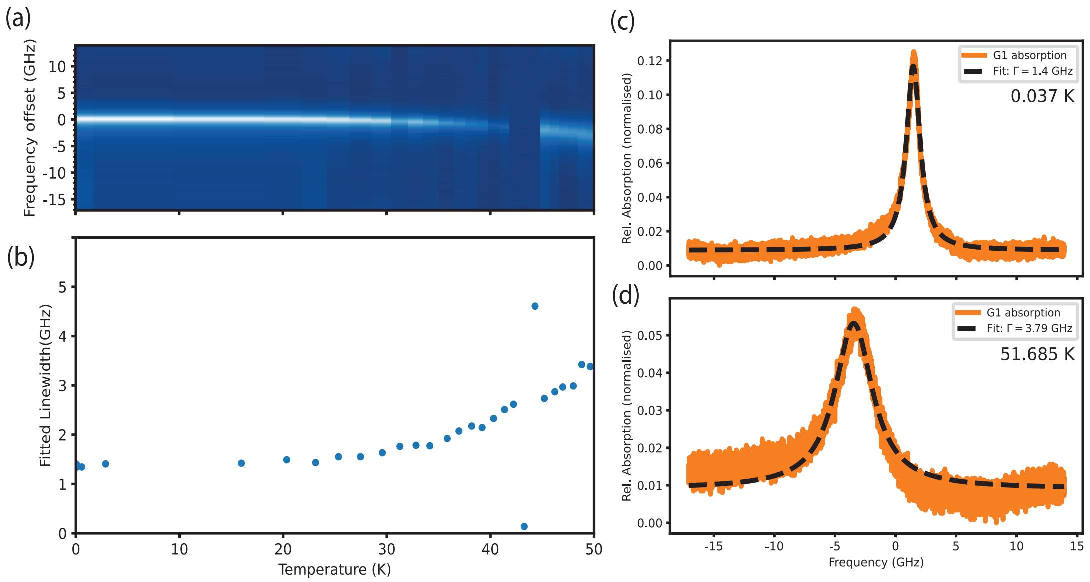

Figure 6.8: **(a)**inhomogeneous linewidth of the G1 site varying in depth, width, and frqeuency with temperature. **(b)** inhomogeneous line width varying w temperature. **(c)** Linewidth at 37 mK.**(d)** Linewidth at over 50 K

Holeburning

In our initial, more heavily doped samples, we conducted a number of holeburning experiments across temperature and magnetic field. I present some insights from those here.

Upper Bound on Homogeneous Linewidth: Our first upper bound on homogeneous linewidth came from hole burning experiments, originally presented in [182]. By analyzing the hole decay as a function of magnetic field, crystal orientation and temperature, we deduce bounds on lifetimes, coherence times and the extent of spin-lattice relaxation processes. We can also probe the electron and nuclear spin lifetimes of the system.

A Brimrose fibre-coupled acousto-optic modulator is used to gate and sweep the frequency of our laser about the $Z_1 \rightarrow Y_1$ transition. The AOM was driven by a Brimrose acousto-optic driver. Our recorded hole linewidth was limited to 0.628 MHz. This is broadened by a number of different factors – including laser stability and linewidth, but most notably the 0.5 MHz linewidth of the acousto-optic driver itself. The upper bound on T_2 in this system is therefore 1 µs ± 0.05, an estimate that we significantly improve using echoes.

Long-Lived Structure: We have also probed the electron and nuclear spin lifetimes of the system. Figure 6.9 shows an exceptionally long-lived feature: with no AOM in the path, the laser was gated using its shutter and swept using its internal piezo. Shown is the hole present after 1 hour, suggesting a $T_{1,nuc}$ in excess of 7 hours. This long T_1 is most likely due to the presence of ^{167}Er in our samples, in natural (20%) abundance.

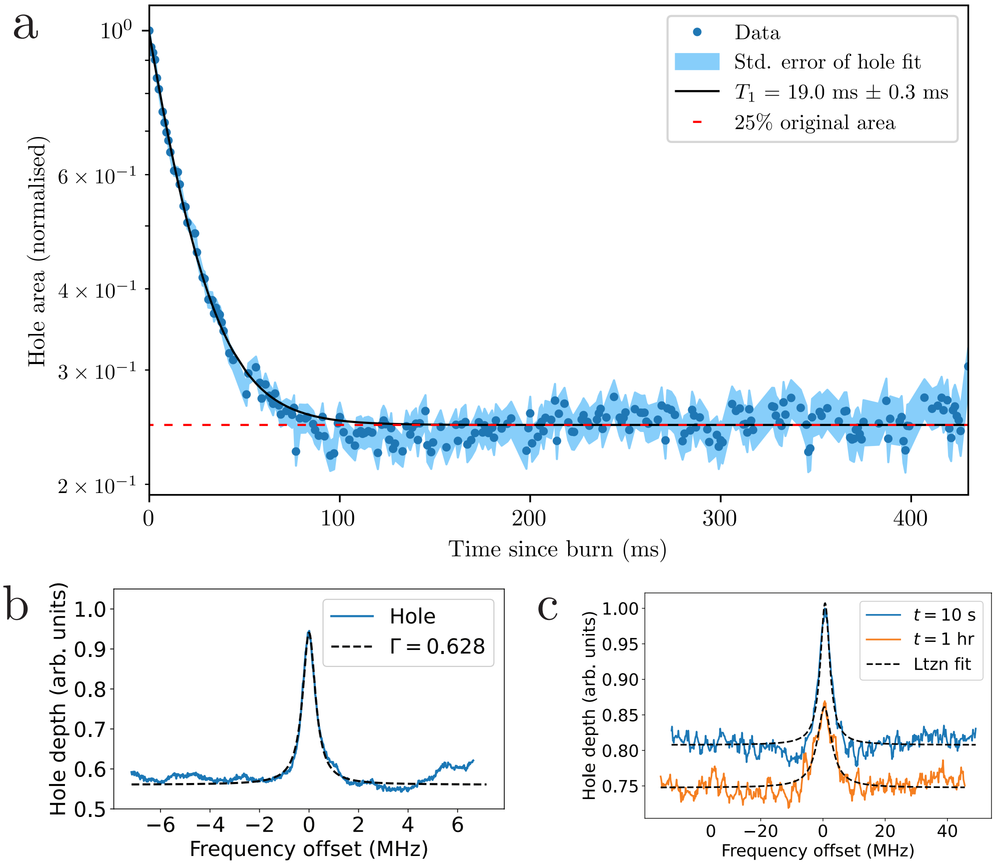

Figure 6.9: **(a)** Hole lifetime: A typical holeburning lifetime decay, fitted to a single exponential. **(b)** Homogeneous Linewidth Upper Bound: The narrowest hole that our initial setup was able to burn in the G1 absorption line. This was limited by the linewidth of the RF source used for our AOM, and fits to a Γ_h of ~314 kHz. **(c)** Evidence of long-lived structure in our doped samples: Relative transmission data, and a Lorentzian fit for a long-lived spectral hole. The long lifetime is most likely due to ^{167}Er present in our samples in natural abundance. These data are normalised to the transmission peak in the 10-second trace.

6.4.2 Characterisation of g Tensors

Whilst ground state g tensors are available from the EPR literature [188, 199, 299], the excited state magnetic sensitivity of Er^{3+} sites in CaF_2 had not been characterised prior to our studies. We conduct field-dependent absorption and fluoresence spectrum studies of the sites to identify our crystal orientation and fit g_e simultaneously.

Single Axis Field Ramps: The excited state g tensor of the G1 site was presented in our work in [182], and compared to calculated values from a crystal field model produced by Moull [157, 158]. This initial work was conducted with a single axis magnet, and a crystal whose orientation was initially unknown. Our results for the G1 site closely aligned with Moull's crystal field calculations for g_e, deduced from experiments conducted on the same sample using different experimental methods, data and modelling. Later studies were performed in a two-axis electromagnet as described in Section 5.1.4.

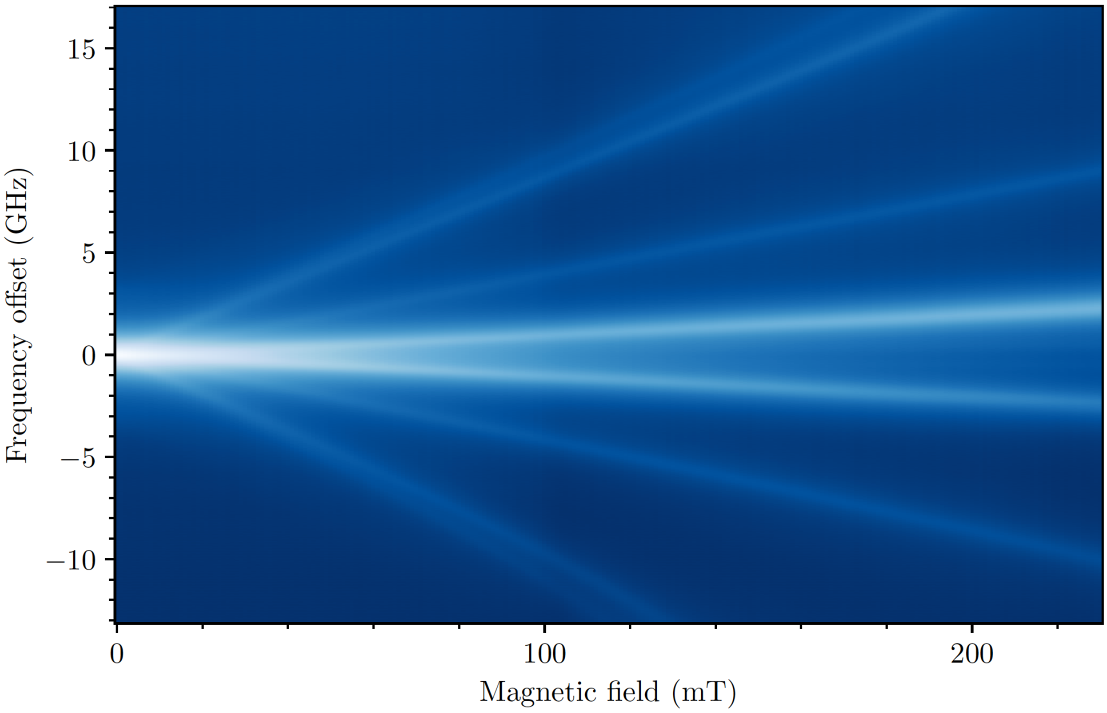

Figure 6.10: Magnetic field ramp at the G1 $Z_1 \longleftrightarrow Y_1$ transition. These data were taken at 4K, and thus show population in all lines. Using these data and a temperature sweep, the Y_1 level's g tensor was extracted in [182].

Nonlinear Zeeman Behaviour in the Cubic Site In the Cubic $Z_1 \longleftrightarrow Y_1$, we observe nonlinear Zeeman behaviour, at fields above 500 mT. This is shown in Figure 6.11. The data show the optical transition split at linear rates of ∼25 GHz/T, until flattening at higher fields.

This suggests an avoided crossing of energy levels in the cubic site - most likely the Y_2 in the excited state manifold, since this is the closest of the nearby crystal-field levels [156].

Nonlinear zeeman behaviour has been observed and characterised in Er:YVO$_4$ [124, 300], and characterised in YLiF$_4$ [298]. An investigation of the $Z_1 \longleftrightarrow Y_2$ transition's fluorescence spectrum at these fields will provide further insight on the the precise nature of this avoided crossing.

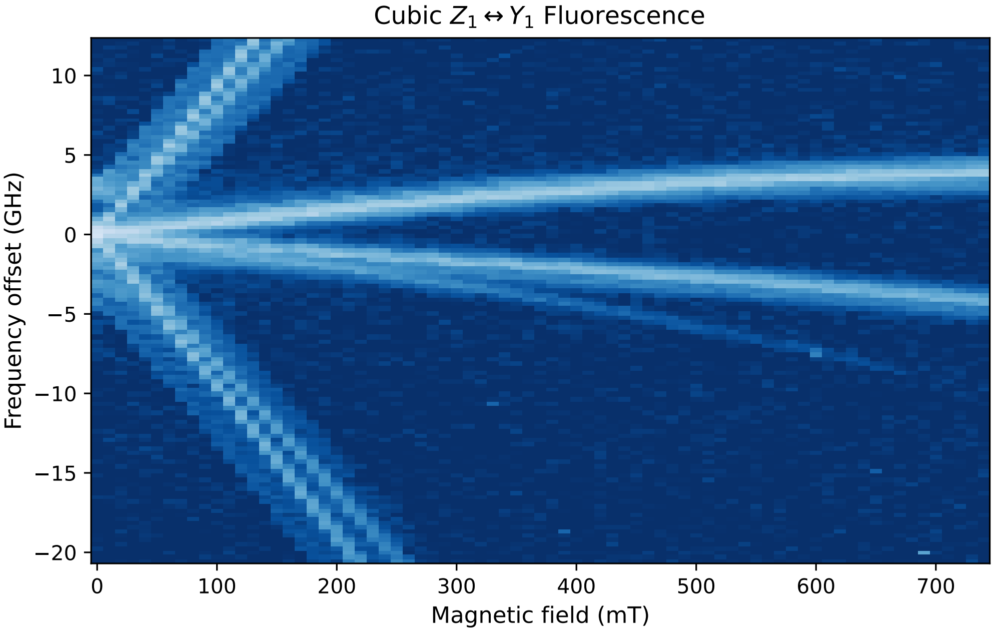

Figure 6.11: Linear magnetic field ramp in the Cubic $Z_1 \longleftrightarrow Y_1$ transition. Above 500 mT, the main line starts to curve, suggesting an avoided crossing with a nearby crystal field level – most likely Y_2

Magnetic Field Rotations

After the integration of a second home built magnet into our setup, we conducted a number of magnetic field rotation measurements. Crystal samples were aligned (to the best of our ability) such that one of the crystal <111> axes was parallel to the incoming beam, and the principal axis of our rotating magnetic field. For the purpose of fitting our later rotation patterns, this alignment provides a good 'initial estimate' however the angular orientation of the crystal relative to the field is not fixed in our fits of g_e.

Cubic Site Absorption Rotation: First, we use an absorption measurement and rotation in the cubic site to assess the relative strength, symmetry, and orthogonality of our magnets, shown in Figure 6.12. The known isotropic magnetic sensitivity of the cubic site means that these lines should be flat with respect to field orientation for a constant field.

We find that relative to our simulated (expected) magnetic field value, the "split coil pair" provides $\sim$10% less magnetic field than expected. This too is noted as a good initial estimate, but left as a free parameter in our later fits. From these data we also record the excited state g_e value of the cubic site: 5.2 ± 0.2.

G1 and B Site Rotations: We performed magnetic field rotations in the G1 and B sites, and used these data to confirm and extend our knowledge of these sites, our samples, and the experimental apparatus. Rotations were performed at a set field of 160 mT, although this was revised during our fitting. These are shown in Figure 6.13 and Figure 6.14, with the best fit we have achieved for each of these.

The process of fitting these data is iterative, based on our previous excited state g fits for the G1 from [182]. We use a numerical model that can account for variations in: overall field strength, the strength of our lateral coils relative to the solenoid, crystal orientation (θ, ϕ), and in the case of the B site, excited state g tensor. Therefore we bootstrap one fit from another, iterating towards an improved measurement of excited state g in both the G1 and B sites.

We start in the G1 site, with the acquired excited state g_e tensor values of $g_{e\perp} = 6.95 \pm 0.1$ and $g_{e\parallel} = 2.09 \pm 0.1$ as our initial guess. From these, we find both the angular orientation of crystal in the field, the field strength, and a 'Helmholtz Correction Factor' - which accounts for the fact that our split coil is $\sim$10% weaker than the solenoid. The fits are done using a Nelder-Mead simplex optimiser. The results of this fit are summarised in the Table 6.5:

We then use the angles and field strengths in the G1 fit as a starting point to fit the excited

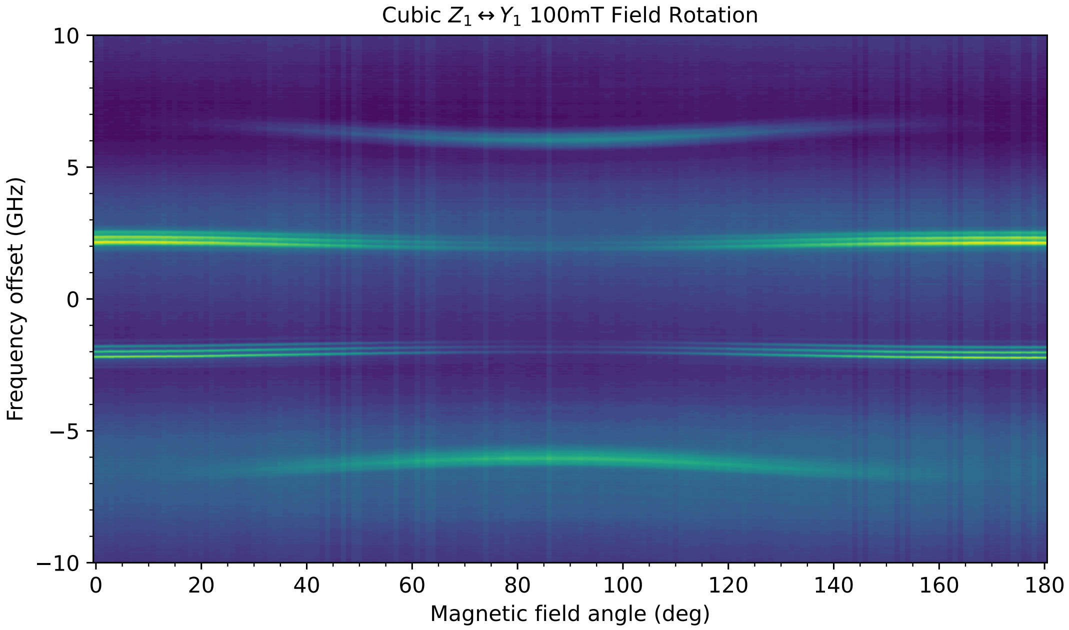

Figure 6.12: A magnetic field rotation was conducted in the cubic site. A known standard site like the cubic which has a scalar g can be used to calibrate the relative strength of our magnets. The lines which turn on and off around 90° are likely attributed to a change in transition selection rules at these angles, due to the symmetry-breaking effects of the magneti field [218]. There is also an increased temperature at these angles, since the split-coil magnet used in this rotation produced a non-trivial heat load. T_{mxc} reached 300 mK during this rotation.

state g tensor of the B site. We provide the angles, field strength, and field correction factor as initial guesses to the fit function, but ultimately leave these parameters free. The B site ground state g tensor is known: $g_{g\|} = 3.3$, $g_{g\perp} = 8.54$ [188]. The results of this fit are summarised in Table 6.6. We note a strong agreement between the fitted values for the crystal orientation in both of our fits, as well as a within-error-bounds agreement for the magnetic field strength and correction factors.

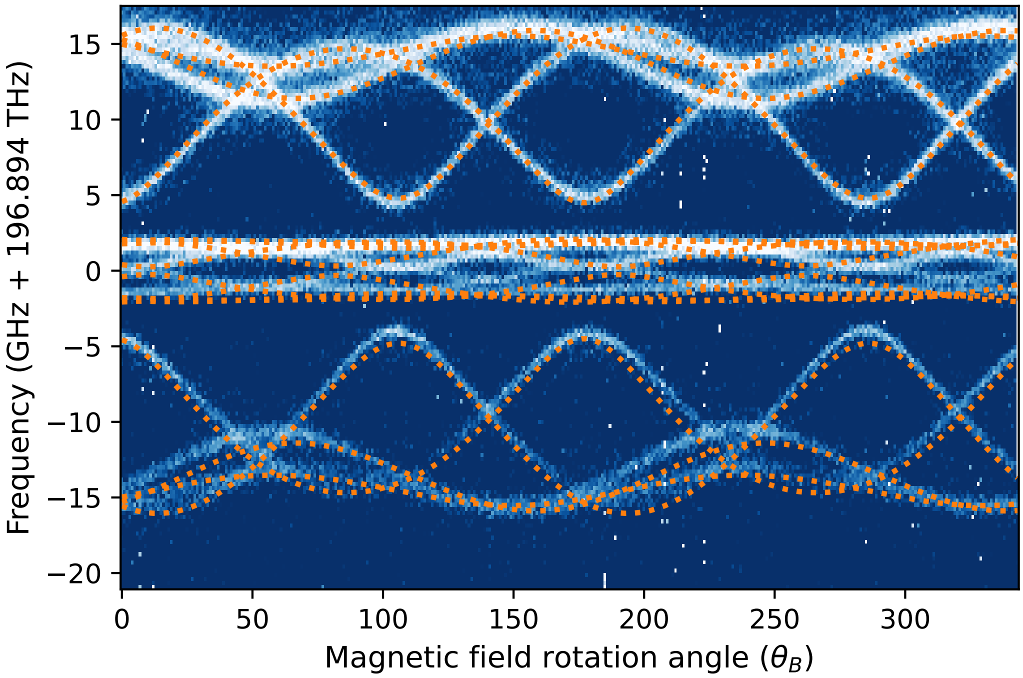

Figure 6.13: Rotation pattern in the G1 site with its fit, produced by iterating upon original fitted values presented in [182]

Parameter	Initial Estimate	Fitted Value	Error
θ(Azimuthal Angle)	0°	4.1°	±1°
ϕ (Roll Angle)	0°	-139.7°	±1°
Field Strength (mT)	160	151	±5%
Field Correction	0.9	0.899	±2%
$g_{e\parallel}$	2.09 ± 0.1	1.96	± 0.2
$g_{e\perp}$	6.95 ± 0.1	6.61	± 0.2

Table 6.5: Fitted parameters of the G1

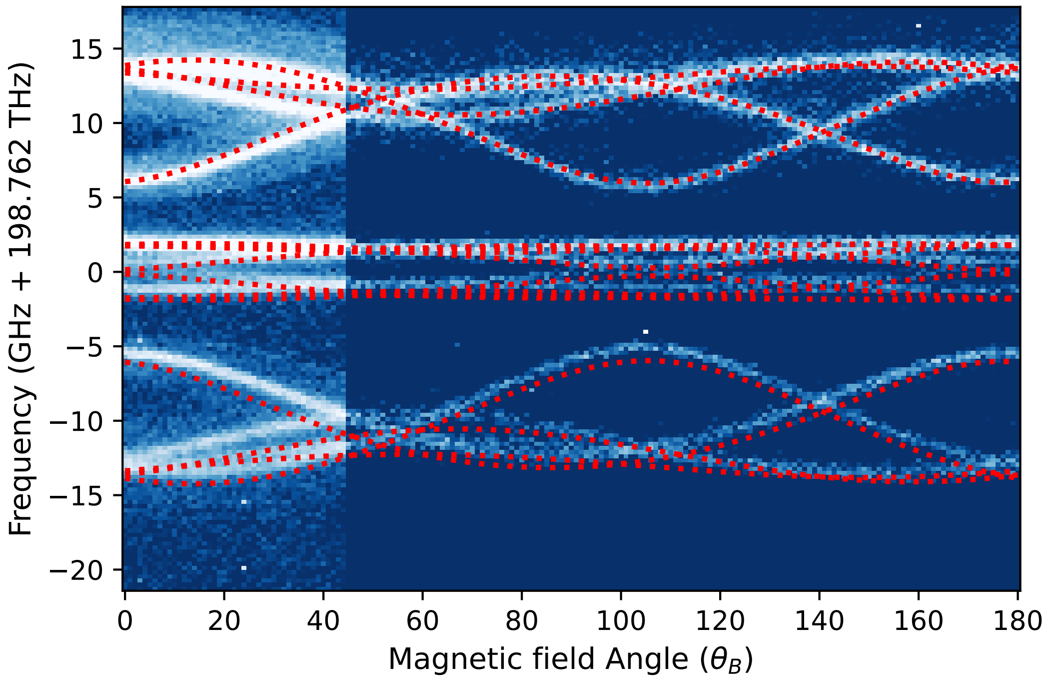

Figure 6.14: A Rotation pattern in the B site, with an overlaid model based on fitted parameters. Note that these data are stitched together from two sweeps, around 44°. The only experiment parameter that was changed was integration time.

Parameter	Initial Estimate	Fitted Value	Error
θ(Azimuthal Angle)	4°	4.2°	±1°
ϕ(Roll Angle)	-140°	-139.7°	±1°
Field Strength (mT)	160	144	±5%
Field Correction	0.9	0.91	±2%
$g_{e\parallel}$	—	2.63	± 0.2
$g_{e\perp}$	—	5.63	± 0.2

Table 6.6: Fitted parameters from the B site rotation pattern.

A Site Rotations We have also conducted rotation patterns in the A site, in absorption. These are shown in Figure 6.15. Extracting useful values from this pattern is challenging, due to Fabry-Perot artefacts in the experimental setup. Further to this, we have not successfully measured photon echoes in the A site, and so a detailed sensitivity analysis has not yet been conducted.

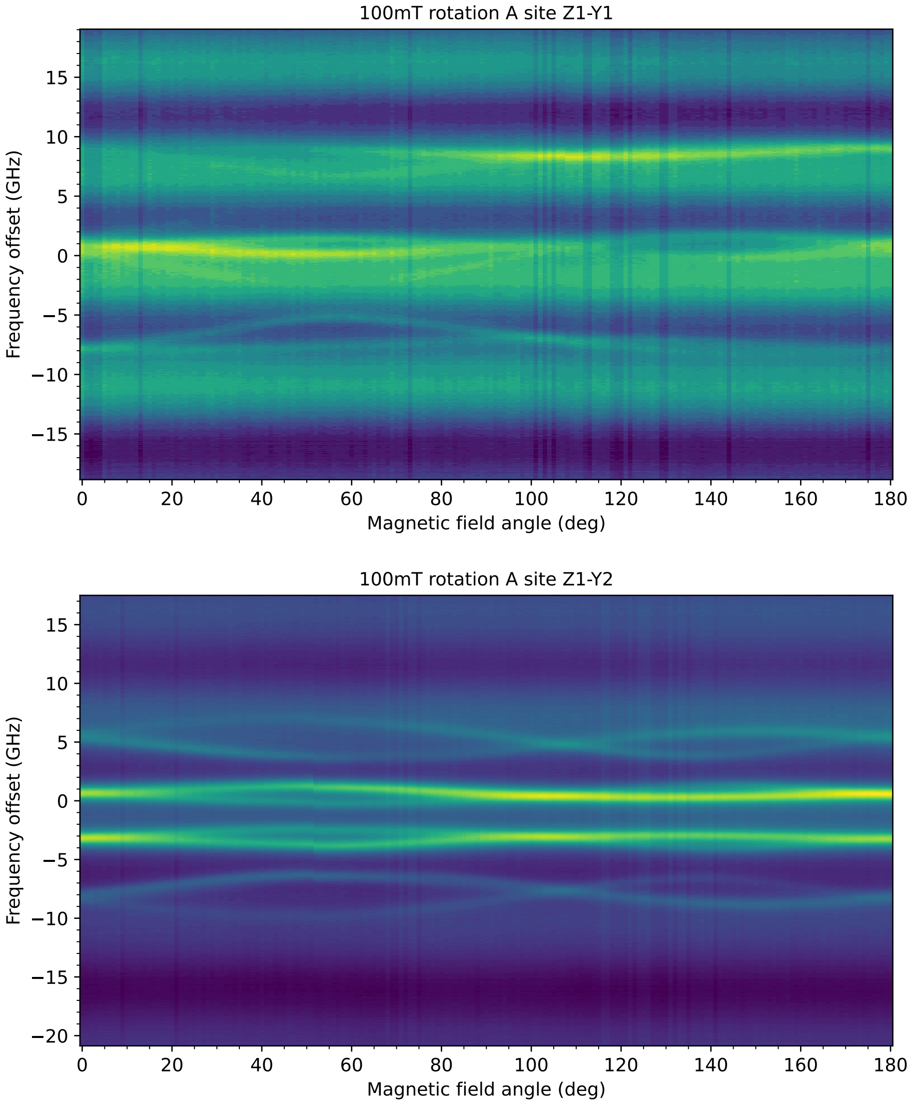

Figure 6.15: Rotation patterns in the A site, taken at millikelvin temperatures at 100 mT, in absorption. The topology of the rotation pattern identifies the C_{4v} symmetry of the site, shared by both plots. From these data we see that the Y_1 level has a sensitivity which is similar in magnitude to those of the B and G1 sites, however a detailed analysis has not been conducted. The Y_2 level is considerably more sensitive than our other sites - with optical transitions moving at a rate of at least 40 GHz/T.

Insights from Magnetic Field Studies:

From the rotations and field ramps presented, we acquire insights into our sites that extend the knowledge of the magnetic sensitivity of the G1 and B sites, with implications for our single ion devices. Firstly, excited state g tensors inform further steps of material characterisation, including optical coherence properties, which will be discussed in Section 6.4.3. An understanding of the transition properties at low field allows us to predict transition frequencies.

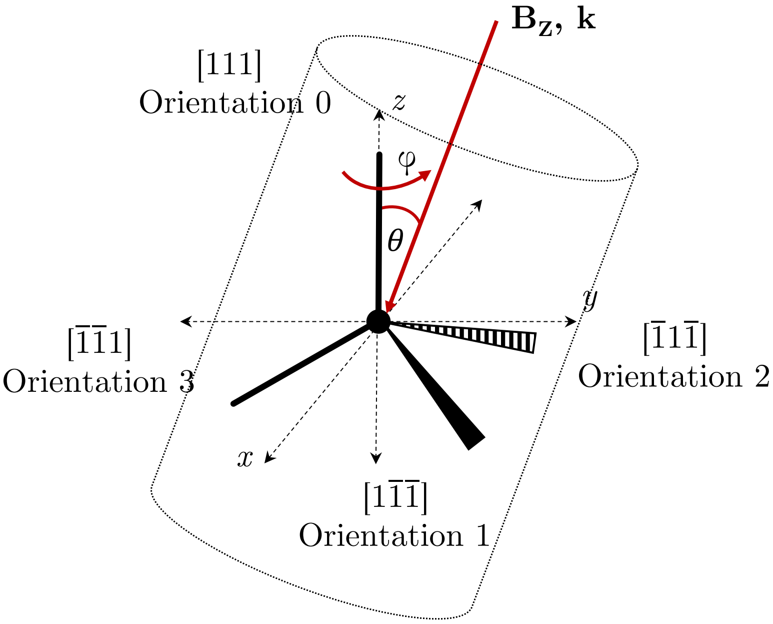

Figure 6.16: Highlighting our labelling convention for the different orientations for the two C_{3v} sites studied in this work, the B and the G1. We have identified the relative alignment of our crystal to the field. The wireframe cylinder is an indicative drawing of the alignment of our solenoid magnet to the crystal axes: the [111] direction called Orientation 0 is within 5 degrees of the solenoid axis. Of the other three orientations, one is 20° our of plane with the magnetic field, and the other two 100° and 140° respectively.

Based on the first-order sensitivity of these transitions, we can also seek regions where we may see enhanced coherence. Critical points in magnetic response provide an indication that there may be access to higher coherence times at particular angles or field strengths, since first-order sensitivity to magnetic field is turned off. This has been used extensively in the Y_2SiO_5 literature [176, 301], as well as more recently in spins rich in electronic spins [44].

We use the g tensors fitted from the above work to find magnetic field angles at which the magnetic sensitivity of the optical transition will be minimised. This g_{eff} is calculated using the difference between ground and excited state g values, for a given angle relative to the site axis, α.

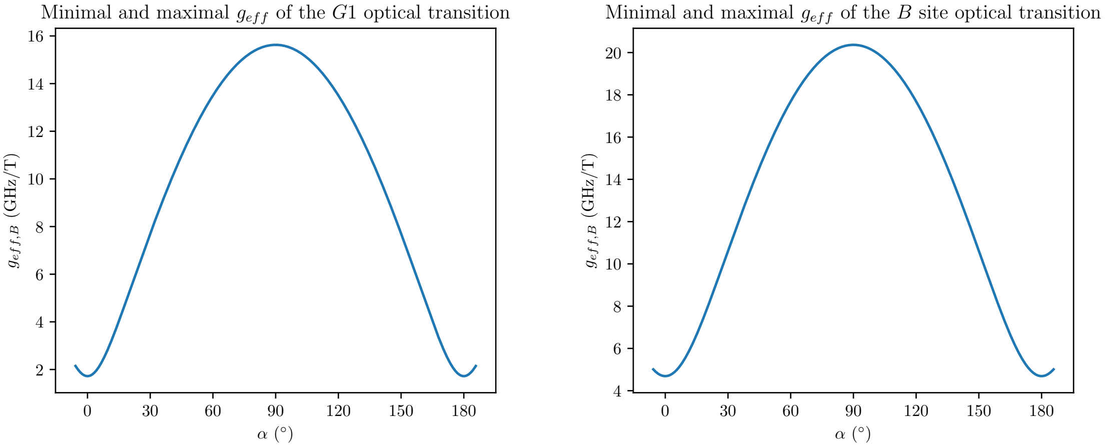

Figure 6.17: Using the (known) ground and (fitted) excited state g tensors of the G1 and B sites, we can predict regions where the optical transition is maximally, or minimally sensitive to changes in magnetic field. These are shown for the G1 and the B site, since the cubic site will have no theoretical anisotropy to magnetic field direction.

Using the turning points in our rotations, or the flattened response of the cubic site for our experiments could highlight regimes of increased coherence due to this limited sensitivity. We take the analysis one step further, and calculate what could be achieved in our crystal in its current setup, given the angles that we now know from fitting rotation patterns. Shown in Figure 6.18 are the sensitivity curves for the G1 and B sites, given the achievable orientations of our sites relative to applied magnetic field. We note that the minimum sensitivity of the B site is ~twice that of the G1, however the region of reduced sensitivity for the B site orientations is broader. Turning off first order sensitivity does not decouple spins from the fluorine bath. This will be discussed further in Section 6.4.3.

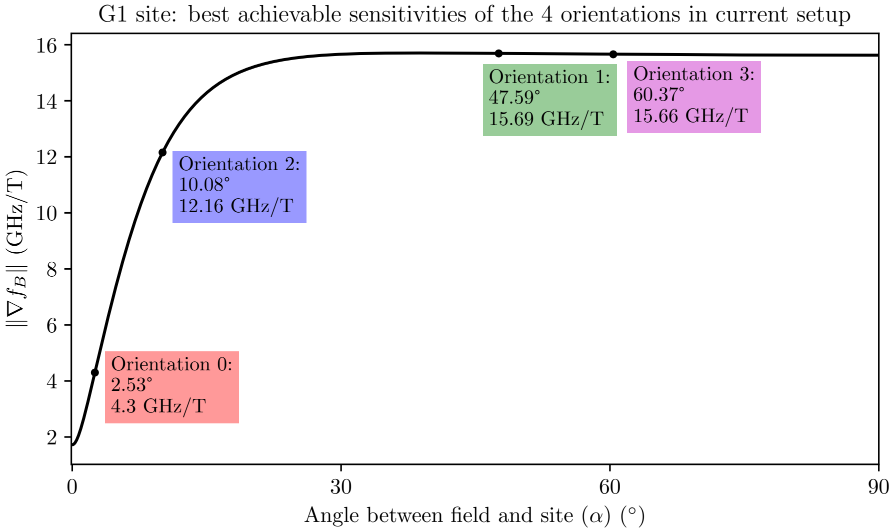

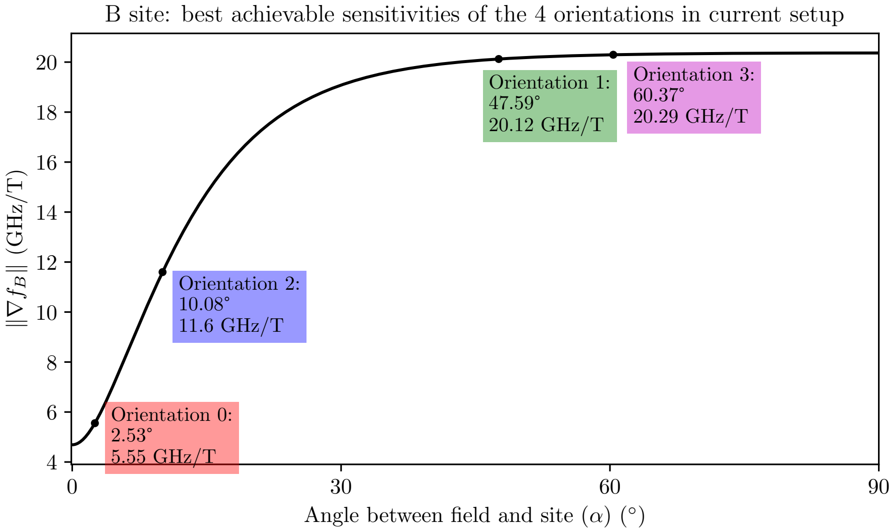

Figure 6.18: A plot for the G1 and B sites, of sensitivity to magnetic field plotted against the angle between site axis and field vector. Note that α represents a change of perspective from the original θ, ϕ coordinates, such that each orientational subgroup can be discussed in the same frame. Highlighted in the coloured panels are the four subgroup orientations of each of these sites relative to our current magnetic field plane, their sensitivity, and the angle α to the field vector when the only the solenoid field is ramped. We use these calculated figures to inform the angles at which we take coherence measurements.

6.4.3 Coherent Spectroscopy

Incoherent spectroscopy techniques provide useful information, however are sensitive to population effects, inhomoegeneous broadening, and laser linewidth, which limit measurements of homogeneous line properties. We have developed schemes for coherent transient experiments, including two- and three-pulse photon echo measurements, described in Chapter 5. These allow measurement of homogeneous properties in the B, Cubic, and G1 absorption lines. To date, we have not observed an echo in the A site.

Rabi Oscillations

As described in Section 5.3.3, we use a Rabi oscillation experiment to acquire a direct comparison between the optical dipole moments of our sites. These direct measurements yield more accurate estimates of the dipole moment of the sites than our prior analysis from T_1 experiments. Again, the optical dipole moments of our sites are both electric and magnetic in nature, so our we conduct our analysis twice, assuming solely electric dipole transitions for ease of comparison with the literature. For details on the suspected electric/magnetic dipole balance, see [157, 158].

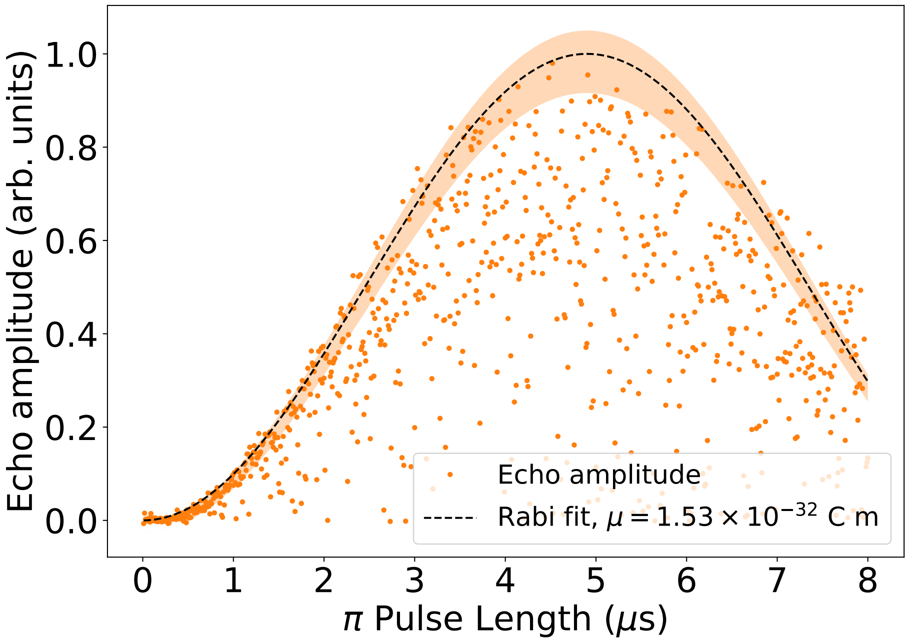

Figure 6.19: Rabi oscillation in the G1 site in Sample B - with fitted dipole moment. data recorded in heterodyne - as described in Section 5.2.4. Optical phase fluctuations between LO and IF paths leads to ‘blinking’ effects. Thus, we can use the upper bound of these data for a fit.

Measuring the G1 Dipole Moment We have evaluated the dipole moment of the G1 using our initial, single axis magnet system with a higher concentration sample (Sample B) in the Thorlabs U-Bench while detecting in heterodyne at $<$50 mK. This system has a very well known beam waist (0.38 mm), and the excitation system we used for this experiment was based solely on an AOM whose rise time is $<$ 5ns. Thus these data may used to precisely measure optical dipole moments.

We can find the dipole moment of our transition – assuming it is electric dipole only – using:

$$\mu_E = \frac{\Omega_r \hbar}{E} \tag{6.5}$$

We acquire $\mu = 1.53 \times\ 10^{-32}$ C $\cdot$ m. The primary source of error in this measurement is a precise knowledge of the pulse power arriving at the sample itself during the measurement. We err on the side of caution, and fit data using the power measured at the last fibre in our room temperature setup (4 mW). The true power at the sample is less than this - likely by 1-2 dB, depending on the quality of APC connections and losses in the U-Bench lens assembly.

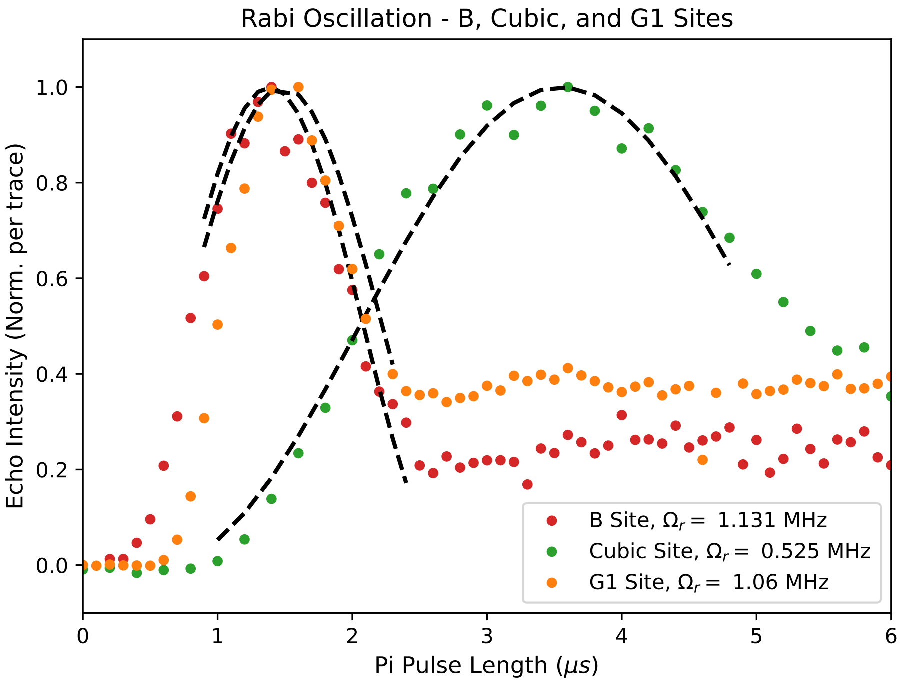

Figure 6.20: Rabi oscillation measured by photon counting in our 3 sites of interest: the G1, the cubic, and the B site, measured in sample D at a field $<$300 mT, at millikelvin temperature. Data are normalised to each trace's peak. Data are fitted to a $\sin^2$ curve, for pi lengths between 0.8μs and 2.5 μs for the G1 and B, and between 1 and 5 μs for the Cubic site. More accurate models do exist for long-term behaviour, however all point to the same characterisation of a pi pulse length [302].

Relative Dipole Moments of Other Sites: When moving to more dilute samples (samples C and D) and a reflection geometry, a new set of experimental challenges emerges. Firstly, the beam parameters are not known with the same level of certainty as in the transmission U-Bench setup. Secondly, while heterodyne detection is still possible, it becomes increasingly challenging for longer delays, and the less populated sites. Finally, the switching apparatus for reflection experiments relies upon a pair of 'fast' optical switches. These have a finite (∼800 ns to 90%) turn on time, and as such, pulse areas are reduced for short $\pi-$pulse length.

Thus, we first use photon-counted Rabi flopping data from the G1 site to calibrate the difficult-to-ascertain beam parameters in our compact optical system, and then benchmark other sites relative to this known standard.

When fitting to find Rabi frequencies we can take one of two approaches. One can either simply pick the peak of the response, identify this as the π pulse and work from there, or one can fit the data using an appropriate function. We perform the latter, ignoring data where pi-pulses are shorter than 0.8 μs. This is because the pulse area scales non-linearly with time during this period, due to the slow behaviour of the switches. Using these data however, we fit to a $\sin^2$ curve, and can evaluate the relative dipole moments of our sites.

Since these data were all taken in the same conditions (crystal, beam parameters, magnetic field, temperature), we can make direct comparisons between them – up to the uncertainty in pulse area, which may vary over the ∼12 nm of optical wavelength between these sites. From these data it appear clear that the cubic site has a lower dipole moment than the G1 and B sites, which have comparable (within 10% of each other) dipole moments to each other.

Finding Branching Ratios: Recalling from Chapter 3, the expected excited state lifetime from a transition with electric dipole moment μ is:

$$A = \frac{1}{T_{\text{spon}}} = \frac{8\pi^2 n^3 \chi_L^2}{3\epsilon_0 \hbar \lambda^3}\mu^2 \tag{6.6}$$

where χ_L is the local field correction factor $\chi_L = 3n^2/(2n^2+1)$, and ϵ_0 the permittivity of free space. Using this calculated value and our T_1 lifetimes from Section 6.4.1, we can find the branching ratio of each $Y_1 \rightarrow Z_1$ transition via:

$$\Upsilon = \frac{T_1}{T_{spon}} \tag{6.7}$$

The highest calculated branching ratio is 18% – for the G1 site. It is important to highlight the choice of local field correction in this context too: these branching ratios are calculated using the Real Cavity Model. Should the same analysis be conducted using the Virtual Cavity, branching ratios look more favourable. Both are provided in the following summary, Table 6.7.

Site	λ (nm)	f_{Rabi} (MHz)	μ (C.m)	Υ ($\chi_L^{(R)}$)	Υ ($\chi_L^{(V)}$)
Cubic	1507.00	0.506	$0.76 \pm 0.1 \times 10^{-32}$	0.07	0.09
B	1508.29	1.131	$1.63 \pm 0.2 \times 10^{-32}$	0.10	0.12
'G1'	1518.18	1.06	$1.53 \pm 0.2 \times 10^{-32}$	0.18	0.23

Table 6.7: Improved bounds on electric dipole moments from Rabi Oscillation measurements. We assume an electric dipole transition and calculate electric dipole moments from Rabi frequencies. Using these dipole moments we calculate Υ, the branching ratio for each site, using both both Real Cavity χ_L^R and Virtual Cavity χ_L^V local field corrections.

Two Pulse Echoes

Two pulse echoes were used to evaluate the coherence and phase memory time (T_2 and T_m) of the sites in which we observe echoes (Cubic, B, and G1). When studied in a directional magnetic field, measurements of coherence times in sites with anisotropic g can be used to evaluate the link between an ion's magnetic sensitivity and its coherence properties [142]. I have conducted experiments in our current setup to get as close as possible to one of these orientations for our axial sites.

Initial Coherence Measurements:
Similarly to our Rabi Experiments, we first observed echoes in our first, more heavily doped samples using heterodyne detection. Figure 6.21 shows one of the first directly detected echoes in calcium fluoride in our lab. The longest coherence time measured in this experimental configuration was ∼10 μs. This provided a valuable point of comparison, informing pulse parameters and expected signal levels as we moved toward more dilute samples, and hence lower signals.

In More Dilute Samples:
We then measured optical coherence times in Sample D, in a field applied by the solenoid magnet. In the case of the G1 and B sites, these data were conducted in the brightest spectral feature, which is the line produced by Orientations 2 and 3, from Figure 6.2. The axes of these orientations make a close-to-equal angle with the magnetic field plane (they differ by ∼15°, but given the direction of the applied field, their sensitivity to the solenoid field are close to equal). Data are shown in Figure 6.22.

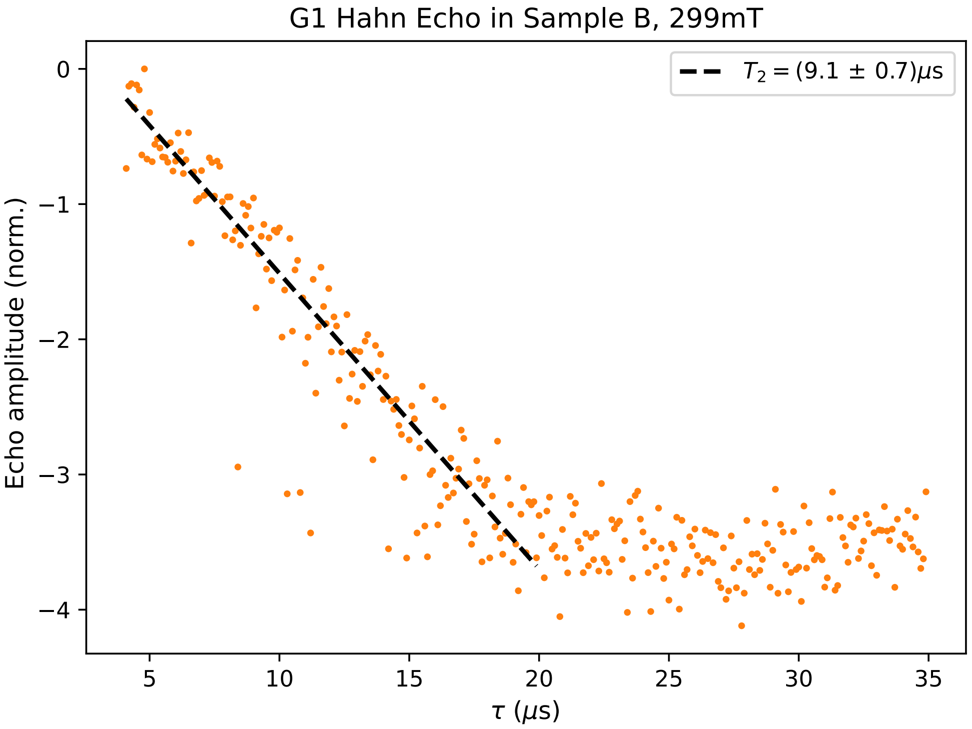

Figure 6.21: Hahn echo in the G1 site in our initial sample (Sample B), at 299mT. Echoes were read out using our heterodyne setup. These data were used for initial coherence time estimates.

We also improve our fitting, modeling these later data using a Mims Phase memory time. Similar to the local field correction, there are multiple ways to fit phase memory data. We use the model provided in [294, 296]:

$$I = I_0 e^{-(4\tau/T_m)^x} \tag{6.8}$$

where T_m is the phase memory time, x is the Mims Exponent, and τ is the delay between pulses. There are a number of different models that can be used to predict x [186, 295], however we leave this as a free parameter.

In these more dilute samples we measure phase memory times in excess of 24 μs in both the Cubic and B sites, and 43.9 μs in the G1. We note that we have not observed echoes in the A site in any of our samples for any experimental conditions.

It is likely that magnetic decoherence plays a role in the properties of the A site, particularly in light of our measurements of its rotation pattern, and the our B and G1 site results. However, further work is needed to understand precisely why echoes are not observed.

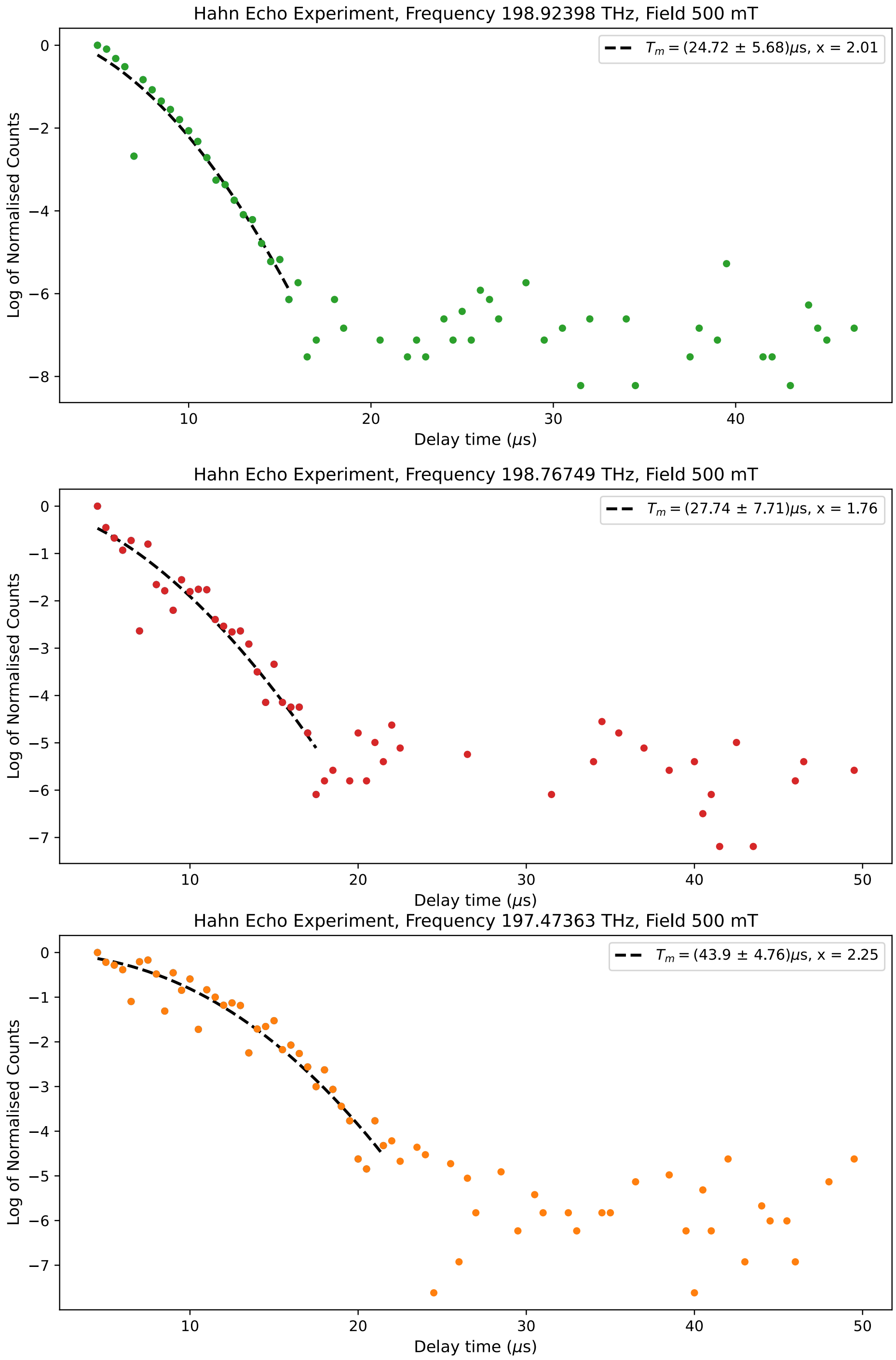

Figure 6.22: Hahn Echoes measured in sample D, in the Cubic (green), B (red) and G1 (orange) Sites, measured at 500 mT. Fits to T_m are both provided. The longest phase memory time we have recorded in this configuration is in the G1 is $T_{m,opt} = 43.9\ \mu s$.

Coherence Behaviour With Field Strength: Given the enhanced coherence we measure with more dilute samples, we wish to further probe the system to understand what limits erbium coherence.

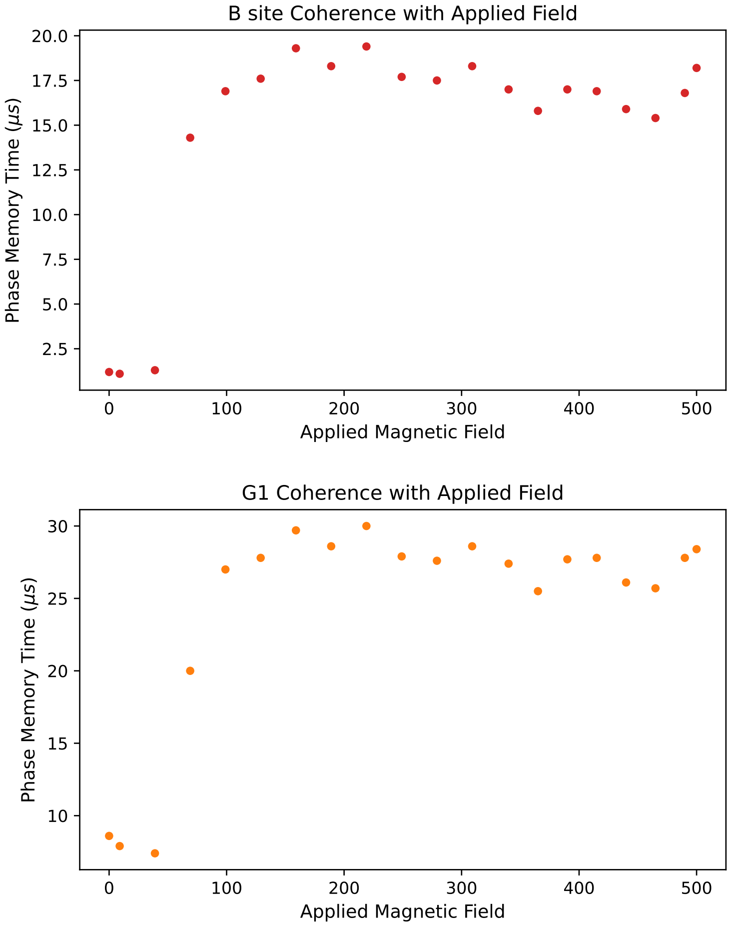

Figure 6.23: Coherence times in the B(top) and G1 (bottom), with respect to applied magnetic field.

The coherence times we measure 'turn on' rapidly with increased magnetic field, generally reaching close to their maximum value after about 150 mT applied field. We believe this is associated with a decrease in the rate of Er-Er spin flips, as the Er become polarised with increasing field at low temperature.

The coherence times achieved by both sites plateau. Given the angle that these sites make with the solenoid field (in both cases we saw our strongest signals from orientations 1,2, and 3), we can make an assessment of their magnetic sensitivity, using Figure 6.18. The ratio of coherence times (20 μs in the B site and just under 30 μs in the G1) matches the ratio of magnetic sensitivity of each, providing evidence that decoherence in this system is at least in part due to the fluorine spin bath - an expected result in calcium fluoride.

Seeking a Low-Sensitivity Direction of Magnetic Field:
An important question to us is ‘how long can coherence times be?’ In the case of a single-ion device, longer coherence means less challenges to reach lifetime-limited coherence. Understanding the dynamics of the crystal system is important for extending these coherence times. Using the principles described in [142], and the results from our sensitivity modelling in Section 6.4.2, we seek directions of magnetic field which entirely minimise Er^{3+} sensitivity to noise. In this regime we could characterise the limits on coherence presented by the fluorine spin bath. In Ref [142], this method was used in Er^{3+}:Y_2SiO_5 to achieve an optical homogeneous linewidth of 73 Hz.

Along with longer coherence, we also seek to operate at lower fields, such that ground state spin levels are split only by up to a few GHz. This will avoid direct phonon relaxation, and enable spin control at microwave frequencies that are compatible with our coaxial cables - limited to 18 GHz. At the ∼5° offset that our sites are at, the splitting is close to 32 GHz/T, so the ground state spin splitting is already 16 GHz at 500 mT.

From Figure 6.18, we expect a four-fold reduction in magnetic sensitivity (from about 16 GHz/T to <4) for angles between site and field less than 3°, and a maximum of an 8-fold improvement for well-aligned fields. The B site has a broader region of reduced sensitivity, from 30° to the axis, but is more sensitive overall: its maximum sensitivity of 20 GHz/T is only reduced to ∼5 GHz/T at angles less than 5°.

The obvious choice for this investigation would be the orientation in which each of B and G1 sites which are parallel to the solenoid Z axis - Orientation 0. This is already within 5° of the crystal axis in our setup. However, echo signals from this specific orientation of both the G1 and B site are small, since the optical dipole is at its weakest there due to polarisation selection rules [156]. Given the current orientation of the sites to the field, achieving the best possible improvement would require a third magnetic field axis. Therefore, we rotate the field to 110°, where we hope to be able to address the population in Orientation 3. This is the closest subgroup to the plane of the magnet - at an angle <15° to the plane, based on our fits.

In performing these experiments, we have observed some variation of coherence with respect to the applied field direction, however we have not yet seen a large variance. In Figure 6.24, a well-chosen angle in the B and G1 site are shown. Each of these is at a low field, such that ground state spins would be separated by <8 GHz. In the G1, the ground state splitting would be around 6.5 GHz, and in the B site, this would be 8.1 GHz.

An extended coherence investigation was also conducted in the cubic site. Since this site has no first order direction-dependent field sensitivity, we instead make use of the turning point

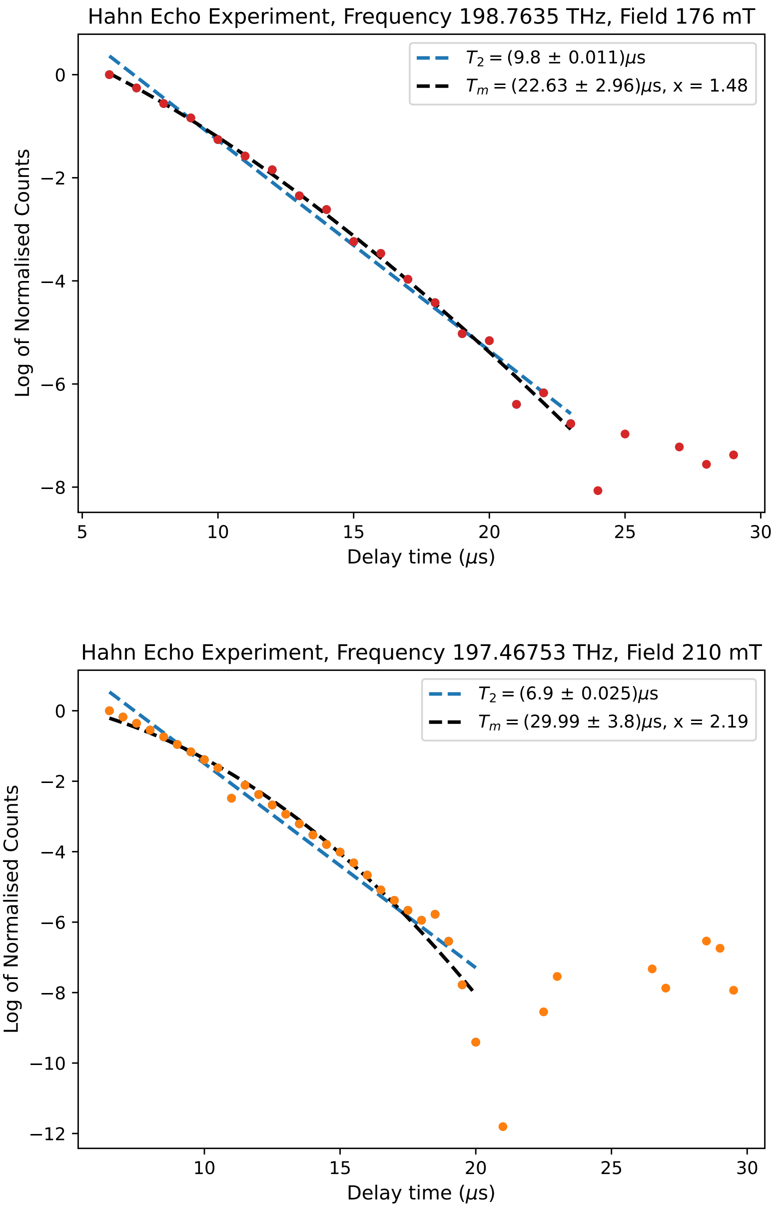

Figure 6.24: Coherence times in the B and G1 sites at a well-chosen direction. In these experiments we rotated the magnetic field to -73° from the solenoid axis, as close as we could get to the <111> axis for the G1 and B sites (given our understanding of the crystal from fits). Both an exponential decay and a Mims decay are fitted to these data showing the B site's low fitted Mims exponent of ∼1.4 is indivative of predominantly exponential decay [294]

observed in Figure 6.11. We observed no significant increase in coherence, but further study on the $Z_1 \longleftrightarrow Y_2$ and $Z_1 \longleftrightarrow Y_1$ is required to understand the turning point fully.

While we have not yet observed the increase in coherence that we expected, we note that the angle between site and field was still over 10°, and that these measurements were conducted at an elevated temperature (about 100 mK) due to limits in our setup. The next steps are clear: we intend to precisely orient a crystal axis with that of the applied field, by adding a new magnet axis or preparing a new sample. We will also align the site axis perpendicular to the incoming beam, to ensure a maximised $\mathbf{E} \cdot \mu$.

Evidence of Super-hyperfine Structure: In some of our data, we observe evidence of super-hyperfine structure at low fields. This points to the potential in the long term of using the fluorine spins immediately adjacent to an Er^{3+}as a resource [54]. This effect has only been observed at low fields, and is typically entirely washed out of the data below 50 mT, considerably lower than the field at which the same occurs in $\mathrm{Er{:}Y_2SiO_5}$ [186].

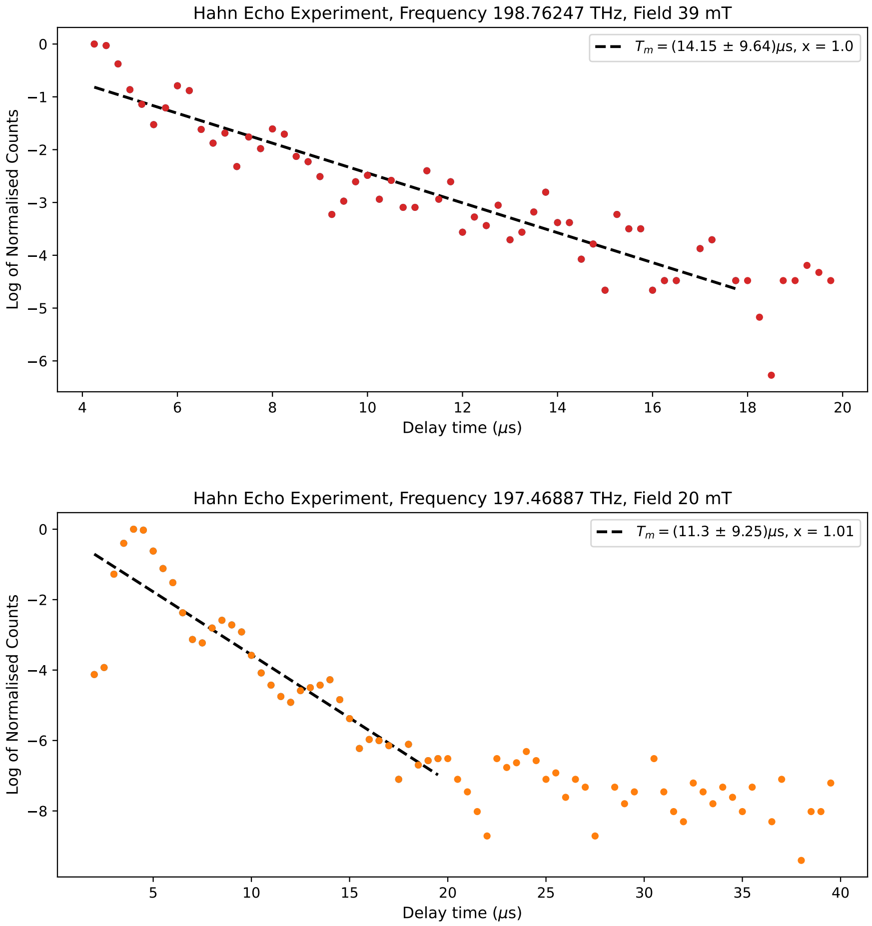

Figure 6.25: Evidence of super-hyperfine structure in the B (top, red) and G1 (lower, orange) sites at low fields. Oscillations in echo amplitude are thought to come from erbium ions coupling to nearby fluorine nuclear spins at specific frequencies. The regions in which we have seen this behaviour are narrow, and warrant further investigation.

Temperature Analysis Finally in the suite of two-pulse echo measurements, I have measured the coherence of both the G1 and B sites at temperatures up to 1K. Higher temperatures than these are not accessible in photon counting experiments, since our SNSPD (superconducting nanowire single photon detector) is in the same cryogenic system. We measure a rapid increase in homogeneous linewidth (calculated from phase memory time), which plateaus quickly at close to 200 mK.

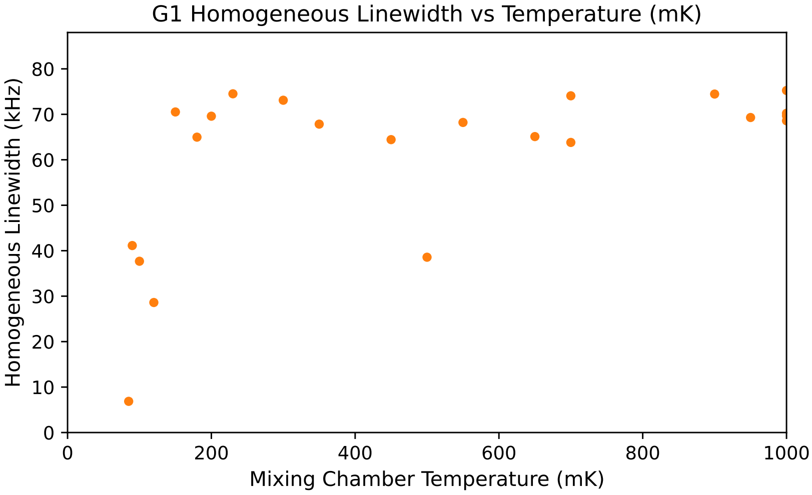

Figure 6.26: Coherence trend across temperature in the G1 site. Data are fitted T2 coherence times at each temperature.

Three Pulse Echoes

Using three-pulse echo measurements we evaluate the short-term (up to 1 ms) spectral diffusion of the B and G1 sites. Spectral diffusion describes the time dependent wandering of the transition frequency of an emitter in its environment. In our system, spectral diffusion provides a measurement of the lifetime of the fluorine nuclear spin bath. In both sites, spectral diffusion was measured at a high magnetic field (900 mT). Homogeneous linewidths are stable for the first 10 microseconds, and then broaden. Using the model provided in [297], one can estimate spectral diffusion timescales:

$$\Gamma_{\text{eff}}(T_W) = \Gamma_0 + \frac{1}{2}\Gamma_{\text{SD}}[1 - \exp\{-RT_W\}] \tag{6.9}$$

Where Γ_{eff} is the effective homogeneous linewidth at a time (T_w), Γ_0 is the initial homogeneous linewidth, Γ_{SD} is the spectrally diffused linewidth, and R is the characteristic rate of diffusion processes.

In the case of the G1, the linewidth shows signs of plateauing after 300 ms, to a value less than 100 kHz. This long term plateau is still narrower than our narrowest burned hole in Figure 6.9, which was read out 1 ms after burning. This corresponds to a (fitted) spectrally diffused linewidth of 142 kHz. In the B site, the data are cleaner but less conclusive - there is not as clear of a plateau in the same way as there is for the G1, however the fits do converge well. The fitted linewidth of 148 kHz is greater than that of the G1, which is expected from our sensitivity analyses. In both cases, the Mims exponents quickly decreased below 1.5, so fits were conducted as direct exponentials. Thus linewidths were calculated using $\Gamma_H = 1/\pi T_2$.

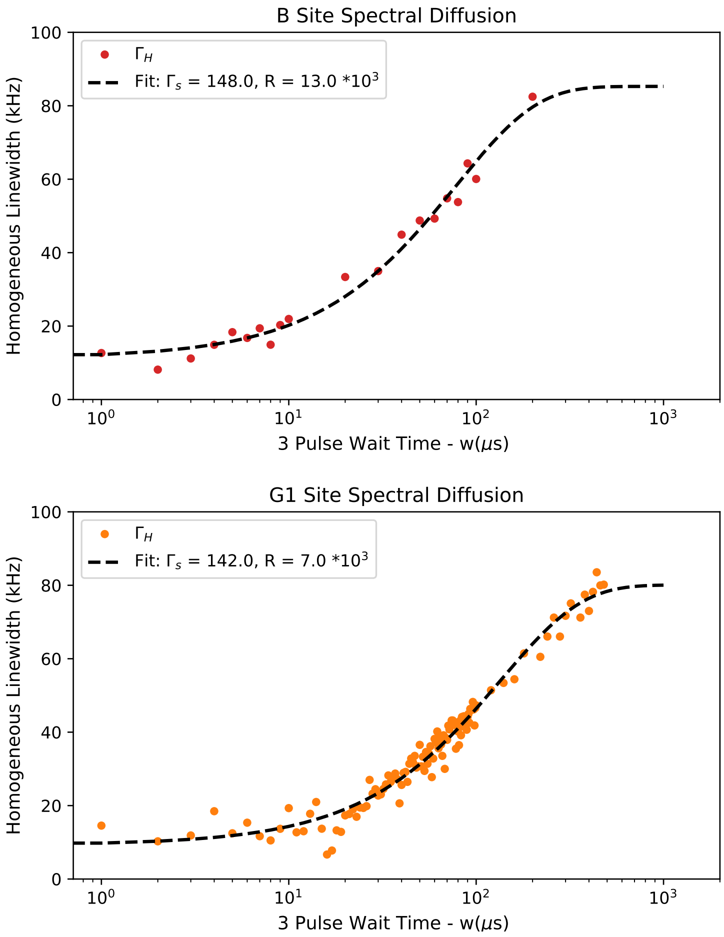

Figure 6.27: Three Pulse echoes in the B site (Red, Upper) and G1 (Orange, Lower). These data show that spectral diffusion starts to accelerate in the B after 10-20 μs, with the homogeneous linewidth growing toward a value of ~90 kHz at 200 μs. In the G1 this acceleration is later - only starting after nearly 100 μs. Notable from this plot is that the linewidth in the G1 is starting to plateau after 500 μs - to a linewidth of about 100kHz, narrower than the narrowest homogeneous linewidth measured in hole-burning (314 kHz). The B site spectral diffusion rate R is nearly double that of the G1, fitted using the model provided in [297].

6.5 Summary of Measured Site Properties

Table 6.8 below summarises the experimental results from all sites we have observed in our experiments. This side-by-side comparison table provides insight into our decision to target both G1 and B site single ions. Coherence times quoted are the longest that we have measured in our current experiments.

Site	**CF level**	**f (THz)**	**λ (nm)**	**T_1 (ms)**	**Υ ($\chi_L^{(R)}$)**	**Γ_{inh} (GHz)**	**T_2 (μs)**	**Γ_{SD} (MHz)**	**μ ($\times10^{-32}$ C.m)**
‘Cubic’	$Z_1 - Y_1$	198.928	1507.05	35.7	0.07	0.21	24.7	-	0.76
‘A’	$Z_1 - Y_1$	197.049	1521.13	21.2	-	3.56	-	-	-
‘B’	$Z_1 - Y_1$	198.762	1508.29	11.5	0.10	1.51	27.7	148	1.63
‘G1’	$Z_1 - Y_1$	197.469	1518.18	23.1	0.18	0.99	43.9	142	1.53

Table 6.8: Summary of site properties measured using coherent spectroscopy techniques

6.6 Outlook and Next Steps

In this section I outline our current experimental aims, and the next steps in the experimental systems I have described. I discuss the mechanisms which we hypothesise are currently limiting coherence and signal intensities. Then I focus on the next steps for these experiments, both in the ‘doped bulk’ crystals, and the ‘implanted pure’ crystals. Following this, I justify our selected site for single ion investigations, and provide concluding remarks.

6.6.1 The Current Experiments

The bulk spectroscopy experiments we have conducted are the beginnings a detailed analysis of the dynamics of Er^{3+}:CaF_2. This is motivated by the search for an optimal site for single ion investigations, by investigating individual site dipole moments. The bulk investigations also help develop our understanding of what will ultimately limit the performance of single ion devices in CaF_2 and other analogous materials.

Limits on Coherence For single ion devices, long coherence times will assist in achieving lifetime-limited coherence times in single ion experiments. The required Purcell factor to lifetime limited coherence in the G1 site is ~600. This is achievable in many optical resonator architectures including CaF_2 whispering-gallery-mode resonators, with considerably higher values possible with some concerted fabrication effort [206, 207]. That said, we seek to understand what is limiting the coherence in the long term.

We have significant evidence that suggests that the dominant source of decoherence in our samples is magnetic noise, caused both by interactions with other Er^{3+} and as fields increases, with the fluorine spin bath. This is supported by the rapid turn-on of coherence shown in Figure 6.23, and the good agreement of our echo coherence data with non exponential decays with Mims exponent ∼2 for higher fields. It is also supported by the appearance of super-hyperfine structure in Figure 6.25, though a more thorough characterisation of this effect is required.

If this is the case, we expect to see enhanced coherence at low fields when using a judicious choice of magnetic field direction. Based on the modelling presented in Figure 6.18, we calculate an expected decrease in sensitivity to magnetic field by a factor of eight when site axis and field align. We have not been able to test this at angles between field and site of less than 20°, fields in excess of 200 mT or temperatures below 200 mK, due to limitations of our setup at the time of measurement. This will soon be evaluated, using our lab's forthcoming three-axis vector magnet and a well-aligned crystal, along with the use of dynamical decoupling sequences [54, 176] for extended coherence.

The reduced coherence of the B site when compared to the G1, and the fact that its decays do not follow the characteristic Mims-type decay [295] with as high of an exponent as is seen in both the G1 and cubic sites. The fits resolve a Mims exponent of 1.4 for the B site, against in excess of 2 for the G1 and cubic. This suggests that the B site has a higher sensitivity to magnetic field - and hence the fluorine spin bath of our material. The form of the rotation patterns, and the modelling of Figure 6.18 confirm this. The B site's minimum sensitivity is greater than that of the G1 (5 GHz/T as opposed to <2 GHz/T in the G1), but it has a broader region of decreased sensitivity.

Limits on Signal Intensity At the moment, signals in our system are limited by the alignment between the laser field and the dipole in a given orientation. Higher effective $\mathbf{E} \cdot \mu$ than we are currently accessing is available. This had significant implications for our initial studies of field orientation, as the subgroup which was aligned closest to our applied field had the lowest optical response.

Selecting just one of the four subgroups of $\langle 111 \rangle$ axes, and optimising polarisation and incoming beam geometry for this direction will yield a modest (5 - 10 % over current measured dipole moments) increase in optical signals.

When designing whispering-gallery-mode resonators for single ion experiments, the axis of rotational symmetry governs the direction of light propagation around the circumference. Therefore this axis should be parallel to one of the $\langle 111 \rangle$ directions - as are many of the fabricated resonators in Chapter 7.

6.6.2 Further work

The experiments which I describe in this chapter are a thorough, and yet not exhaustive characterisation of Er^{3+}:CaF_2. This crystal system is an excellent testbed in which to test and assess some of the fundamental properties of the Er^{3+} optical transitions.

In the Current Reflection Setup There are also a number of experiments which could be conducted in the cryogenic and room temperature setup as they currently stand. Samples which are even more dilute could be used to precisely measure the Er-Er flip-flop rate as concentration decreases, and samples with precisely aligned crystal axes – specifically $\langle 111 \rangle \perp \mathbf{k}$, such that the maximum dipole moment can be achieved. Increased optical power could be attained by splicing each fibre connection, and realigning cryo-optics for smaller beam and hence a higher Rabi Frequency - enabling more ions to be addressed as pulses become shorter. With fast, sweepable, and narrow control over AOM frequency, hole-burning experiments could be conducted in the reflection geometry, or modified echo schemes explored.

Fully polarising the fluorine nuclear spin bath would require many T of magnetic field [303]. However we benefit greatly from the fact that axial sites have anisotropic g tensors. Choosing the an optimal direction for a strong magnetic field could minimise the first-order sensitivity of our ions to magnetic noise - from each other and from the bath. This approach has yielded significant coherence improvement in other rare-earth ion systems [142].

The highest optical response is seen when the beam wave-vector $k \perp \langle 111 \rangle$, and the lowest magnetic field sensitivity is seen when $B \parallel \langle 111 \rangle$. These two results imply a clear optimal orientation for further bulk spectroscopy work on these two sites, and also provide insight into the design of optical resonators.

For further bulk spectroscopy in the G1 and B sites in our current setup, this is possible to achieve. Optical faces need to be prepared on two different surfaces to those that we have traditionally used. For direct comparisons with the A site (assuming we eventually see echoes there), a second sample would be required, that is aligned as well as these, with the $\langle 100 \rangle$ axis perpendicular to the beam.

For applying stronger fields, a new pair of split-coil magnets has been developed allow for operation above 200 mT. However, stronger fields may not be desirable, since spin addressing experiments may be limited. A 600 mT field splits the ground state of the G1 by ~18 GHz, the rated frequency limit of our coaxial lines.

A thorough investigation of the superhyperfine effects hinted at in our two-pulse echoes is required to characterise the dynamics of the F^- spin bath. While it is not practical to apply the field required to fully polarise this bath in our samples, radio frequency pulses delivered to the sample could be used to control the bath [54]. A study of the effects of varied polarisation on our samples may shed light on the electric and magnetic dipole nature of our transitions, and confirm the selection rules of our transition [156].

Coupling the work we have done on the B and Cubic sites to crystal field models similar to Moull [157] will reveal the electric/magnetic dipole nature of these sites.

Finally, There are a number of other spectral features in our samples. The A site was studied in less depth throughout this work, and we are et to probe the other oxygen compensated sites, such as the G4 [156]. Other features are not identified - these could be pair sites, clusters, or other charge compensated sites that are not yet well characterised. Further investigations of these sites will allow comparison of crystal fields of different symmetry to those which we have already developed a good understanding.

Implanted Sample Investigations Our investigations of implanted Er^{3+}:CaF_2 have recently begun, with high-fluence implantation of both $Er^{3+}$and O^{2-}. While we have not yet observed signals from the G1 site in these samples, we will soon anneal the current batch of samples under vacuum to attempt to produce oxygen complexes using the implanted oxygen ions.

Following this, our goal in these samples is to step towards the lowest implantation concentrations possible, and use these samples to inform (or as part of) our studies of high Q/V resonators. A study of the effects of implantation depth will be conducted, targeting the ∼few μm regime; the depth of the mode of a whispering-gallery-mode resonator.

Further Developments There are a number of extensions to this work which new capabilities would enable. An extra magnetic field axis would enable precise control over field direction, ideally targeting $B \parallel \langle 111 \rangle$, furthering our search for enhanced coherence. Incorporating a microwave antenna in the cryostat near the sample, or electro-optic modulators in the path would enable spin control via microwave pulsing and Raman heterodyne techniques. A locked laser would enable narrower ensembles to be selected in echo experiments.

6.6.3 Choosing a site for Single-Ion Investigations

When beginning this project, we arrived upon a number of desirable criteria for our Er^{3+} site. Our target site must satisfy three competing requirements: a strong optical transition dipole moment (μ), sufficient optical coherence (T_2), first-order sensitivity to electric fields (Stark effect) for fast tuning, and an optical lifetime that is suitable for achieving lifetime-limited coherence using achievable Purcell enhancement. This will enable us to achieve both $C > 1$, and lifetime-limited coherence in our experimental architecture.

The Cubic site is considered unsuitable for single-ion applications under these criteria, despite its narrow inhomogeneous linewidth. Its high symmetry (O_h) forbids electric dipole transitions to first order, resulting in a weak transition dipole moment roughly one-third that of the charge-compensated sites. Furthermore, the lack of a polar crystal field eliminates the linear Stark effect, precluding the use of fast electric field tuning schemes essential for cavity integration [57].

The remaining candidates, the G1 and B sites, both exhibit dipole moments three times that of the cubic ($\mu \approx 1.5 \times 10^{-32}$ C·m), relaxing the Q/V requirements for strong coupling. However, they differ in their transition nature and coherence.

Crystal field modelling [158] identifies the G1 transition as predominantly electric-dipole in nature. While such an analysis has not yet been conducted for the B site, our spectroscopy results in both the G1 and B site provide experimental data for a direct comparative crystal field analysis between these two sites. The B site optical transition shows a higher sensitivity to magnetic noise (Section 6.4.2), which may limit the achievable coherence times in the long term. It also shows shorter coherence, and faster spectral diffusion rates (in Table 6.8, along with its marginally higher dipole moment.

The G1 site represents the best compromise in this system. Its high dipole moment is comparable to a number of other erbium sites [148], but with long coherence times ($T_m > 40\,\mu$s) and proven spectral stability. Unlike the Cubic site, it retains the Stark sensitivity required for tuning; unlike the B site, it is less susceptible to the magnetic noise of the fluorine bath.

Consequently, the G1 site is selected as the primary target for the resonator integration experiments detailed in Chapter 7. The combination of this optimised atomic interface with the high-Q/V electromagnetic confinement of whispering-gallery mode resonators defines our route toward cooperativity $C > 1$ with individual rare-earth ions.[1]

6.7 Conclusion

This chapter has established Er^{3+}:CaF_2 as our platform for high-resolution spectroscopy and identified the specific site for our single-ion experiments. We have conducted a comprehensive

---

[1] This decision is happily non-binding: while the G1 is the primary target, the ubiquitous presence of B and Cubic sites in doped crystals means they remain available for comparative study in any resonator fabricated in UC Crystals.

survey of the Cubic, A, B, and G1 sites using absorption, fluorescence, and coherent transient spectroscopy. I have quantified the optical dipole moments, finding that the symmetry-breaking charge compensation in the G1 and B sites enhances the transition dipole moment by a factor of three compared to the cubic site. Through magnetic field rotation studies, we extracted the excited-state g-tensors, providing a means of minimising magnetically induced decoherence through precise field alignment.

Importantly, this work resolves the selection problem for future device fabrication. By demonstrating that the G1 site combines a high optical dipole moment ($\mu \approx 1.53 \times 10^{-32}$ C·m) with superior optical coherence ($T_m > 44\,\mu$s) and first-order sensitivity to electric fields, we have identified it as our targeted interface for cavity QED. The bulk properties measured here have identified the starting points for the next phase of this research. With a dipole moment of $\sim 1.5 \times 10^{-32}$ C·m and a homogeneous linewidth of 22.7 kHz, achieving a cooperativity $C > 1$ requires an optical resonator with a high ${}^{Q}/_{V}$. The design, fabrication, and characterisation of whispering-gallery-mode resonators capable of meeting this stringent requirement is the subject of the following chapter.

"God made the bulk; the surface was the work of the devil"

Wolfgang Pauli

7

Whispering-Gallery Mode Resonators

The work of this thesis focuses on enhancing interactions between erbium ions and light using two distinct methodologies: engineering the nanoscopic environment of the atom, and engineering the photonic environment using a cavity. Having chosen our site for single ion hardware in Chapter 6, I now focus on the second challenge: high Q/V optical resonators.

In this chapter I outline our work developing whispering-gallery-mode resonators in Er^{3+}:CaF_2. I have fabricated resonators with quality factors with quality factors in the range of 1×10^9 at room temperature, and small toroidal resonators with major radii as small as 340 μm – corresponding to mode volumes of approximately 6×10^4 μm^3. I have prototyped and performed initial tests on a cryogenic coupling scheme for these devices. I present background theory on whispering-gallery mode resonators (WGMRs), and outline the devices that I have fabricated. These were fabricated over two visits to The University of Otago.

While I have briefly acknowledged them already, I must start this chapter by thanking the Resonant Optics team: Professor Harald Schwefel, Dr Nicholas Lambert, Dr Florian Sedlmeir, Dr Malika Suresh, Dr Chengcai Tan, and Dr Luke Trainor. I am particularly grateful to Professor Schwefel for his enthusiasm for this project, and to Dr Trainor, for his training and guidance.

7.1 The Goal: Cavity QED With Whispering Galleries

Before launching into the specifics of the whispering-gallery-mode resonator architecture, it is important to motivate this entire study with the key goal - high cooperativity interactions between Er^{3+}ions and a resonator mode in CaF_2. Let us discuss this in isolation of the material constraints of whispering-gallery-mode resonators first. The interested reader is directed towards texts by Kimble and Vernooy [147].

The definition of high cooperativity is $C > 1$. This can also be rearranged to the following form:

$$C = \frac{Q}{V}\frac{2\mu^2}{\epsilon_0\epsilon_r\hbar\Gamma} \tag{7.1}$$

where Q is the quality factor, V is the mode volume, μ is the atomic transition dipole moment (1.53×10^{-32} for the G1), ϵ_0 is the permittivity of free space, and ϵ_r the relative permittivity of the cavity material (2.05 for CaF_2). Γ is the homogeneous linewidth of the atom ($1/\pi T_2$) - which is not to be confused with the spontaneous emission linewidth ($1/T_1$), which is used to calculate the Purcell factor. Based on our measured coherence times and dipole moments from Chapter 6, we attain a simple inequality for each site (again, motivating our choice of target sites for single ion investigations). For the G1 site, this reduces to:

$$\frac{Q}{V} > 3.07 \times 10^4 \mu m^{-3}$$

This raises the obvious and important question – 'can a whispering-gallery mode resonator achieve such a Q/V ratio?' Whispering-gallery mode resonators are routinely made with high quality factors in CaF_2 and MgF_2 [116]. Q factors in excess of 10^{11} have been demonstrated [207], and resonators with major diameters as small as 80 μm have been produced in CaF_2 [116], although with a lower Q. For our initial estimates, we therefore assume a Q of 1×10^9. This is in line with what was made during the first fabrication run in the Resonant Optics lab, though we note that higher Q can be achieved in this process [304, 305]. A Q of up to 3×10^9 would still maintain a cavity linewidth (66kHz at $Q \sim 3 \times 10^9$) well in excess of the Er^{3+} homogeneous linewidth (~10 kHz, from our a 45 μs T_m). The next question then is: 'is it possible to achieve the required mode volumes for high cooperativity?' This is addressed in Figure 7.1 and Figure 7.2. From 7.1, it is clear that there exist regimes of mode volume whereby high cooperativity can be achieved, even for the modest fabrication goal of $Q = 1 \times 10^9$. Given the known dipole moment of the G1, this is for mode volumes less than $3.2 \times 10^4 \mu m^3$. Can we achieve this goal?

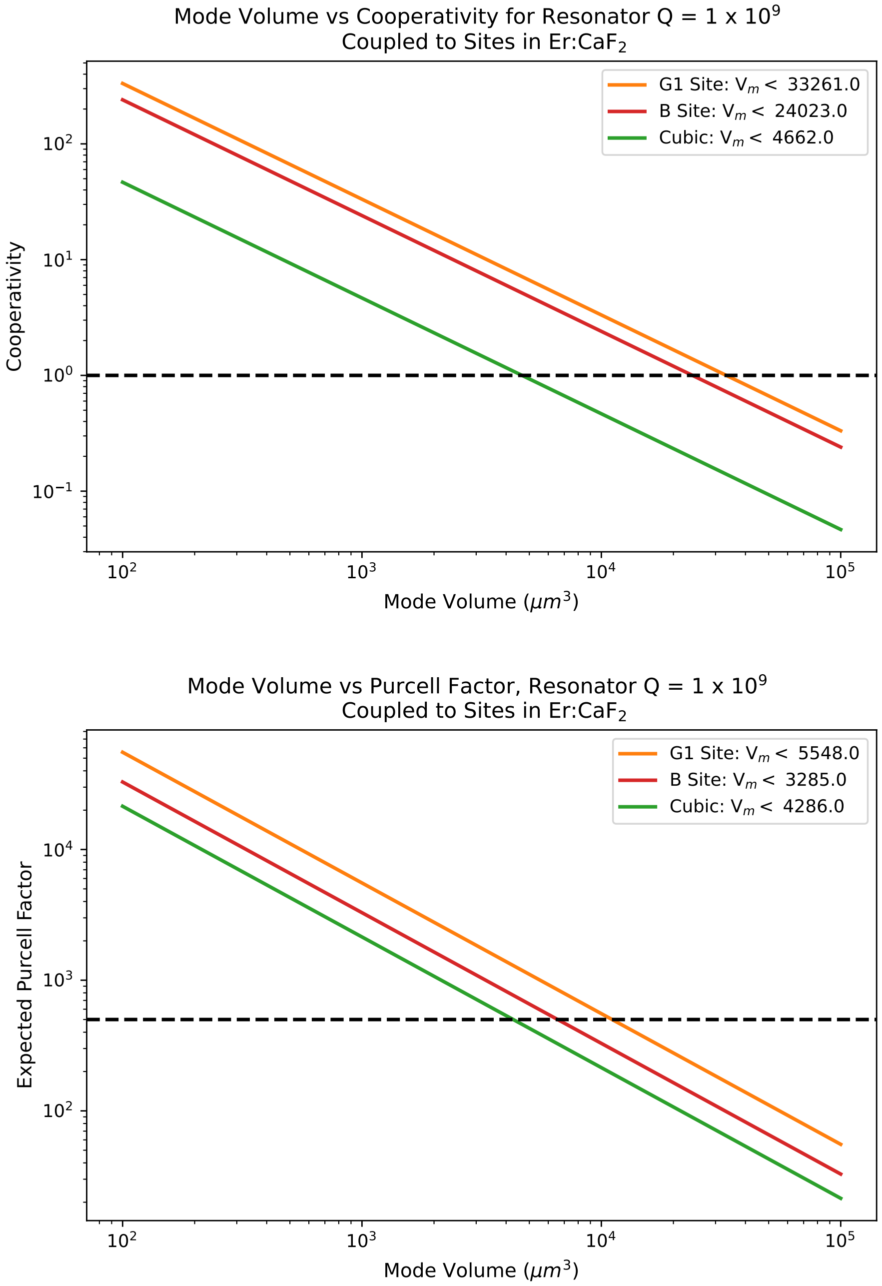

Figure 7.1: Based on the coherence times (homogeneous linewidths) and dipole moments of our sites in Er^{3+}:CaF_2, we calculate the required mode volume for an optical cavity of quality factor $Q = 1 \times 10^9$ to achieve High Cooperativity $C > 1$ (top). The dashed line represents the threshold cooperativity $C = 1$, and shown in the legend is the required mode volume to achieve this. Beyond this, we use measured lifetimes to find expected Purcell Factors (bottom). The dashed line is where $F_p = 500$ - above this line, the G1 site be in the regime of lifetime-limited coherence. Not shown are the Purcell Factors at which this is achieved for the Cubic and B sites - $F_p = 1500$ and 410 respectively. It is notable here that the B site, despite its higher dipole moment, retains a lower Cooperativity than the G1 due to ites reduced coherence.

7.2 Theory and Fabrication of WGMRs

Optical resonators to enhance interaction with rare-earth ions have be realised in numerous architectures – including free-space Fabry-Pérot cavities [27] and photonic crystal structures in semiconductor waveguides [117] or host crystals [235]. Whispering-gallery mode resonators, named for the acoustic phenomenon first observed in St. Paul's Cathedral in London, confine light via total internal reflection in dielectric structures with cylindrical symmetry.

Whispering-gallery mode resonators span a geometric continuum from thin planar disks through spheres, to perfect cylinders. They may be realised in a number of distinct physical systems, including toroidal crystalline structures [208] like ours, on-chip micro-discs [306, 307], micro-spheres [308], and even fluid-filled polymer capillaries [309]. They have been deployed in many applications, including sensing [310], as laser cavities [311], and transduction [103, 122, 312]. We note a similar effort to ours investigating coupling a different rare-earth ion (ytterbium) to a WGMR in a different material ($LiNbO_3$) [313], which is also a proven material for these devices [122].

7.2.1 Spatial Form of Modes

These resonators sustain high-finesse optical modes, characterised by exceptionally high quality factors Q and small mode volumes V, enabling the strong light-matter coupling required for cavity quantum electrodynamics. Each mode arises as a solution to Maxwell's equations subject to the boundary conditions set by the resonator's geometry, material refractive index, and curvature. The spatial structure and resonance frequency of each mode are determined by three quantum numbers: azimuthal *(l)*, radial *(p)*, and polar *(m)*, which describe the phase accumulation around the circumference, radial node structure, and polar confinement, respectively [147, 308, 314–316].

Schiller's approximation [314, 315] provides a simplified method to estimate the resonant modes of whispering-gallery mode resonators, treating the optical modes as rays circulating near the resonator surface by total internal reflection. In this approach, the modes are characterized by an azimuthal mode number m approximately equal to nkR, where n is the refractive index, $k = 2\pi/\lambda$ is the wavenumber, and R is the resonator radius. Additional mode numbers describe the radial and polar field distributions. This approximation allows for analytical expressions of mode frequencies and spacing, linking them to the resonator's geometry and material properties. Schiller's method helps explain mode confinement, bending losses, and quality factors in CaF_2 and MgF_2 resonators, providing useful insights for designing devices with high quality factors and small mode volumes essential for sensing and nonlinear optical applications [316]. Schiller's approximation can be used to find the frequency of a mode in terms of other parameters, if that mode is a sphere:

$$\nu \approx \frac{c}{2\pi a}\left[l + \frac{1}{2} + t_p^0\left(\frac{l+1/2}{2}\right)^{1/3} - \frac{qs}{\sqrt{q^2-1}} \right. \\ \left. + \frac{3t_p^0}{2^{2/3}10(l+1/2)^{1/3}} - \frac{q^3 s(2s^2/3-1)t_p^0}{2^{1/3}(q^2-1)^{3/2}(l+1/2)^{2/3}}\right] \tag{7.2}$$

where: $q = n_r/n_a$, $s = 1$ for TE, $s = 1/q^2$ for TM modes, t_p^0 is the perturbation parameter, a is the radius of the sphere, and l is the angular mode number. Equation 7.2.1 is a transcendental equation which has no precise solution but can be numerically solved.

7.2.2 Mode Volume

Using frequencies found using Schiller's approximation, mode volumes of cavities may be calculated using the following equation, from Braginsky [314, 317]:

$$V_m \approx 3.4\pi^{3/2}\left(\frac{\lambda_0}{2\pi n_r}\right)^3 l^{11/6}\sqrt{l-m+1} \tag{7.3}$$

where m is the azimuthal mode number, and $m = l$ for the fundamental modes. While spherical resonators may be analysed using the Schiller approximation, our devices are not spheres. As such, spherical approximations will severely overestimate the mode volume. Practical whispering-gallery-mode resonators come in many forms, including toroids, disks, and bottles – and there are a number of adapted approaches to estimating mode volume V_m. For non-spherical cavities a number of estimation methods can be used [208, 213, 306, 308, 318]:

For toroidal resonators with major radius R and minor radius ρ, a simple scaling factor can be added to the Schiller approximation to account for vertical mode confinement [306, 314]:

$$V_m \approx 3.4\pi^{3/2}\left(\frac{\lambda_0}{2\pi n_r}\right)^3 l^{11/6}(\rho/R)^{1/4} \tag{7.4}$$

This mode volume may also be estimated as the volume of a toroid [307, 319], as $V \approx \pi^2 R\rho^2/n$, however this over-estimates mode volumes for resonators of our dimensions. For thin disk resonators of radius r and height h, a practical estimate is: $V \approx \pi Rh(\lambda/2n)$, which accounts for vertical mode confinement proportional to the wavelength. For geometries with strong asphericity or bottle-type profiles, the mode localises at the position of minimum effective radius, and V_m can be approximated using the Schiller formula with an effective angular mode number $l \approx 2\pi\rho_{curv}n_r/\lambda_0$, where ρ_{curv} is the local radius of curvature. In this work, we assume that the mode is toroidal, and calculate estimated mode volumes using Equation 7.4.

Finally, we note that numerical methods such as finite element method (FEM) and finite-difference time-domain (FDTD) methods can be used to estimate cavity parameters. Tools such as MEEP, COMSOL, and Ansys Lumerical [317, 320–322] enable calculation of quality factors and mode volumes in cases where resonator geometries are well known. That said, these tools rely on precise knowledge of resonator geometry and surface quality, which are hard to know with precision in the case of our devices.

7.2.3 Q Factor and Finesse

The quality factors of whispering-gallery-mode resonators in crystalline materials can be very high, with demonstrations showing Q in excess of 10^{11}, and finesse in excess of ten million [116, 207]. The uppermost limits that may be achieved due to scattering losses are in excess of 10^{14} [323], however accessing this parameter space with current fabrication is likely not possible. Simulating resonators to find Q is challenging, so these parameters are mostly found through characterisation.

7.2.4 Fabrication

The fabrication of CaF_2 whispering-gallery-mode resonators typically involves a sequence of high-precision machining and surface finishing steps to achieve the smooth surfaces required for high optical quality factors. A single crystal is cut into a rough disk or spherical shape, followed by progressively finer and finer grinding to define the final resonator geometry, often including single-point diamond turning. This is a precision micro-machining process where a diamond-tipped tool shapes the crystal on a controlled, fast-spinning rotary stage – generally an air-bearing lathe. This technique allows accurate fabrication of resonator shapes such as spheres or disks by carefully controlling lathe parameters. Feed rate, cutting speed, and cut depth are optimised to minimise both surface and subsurface damage in the crystal. Interestingly, in some crystalline materials such as CaF_2 and MgF_2 it is possible to achieve a 'ductile' machining regime - similar to the target machining regime of metals [204]. Using just this process, it is possible to produce a resonator with a quality factor in excess of 10^7 [205].

Following the initial shaping, the resonator surface is polished using fine diamond abrasives to reduce roughness and scattering losses. To ensure dimensional accuracy and surface quality, the resonator is imaged during the process, however it is important to note that all of these subtractive machining processes involve the removal of material from the sample, and as such the 'as-cut' profile is not possible to maintain. Using progressively finer and finer abrasives (1 μm, 0.25 μm and 0.1 μm diamond slurries were used in this work) it is possible to increase the quality factor of cut resonators by several more orders of magnitude [116]. Producing the highest quality-factors achievable requires considerable post-processing in which resonators are polished, cleaned, and then annealed, and this process repeated several times [207].

7.2.5 Challenges Associated With WGMRs

Working with whispering-gallery mode resonators presents several challenges, primarily related to achieving and maintaining ultrahigh quality factors and precise mode control. Precision is required, as any surface roughness or subsurface damage introduced during cutting or polishing can increase scattering losses, and hence reduce Q. The brittle nature of crystalline materials can complicate machining, requiring carefully optimised cutting parameters to avoid cracking or chipping.

Due to the nature of the fabrication processes often used (including those used in this work), precise knowledge of the machined geometry is difficult to attain. Polishing leads to further changes to machined geometries, and polishing with various levels of efficacy leads to higher of lower Q factors. Because of this, simulations and precise prediction of mode structure and resonant frequencies is challenging. Free spectral range measurements can often be the best measure of a resonator's geometry.

During characterisation, WGMRs are highly sensitive to temperature fluctuations, which cause shifts in refractive index and physical dimensions, leading to resonance frequency drifts. Mechanical vibrations also perturb the resonator coupling conditions, particularly considering efficient coupling requires sub-micron precision alignment. Environmental contamination such as dust or adsorbed molecules on the resonator surface can significantly degrade the quality factor by introducing scattering and absorption losses. We note that it is precisely these effects that make whispering-gallery-mode resonators such excellent sensors.

7.2.6 Fabrication Process

During the course of this project, two fabrication-focused visits to the University of Otago were made. The results of these trips are summarised in the Table 7.1. The fabrication recipe follows the processes detailed in [304]. This section will provide a high-level overview of the process.

Sample Preparation and Mounting

Samples of CaF_2 are prepared for mounting on a brass post. In the work of this thesis, resonators were made both using Er^{3+}:CaF_2 and nominally undoped CaF_2. All doped samples were grown (and in some cases, annealed) at the University of Canterbury (Te Whare Wānanga o Waitaha) by Michael Moull and Dr Jamin Martin, at the University of Canterbury Crystal Growth Facility under the supervision of Professors Mike Reid and Jon-Paul Wells. Undoped samples are excimer-grade CaF_2 from Fairfield Crystal Technology. Individual samples from growth are oriented based on a controlled cleaving process, and the known preferred cleavage planes of CaF_2[218].

From the larger samples, blanks are cut using a combination of tools: reductions in diameter are either achieved by 'coring', and 'slices' can be taken using a diamond wire saw. These blanks are then glued to metal rods, also made of brass, with a narrow 'pedestal' feature in the centre. As the diameter of the resonator being cut reduces, this gluing method needs to be as strong as possible. Larger ($R > 1$mm) resonators can be stuck to their post using wax (Oxford Instruments QuickStick Mounting Wax), however the smaller resonators are affixed using epoxy.

An alternative method to initial shaping prior to mounting is to fix an un-shaped, but close-to-cylindrical sample to its metal rod, and use a linishing / grinding process for the initial shaping using a strip of sandpaper on controlled stage. This must be done delicately, as the force exerted on the resonator blank can be high if a large area is contacted, and samples may be knocked off their posts. Further, grinding is known to introduce sub-surface cracks in whispering-gallery-mode resonators, which could lead to an increased likelihood of cleaving during later processes.

Single Point Turning

The blank is mounted to a balanced air-bearing lathe. The resonator profile is cut using a single-crystal diamond tool mounted on translation stages. The feed rate, rotation speed, and rake angle are carefully controlled. Cuts are coarser, and hence faster during the first passes, and finer as the resonator approaches the target geomoetry.

A 1 µm cut at 100 µm/s feed rate corresponds to a material removal rate (MRR) of CaF_2 of approximately 6.3×10^{-4} mm^3/s. It has been noted that low MRRS are required for ductile machining of CaF_2 crystals [204]. MRR scales linearly with each cutting parameter, and is approximated as follows:

$$MRR = \pi \cdot D \cdot f \cdot d \cdot N \tag{7.5}$$

where D is the approximate diameter of the workpiece, f is the feed rate per revolution, d is the cut depth, and N the rotational speed in revolutions/s. Tapering these cutting parameters for small resonators is particularly important when cutting a crystal with cleavage planes such as CaF_2, since the force applied to the sample by the cutting tool increases with decreasing radius.

The cutting process is monitored using two cameras - one connected to a stereoscopic microscope observing from above the sample, and the other looking down the axis of rotation. Both of these are used to assess cut quality, tool wear, and resonator progress.

Polishing

Once the resonator achieved its target diameter - in our case, less than 800 μm of outer diameter - cutting ceases, and the resonators are polished to achieve the highest possible Q. While a smaller major diameter is beneficial for achieving low mode volumes, cuts become more risky as the major diameter becomes smaller. Cutting feeds and speeds are managed carefully as the resonators become smaller, but smaller samples are more prone to cleaving or falling off their support posts.

Resonators were polished on the same air bearing lathe, at a much slower speed. After cleaning with isopropyl alcohol, the resonators are polished with varying grades of diamond slurry on lens cleaning tissues, with successively smaller particle sizes. This is typically done by hand, since it is possible to vary pressure and the specific area of the resonator which is being polished. After polishing, resonators are carefully cleaned using a process of applying and removing glycerol and isopropyl alcohol in alternating steps. This is conducted at 10 revolutions/second on the same lathe.

Characterisation

Resonators are experimentally characterised in an optical circuit, by carefully tuning the coupling between the resonator and an external source, commonly using a high-index prism. A beam is focused on the base of the prism, and frustrated total internal reflection is used to couple light from the beam into the resonator. The resonances are monitored as reductions in transmission, whose depth and FWHM provide information on the quality factor, Q. The free-spectral range may be approximated from measurements of the resonator's diameter - however there is a well-established technique [304] which can be used to provide a more accurate measurement. As the RF source that is used to drive a modulator is swept, sideband peaks move until they overlap with its neighbouring peak in the adjacent free-spectral range.

7.3 Target Parameters

With our new understanding of whispering-gallery-mode resonators we can take the analysis from Figure 7.1 further, asking: ‘What is the required geometry to yield $C > 1$?’ Figure 7.2 highlights our target parameters for fabrication: Assuming a resonator $Q = 1 \times 10^9$ and a toroid minor radius of $20\mu m$, we plot the relationship between major radius and mode volume. This is calculated using the Braginsky approximation, provided in Equation 7.4 [314]. Also shown is the relationship between major radius and cooperativity for such a device, and the maximum major radius required to achieve $C > 1$. This clarifies our fabrication goals.

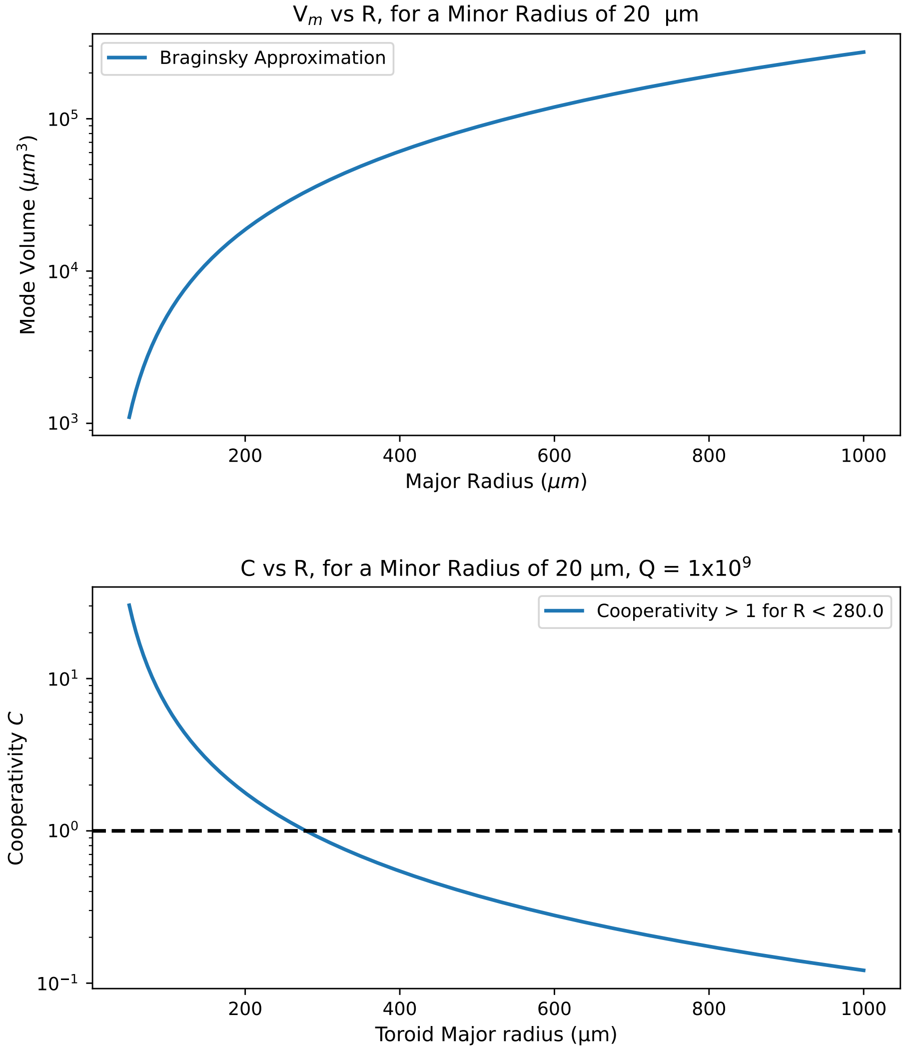

Figure 7.2: Top: The relationship between R and V_m for a toroidal resonator of minor radius $\rho = 20\ \mu m$. We note that the approximation used here is likely an over-estimate of true mode volume. **Bottom:** The relationship between R and C. We assume a quality factor of $Q = 1 \times 10^9$, and that the resonator couples well to an G1 centre in Er^{3+}:CaF_2. Major radii $< 280\ \mu m$ lead to $C > 1$.

7.4 Our Devices

Table 7.1 provides a summary of the resonators that were fabricated over the course of this work. Images of these are shown in Figure 7.3. It is worth noting that the dimensions listed here are nominal: Er^{3+}concentrations are based on the best knowledge we have from the crystal growth process and crystal orientations are known only up to approximately a 5° margin of error, due to inherent instabilities in the cleaving, mounting, and cutting process. Major radii of the resonators are measured using a scale bar on a calibrated optical microscope above the cutting tool, and minor radii are based on tool path and tool radius during the cutting process. Both of these are re-verified after polishing and before packaging.

Sample	Er^{3+}%/Annealing	Orientation	Max. Extent (μm)	Minor Radius (μm)	Toroid Radius (μm)
"A"	0 / None	$\langle 111 \rangle$	~3000	~1000	~1500
"B"	0.01 / None	$\langle 100 \rangle$	~2000	~500	~1000
"Mike"	0.001/ 5hrs	$\langle 111 \rangle$	~1700	20	830
"Donato"	0.001/ 5hrs	$\langle 111 \rangle$	740	40	330
"Eric"	0.001/ 5hrs	$\langle 111 \rangle$	880	20	420

Table 7.1: The WGMRs fabricated over the course of this work. The measurements of maximum extent come from distance measurements taken under the microscope used in cutting and polishing, using a calibrated reticle. We estimate measurement errors of $\pm 2\ \mu m$. Minor radii provided are based on the cutting curve used and confirmed under the microscope, with similar error bounds, mostly due to the non-zero change that polishing will produce. Toroid radii are calculated by subtracting the Minor Radius from half of the Maximum Extent

7.4.1 Projected Cavity QED Metrics

All current devices have radii which should enable them to reach a moderate cooperativity regime ($C \approx 0.5 - 1$). However no resonator has yet lasted the entire fabrication and polishing process with a radius below the $R < 280\ \mu m$ threshold presented in Figure 7.2. We have estimated of the achievable cavity QED parameters in our devices. Calculations were conducted using the dipole moment and homogeneous linewidths found in Chapter 6 to calculate the Q factor that each device would require to achieve $C > 1$. Based on this Q factor and the measured lifetime of the G1 site, we can also deduce the Purcell Factor that each would achieve at $C = 1$, which is approximately 640 for all devices. This provides to us an indication of target room-temperature parameters when polishing and re-preparing the resonators for cryogenic experiments.

Mode volumes are approximated using the toroidal approximation in Equation 7.4. We note that this provides only an approximation (and quite likely an overestimate) of the mode

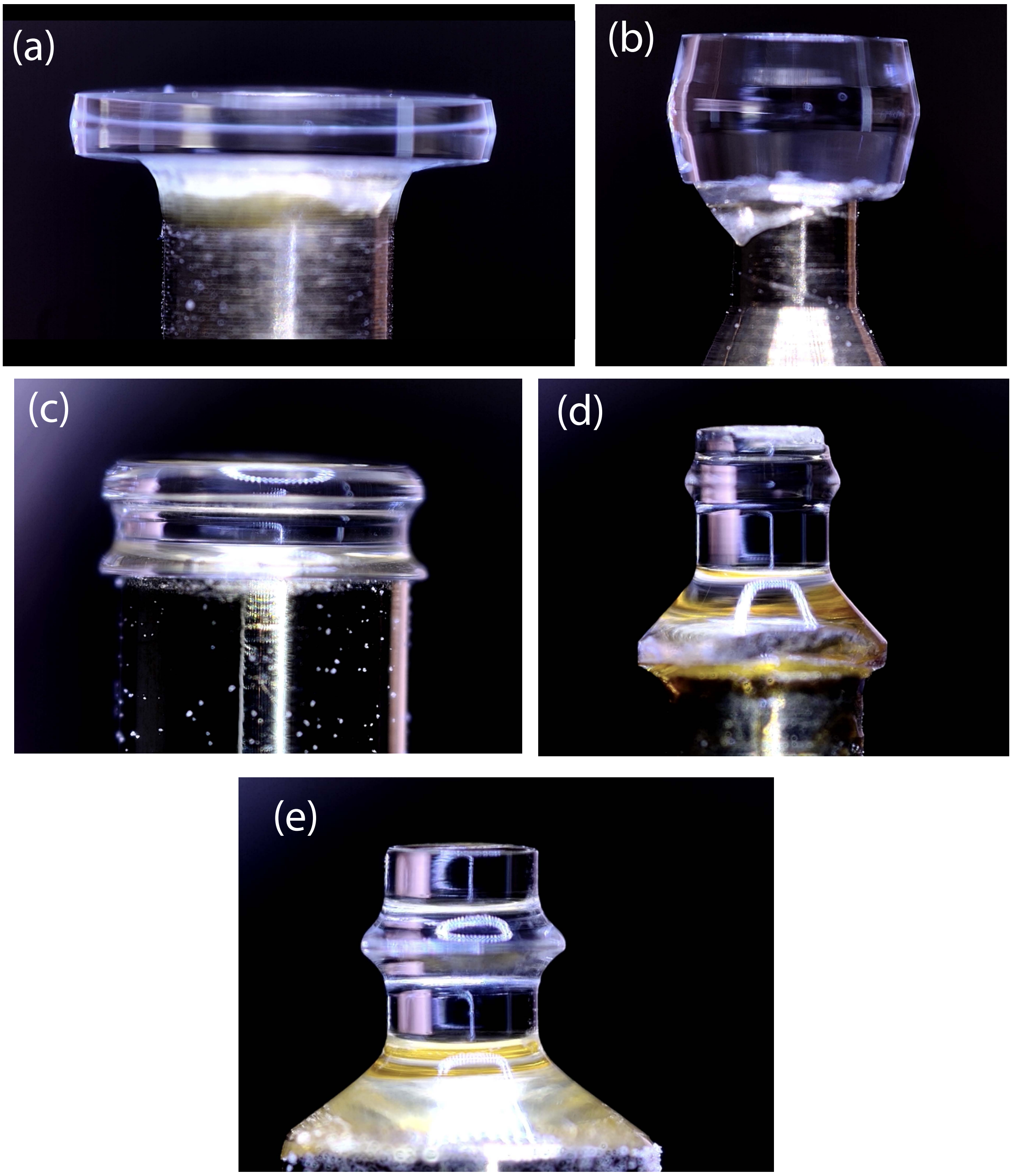

Figure 7.3: The five devices successfully fabricated in the course of this work. 'Major Diameter' measurements provide the measurement of the resonator at its maximum width. **(a)** Device A - major diameter 3mm. **(b)** Device B - Major diameter 2mm. **(c)** 'Mike' - Major diameter 850 μm **(d)** 'Donato' - major diameter 740 μm **(e)** 'Eric' - major diameter 880 μm.

volume of these devices, however this provides an indication of how close to high cooperativity these devices could take us. Having now achieved estimated mode volumes using the Braginsky approximations, the next step will be to incorporate FEM or FDTD methods into the design process. Using these simulations to accurately represent real world devices can be challenging, since precise knowledge of the machined device is required, including surface finish and geometry after polishing. To ameliorate this, it is possible to simply cut without polishing.

Sample	V_m (Braginsky) (μm^3)	Q_{min} for $C > 1$
"A"	63.3×10^4	7.72×10^9
"B"	21.11×10^4	6.49×10^9
"Mike"	21.06×10^4	6.49×10^9
"Donato"	5.81×10^4	1.79×10^9
"Eric"	7.16×10^4	2.20×10^9

Table 7.2: Estimated mode volumes for each resonator, using the Braginsky approximation from Equation 7.4. Using these estimated mode volumes, we calculate the minimum quality factor, Q_{min} for these devices to yield $C > 1$. This approximation likely over-estimates mode volumes and hence the required Q factors regime, with only two of our final resonators in the low 10^9 regime. These provide targets for any subsequent surface preparation.

7.5 Coupling Schemes for Whispering-Gallery Mode Resonators

Efficient coupling to high-Q whispering-gallery mode resonators requires precise phase and field-profile matching. Several methods exist for coupling light in and out of whispering-gallery-mode resonators.

Prism Coupling: Prism coupling uses Frustrated Total Internal Reflection when evanescent modes of the prism and resonator align sufficiently. While highly sensitive to alignment, it requires minimal fabrication and achieves state-of-the-art efficiencies around 99.96% (less than 0.1 dB insertion loss) [308, 324], making it ideal for initial experiments at room temperature.

Tapered Optical Fibres: Tapered fibres couple evanescently by reducing diameter to a few microns, extending the mode field beyond the core. Single-sided tapers are simple to fabricate using hydrogen flames. Double-sided tapers achieve coupling efficiencies exceeding 90% with careful positioning but are mechanically fragile and challenging in cryogenic environments due to thermal contraction issues [325].

Angle-Polished Fibre Couplers: These couplers use fibres cleaved at precise angles, between 8-15°, directing modes toward the resonator via refraction [326]. They achieve comparable efficiencies to tapered fibres while maintaining mechanical robustness and surviving thermal cycling to dilution refrigerator temperatures—particularly attractive for cryogenic cavity QED experiments with rare-earth ions. The trade-off is that both input and output beams require free-space or fibre collection, complicating full integration.

Photonic Wirebonds: Photonic wirebonds are 3D polymer waveguides written via two-photon polymerisation [327, 328]. They have been shown interfacing with crystalline micro-resonators, including a Kerr comb demonstration in a $\mathrm{MgF_2}$ whispering-gallery-mode resonator [329]. They provide stable mechanical connections with low (<3 dB) insertion loss, and have been recently demonstrated functioning at deep cryogenic temperatures [330, 331].

Waveguide Couplers: Integrated waveguide couplers offer the most mechanically robust and scalable approach for cryogenic and on-chip environments. Silicon nitride provides a favourable balance: its moderate refractive index ($n \approx 2$ in bulk) allows larger features than silicon while $\mathrm{XeF_2}$ dry etching enables straightforward undercut release for suspended waveguides. SPARROW waveguides achieve the lowest optical loss but require complex multi-layer deposition [332]. Photonic crystal waveguides have been demonstrated, though require complex fabrication [333]. In our work, SiN tapered waveguides were selected due to established fabrication protocols, mechanical rigidity under thermal cycling, and sufficient mode-matching capability to CaF resonators ($n \approx 1.43$).

7.6 A Cryogenic Optical Coupling Setup

There were two key motivations for our approach to coupling to whispering-gallery-mode resonators. First was to develop an efficient, low loss coupling mechanism for use within the confines of our dilution refrigerator. The second goal was to minimise the number of unconstrained mechanical degrees of freedom in the experiment. This should lead to a system that with less moving parts and as such is less prone to failure.

During the prototyping phase of the optical coupling setup, we evaluated several coupling strategies for our $\mathrm{CaF_2}$ WGMRs. Early efforts focused on direct fibre coupling, including the use of a pair of single-sided tapered fibres, which have shown evanescent coupling to the resonator modes [304, 334]. Our initial trials based on two single-sided tapers were unreliable in our configuration, with inconsistent coupling efficiency due to the mechanical instability of the long, suspended cantilever of the fibre. A double-sided taper scheme was also considered, however the challenges associated with precise tensioning of a fibre over a 300 K thermal gradient led to this being deemed impractical for experiments in a cryostat.

7.6.1 Waveguide Coupler Design

Our investigation into integrated photonic waveguides revealed several advantages. A number of substrates, materials, and candidate designs were assessed before the decision to fabricate our couplers on a Si_3N_4 substrate (hereafter SiN).

The effective refractive index of low-numbered modes in a whispering-gallery-mode resonator made of CaF_2 are equal or less than the bulk index of the material ($n = 1.43$ at 1550 nm). Efficient coupling will only occur when the effective index of the waveguide is equal to that of the resonator mode $\widetilde{n}_{res} = \widetilde{n}_{wg}$ [335]. Due to the generally high bulk refractive indices of silicon and other micro- and nano-fabrication compatible materials (Si has index 3.45, while Si_3N_4 has bulk index $\sim$2), waveguides to couple to whispering-gallery-mode resonators must be tapered. Furthermore, since these materials are often provided on a substrate of an oxide with a lower index, any waveguide-based coupler must also be relieved (undercut) from its substrate.

The SiN platform offered excellent optical properties, mechanical rigidity, and compatibility with chip-based fabrication techniques. Importantly, tapered waveguides on SiN provide better control over mode matching to the target WGMR resonances (with measured indices near 1.4), and their robust structure simplified assembly and alignment in the cryostat. Ultimately, the decision to use SiN waveguides was driven by a combination of cryogenic performance, reliable mode matching to CaF_2 WGMRs, and practical considerations in assembly and fabrication.

7.6.2 Fabrication and Characterisation of Silicon Nitride Couplers

Method

Silicon nitride waveguide couplers were fabricated by Dr Igor Marinkovic on 300nm thick SiN on Si, at the University of Queensland, via electron-beam lithography and reactive ion etching to define tapered waveguide structures. These have two tapered sections - a shorter taper from 180nm width up to 350nm (to which the fibre taper is attached), and a longer ($\sim$3-5mm depending on design) region, which tapers down to about 150nm waveguide width, and ends in a reflector. Following fabrication, individual chips were separated by scoring the wafer with a diamond scribe and cleaving along crystallographic planes, yielding chips approximately 3 × 8 mm in size. Each chip contained multiple tapered waveguides, allowing selection of the optimal coupler or providing backup devices in case of damage during assembly.

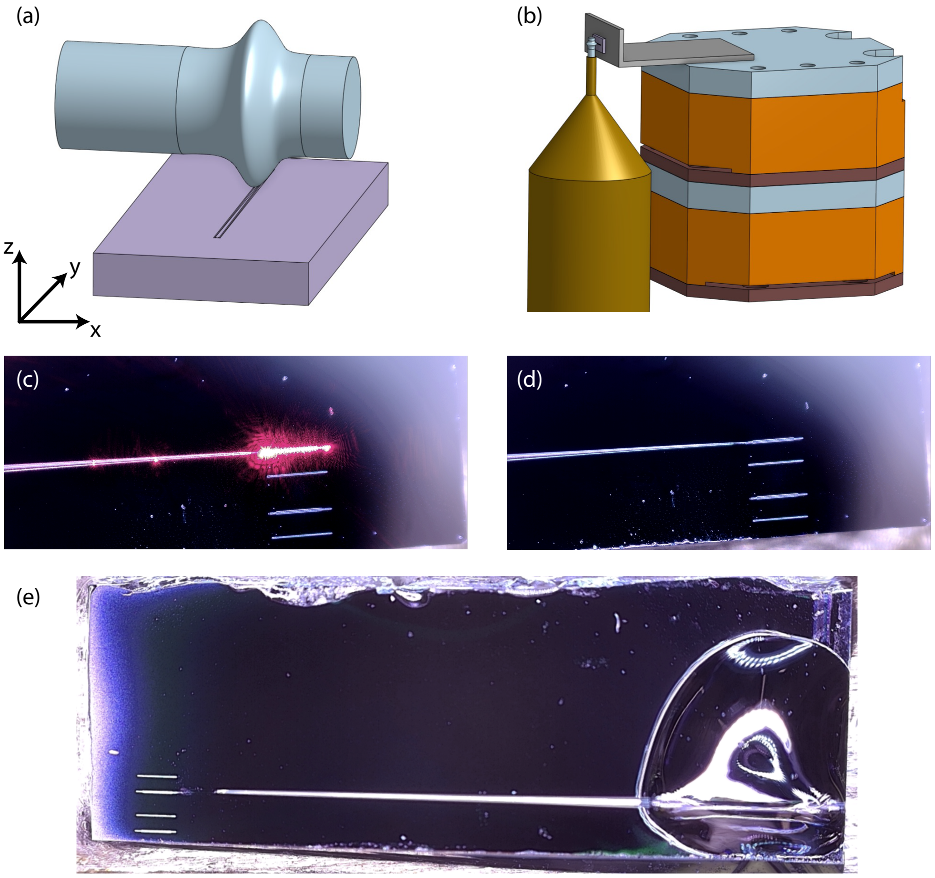

Figure 7.4: The concept and images for the coupler designed in this work. **(a)** A tapered waveguide chip is moved relative to the outer diameter of a whispering-gallery-mode resonator. **(b)** The chiplet containing the device is mounted on a nanopositioner, such that the resonator remains stationary but the coupler moves. **(c)** One of our devices - CP03 under illumination from 633nm light. **(d)** CP03 again, showing the fibre, epoxied in place against its waveguide. **(e)** CP02, another of the coupler devices, showing the considerably larger epoxy droplet, used to strain relieve the fibre taper.

Coupling into the waveguide is achieved via a tapered single mode fibre, glued to a tapered portion of the SiN waveguide. The tapered fibre was fabricated in-house using an hydrogen flame and solenoid pulling technique, reducing the fibre diameter from 125 μm to approximately 3–5 μm over a 10 mm taper region. The taper and chip were positioned using a pair of three-axis translation stages (Thorlabs Nanomax) and aligned under optical microscopy while monitoring reflected power. Once optimal alignment was achieved (generally above 50% reflected power), the junction was permanently bonded using Norland Optical Adhesive 86H (NOA-86H), a UV-curing epoxy with refractive index ≈ 1.55. The fibre is further strain relieved, about 3mm behind the tapered region, again using Norland. All epoxy is cured, and the assembled chip was then mounted to a copper platform for thermal anchoring during cryogenic operation. This copper platform is bolted to a nanopositioner for cryogenic positioning. The coupling schema images of these devices are shown in Figure 7.4

Results

Transmission characterisation of the assembled SiN waveguide couplers was performed by launching 1550 nm light into the tapered fibre input and measuring the reflected power using a 1/99 fibre beam splitter and photodetector. Single-pass (one-way) coupling efficiency, defined as the fraction of input power coupled into the fundamental waveguide mode, was measured at >50%, corresponding to a round-trip return of >30 %. Numerical simulations using COMSOL further confirmed that the tapered SiN waveguide supports a quasi-TM mode with effective index 1.4 at the narrowest point (150 nm width), closely matching the effective index of target WGM resonances in CaF_2.

Table of Coupler Properties

Device	Details	One-way Efficiency	Notes
CP01	Straight waveguide	>20%	Used for initial room temperature measurement at UQ
CP02	Tapered waveguide	>30%	Failed during room temperature tests at USYD
CP03	Tapered waveguide	>50%	Failed during room temperature tests at USYD

Table 7.3: The properties of the couplers fabricated at UQ

7.6.3 Attempts to Couple to Resonators

Following assembly, the SiN waveguide coupler was mounted on a copper substrate and installed on a two-axis piezoelectric nanopositioner stack (Attocube ANPx101 and ANPz101) and a precision micrometer translation stage, to enable precise positioning relative to the WGMR, with independent control over x, y, and z position at nanometre resolution. Initial alignment was performed under optical microscopy using a side-view camera to position the resonator ridge to within ∼10 μm of the waveguide, followed by a top-down camera to monitor the gap distance between the outer diameter of the whispering-gallery-mode resonator and the waveguide itself.

The ECDL was coupled into the input fibre, with reflected power monitored via photodetector to identify resonant transmission dips. Optimisation of coupling efficiency was achieved by iteratively adjusting the Attocube stack while monitoring reflected power. This configuration allows systematic exploration of the coupling gap distance (typically 100–300 nm for optimal evanescent overlap) and lateral alignment along the waveguide - seeking the point where the

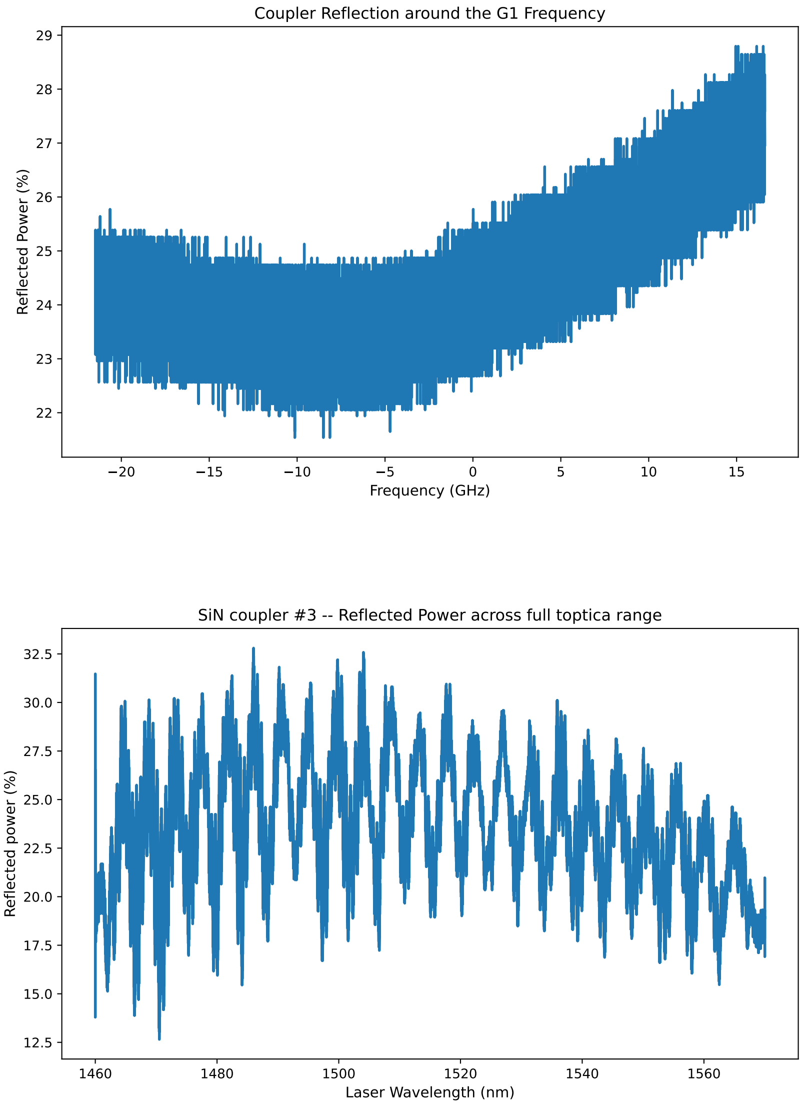

Figure 7.5: Response of the waveguide coupler in two regimes. **(a)** Narrow-band around the transition frequency of the G1 site **(b)** Broadband response of the coupler across the range of our CTL1500

waveguide's effective index matches that of the resonator mode.

Integration trials of the SiN waveguide couplers revealed a mechanical constraint for larger resonators: the resonator outer diameter contacted the fibre strain-relief epoxy before mode overlap could be stably established. Both devices failed in the same mode, whereby the resonator touched, and subsequently snapped the tapered fibre in the region between its strain relieving glue and the waveguide. For smaller resonators, a different problem emerges if the resonator's diameter is significantly less than that of the brass post on which it is mounted. The SiN surface interferes with the brass itself, again preventing mode matching.

These destructive tests on prototype devices CP02 and CP03 provided definitive design parameters for Generation 2 couplers. Specifically:

- Waveguide interaction length must exceed 15 mm (vs. current 3-5 mm) to provide clearance for resonators with R > 500 μm.
- Chiplet geometry must position waveguides within 2 mm of the cleaved edge to avoid interference with the resonator mount.

7.7 Selection of Resonator For Cryogenic Experiments

A preliminary quality factor estimate was measured for Resonator A during the first fabrication run, with an estimated Q between $0.8 - 2 \times 10^9$. The work of characterising the rest of the devices described in this chapter is currently underway in our lab. Further work will involve developing cleaning and polishing schemes to maintain high quality factors, which can be compromised during experiments and integration.

Based on the geometries achieved of the second round of resonators, two of the named devices (Donato and Eric) are the current best candidates for integration into a cryogenic experiment. That said, room temperature characterisation of these devices could lead to any of the four resonators which currently contain erbium being used for these experiments. Table 7.4 provides estimates of C, F_p, and g for the G1 site coupled to our devices, with $Q = 1 \times 10^9$. This is chosen as an achievable, maintainable quality factor for these devices in experimental conditions.

Device	$g/2\pi$ (kHz)	C	F_P
"A"	4.4	0.13	44
"B"	6.7	0.16	53
"Mike"	14	0.16	53
"Donato"	31	0.57	190
"Eric"	32.28	0.46	155

Table 7.4: Given the devices we have, what could we do with a sufficiently high Q? These calculations assume the Braginsky mode volume, and a Q of 1×10^9, a maintanable target.

Using these estimates, we are confident about the potential of the existing devices in upcoming cavity QED experiments. The two smallest mode volume devices, ‘Donato’ and ‘Eric,’ both would have sufficient cooperativity and enhancement for initial single ion experiments. The achievable cooperativity of ~ 0.5 provides access to some cavity QED protocols, but fidelities are limited [336, 337]. The Purcell Factor of < 100 enhances T_1 of the G1 site from 23 ms to < 300 μs. This is well short of achieving lifetime limited coherence, but would likely enable single ion detection: the single ion emission rate will be in excess of 3000 s^{-1}, enabling detection using our current photon counting infrastructure, where dark count rates are less than 1000 s^{-1}.

We are also optimistic that our smallest mode-volume devices can achieve $C > 1$, with some effort. Both 'Donato' and 'Eric' would require polishing into the $\sim 2 \times 10^9$ regime to achieve this, however we note that from preliminary characterisations of Device A, such a quality factor should be achievable. Future fabrication runs will continue to target smaller devices, relaxing requirements on quality factor further.

7.8 Conclusion and Outlook

This chapter has presented the design, fabrication, and initial steps towards characterisation of high Q/V calcium fluoride whispering-gallery mode resonators, designed for cavity quantum electrodynamics with single erbium ions. The work outlined in this chapter has been one of defining and identifying design constraints, and completing the initial engineering cycles of each component in our prototype system. There are a number of clear next steps in this work, which I outline here.

We have proven that we are capable of machining toroidal resonators using the Er^{3+}:CaF_2 crystals grown at The University of Canterbury. We have also proven that we can prepare crystals with high quality factors - in the range of at least $Q \sim 1 \times 10^9$. While the current geometries place these devices below the threshold of $C > 1$, even for ultra-high Q, our demonstration of $Q \sim 10^9$ in our initial fabrication run (in resonator A) confirms that surface quality can be achieved.

Regardless of whether $C > 1$ is achieved with the first batch of devices, we have developed the techniques required to progress from these initial prototypes to demonstrations. Future devices will target smaller mode volumes - primarily by reducing major radius. This remains challenging, however is not out of our grasp. Scaling down to smaller radii, even as small as 80 μm is a known engineering path [206]. The smaller the R, the more relaxed requirements are on Q.

Two complementary coupling schemes have been developed: prism-based evanescent coupling for rapid room-temperature screening, and SiN tapered waveguide couplers were prototyped for integration into cryogenic environments. Mechanical validation of the waveguide coupler identified interference as the limiting factor, in two locations. First, between the strain relieved tapered section of the fibre and the circumference of our resonators - especially those from the first fabrication run (A and B). The second issue is more subtle: for resonators whose outer diameter is smaller than that of the brass mount, the distance from the edge of the chip to the waveguide must be less than the distance from the resonator structure to the next increase in diameter.

A redesigned geometry has been designed to resolve both of these issues. Future waveguides will be longer - in excess of 15 mm - to ensure that resonators of diameter 500 μm or greater do not interfere with the tapered fibre. Cleaving schemes will change too, such that waveguides will also be closer to the edge of their host chiplets. These updated designs will provide the required clear space for resonators to move along the waveguide length without interfering with the tapered fibre or its strain relief.

In the interim there are many more waveguide devices on each chip - seen in the photo in Figure 7.4. The broken tapered fibre can be removed, or the chip diced or cleaved to provide access to any of the other waveguides on this chip.

The successful realisation of these high-Q CaF_2 resonators combined with the high-dipole-moment erbium sites identified in Chapter 6 will establish the platform for our single-ion cavity QED experiments. Near-term milestones include cryogenic verification of coupler and resonator performance, followed by measurements of ensemble and single-ion properties in the resonator. With the core components of the experimental infrastructure now in place, the transition from ensemble spectroscopy to single-emitter strong coupling is within reach.

"Science is an ongoing process. It never ends. There is no single ultimate truth to be achieved, after which all the scientists can retire."

Carl Sagan

8

Conclusion

This thesis has outlined the beginning of our group's experimental efforts towards single ion cavity QED with erbium ions. In this concluding chapter, I will provide a brief summary of the thesis itself, highlighting the key results from my experiments, and discuss their potential contribution to the field. I then discuss both the immediate and near-future experimental opportunities, and provide a perspective on the long-term goals of this research direction.

8.1 Summary of this Thesis

Within this thesis, I have outlined the development of the foundational components of a single erbium ion cavity QED architecture. In Chapter 2, I provided a high level motivation for the work – photonic interconnects are a path to scaling quantum technologies, and erbium ions are a candidate to build these. In Chapter 3, I outlined the theoretical framework for our experiments. I highlighted the properties of the rare earths, focusing on erbium, linking unique atomic physics of the lanthanides to their potential as quantum interfaces. The choice of host material was discussed, motivating calcium fluoride as the host for our site engineering studies. I then provided an introduction to cavity quantum electrodynamics, discussing the figures of merit associated with cavity QED systems. Importantly, I introduced cooperativity as the key figure of merit that we seek to optimise in our work.

Chapter 4 discussed existing efforts in single rare-earth ion cavity QED, building the context for our work. I focused on the pioneering work of the Faraon and Thompson labs, which were the two first - and at the time we started this project, only - groups to achieve high fidelity single ion spin-state readout. I highlighted the similarities and differences between their experimental platforms, and discussed a number of other single ion efforts that have emerged in the five years since their initial demonstrations. In this Chapter, I also outlined the long-term architecture of our testbed system – single erbium ions, in high Q/V whispering-gallery-mode resonators made from calcium fluoride, and contrasted this with other efforts examining single erbium ions.

From Chapter 5 onwards, the focus turned directly to what we have built and the experiments I have conducted so far in our system. Chapter 5 focuses on the tools and techniques that have enabled our experiments so far. Over the course of this work I have designed, built, and performed experiments with a low-temperature, high sensitivity, high resolution spectroscopy setup. I provided characterisation metrics of this system for addressing increasingly dilute samples of rare-earth ion materials. I described the spectroscopic techniques that we have employed in this work. Although our software and hardware continues to evolve, the set of tools and techniques in Chapter 5 is what we will use to progress toward single ion addressing.

In Chapter 6, I outlined the characterisation of four erbium sites in calcium fluoride, and identified our site for the path forward in single ion experiments. I presented our novel experimental results on this system, including excited state lifetimes of 8 optical transitions, the excited state g tensors and coherence properties of the Cubic, G1 and B sites, and a quantified spectral diffusion measurement in the G1 and B sites. The longest coherence times we have measured are in the G1 site, with 43.9 μs, significantly longer than measured in calcium fluoride in the past [294, 296], and within the same order of magnitude as similar work in Er:YLiF$_4$ [298].

We have identified the most likely source of decoherence and quantified the angle-dependent magnetic sensitivity of the two axial sites - the G1 and B. This analysis points to the opportunity of extending coherence times. We calculate an improvement of up to a factor of eight in the G1, as long as magnetic decoherence continues to be the dominant dephasing mechanism as linewidths narrow beyond 1 kHz. We have also measured the temperature effects on both coherence and inhomogeneous line properties.

The most important results in our pursuit of single ion devices are the strengths of optical dipole moments of three of these sites. This is the first step in two projects: the single ion cavity QED project, which benefits from the site that yields the highest cooperativity; and the crystal field engineering project, in which we seek to understand the link between crystal environment and dipole moment. The dipole moments measured in the G1 and B sites were 1.53 and 1.63×10^{-32} C · m respectively, each about twice that of the cubic site. These dipole moments similar to Er^{3+}:Y_2SiO_5 [267].

In Chapter 7, I outlined our work on whispering-gallery-mode resonators in both doped and ultra-pure calcium fluoride, towards the goal of addressing single ions in a cavity QED architecutre. I outlined the design, fabrication and initial work on whispering-gallery-mode resonators in our lab, along with the design and characterisation of a waveguide coupler for use in our dilution fridge.

I have fabricated five whispering-gallery-mode resonators over the course of this project, during two trips to The University of Otago. These engineering cycles each served a clear purpose: in the initial trip, we proved that high-Q resonators could be fabricated in both our grown-and-doped crystals and in commercially purchased samples. The second cycle investigated the fabrication parameter space, with a view to cutting progressively smaller resonators – something that is not normally explored within the Resonant Optics lab. The current smallest device I have fabricated has a major radius of 330 μm, and during these fabrication runs, blanks were cut as small as 285 μm. While none of the smaller devices made it to completion as a device, we are confident that we can fabricate the required geometry.

Based on the dimensions of these devices, we have two which could achieve Purcell Enhancement close to 200 with realistically achievable quality factors $Q \sim 10^9$, and $C \sim 0.5$. This is likely high enough for preliminary single ion work, and in future revisions we will target even smaller geometry still.

A cryogenic coupler concept was developed for the purpose of coupling to these devices in our dilution fridge. Similar to the resonators themselves, there were two engineering cycles: an initial prototype and an improved device, designed for room temperature and initial cryogenic experiments. From both of these we have updated the designs for the next generation of these couplers.

While direct cavity-enhanced spectroscopy remains a next-step milestone, this thesis has established both the atomic platform (sites) and photonic platform (resonators) as separate validated components. Integration is the remaining engineering challenge, and the path forward is clear.

8.2 Future Work in the Current Experiments

With minimal changes to the current experimental setup, there are a number of investigations that could be conducted that could provide insight into our material system, as well as into the properties of the rare-earth ion optical transitions themselves.

8.2.1 Bulk Spectroscopy of Doped Crystals

The continued study of doped bulk crystals will help to uncover the precise limits on coherence in calcium fluoride, provide better estimates on magnetically induced decoherence, and at the fundamental level will help us to understand the link between erbium sites and their properties.

The data we have already taken can be used to fit improved crystal field models for the G1, the B, and the cubic sites. We seek to understand the link between the crystal field Hamiltonian and optical dipole moment, and the extent of any trade off between dipole moment and coherence time. A preliminary numerical analysis of the crystal field parameter space has been conducted in our lab to find which crystal field parameters provide the largest dipole moment for the $^4I_{15/3} \leftrightarrow {}^4I_{15/2}$ optical transition. Initial results suggest that a strong axial perturbation for tetragonal and trigonal point group symmetries leads to higher magnetic dipole moment optical transitions. The next step to this analysis is to investigate the extent to which our experimental observations of the B and G1 sites correlate with the results of this study. Future work will extend the current crystal field study to investigate optimising the electric dipole moment.

Immediately available to us are studies of the super-hyperfine effects seen in the G1 and B sites, and further analysis of the spectral diffusion of these sites over longer timescales. Confirming the long-term linewidths from our spectral diffusion measurements in Figure 6.27, or revisiting hole-burning with a narrower linewidth laser excitation could be used for this purpose. Greater magnetic field control, in both direction and amplitude would aid in detailed investigations of the super-hyperfine effects shown in Figure 6.25. An improved understanding of both of these effects will provide a characterisation of the time-scales of the fluorine spin bath.

A clear next experimental step is to continue working on the A site. A new sample, aligned such the $\langle 100 \rangle \perp k$, and $\langle 100 \rangle \| B$ will provide the highest likelihood of seeing an echo. Independent control of the AOMs (< 10 ns rise time) and fast optical switches (limited to $\sim$1 µs rise) in our spectroscopy setup will enable shorter pulses, allowing access to shorter coherence timescales. Even in the continued absence of an echo from the A site, a characterisation of the g tensor of this site will provide valuable insight into field sensitivity.

A third axis magnet, or a well-prepared crystal aligned to the central axis of magnetic field will be used to search for the low magnetic sensitivity direction identified in Figure 6.17. This third axis would also enable a spiral rotation pattern [47] to verify our fitted g tensors for the G1, B, and cubic sites, with particular benefit for sites of lower symmetry. For further detail on any of the following experiment proposals, the reader is referred back to Section 6.6.

8.2.2 Implantation Studies

A young and already fruitful direction for spectroscopic investigations in our lab has been the study of implanted (rather than doped) calcium fluoride samples. The confocal microscope detailed in Chapter 5 will enable a series of new studies of the erbium-calcium fluoride system:

Firstly we wish to validate the implantation parameters of these samples. The simulated implant depth given our parameters was 2 μm, however this has not yet been confirmed. A study of depth-dependent fluorescence in our first sample will provide information on the depth of the erbium and oxygen in our samples, confirming the simulated parameters from our collaborators.

Also related to this is the study to confirm that ultra-pure calcium fluoride is in fact the ‘clean slate’ that we hope for. One of the key reasons we chose calcium fluoride for these studies was that there should be no significant naturally occurring erbium concentration. We have not yet confirmed this, and still have a number of non-implanted ultra pure samples. With the confocal system now reaching relative maturity, we will soon perform this experiment.

Our implantation study however is motivated by one key focus - creating erbium complexes without doping. If it is possible to create G1 sites using solely implantation (and possibly annealing), then precise placement of complexes may be possible. This could be achieved by implanting oxygen into a doped crystal, by co-implanting erbium and oxygen (as we have already), or by implanting and then annealing in an oxygen atmosphere. Our goal is a low dopant density - an important parameter when considering a single ion architecture in a cavity that has a mode volume in excess of 1000 μm^3. Should we find a method of manufacturing oxygen complexes directly in this manner, comparing their properties to thsoe measured in bulk will be important.

8.2.3 Resonator Spectroscopy

The next immediate goal for the lab is the integration of the experimental infrastructure which I have built. This is possible with no further fabrication runs. The coupler devices that have broken are each one of a sizeable on-chip array, so preparing a new waveguide coupler using a new tapered fibre is immediately achievable. The cryogenically compatible nanopositioners and mounts for the system have been fabricated and tested at room temperature.

As discussed, all but two of the current devices are most likely too large to achieve $C > 1$ without considerable processing to achieve Q achievable when polishing by hand ($Q > 5 \times 10^9$ is achievable, but challenging to maintain). However, there is still a lot to be done in these devices. A calcium fluoride whispering-gallery-mode resonator has not been measured at millikelvin temperatures before, much less one that has been doped with erbium.

With our current phase memory times of tens of microseconds, it may be challenging, but we believe possible to achieve lifetime limited T2. If we assume the mode volume estimates in Chapter 7, then for $Q \sim 3 \times 10^9$, our smallest resonators achieve $F_P > 120$, leading to optical lifetimes $< 200\mu s$ for both. This should be enough to achieve single-ion readout, even in the low C regime (≤ 0.2). If coherence times could be enhanced further, only a factor of four would be needed to achieve lifetime limited coherence in the G1. We are at least within the same order of magnitude.

With two engineering cycles of resonator design and prototyping complete, we now know what we want from a future device and how to fabricate them. The next section deals with what we will aim to do with smaller, higher Q resonators.

8.3 Long Term Goals

These are a number of experimental goals that we have made significant progress towards, but are further from our reach than those in the previous section. These are experiments for which we would require new crystals, new resonator fabrication runs, or significant new infrastructure; or ideas that are otherwise less technically mature.

8.3.1 Single Ion Cavity QED

Whispering-gallery mode resonators are a unique and interesting system in which to pursue cavity QED, providing access to parts of the parameter space not yet accessible to nanophotonic devices. However, it is challenging to realise such an architecture.

The Engineering Challenge Future fabrication runs will target smaller resonators - if we were to fabricate a toroid of major radius 90 μm and a 10 μm minor radius, for which polishing to a Q of 6×10^8 would yield $C > 1$, with a Purcell Factor of over 350, a considerable relaxing of the parameters compared with our initial batches of devices. A device of this size would be involved to fabricate. Based on the precedents in the Resonant Optics lab, a resonator of major radius $R \sim 180\mu m$ would be possible to fabricate - requiring a $Q > 6 \times 10^8$ for $C > 1$.

It is clear that coupling into these devices in a cryogenic environment is a significant challenge. Our silicon nitride waveguides are a prototype system, which we will continue to refine and update. Precise simulations in FDTD or FEM solvers will provide insight into future design revisions, and should these not be fit for use, there are other options. Some groups who work with whispering-gallery-mode resonators accept the reduced efficiency that prism coupling setups face, due to the effects of thermal contraction [122, 338]. Others are pursuing waveguide designs similar to ours - though off chip coupling is often lateral. Other approaches to this challenge - including SPARROW waveguides [339] or photonic wirebonds [327, 329, 330] could also be explored.

Experimental Outcomes A long-term direction, beyond addressing and measuring single ions is addressing multiple ions in a single cavity. The narrow cavity linewidth and the opportunities posed by polar sites in CaF_2 create an opportunity for using the Stark shift to tune ions in and out of resonance. With sufficiently high cooperativity, these ions could be coupled together through the resonant mode of the cavity. If they could also be dynamically tuned in and out of resonance with the cavity, this system would have access to a new set of degrees of freedom. A characterisation of the Stark shifts in Er^{3+}:CaF_2 in our system is one of many experimental priorities.

An additional degree of freedom not explored in this thesis is control of the ion's electron spin, which could be achieved in a number of ways: most simply an antenna could be placed proximal to the sample [340], or the device itself could be embedded in a bulk microwave resonator [105]. Spins could be controlled using an optical 'global illumination' beam, distinct from the resonator's coupling channel, driving transitions that are on or off resonance with the mode.

Single ion cavity QED measurements would allow characterisation to know whether some considerably more complex quantum information experiments are feasible in this system. Throw-and catch experiments between two resonators separated by a long fibre - either in the same or distinct cryogenic systems are a long-term goal in our lab. These experiments would lay the groundwork for future tests of fundamental physics, including Bell Tests over long distances [19, 341].

8.3.2 Site Engineering

The study of the dipole moments of the sites in Er^{3+}:CaF_2 in this work is our lab's first step down the path of engineering emitters. Developing our understanding of site dipole moments is motivated both by choosing the best site possible for our single ion work in CaF_2, and to develop models which inform our goal of precisely engineered sites. Once we understand the mechanisms that increase optical dipoles, the next step is to deliberately alter them.

To that end, our spectroscopy efforts have already assisted in the development of more accurate crystal-field models for Er^{3+}:CaF_2 [158, 182]. The next step is to assess whether these models have predictive power well outside of the regime of the data upon which the crystal field parameter fits are based. Beyond this, techniques from computational chemistry may become of use: there has been considerable recent work on *ab initio* calculations for lanthanides, including single molecule magnets [342], chiro-optical properties [343], and predictions of spin dynamics [344]. This provides an early indication that the calculations once deemed too challenging may be nearly within our reach.

It may be possible to deterministically create complexes through a combination of implantation and annealing. Should this be possible, one option would be to select isotopes for implantation. The obvious choice is the well characterised ^{167}Er with nuclear spin 7/2 providing long coherence times [34]. Another option is ^{17}O, which has a nuclear spin 5/2 [166]. Any nuclear spin will have a zero field clock transition, possibly providing another degree of freedom.

This would also provide a route to exploring different perturbations to the crystal field other than that produced by oxygen. Could an implanted, charge compensated complex like the G1 have an even larger perturbation? If so, then implantation with heavier atoms with with 2^- ionisation states may offer a route toward even greater crystal field perturbations. Similar to the directions currently pursued in the silicon donor spin qubit community [271, 272], implantation with sulfur or selenium could create designer sites with controlled perturbations to the crystal field.

In the long term, it is worth saying clearly that calcium fluoride is not necessarily the final host for this work: a designer site could conceivably be fabricated or selected in any material. There are a number of options here, including doped crystals and precision implantation. An exploration of the dipole moments of erbium sites in other materials could be conducted, with lessons from the calcium fluoride system applied to other materials of interest such as $CaWO_4$, YVO_4, and Si. I also note a pair of approaches to precise, shallow implantation in silicon, which could be adapted for designer erbium sites near the surface of many different hosts [345, 346]. This of course comes with the challenges associated with working near the surface.

Finally, one could create designer sites by removing the crystalline host entirely, working in molecules, as has been demonstrated in a number of organo-erbium or other molecules [67, 347].

8.4 Conclusion

Quantum computers are not yet large enough to solve problems of societal utility. Many solid-state qubit systems continue to grow at impressive rates, but could eventually be hindered by the bottlenecks associated with heat, length, and time. Photonic interconnects based on telecom photons in fibre provide a promising path to scaling, due to the low loss in fibre in the near infra-red, and the extremely low thermal conductivity of fibre. The development of such a high-efficiency light-matter interface is a significant challenge, but also a unique opportunity for the field.

Single erbium ions show promise as light-matter interfaces. They have demonstrated exceptional properties in a number of hosts, however we seek to optimise these, by examining the relationship between an ion's site and its quantum properties. Aside from the utility in the development of quantum interconnects, this system also provides a means of understanding the rich physics of the lanthanides. An improved understanding of the mechanisms that give rise to the (weakly) allowed $4f \longleftrightarrow 4f$ optical transitions would be valuable to the field.

For the purposes of our crystal field engineering studies, the choice of erbium-doped calcium fluoride was initially dual purpose: it served as an accessible testbed to precisely evaluate the effects of the crystal field on erbium's optical properties; and it could be a pathway to a cavity QED architecture in an under-explored corner of the parameter space, likely with acceptable coherence and spectral diffusion properties. Over the course of my research, we have characterised Er site properties that greatly inform the next steps for both the site engineering and single ion investigations. Given the promising coherence properties and dipole moments that we have identified, investigating how far this testbed can push beyond its original intended purpose as a prototype is an exciting prospect.

*Free interpretations of this plan are **sincerely solicited**.*

Excerpt from the score of "Tactus Tempus,"
by Frank L McCarty, 1973

Bibliography

[1] Richard P Feynman. “Simulating physics with computers”. en. In: (), p. 22 (cit. on p. 1).

[2] Frank Arute et al. “Quantum supremacy using a programmable superconducting processor”. en. In: *Nature* 574.7779 (Oct. 2019), pp. 505–510. ISSN: 1476-4687. DOI: `10.1038/s41586-019-1666-5` (cit. on p. 1).

[3] Dmitry A. Abanin et al. “Observation of constructive interference at the edge of quantum ergodicity”. en. In: *Nature* 646.8086 (Oct. 2025). Publisher: Nature Publishing Group, pp. 825–830. ISSN: 1476-4687. DOI: `10.1038/s41586-025-09526-6` (cit. on pp. 1, 2).

[4] PsiQuantum team et al. “A manufacturable platform for photonic quantum computing”. en. In: *Nature* 641.8064 (May 2025), pp. 876–883. ISSN: 0028-0836, 1476-4687. DOI: `10.1038/s41586-025-08820-7` (cit. on pp. 1, 2, 15, 16, 18, 65).

[5] Charles H. Bennett and Gilles Brassard. “Quantum cryptography: Public key distribution and coin tossing”. In: *Theoretical Computer Science*. Theoretical Aspects of Quantum Cryptography – celebrating 30 years of BB84 560 (Dec. 2014), pp. 7–11. ISSN: 0304-3975. DOI: `10.1016/j.tcs.2014.05.025` (cit. on pp. 1, 11).

[6] Jonathan P. Dowling and Gerard J. Milburn. “Quantum technology: the second quantum revolution”. In: *Philosophical Transactions of the Royal Society of London. Series A: Mathematical, Physical and Engineering Sciences* 361.1809 (June 2003). Publisher: Royal Society, pp. 1655–1674. DOI: `10.1098/rsta.2003.1227` (cit. on p. 1).

[7] Michael A. Nielsen and Isaac L. Chuang. *Quantum computation and quantum information*. en. 10th anniversary edition. Cambridge: Cambridge university press, 2010. ISBN: 978-1-107-00217-3 (cit. on pp. 2, 8–10).

[8] Deutsch David and Jozsa Richard. “Rapid solution of problems by quantum computation”. In: *Proceedings of the Royal Society of London. Series A: Mathematical and Physical Sciences* 439.1907 (Dec. 1992), pp. 553–558. DOI: `10.1098/rspa.1992.0167` (cit. on p. 2).

[9] H. J. Kimble. “The quantum internet”. en. In: *Nature* 453.7198 (June 2008), pp. 1023–1030. ISSN: 0028-0836, 1476-4687. DOI: `10.1038/nature07127` (cit. on pp. 2, 16, 17, 23, 35, 50).

[10] Professor Michael Bremner, Professor Ping Koy Lam, and Professor Timothy Ralph. "The impact of quantum technologies on secure communications". en. In: (2021), p. 47 (cit. on p. 2).

[11] Peter W. Shor. "Polynomial-Time Algorithms for Prime Factorization and Discrete Logarithms on a Quantum Computer". en. In: *SIAM Journal on Computing* 26.5 (Oct. 1997). arXiv: quant-ph/9508027, pp. 1484–1509. ISSN: 0097-5397, 1095-7111. DOI: `10.1137/S0097539795293172` (cit. on pp. 2, 10).

[12] Lov K. Grover. "A fast quantum mechanical algorithm for database search". en. In: *Proceedings of the twenty-eighth annual ACM symposium on Theory of computing - STOC '96*. Philadelphia, Pennsylvania, United States: ACM Press, 1996, pp. 212–219. ISBN: 978-0-89791-785-8. DOI: `10.1145/237814.237866` (cit. on pp. 2, 10).

[13] Michael E. Beverland et al. *Assessing requirements to scale to practical quantum advantage*. en. arXiv:2211.07629 [quant-ph]. Nov. 2022 (cit. on pp. 2, 11, 18).

[14] Ashley Montanaro. "Quantum algorithms: an overview". en. In: *npj Quantum Information* 2.1 (Jan. 2016). Publisher: Nature Publishing Group, p. 15023. ISSN: 2056-6387. DOI: `10.1038/npjqi.2015.23` (cit. on p. 2).

[15] M. AbuGhanem. "IBM Quantum Computers: Evolution, Performance, and Future Directions". In: *The Journal of Supercomputing* 81.5 (Apr. 2025). arXiv:2410.00916 [quant-ph], p. 687. ISSN: 1573-0484. DOI: `10.1007/s11227-025-07047-7` (cit. on pp. 2, 8, 11).

[16] Stephanie Simmons. *Scalable Fault-Tolerant Quantum Technologies with Silicon Colour Centres*. arXiv:2311.04858 [quant-ph]. Nov. 2023 (cit. on pp. 2, 4).

[17] Photonic Inc et al. *Distributed Quantum Computing in Silicon*. en. arXiv:2406.01704 [quant-ph]. June 2024 (cit. on pp. 2, 3, 8, 18).

[18] *Scaling beyond our roadmap with networked quantum computers | IBM Quantum Computing Blog*. en (cit. on pp. 2, 18).

[19] Simon Storz et al. "Loophole-free Bell inequality violation with superconducting circuits". en. In: *Nature* 617.7960 (May 2023), pp. 265–270. ISSN: 0028-0836, 1476-4687. DOI: `10.1038/s41586-023-05885-0` (cit. on pp. 3, 16, 178).

[20] W. K. Yam et al. "Cryogenic microwave link for quantum local area networks". en. In: *npj Quantum Information* 11.1 (May 2025). Publisher: Nature Publishing Group, p. 87. ISSN: 2056-6387. DOI: `10.1038/s41534-025-01046-5` (cit. on p. 3).

[21] P. Magnard et al. "Microwave Quantum Link between Superconducting Circuits Housed in Spatially Separated Cryogenic Systems". en. In: *Physical Review Letters* 125.26 (Dec. 2020), p. 260502. ISSN: 0031-9007, 1079-7114. DOI: `10.1103/PhysRevLett.125.260502` (cit. on pp. 3, 13).

[22] Arian J. Stolk et al. *Metropolitan-scale heralded entanglement of solid-state qubits*. en. arXiv:2404.03723 [quant-ph]. Apr. 2024 (cit. on pp. 3, 16).

[23] Eric Bersin et al. "Development of a Boston-area 50-km fiber quantum network testbed". en. In: *Physical Review Applied* 21.1 (Jan. 2024), p. 014024. ISSN: 2331-7019. DOI: `10.1103/PhysRevApplied.21.014024` (cit. on pp. 3, 16).

[24] Andrei Ruskuc et al. *Scalable Multipartite Entanglement of Remote Rare-earth Ion Qubits*. en. arXiv:2402.16224 [quant-ph]. Feb. 2024 (cit. on pp. 3, 4, 50, 54, 67, 77).

[25] Fudong Wang et al. "Nuclear Spins in a Solid Exceeding 10-Hour Coherence Times for Ultra-Long-Term Quantum Storage". In: *PRX Quantum* 6.1 (Jan. 2025). Publisher: American Physical Society, p. 010302. DOI: `10.1103/PRXQuantum.6.010302` (cit. on pp. 3, 20, 34).

[26] C.W. Thiel, Thomas Böttger, and R.L. Cone. "Rare-earth-doped materials for applications in quantum information storage and signal processing". en. In: *Journal of Luminescence* 131.3 (Mar. 2011), pp. 353–361. ISSN: 00222313. DOI: `10.1016/j.jlumin.2010.12.015` (cit. on pp. 3, 23, 36, 37, 42).

[27] Bernardo Casabone et al. "Dynamic control of Purcell enhanced emission of erbium ions in nanoparticles". en. In: *Nature Communications* 12.1 (Dec. 2021), p. 3570. ISSN: 2041-1723. DOI: `10.1038/s41467-021-23632-9` (cit. on pp. 3, 71, 154).

[28] James Stuart et al. *Progress towards efficient 4 level photon echo memories*. Sept. 2024. DOI: `10.48550/arXiv.2409.12503` (cit. on pp. 3, 42, 56).

[29] Thierry Chanelière et al. "Opto-RF transduction in Er3+:CaWO4". In: *Journal of Luminescence* 272 (Aug. 2024), p. 120647. ISSN: 0022-2313. DOI: `10.1016/j.jlumin.2024.120647` (cit. on pp. 3, 56).

[30] Chetan Deshmukh et al. *Detection of single ions in a nanoparticle coupled to a fiber cavity*. arXiv:2303.00017 [quant-ph]. Feb. 2023 (cit. on pp. 3, 4, 23, 38, 71, 77).

[31] Mehmet T. Uysal et al. *Spin-photon entanglement of a single Er^{3+} ion in the telecom band*. arXiv:2406.06515 [quant-ph]. June 2024. DOI: `10.48550/arXiv.2406.06515` (cit. on pp. 3–5, 42, 44, 54, 59, 60, 63, 67, 77).

[32] Paul Stevenson et al. "Erbium-Implanted Materials for Quantum Communication Applications". en. In: (), p. 18 (cit. on p. 3).

[33] Morgan P. Hedges et al. "Efficient quantum memory for light". en. In: *Nature* 465.7301 (June 2010), pp. 1052–1056. ISSN: 0028-0836, 1476-4687. DOI: `10.1038/nature09081` (cit. on p. 3).

[34] Miloš Rančić et al. "Coherence time of over a second in a telecom-compatible quantum memory storage material". In: *Nature Physics* 14.1 (Jan. 2018). arXiv:1611.04315 [quant-ph], pp. 50–54. ISSN: 1745-2473, 1745-2481. DOI: `10.1038/nphys4254` (cit. on pp. 3, 17, 23, 34, 40, 84, 179).

[35] Mohammed K. Alqedra et al. *Stark control of solid-state quantum memory with spin-wave storage*. arXiv:2211.17206 [quant-ph]. Nov. 2022 (cit. on p. 3).

[36] Antonio Ortu et al. *Multimode capacity of atomic-frequency comb quantum memories*. Tech. rep. arXiv:2202.12383. arXiv:2202.12383 [quant-ph] type: article. arXiv, Feb. 2022 (cit. on p. 3).

[37] C. M. Knaut et al. "Entanglement of nanophotonic quantum memory nodes in a telecom network". en. In: *Nature* 629.8012 (May 2024). Publisher: Nature Publishing Group, pp. 573–578. ISSN: 1476-4687. DOI: `10.1038/s41586-024-07252-z` (cit. on p. 3).

[38] Ruo-Ran Meng et al. "Solid-state quantum nodes based on color centers and rare-earth ions coupled with fiber Fabry–Pérot microcavities". en. In: *Chip* 3.1 (Mar. 2024), p. 100081. ISSN: 27094723. DOI: `10.1016/j.chip.2023.100081` (cit. on pp. 3, 4).

[39] Dario Lago-Rivera et al. "Telecom-heralded entanglement between multimode solid-state quantum memories". en. In: *Nature* 594.7861 (June 2021). Publisher: Nature Publishing Group, pp. 37–40. ISSN: 1476-4687. DOI: `10.1038/s41586-021-03481-8` (cit. on p. 3).

[40] Joss Bland-Hawthorn, Matt Sellars, and John Bartholomew. "Quantum memories and the double-slit experiment: implications for astronomical interferometry". In: *arXiv:2103.07590 [astro-ph]* (Mar. 2021). arXiv: 2103.07590 (cit. on p. 3).

[41] Tian Xie et al. "Scalable microwave-to-optical transducers at the single-photon level with spins". en. In: *Nature Physics* 21.6 (June 2025). Publisher: Nature Publishing Group, pp. 931–937. ISSN: 1745-2481. DOI: `10.1038/s41567-025-02884-y` (cit. on pp. 3, 67).

[42] Gavin G. G. King et al. "Probing strong coupling between a microwave cavity and a spin ensemble with Raman heterodyne spectroscopy". en. In: *Physical Review B* 103.21 (June 2021), p. 214305. ISSN: 2469-9950, 2469-9969. DOI: `10.1103/PhysRevB.103.214305` (cit. on pp. 3, 42, 56, 80).

[43] Matthew C. Berrington et al. *Negative refractive index in dielectric crystals containing stoichiometric rare-earth ions.* arXiv:2205.02739 [cond-mat, physics:physics]. May 2022 (cit. on pp. 4, 38, 84).

[44] Masaya Hiraishi et al. *Long optical coherence times and coherent rare earth-magnon coupling in a rare earth doped anti-ferromagnet.* arXiv:2411.05182. Nov. 2024 (cit. on pp. 4, 34, 74, 130).

[45] Donny R. Pearson et al. "Narrow Optical Linewidths in Stoichiometric Layered Rare-Earth Crystals". In: *Physical Review Letters* 134.23 (June 2025). Publisher: American Physical Society, p. 233603. DOI: `10.1103/p39m-pnvt` (cit. on p. 4).

[46] Adam Kinos et al. *Roadmap for Rare-earth Quantum Computing.* arXiv:2103.15743 [quant-ph]. Mar. 2021. DOI: `10.48550/arXiv.2103.15743` (cit. on pp. 4, 35).

[47] Jevon Joseph Longdell. "Quantum Information Processing in Rare Earth Ion Doped Insulators". en. In: () (cit. on pp. 4, 176).

[48] John G. Bartholomew, Rose L. Ahlefeldt, and Matthew J. Sellars. "Closing optical transitions for single rare-earth ion spin readout". en. In: *Conference on Lasers and Electro-Optics*. San Jose, California: OSA, 2016, FM4C.4. ISBN: 978-1-943580-11-8. DOI: `10.1364/CLEO_QELS.2016.FM4C.4` (cit. on p. 4).

[49] R. Kolesov et al. “Optical detection of a single rare-earth ion in a crystal”. en. In: *Nature Communications* 3.1 (Aug. 2012). Number: 1 Publisher: Nature Publishing Group, p. 1029. ISSN: 2041-1723. DOI: `10.1038/ncomms2034` (cit. on pp. 4, 25, 57, 58).

[50] A. M. Dibos et al. “Atomic Source of Single Photons in the Telecom Band”. en. In: *Physical Review Letters* 120.24 (June 2018), p. 243601. ISSN: 0031-9007, 1079-7114. DOI: `10.1103/PhysRevLett.120.243601` (cit. on pp. 4, 37, 42, 58–60, 62, 63).

[51] Tian Zhong et al. “Optically Addressing Single Rare-Earth Ions in a Nanophotonic Cavity”. en. In: *Physical Review Letters* 121.18 (Oct. 2018), p. 183603. ISSN: 0031-9007, 1079-7114. DOI: `10.1103/PhysRevLett.121.183603` (cit. on pp. 4, 23, 24, 37, 56, 58, 65, 67, 68, 116).

[52] Jonathan M. Kindem et al. “Control and single-shot readout of an ion embedded in a nanophotonic cavity”. en. In: *Nature* 580.7802 (Apr. 2020), pp. 201–204. ISSN: 0028-0836, 1476-4687. DOI: `10.1038/s41586-020-2160-9` (cit. on pp. 4, 23, 33, 34, 40, 44, 55–57, 66–68).

[53] Mouktik Raha et al. “Optical quantum nondemolition measurement of a single rare earth ion qubit”. en. In: *Nature Communications* 11.1 (Dec. 2020), p. 1605. ISSN: 2041-1723. DOI: `10.1038/s41467-020-15138-7` (cit. on pp. 4, 23, 55, 61–63, 67, 68).

[54] Andrei Ruskuc et al. “Nuclear spin-wave quantum register for a solid-state qubit”. en. In: *Nature* 602.7897 (Feb. 2022), pp. 408–413. ISSN: 0028-0836, 1476-4687. DOI: `10.1038/s41586-021-04293-6` (cit. on pp. 4, 5, 33, 43–45, 67, 68, 142, 146, 148).

[55] Mehmet T. Uysal et al. “Coherent Control of a Nuclear Spin via Interactions with a Rare-Earth Ion in the Solid State”. en. In: *PRX Quantum* 4.1 (Mar. 2023), p. 010323. ISSN: 2691-3399. DOI: `10.1103/PRXQuantum.4.010323` (cit. on pp. 4, 33, 45, 63, 67).

[56] Andreas Gritsch et al. “Optical single-shot readout of spin qubits in silicon”. en. In: *Nature Communications* 16.1 (Jan. 2025), p. 64. ISSN: 2041-1723. DOI: `10.1038/s41467-024-55552-9` (cit. on pp. 4, 70, 71, 77).

[57] Likai Yang et al. “Controlling single rare earth ion emission in an electro-optical nanocavity”. en. In: *Nature Communications* 14.1 (Mar. 2023), p. 1718. ISSN: 2041-1723. DOI: `10.1038/s41467-023-37513-w` (cit. on pp. 4, 33, 54, 58, 77, 149).

[58] A. Wallraff et al. “Strong coupling of a single photon to a superconducting qubit using circuit quantum electrodynamics”. en. In: *Nature* 431.7005 (Sept. 2004), pp. 162–167. ISSN: 0028-0836, 1476-4687. DOI: `10.1038/nature02851` (cit. on pp. 4, 50).

[59] Alexandre Blais et al. “Cavity quantum electrodynamics for superconducting electrical circuits: An architecture for quantum computation”. en. In: *Physical Review A* 69.6 (June 2004). ISSN: 1050-2947, 1094-1622. DOI: `10.1103/PhysRevA.69.062320` (cit. on p. 4).

[60] D. D. Sukachev et al. “Silicon-Vacancy Spin Qubit in Diamond: A Quantum Memory Exceeding 10 ms with Single-Shot State Readout”. en. In: *Physical Review Letters* 119.22 (Nov. 2017), p. 223602. ISSN: 0031-9007, 1079-7114. DOI: `10.1103/PhysRevLett.119.223602` (cit. on p. 4).

[61] Maximilian Ruf et al. “Quantum networks based on color centers in diamond”. In: *Journal of Applied Physics* 130.7 (Aug. 2021). arXiv:2105.04341 [quant-ph], p. 070901. ISSN: 0021-8979, 1089-7550. DOI: `10.1063/5.0056534` (cit. on p. 4).

[62] Wolfgang Tittel et al. *Quantum networks using rare-earth ions*. arXiv:2501.06110 [quant-ph]. Jan. 2025. DOI: `10.48550/arXiv.2501.06110` (cit. on pp. 4, 17).

[63] David D. Awschalom et al. “Quantum technologies with optically interfaced solid-state spins”. en. In: *Nature Photonics* 12.9 (Sept. 2018). Number: 9 Publisher: Nature Publishing Group, pp. 516–527. ISSN: 1749-4893. DOI: `10.1038/s41566-018-0232-2` (cit. on p. 4).

[64] H. J. Kimble. “Strong Interactions of Single Atoms and Photons in CavityQED”. en. In: *Physica Scripta* T76.1 (1998), p. 127. ISSN: 0031-8949. DOI: `10.1238/Physica.Topical.076a00127` (cit. on pp. 4, 51).

[65] John G Bartholomew. “Investigation of the scalability of rare-earth-ion quantum hardware”. en. PhD thesis (cit. on pp. 5, 27, 37, 47, 75, 83, 95, 101, 108).

[66] Frederick J. Gustafson and John C. Wright. “Trace analysis of lanthanides by laser excitation of precipitates”. en. In: *Analytical Chemistry* 51.11 (Sept. 1979), pp. 1762–1774. ISSN: 0003-2700, 1520-6882. DOI: `10.1021/ac50047a039` (cit. on pp. 5, 46, 47).

[67] Leah R. Weiss et al. “A high-resolution molecular spin-photon interface at telecommunication wavelengths”. In: *Science* 390.6768 (Oct. 2025). Publisher: American Association for the Advancement of Science, pp. 76–81. DOI: `10.1126/science.ady8677` (cit. on pp. 5, 180).

[68] Fabian Becker et al. *Spectroscopic Investigations of Multiple Environments in Er:CaWO4 through Charge Imbalance*. arXiv:2412.03948 [cond-mat]. Dec. 2024. DOI: `10.48550/arXiv.2412.03948` (cit. on pp. 5, 38, 39, 43).

[69] Mehmet T. Uysal and Jeff D. Thompson. “Rephasing spectral diffusion in time-bin spin-spin entanglement protocols”. In: *Physical Review A* 110.5 (Nov. 2024). Publisher: American Physical Society, p. 052606. DOI: `10.1103/PhysRevA.110.052606` (cit. on pp. 5, 70).

[70] Koen Alexander et al. *A manufacturable platform for photonic quantum computing*. en. arXiv:2404.17570 [physics, physics:quant-ph]. Apr. 2024 (cit. on p. 8).

[71] Matthias F. Brandl. *A Quantum von Neumann Architecture for Large-Scale Quantum Computing*. en. arXiv:1702.02583 [quant-ph]. Nov. 2017 (cit. on p. 8).

[72] Philipp Schindler et al. “A quantum information processor with trapped ions”. en. In: *New Journal of Physics* 15.12 (Dec. 2013), p. 123012. ISSN: 1367-2630. DOI: `10.1088/1367-2630/15/12/123012` (cit. on p. 8).

[73] J. M. Hornibrook et al. “Cryogenic Control Architecture for Large-Scale Quantum Computing”. en. In: *Physical Review Applied* 3.2 (Feb. 2015). arXiv: 1409.2202. ISSN: 2331-7019. DOI: `10.1103/PhysRevApplied.3.024010` (cit. on p. 8).

[74] Samuel K. Bartee et al. "Spin-qubit control with a milli-kelvin CMOS chip". en. In: *Nature* 643.8071 (July 2025). Publisher: Nature Publishing Group, pp. 382–387. ISSN: 1476-4687. DOI: `10.1038/s41586-025-09157-x` (cit. on pp. 8, 14, 15).

[75] Sebastian Krinner et al. "Engineering cryogenic setups for 100-qubit scale superconducting circuit systems". en. In: *arXiv:1806.07862 [cond-mat, physics:quant-ph]* (June 2018). arXiv: 1806.07862 (cit. on pp. 8, 14, 15, 79, 80).

[76] J. Bardeen and W. H. Brattain. "The Transistor, A Semi-Conductor Triode". en. In: *Physical Review* 74.2 (July 1948), pp. 230–231. ISSN: 0031-899X. DOI: `10.1103/PhysRev.74.230` (cit. on p. 9).

[77] Carver Mead and Lynn Conway. *Introduction to VLSI systems*. eng. Reading, Mass. : Addison-Wesley, 1980. ISBN: 978-0-201-04358-7 (cit. on p. 9).

[78] K.C. Kao and G.A. Hockham. "Dielectric-fibre surface waveguides for optical frequencies". In: *Proceedings of the Institution of Electrical Engineers* 113.7 (July 1966). Publisher: The Institution of Engineering and Technology, pp. 1151–1158. DOI: `10.1049/piee.1966.0189` (cit. on p. 9).

[79] Richard Jozsa. "Entanglement and Quantum Computation". In: *arXiv:quant-ph/9707034* (July 1997). arXiv: quant-ph/9707034 (cit. on p. 9).

[80] Craig Gidney and Martin Ekerå. "How to factor 2048 bit RSA integers in 8 hours using 20 million noisy qubits". In: *Quantum* 5 (Apr. 2021). arXiv: 1905.09749, p. 433. ISSN: 2521-327X. DOI: `10.22331/q-2021-04-15-433` (cit. on p. 11).

[81] Craig Gidney. *How to factor 2048 bit RSA integers with less than a million noisy qubits*. arXiv:2505.15917 [quant-ph]. May 2025. DOI: `10.48550/arXiv.2505.15917` (cit. on p. 11).

[82] Austin G. Fowler et al. "Surface codes: Towards practical large-scale quantum computation". en. In: *Physical Review A* 86.3 (Sept. 2012), p. 032324. ISSN: 1050-2947, 1094-1622. DOI: `10.1103/PhysRevA.86.032324` (cit. on p. 11).

[83] Alexander J. Malcolm et al. *Computing Efficiently in QLDPC Codes*. arXiv:2502.07150 [quant-ph]. Feb. 2025. DOI: `10.48550/arXiv.2502.07150` (cit. on p. 11).

[84] T. Symul, S. M. Assad, and P. K. Lam. "Real time demonstration of high bitrate quantum random number generation with coherent laser light". In: *Applied Physics Letters* 98.23 (June 2011), p. 231103. ISSN: 0003-6951. DOI: `10.1063/1.3597793` (cit. on p. 11).

[85] Murat Muradoglu et al. *Quantum-assured magnetic navigation achieves positioning accuracy better than a strategic-grade INS in airborne and ground-based field trials*. arXiv:2504.08167 [quant-ph]. Apr. 2025. DOI: `10.48550/arXiv.2504.08167` (cit. on p. 11).

[86] David E. J. Waddington et al. "High-sensitivity in vivo contrast for ultra-low field magnetic resonance imaging using superparamagnetic iron oxide nanoparticles". In: *Science Advances* 6.29 (July 2020). Publisher: American Association for the Advancement of Science, eabb0998. DOI: `10.1126/sciadv.abb0998` (cit. on p. 11).

[87] Mohamed I. Ibrahim et al. *High-Scalability CMOS Quantum Magnetometer with Spin-State Excitation and Detection of Diamond Color Centers.* arXiv:2005.05638 [physics]. July 2020. DOI: `10.48550/arXiv.2005.05638` (cit. on p. 11).

[88] F. Couëdo et al. “Sample-based calibration for cryogenic broadband microwave reflectometry measurements”. en. In: *arXiv:1801.00436 [cond-mat]* (Jan. 2018). arXiv: 1801.00436 (cit. on p. 13).

[89] P. Diener et al. “Cryogenic calibration setup for broadband complex impedance measurements”. en. In: Shymkent, Kazakhstan, 2014, pp. 113–118. DOI: `10.1063/1.4893520` (cit. on p. 13).

[90] Jen-Hao Yeh and Steven M. Anlage. “*In situ* broadband cryogenic calibration for two-port superconducting microwave resonators”. en. In: *Review of Scientific Instruments* 84.3 (Mar. 2013), p. 034706. ISSN: 0034-6748, 1089-7623. DOI: `10.1063/1.4797461` (cit. on p. 13).

[91] S. Hähnle et al. “Suppression of radiation loss in high kinetic inductance superconducting co-planar waveguides”. In: *Applied Physics Letters* 116.18 (May 2020), p. 182601. ISSN: 0003-6951. DOI: `10.1063/5.0005047` (cit. on p. 13).

[92] C. Schollhorn et al. “Attenuation mechanisms of aluminum millimeter-wave coplanar waveguides on silicon”. In: *IEEE Transactions on Electron Devices* 50.3 (Mar. 2003), pp. 740–746. ISSN: 1557-9646. DOI: `10.1109/TED.2003.810466` (cit. on p. 13).

[93] S. J. Pauka et al. “A cryogenic CMOS chip for generating control signals for multiple qubits”. en. In: *Nature Electronics* 4.1 (Jan. 2021), pp. 64–70. ISSN: 2520-1131. DOI: `10.1038/s41928-020-00528-y` (cit. on pp. 14, 15).

[94] H. Al-Taie et al. “Cryogenic on-chip multiplexer for the study of quantum transport in 256 split-gate devices”. en. In: *Applied Physics Letters* 102.24 (June 2013), p. 243102. ISSN: 0003-6951, 1077-3118. DOI: `10.1063/1.4811376` (cit. on p. 14).

[95] D.P. Franke et al. “Rent’s rule and extensibility in quantum computing”. en. In: *Microprocessors and Microsystems* 67 (June 2019), pp. 1–7. ISSN: 01419331. DOI: `10.1016/j.micpro.2019.02.006` (cit. on p. 14).

[96] Fernando Alcalde Cuesta, Pablo González Sequeiros, and Álvaro Lozano Rojo. “A method for validating Rent’s rule for technological and biological networks”. en. In: *Scientific Reports* 7.1 (July 2017). Publisher: Nature Publishing Group, p. 5378. ISSN: 2045-2322. DOI: `10.1038/s41598-017-05670-w` (cit. on p. 14).

[97] Francesco Borsoi et al. “Shared control of a 16 semiconductor quantum dot crossbar array”. en. In: *Nature Nanotechnology* 19.1 (Jan. 2024). Publisher: Nature Publishing Group, pp. 21–27. ISSN: 1748-3395. DOI: `10.1038/s41565-023-01491-3` (cit. on p. 14).

[98] R. W. Andrews et al. “Bidirectional and efficient conversion between microwave and optical light”. In: *Nature Physics* 10.4 (Mar. 2014), pp. 321–326. ISSN: 1745-2473, 1745-2481. DOI: `10.1038/nphys2911` (cit. on p. 14).

[99] Jonathan R. Everts et al. “Microwave to optical photon conversion via fully concentrated rare-earth-ion crystals”. en. In: *Physical Review A* 99.6 (June 2019), p. 063830. ISSN: 2469-9926, 2469-9934. DOI: `10.1103/PhysRevA.99.063830` (cit. on p. 14).

[100] Mohammad Mirhosseini et al. “Superconducting qubit to optical photon transduction”. en. In: *Nature* 588.7839 (Dec. 2020), pp. 599–603. ISSN: 0028-0836, 1476-4687. DOI: `10.1038/s41586-020-3038-6` (cit. on p. 14).

[101] John G. Bartholomew et al. “On-chip coherent microwave-to-optical transduction mediated by ytterbium in YVO4”. en. In: *Nature Communications* 11.1 (June 2020). Publisher: Nature Publishing Group, p. 3266. ISSN: 2041-1723. DOI: `10.1038/s41467-020-16996-x` (cit. on pp. 14, 67).

[102] T. C. van Thiel et al. *Optical readout of a superconducting qubit using a scalable piezo-optomechanical transducer.* arXiv:2310.06026 [quant-ph]. Nov. 2023 (cit. on pp. 14, 16).

[103] Alfredo Rueda et al. “Efficient microwave to optical photon conversion: an electro-optical realization”. en. In: *Optica* 3.6 (June 2016), p. 597. ISSN: 2334-2536. DOI: `10.1364/OPTICA.3.000597` (cit. on pp. 14, 154).

[104] Linran Fan et al. “Superconducting cavity electro-optics: A platform for coherent photon conversion between superconducting and photonic circuits”. In: *Science Advances* 4.8 (Aug. 2018). Publisher: American Association for the Advancement of Science, eaar4994. DOI: `10.1126/sciadv.aar4994` (cit. on p. 14).

[105] Xavier Fernandez Gonzalvo. “Coherent Frequency Conversion from Microwave to Optical Fields in an Erbium Doped Y2SiO5 Crystal: Towards the Single Photon Regime”. en. In: () (cit. on pp. 14, 178).

[106] Nicholas J. Lambert et al. “Coherent conversion between microwave and optical photons – an overview of physical implementations”. In: *Advanced Quantum Technologies* 3.1 (Jan. 2020). arXiv:1906.10255 [physics, physics:quant-ph], p. 1900077. ISSN: 2511-9044, 2511-9044. DOI: `10.1002/qute.201900077` (cit. on p. 14).

[107] F. Lecocq et al. “Control and readout of a superconducting qubit using a photonic link”. en. In: *Nature* 591.7851 (Mar. 2021), pp. 575–579. ISSN: 0028-0836, 1476-4687. DOI: `10.1038/s41586-021-03268-x` (cit. on pp. 14, 15).

[108] I. D. Conway Lamb and D. J. Reilly. “Cryogenic Control Beyond 100 QuBits”. en. PhD thesis. University of Sydney, July 2017 (cit. on pp. 15, 79).

[109] Timothy Geoffrey Meadows Newman. “Hardware and Methods for Scaling Up Quantum Information Experiments”. en. In: (), p. 128 (cit. on p. 15).

[110] Amir Youssefi et al. “A cryogenic electro-optic interconnect for superconducting devices”. en. In: *Nature Electronics* 4.5 (May 2021), pp. 326–332. ISSN: 2520-1131. DOI: `10.1038/s41928-021-00570-4` (cit. on p. 15).

[111] J. Van Damme et al. “Advanced CMOS manufacturing of superconducting qubits on 300 mm wafers”. en. In: *Nature* 634.8032 (Oct. 2024). Publisher: Nature Publishing

Group, pp. 74–79. ISSN: 1476-4687. DOI: `10.1038/s41586-024-07941-9` (cit. on p. 15).

[112] Paul Steinacker et al. "Industry-compatible silicon spin-qubit unit cells exceeding 99% fidelity". en. In: *Nature* 646.8083 (Oct. 2025). Publisher: Nature Publishing Group, pp. 81–87. ISSN: 1476-4687. DOI: `10.1038/s41586-025-09531-9` (cit. on p. 15).

[113] Olivia Seidel et al. *CryoPDK Development for 22nm FDSOI CryoCMOS*. English. Tech. rep. FERMILAB-SLIDES-24-0010-ETD. Fermi National Accelerator Laboratory (FNAL), Batavia, IL (United States), Aug. 2024. DOI: `10.2172/2426440` (cit. on p. 15).

[114] Stephan Rinner et al. "Erbium emitters in commercially fabricated nanophotonic silicon waveguides". In: *Nanophotonics* 12.17 (Aug. 2023). arXiv:2307.14017 [physics, physics:quant-ph], pp. 3455–3462. ISSN: 2192-8614. DOI: `10.1515/nanoph-2023-0287` (cit. on pp. 15, 58, 70, 71, 75, 119).

[115] Ryota Katsumi et al. "Recent progress in hybrid diamond photonics for quantum information processing and sensing". en. In: *Communications Engineering* 4.1 (May 2025). Publisher: Nature Publishing Group, p. 85. ISSN: 2731-3395. DOI: `10.1038/s44172-025-00398-2` (cit. on pp. 15, 65).

[116] Ivan S. Grudinin et al. "Ultra high Q crystalline microcavities". en. In: *Optics Communications* 265.1 (Sept. 2006), pp. 33–38. ISSN: 00304018. DOI: `10.1016/j.optcom.2006.03.028` (cit. on pp. 16, 152, 156, 157).

[117] Songtao Chen et al. "Parallel single-shot measurement and coherent control of solid-state spins below the diffraction limit". In: *Science* 370.6516 (Oct. 2020). arXiv: 2006.01823, pp. 592–595. ISSN: 0036-8075, 1095-9203. DOI: `10.1126/science.abc7821` (cit. on pp. 16, 61, 69, 154).

[118] Srivatsa Chakravarthi et al. "Hybrid Integration of GaP Photonic Crystal Cavities with Silicon-Vacancy Centers in Diamond by Stamp-Transfer". en. In: *Nano Letters* 23.9 (May 2023), pp. 3708–3715. ISSN: 1530-6984, 1530-6992. DOI: `10.1021/acs.nanolett.2c04890` (cit. on pp. 16, 61).

[119] *HARQ: Heterogeneous Architectures for Quantum | DARPA* (cit. on p. 16).

[120] Marcelo Davanco et al. "Heterogeneous integration for on-chip quantum photonic circuits with single quantum dot devices". en. In: *Nature Communications* 8.1 (Oct. 2017). Publisher: Nature Publishing Group, p. 889. ISSN: 2041-1723. DOI: `10.1038/s41467-017-00987-6` (cit. on p. 16).

[121] Hana K. Warner et al. "Coherent control of a superconducting qubit using light". en. In: *Nature Physics* 21.5 (May 2025). Publisher: Nature Publishing Group, pp. 831–838. ISSN: 1745-2481. DOI: `10.1038/s41567-025-02812-0` (cit. on p. 16).

[122] Georg Arnold et al. "All-optical superconducting qubit readout". en. In: *Nature Physics* (Feb. 2025). ISSN: 1745-2473, 1745-2481. DOI: `10.1038/s41567-024-02741-4` (cit. on pp. 16, 154, 178).

[123] Jake Rochman et al. “Microwave-to-optical transduction with erbium ions coupled to planar photonic and superconducting resonators”. en. In: *Nature Communications* 14.1 (Mar. 2023), p. 1153. ISSN: 2041-1723. DOI: `10.1038/s41467-023-36799-0` (cit. on pp. 16, 64).

[124] Tian Xie et al. “Characterization of Er 3 + : YV O 4 for microwave to optical transduction”. en. In: *Physical Review B* 104.5 (Aug. 2021), p. 054111. ISSN: 2469-9950, 2469-9969. DOI: `10.1103/PhysRevB.104.054111` (cit. on pp. 16, 27, 29, 33, 39, 65, 124).

[125] Jordan M. Thomas et al. “Quantum teleportation coexisting with classical communications in optical fiber”. en. In: *Optica* 11.12 (Dec. 2024), p. 1700. ISSN: 2334-2536. DOI: `10.1364/OPTICA.540362` (cit. on p. 16).

[126] Jian-Long Liu et al. “Creation of memory–memory entanglement in a metropolitan quantum network”. en. In: *Nature* 629.8012 (May 2024). Publisher: Nature Publishing Group, pp. 579–585. ISSN: 1476-4687. DOI: `10.1038/s41586-024-07308-0` (cit. on p. 16).

[127] Sebastian Krinner et al. “Realizing Repeated Quantum Error Correction in a Distance-Three Surface Code”. In: *Nature* 605.7911 (May 2022). arXiv:2112.03708 [cond-mat, physics:quant-ph], pp. 669–674. ISSN: 0028-0836, 1476-4687. DOI: `10.1038/s41586-022-04566-8` (cit. on p. 16).

[128] H.-J. Briegel et al. “Quantum Repeaters: The Role of Imperfect Local Operations in Quantum Communication”. In: *Physical Review Letters* 81.26 (Dec. 1998). Publisher: American Physical Society, pp. 5932–5935. DOI: `10.1103/PhysRevLett.81.5932` (cit. on p. 17).

[129] Nicolas Sangouard et al. “Quantum repeaters based on atomic ensembles and linear optics”. In: *Reviews of Modern Physics* 83.1 (Mar. 2011). Publisher: American Physical Society, pp. 33–80. DOI: `10.1103/RevModPhys.83.33` (cit. on p. 17).

[130] V. Krutyanskiy et al. “Telecom-Wavelength Quantum Repeater Node Based on a Trapped-Ion Processor”. In: *Physical Review Letters* 130.21 (May 2023). Publisher: American Physical Society, p. 213601. DOI: `10.1103/PhysRevLett.130.213601` (cit. on p. 17).

[131] Paul Stevenson et al. “Erbium-Implanted Materials for Quantum Communication Applications”. In: *Physical Review B* 105.22 (June 2022). arXiv:2110.04876 [cond-mat, physics:quant-ph], p. 224106. ISSN: 2469-9950, 2469-9969. DOI: `10.1103/PhysRevB.105.224106` (cit. on pp. 17, 63).

[132] Andrei Ruskuc. “Single Rare-Earth Ions in Solid-State Hosts: A Platform for Quantum Networks”. en. In: () (cit. on pp. 17, 67).

[133] D. Main et al. “Distributed quantum computing across an optical network link”. en. In: *Nature* 638.8050 (Feb. 2025). Publisher: Nature Publishing Group, pp. 383–388. ISSN: 1476-4687. DOI: `10.1038/s41586-024-08404-x` (cit. on p. 18).

[134] Lawrence Z. Cohen et al. "Low-overhead fault-tolerant quantum computing using long-range connectivity". In: *Science Advances* 8.20 (May 2022). Publisher: American Association for the Advancement of Science, eabn1717. DOI: `10.1126/sciadv.abn1717` (cit. on p. 18).

[135] Jared F. Bauters et al. "Ultra-low-loss high-aspect-ratio Si_3N_4 waveguides". EN. In: *Optics Express* 19.4 (Feb. 2011). Publisher: Optica Publishing Group, pp. 3163–3174. ISSN: 1094-4087. DOI: `10.1364/OE.19.003163` (cit. on p. 19).

[136] J. H. Van. Vleck. "The Puzzle of Rare-earth Spectra in Solids." en. In: *The Journal of Physical Chemistry* 41.1 (Jan. 1937), pp. 67–80. ISSN: 0092-7325, 1541-5740. DOI: `10.1021/j150379a006` (cit. on pp. 20, 24, 26).

[137] Salim Ourari et al. "Indistinguishable telecom band photons from a single Er ion in the solid state". en. In: *Nature* 620.7976 (Aug. 2023). Number: 7976 Publisher: Nature Publishing Group, pp. 977–981. ISSN: 1476-4687. DOI: `10.1038/s41586-023-06281-4` (cit. on pp. 23, 40, 43, 59, 61–63, 67, 68, 76).

[138] Mikael Afzelius et al. "Multimode quantum memory based on atomic frequency combs". en. In: *Physical Review A* 79.5 (May 2009), p. 052329. ISSN: 1050-2947, 1094-1622. DOI: `10.1103/PhysRevA.79.052329` (cit. on pp. 23, 56).

[139] Thomas Böttger. "Laser Frequency Stabilization To Spectral Hole Burning Frequency References in Erbium-Doped Crystals: Material and Device Optimization". en. In: () (cit. on pp. 23, 38, 95).

[140] Sarah E. Beavan, Elizabeth A. Goldschmidt, and Matthew J. Sellars. "Demonstration of a dynamic bandpass frequency filter in a rare-earth ion-doped crystal". EN. In: *JOSA B* 30.5 (May 2013). Publisher: Optica Publishing Group, pp. 1173–1177. ISSN: 1520-8540. DOI: `10.1364/JOSAB.30.001173` (cit. on p. 23).

[141] O. Guillot-Noel et al. "Correlation between rare-earth oscillator strengths and rare-earth–valence-band interactions in neodymium-doped Y M O 4 (M = V , P, As), Y 3 Al 5 O 12 , and LiYF 4 matrices". en. In: *Physical Review B* 60.3 (July 1999), pp. 1668–1677. ISSN: 0163-1829, 1095-3795. DOI: `10.1103/PhysRevB.60.1668` (cit. on pp. 23, 27, 47).

[142] Thomas Böttger et al. "Effects of magnetic field orientation on optical decoherence in Er 3 + : Y 2 SiO 5". en. In: *Physical Review B* 79.11 (Mar. 2009), p. 115104. ISSN: 1098-0121, 1550-235X. DOI: `10.1103/PhysRevB.79.115104` (cit. on pp. 23, 42, 106, 136, 140, 147).

[143] Guokui Liu and Bernard Jacquier, eds. *Spectroscopic properties of rare earths in optical materials: with tables.* en. Springer series in materials science 83. Beijing: Tsinghua Univ. Press, 2005. ISBN: 978-3-540-23886-7 978-7-302-07409-0 (cit. on pp. 23, 24, 27, 29–31, 35, 38, 39, 93).

[144] Marianne Le Dantec et al. "Twenty-three millisecond electron spin coherence of erbium ions in a natural-abundance crystal". In: *arXiv:2106.14974 [cond-mat, physics:quant-ph]* (June 2021). arXiv: 2106.14974 (cit. on p. 24).

[145] C. W. Thiel, W. R. Babbitt, and R. L. Cone. "Optical decoherence studies of yttrium oxyorthosilicate Y 2 SiO 5 codoped with Er 3 + and Eu 3 + for optical signal processing and quantum information applications at 1.5 microns". en. In: *Physical Review B* 85.17 (May 2012), p. 174302. ISSN: 1098-0121, 1550-235X. DOI: `10.1103/PhysRevB.85.174302` (cit. on pp. 24, 26, 98).

[146] Serge Haroche. "A short history of Cavity Quantum Electrodynamics". EN. In: *Conference on Coherence and Quantum Optics (2007), paper CTuF2*. Optica Publishing Group, June 2007. DOI: `10.1364/CQO.2007.CTuF2` (cit. on p. 24).

[147] D. W. Vernooy et al. "Cavity QED with high- Q whispering gallery modes". en. In: *Physical Review A* 57.4 (Apr. 1998), R2293–R2296. ISSN: 1050-2947, 1094-1622. DOI: `10.1103/PhysRevA.57.R2293` (cit. on pp. 24, 152, 154).

[148] D. L. McAuslan, J. J. Longdell, and M. J. Sellars. "Strong-coupling cavity QED using rare-earth-metal-ion dopants in monolithic resonators: What you can do with a weak oscillator". en. In: *Physical Review A* 80.6 (Dec. 2009), p. 062307. ISSN: 1050-2947, 1094-1622. DOI: `10.1103/PhysRevA.80.062307` (cit. on pp. 24, 50, 75, 149).

[149] Brian G. Wybourne. *Spectroscopic Properties of Rare Earths*. en. Google-Books-ID: zifKnQEACAAJ. Interscience Publishers, 1965. ISBN: 978-0-470-96507-8 (cit. on pp. 25, 29).

[150] R. D. Shannon and C. T. Prewitt. "Effective ionic radii in oxides and fluorides". en. In: *Acta Crystallographica Section B: Structural Crystallography and Crystal Chemistry* 25.5 (May 1969). Publisher: International Union of Crystallography, pp. 925–946. ISSN: 0567-7408. DOI: `10.1107/S0567740869003220` (cit. on pp. 25, 26).

[151] O. Greis and M. S. R. Cader. "Polymorphism of high-purity rare earth trifluorides". In: *Thermochimica Acta* 87 (May 1985), pp. 145–150. ISSN: 0040-6031. DOI: `10.1016/0040-6031(85)85329-6` (cit. on p. 26).

[152] Philippe Goldner, Alban Ferrier, and Olivier Guillot-Noël. "Chapter 267 - Rare Earth-Doped Crystals for Quantum Information Processing". en. In: *Handbook on the Physics and Chemistry of Rare Earths*. Ed. by Jean-Claude G. Bünzli and Vitalij K. Pecharsky. Vol. 46. Elsevier, Jan. 2015, pp. 1–78. DOI: `10.1016/B978-0-444-63260-9.00267-4` (cit. on p. 25).

[153] Ian R. Berkman et al. "Observing Er 3 + Sites in Si With an *In Situ* Single-Photon Detector". en. In: *Physical Review Applied* 19.1 (Jan. 2023), p. 014037. ISSN: 2331-7019. DOI: `10.1103/PhysRevApplied.19.014037` (cit. on pp. 26, 70, 71, 89, 92).

[154] Robert Withnall and Jack Silver. "Physics of Light Emission from Rare Earth-Doped Phosphors". en. In: *Handbook of Visual Display Technology*. Springer, Cham, 2016, pp. 1567–1576. ISBN: 978-3-319-14346-0. DOI: `10.1007/978-3-319-14346-0_68` (cit. on p. 28).

[155] Jonathan M. Kindem et al. "Characterization of Yb 3 + 171 : YVO 4 for photonic quantum technologies". en. In: *Physical Review B* 98.2 (July 2018), p. 024404. ISSN: 2469-9950, 2469-9969. DOI: `10.1103/PhysRevB.98.024404` (cit. on p. 27).

[156] Nigel J Cockroft. “Solid state spectroscopy : laser selective excitation of erbium ions in crystalline solids”. en. In: () (cit. on pp. 29, 38, 42, 43, 45–47, 108, 124, 140, 148).

[157] Michael D Moull. “Revisiting the G1 Site in Er3+:CaF2”. en. In: (), p. 30 (cit. on pp. 29, 38, 42, 43, 45, 93, 107–111, 117, 123, 133, 148).

[158] M. D. Moull et al. “Spectroscopy, crystal-field, and transition intensity analyses of the C3v O2- centre in Er3+ doped CaF2 crystals”. In: *Optical Materials: X* 24 (Dec. 2024), p. 100365. ISSN: 2590-1478. DOI: `10.1016/j.omx.2024.100365` (cit. on pp. 29, 43, 93, 114, 123, 133, 149, 179).

[159] J. J. Longdell, M. J. Sellars, and N. B. Manson. “Hyperfine interaction in ground and excited states of praseodymium-doped yttrium orthosilicate”. en. In: *Physical Review B* 66.3 (June 2002), p. 035101. ISSN: 0163-1829, 1095-3795. DOI: `10.1103/PhysRevB.66.035101` (cit. on pp. 30, 33).

[160] Sebastian P. Horvath et al. “Extending Phenomenological Crystal-Field Methods to C_1 Point-Group Symmetry: Characterization of the Optically-Excited Hyperfine Structure of ^{167}Er^{3+}:Y$_2$SiO$_5$”. en. In: *Physical Review Letters* 123.5 (July 2019). arXiv: 1809.01058, p. 057401. ISSN: 0031-9007, 1079-7114. DOI: `10.1103/PhysRevLett.123.057401` (cit. on pp. 30, 33, 40, 42, 75).

[161] James S. Stuart et al. “Initialization protocol for efficient quantum memories using resolved hyperfine structure”. en. In: *Physical Review Research* 3.3 (Aug. 2021), p. L032054. ISSN: 2643-1564. DOI: `10.1103/PhysRevResearch.3.L032054` (cit. on p. 30).

[162] Jelena Velibor Rakonjac. “Hyperfine Structure and Coherent Properties of Erbium-167-doped Yttrium Orthosilicate”. en. In: (), p. 122 (cit. on p. 30).

[163] Olivier Guillot-Noël, Philippe Goldner, and Yann Le Du. “Analysis of hyperfine structure of Rare-Earth Ions in Single Crystals by Electron Paramagnetic Resonance Spectroscopy”. en. In: *Spectroscopy Letters* 40.2 (Mar. 2007), pp. 247–257. ISSN: 0038-7010, 1532-2289. DOI: `10.1080/00387010701247365` (cit. on p. 30).

[164] Kieran M. Smith et al. “Complete crystal-field calculation of Zeeman hyperfine splittings in europium”. en. In: *Physical Review B* 105.12 (Mar. 2022), p. 125141. ISSN: 2469-9950, 2469-9969. DOI: `10.1103/PhysRevB.105.125141` (cit. on pp. 30, 33).

[165] J. J. Longdell M. J. Sellars. “Selecting ensembles for rare earth quantum computation”. In: *arXiv:quant-ph/0310105* (Oct. 2003). arXiv: quant-ph/0310105 (cit. on p. 30).

[166] N.J. Stone. “Table of nuclear magnetic dipole and electric quadrupole moments”. en. In: *Atomic Data and Nuclear Data Tables* 90.1 (May 2005), pp. 75–176. ISSN: 0092640X. DOI: `10.1016/j.adt.2005.04.001` (cit. on pp. 31, 179).

[167] Yong Yu et al. “Frequency Tunable, Cavity-Enhanced Single Erbium Quantum Emitter in the Telecom Band”. en. In: *Physical Review Letters* 131.17 (Oct. 2023), p. 170801. ISSN: 0031-9007, 1079-7114. DOI: `10.1103/PhysRevLett.131.170801` (cit. on pp. 33, 54, 72, 75, 77).

[168] John G. Bartholomew et al. "Controlling rare-earth ions in a nanophotonic resonator using the ac Stark shift". en. In: *Physical Review A* 97.6 (June 2018), p. 063854. ISSN: 2469-9926, 2469-9934. DOI: `10.1103/PhysRevA.97.063854` (cit. on pp. 33, 67).

[169] Priyash Barya et al. "Ultra High-Q tunable microring resonators by slow light". EN. In: *CLEO 2025 (2025), paper SS191_3*. Optica Publishing Group, May 2025, SS191_3. DOI: `10.1364/CLEO_SI.2025.SS191_3` (cit. on pp. 33, 58).

[170] Likai Yang et al. "Photonic integration of Er $^{3+}$:Y $_{2}$ SiO $_{5}$ with thin-film lithium niobate by flip chip bonding". en. In: *Optics Express* 29.10 (May 2021), p. 15497. ISSN: 1094-4087. DOI: `10.1364/OE.423659` (cit. on pp. 33, 42, 72).

[171] R. Wannemacher et al. "Nuclear spin-flip sidebands in optical spectral holeburning and fluorescence line narrowing of the Er3+ ion". In: *Journal of Luminescence* 48-49 (Jan. 1991), pp. 309–312. ISSN: 0022-2313. DOI: `10.1016/0022-2313(91)90129-J` (cit. on pp. 33, 38, 74, 94).

[172] R. L. Ahlefeldt et al. "Quantum processing with ensembles of rare-earth ions in a stoichiometric crystal". en. In: *Physical Review A* 101.1 (Jan. 2020), p. 012309. ISSN: 2469-9926, 2469-9934. DOI: `10.1103/PhysRevA.101.012309` (cit. on pp. 33, 38).

[173] Adrian Holzäpfel et al. "Characterization of the Spin and Crystal Field Hamiltonian of Erbium Dopants in Silicon". en. In: *Advanced Quantum Technologies* 8.7 (2025). _eprint: https://advanced.onlinelibrary.wiley.com/doi/pdf/10.1002/qute.202400342, p. 2400342. ISSN: 2511-9044. DOI: `10.1002/qute.202400342` (cit. on pp. 33, 71).

[174] Rose Ahlefeldt. "Evaluation of a stoichiometric rare earth crystal for quantum computing". en. In: (), p. 233 (cit. on p. 33).

[175] Ian R. Berkman et al. *Millisecond electron spin coherence time for erbium ions in silicon*. arXiv:2307.10021 [quant-ph]. July 2023 (cit. on pp. 34, 70).

[176] Manjin Zhong et al. "Optically addressable nuclear spins in a solid with a six-hour coherence time". en. In: *Nature* 517.7533 (Jan. 2015), pp. 177–180. ISSN: 0028-0836, 1476-4687. DOI: `10.1038/nature14025` (cit. on pp. 34, 100, 130, 146).

[177] Pengcheng Fan et al. "Detection of single 13C spins coupled to NV center via dynamical decoupling design". en. In: *Journal of Physics D: Applied Physics* 55.1 (Oct. 2021). Publisher: IOP Publishing, p. 015301. ISSN: 0022-3727. DOI: `10.1088/1361-6463/ac27d6` (cit. on p. 34).

[178] Adrian Holzäpfel et al. "Optical storage for 0.53 s in a solid-state atomic frequency comb memory using dynamical decoupling". en. In: *New Journal of Physics* 22.6 (June 2020), p. 063009. ISSN: 1367-2630. DOI: `10.1088/1367-2630/ab8aac` (cit. on p. 34).

[179] Zhiren Wang et al. "Week-long-lifetime microwave spectral holes in an erbium-doped scheelite crystal at millikelvin temperature". en. In: *Nature Communications* 16.1 (Oct. 2025). Publisher: Nature Publishing Group, p. 9032. ISSN: 2041-1723. DOI: `10.1038/s41467-025-64087-6` (cit. on pp. 34, 69, 94, 95).

[180] Flurin Könz et al. "Temperature and concentration dependence of optical dephasing, spectral-hole lifetime, and anisotropic absorption in Eu 3 + : Y 2 SiO 5". en. In:

Physical Review B 68.8 (Aug. 2003), p. 085109. ISSN: 0163-1829, 1095-3795. DOI: `10.1103/PhysRevB.68.085109` (cit. on pp. 34, 120).

[181] Christoph Becher et al. “2022 Roadmap for Materials for Quantum Technologies”. en. In: (), p. 38 (cit. on p. 35).

[182] Alice Jeffery. “INVESTIGATING ERBIUM IN CALCIUM FLUORIDE FOR QUANTUM INFORMATION”. Honours Thesis, 2024 (cit. on pp. 36, 80, 85, 94–96, 103, 106, 111, 113, 114, 121, 123, 125, 127, 179).

[183] A. M. Stoneham. “Shapes of Inhomogeneously Broadened Resonance Lines in Solids”. en. In: *Reviews of Modern Physics* 41.1 (Jan. 1969), pp. 82–108. ISSN: 0034-6861. DOI: `10.1103/RevModPhys.41.82` (cit. on pp. 37, 38).

[184] Adam Kinos et al. “Microscopic treatment of instantaneous spectral diffusion and its effect on quantum gate fidelities in rare-earth-ion-doped crystals”. In: *Physical Review A* 105.3 (Mar. 2022). Publisher: American Physical Society, p. 032608. DOI: `10.1103/PhysRevA.105.032608` (cit. on p. 37).

[185] Austin M. Ferrenti et al. “Identifying candidate hosts for quantum defects via data mining”. en. In: *npj Computational Materials* 6.1 (Aug. 2020). Number: 1 Publisher: Nature Publishing Group, pp. 1–6. ISSN: 2057-3960. DOI: `10.1038/s41524-020-00391-7` (cit. on pp. 38, 44, 59, 63).

[186] B. Car, J.-L. Le Gouët, and T. Chanelière. “Superhyperfine induced photon-echo collapse of erbium in Y$_2$SiO$_5$”. In: *Physical Review B* 102.11 (Sept. 2020). arXiv:2006.04602 [quant-ph], p. 115119. ISSN: 2469-9950, 2469-9969. DOI: `10.1103/PhysRevB.102.115119` (cit. on pp. 38, 137, 142).

[187] R. M. MacFarlane, C. S. Yannoni, and R. M. Shelby. “Optical line narrowing by nuclear spin decoupling in Pr3+: LaF3”. en. In: *Optics Communications* 32.1 (Jan. 1980), pp. 101–104. ISSN: 0030-4018. DOI: `10.1016/0030-4018(80)90323-5` (cit. on pp. 38, 44, 74).

[188] U. Ranon and W. Low. “Electron Spin Resonance of Er 3 + in Ca F 2”. en. In: *Physical Review* 132.4 (Nov. 1963), pp. 1609–1611. ISSN: 0031-899X. DOI: `10.1103/PhysRev.132.1609` (cit. on pp. 38, 43, 45–47, 108, 123, 126).

[189] John G. Bartholomew et al. “High-resolution spectroscopic techniques for studying rare-earth ions in nanoparticles”. In: *Journal of Luminescence* 257 (May 2023), p. 119743. ISSN: 0022-2313. DOI: `10.1016/j.jlumin.2023.119743` (cit. on p. 38).

[190] Robert C. Hilborn. “Einstein coefficients, cross sections, f values, dipole moments, and all that”. en. In: *American Journal of Physics* 50.11 (Nov. 1982), pp. 982–986. ISSN: 0002-9505, 1943-2909. DOI: `10.1119/1.12937` (cit. on pp. 38, 39, 57, 93).

[191] B Henderson and G F Imbusch. “Radiative transition rates and selection rules”. In: *Optical Spectroscopy of Inorganic Solids*. Ed. by B Henderson and G F Imbusch. Oxford University Press, May 2006, p. 0. ISBN: 978-0-19-929862-4. DOI: `10.1093/oso/9780199298624.003.0004` (cit. on pp. 38, 39).

[192] Mouktik Raha. “A Telecom-Compatible Quantum Memory in the Solid-State: Single Erbium Ions Coupled to Silicon Nanophotonic Circuits”. en. In: () (cit. on p. 40).

[193] Yong Yu et al. “Entanglement of two quantum memories via fibers over dozens of kilometres”. In: *Nature* 578.7794 (Feb. 2020). arXiv: 1903.11284, pp. 240–245. ISSN: 0028-0836, 1476-4687. DOI: `10.1038/s41586-020-1976-7` (cit. on p. 40).

[194] S P Horvath. “High-resolution spectroscopy and novel crystal-field methods for rare-earth based quantum information processing”. en. In: (), p. 191 (cit. on pp. 40, 42, 109).

[195] Daniel S Norman et al. “Measuring optical loss in yttrium orthosilicate using a whispering gallery mode resonator”. en. In: *Materials for Quantum Technology* 2.1 (Mar. 2022), p. 011001. ISSN: 2633-4356. DOI: `10.1088/2633-4356/ac4c39` (cit. on p. 42).

[196] Mark Hogg. “Investigation of Monolithic Erbium-Doped Resonators for Application in Cavity Quantum Electrodynamics”. en. In: () (cit. on pp. 42, 73).

[197] Alexander Ulanowski et al. *Spectral Multiplexing of Rare-earth Emitters in a Co-doped Crystalline Membrane.* arXiv:2311.16875 [quant-ph]. Nov. 2023 (cit. on pp. 42, 72).

[198] Zhiren Wang et al. *Single electron-spin-resonance detection by microwave photon counting.* arXiv:2301.02653 [cond-mat, physics:quant-ph]. Jan. 2023 (cit. on pp. 43, 44, 69).

[199] U. Ranon. “Paramagnetic resonance of Nd3+, Dy3+, Er3+ and Yb3+ in YVO4”. en. In: *Physics Letters A* 28.3 (Nov. 1968), pp. 228–229. ISSN: 03759601. DOI: `10.1016/0375-9601(68)90218-1` (cit. on pp. 43, 46, 47, 123).

[200] M. L. Falin et al. “EPR and optical spectroscopy of Yb3+ ions in CaF2: an analysis of the structure of tetragonal centers”. en. In: *Applied Magnetic Resonance* 26.4 (Dec. 2004), pp. 617–632. ISSN: 0937-9347, 1613-7507. DOI: `10.1007/BF03166587` (cit. on p. 43).

[201] D. S. Moore and J. C. Wright. “Laser spectroscopy of defect chemistry in CaF2:Er3+”. In: *The Journal of Chemical Physics* 74.3 (Feb. 1981). Publisher: American Institute of Physics, pp. 1626–1636. ISSN: 0021-9606. DOI: `10.1063/1.441303` (cit. on pp. 43, 45).

[202] Ann Judith Silversmith. “Silversmith - PhD Thesis”. en. In: (), p. 197 (cit. on pp. 43, 46, 112).

[203] J.S. Dryden and H.K. Welsh. “Dielectric relaxation in hydrogenated erbium doped calcium fluoride.” en. In: *Journal of Molecular Liquids* 56 (July 1993), pp. 245–258. ISSN: 01677322. DOI: `10.1016/0167-7322(93)80031-P` (cit. on p. 43).

[204] Ji Wang Yan et al. “Ductile Regime Machining of Single-Crystal CaF_2 for Aspherical Lenses”. en. In: *Key Engineering Materials* 257-258 (Feb. 2004), pp. 95–100. ISSN: 1662-9795. DOI: `10.4028/www.scientific.net/KEM.257-258.95` (cit. on pp. 43, 156, 158).

[205] Jiwang Yan et al. "Single-point diamond turning of CaF2 for nanometric surface". en. In: *The International Journal of Advanced Manufacturing Technology* 24.9-10 (Nov. 2004), pp. 640–646. ISSN: 0268-3768, 1433-3015. DOI: `10.1007/s00170-003-1747-2` (cit. on pp. 43, 156).

[206] Ivan S Grudinin. "CRYSTALLINE WHISPERING GALLERY MODE RESONATORS FOR QUANTUM AND NONLINEAR OPTICS". en. In: () (cit. on pp. 43, 74, 145, 170).

[207] Anatoliy A. Savchenkov et al. "Optical resonators with ten million finesse". en. In: *Optics Express* 15.11 (2007), p. 6768. ISSN: 1094-4087. DOI: `10.1364/OE.15.006768` (cit. on pp. 43, 74, 145, 152, 156, 157).

[208] Vladimir S. Ilchenko et al. "Microtorus: a high-finesse microcavity with whispering-gallery modes". en. In: *Optics Letters* 26.5 (Mar. 2001), p. 256. ISSN: 0146-9592, 1539-4794. DOI: `10.1364/OL.26.000256` (cit. on pp. 43, 154, 155).

[209] T. Césaire et al. "Charge Compensation of Er3+ Ions in Ca1—xErxF2+x Thin Films at Low Rare-Earth Substitution Rates". en. In: *physica status solidi (a)* 168.2 (Aug. 1998), pp. 373–380. ISSN: 00318965, 1521396X. DOI: `10.1002/(SICI)1521-396X(199808)168:2<373::AID-PSSA373>3.0.CO;2-F` (cit. on pp. 43, 47).

[210] L. Pasquali et al. "Calcium fluoride on Si(001): Adsorption mechanisms and epitaxial growth modes". In: *Physical Review B* 72.4 (July 2005). Publisher: American Physical Society, p. 045448. DOI: `10.1103/PhysRevB.72.045448` (cit. on p. 43).

[211] S. Raoux et al. "High Concentration Erbium Implantation of Epitaxially Grown Caf $_2$ /Si Structures." en. In: *MRS Proceedings* 392 (1995), p. 247. ISSN: 0272-9172, 1946-4274. DOI: `10.1557/PROC-392-247` (cit. on pp. 43, 44).

[212] Tianyi Guo et al. "Observation of ultraslow stress release in silicon nitride films on CaF2". In: *Journal of Vacuum Science & Technology A* 33.4 (June 2015), p. 041515. ISSN: 0734-2101. DOI: `10.1116/1.4923029` (cit. on p. 43).

[213] Tobias Jan August Kippenberg. "Nonlinear Optics in Ultra-high-Q Whispering-Gallery Optical Microcavities". en. In: () (cit. on pp. 44, 155).

[214] Andrea Morello et al. "Donor Spins in Silicon for Quantum Technologies". en. In: *Advanced Quantum Technologies* 3.11 (2020), p. 2000005. ISSN: 2511-9044. DOI: `10.1002/qute.202000005` (cit. on pp. 44, 71, 75, 119).

[215] David R. Tallant, Marvin P. Miller, and John C. Wright. "Energy transfer and relaxation phenomena in CaF2:Er3+". In: *The Journal of Chemical Physics* 65.2 (July 1976). Publisher: American Institute of Physics, pp. 510–521. ISSN: 0021-9606. DOI: `10.1063/1.433130` (cit. on p. 45).

[216] Eric Faulques et al. "Synthesis, Fabrication, and Photoluminescence of CaF2 Doped with Rare Earth Ions". en. In: *Journal of Fluorescence* 8.4 (Dec. 1998), pp. 283–287. ISSN: 1573-4994. DOI: `10.1023/A:1020556028008` (cit. on p. 45).

[217] M. V. Johnston and J. C. Wright. "Defect processes involving oxygen-compensated sites in calcium fluoride precipitates doped with lanthanides and actinides". en. In:

The Journal of Physical Chemistry 85.21 (Oct. 1981), pp. 3064–3072. ISSN: 0022-3654, 1541-5740. DOI: `10.1021/j150621a011` (cit. on p. 45).

[218] C A Freeth, G D Jones, and R W G Syme. “The transverse Zeeman effect in calcium fluoride crystals containing erbium”. en. In: *Journal of Physics C: Solid State Physics* 15.27 (Sept. 1982), pp. 5667–5690. ISSN: 0022-3719. DOI: `10.1088/0022-3719/15/27/023` (cit. on pp. 45, 47, 126, 158).

[219] Frederick J. Gustafson and John C. Wright. “Ultra-trace method for lanthanide ion determination by selective laser excitation”. en. In: *Analytical Chemistry* 49.12 (Oct. 1977), pp. 1680–1689. ISSN: 0003-2700, 1520-6882. DOI: `10.1021/ac50020a017` (cit. on p. 45).

[220] Julie Nelson. “Laser and infrared spectroscopy of Nd3+ and Pr3+ ions in fluorite crystals”. en. PhD thesis (cit. on pp. 45, 109).

[221] R. W. Bierig, M. J. Weber, and S. I. Warshaw. “Paramagnetic Resonance and Relaxation of Trivalent Rare-Earth Ions in Calcium Fluoride. II. Spin-Lattice Relaxation”. en. In: *Physical Review* 134.6A (June 1964), A1504–A1516. ISSN: 0031-899X. DOI: `10.1103/PhysRev.134.A1504` (cit. on pp. 45, 94).

[222] A. Kaplyanskii. “NONCUBIC CENTERS IN CUBIC CRYSTALS AND THEIR SPECTRA IN EXTERNAL FIELDS”. In: *Journal de Physique Colloques* 28.C4 (1967), pp. C4–39–C4–48. DOI: `10.1051/jphyscol:1967406` (cit. on p. 45).

[223] Irina Nicoara et al. “Some dielectric and optical properties of ErF3-doped CaF2 crystals”. en. In: *Journal of Crystal Growth* 310.7-9 (Apr. 2008), pp. 2020–2025. ISSN: 00220248. DOI: `10.1016/j.jcrysgro.2007.11.023` (cit. on p. 47).

[224] E. M. Purcell. “Spontaneous Emission Probabilities at Radio Frequencies”. In: *Confined Electrons and Photons: New Physics and Applications*. Ed. by Elias Burstein and Claude Weisbuch. Boston, MA: Springer US, 1995, pp. 839–839. ISBN: 978-1-4615-1963-8. DOI: `10.1007/978-1-4615-1963-8_40` (cit. on p. 49).

[225] Daniel Burgarth et al. “Taming the Rotating Wave Approximation”. en-GB. In: *Quantum* 8 (Feb. 2024). Publisher: Verein zur Förderung des Open Access Publizierens in den Quantenwissenschaften, p. 1262. DOI: `10.22331/q-2024-02-21-1262` (cit. on p. 50).

[226] Hiroki Takahashi et al. “Strong Coupling of a Single Ion to an Optical Cavity”. In: *Physical Review Letters* 124.1 (Jan. 2020). Publisher: American Physical Society, p. 013602. DOI: `10.1103/PhysRevLett.124.013602` (cit. on p. 50).

[227] Niclas S. Mueller et al. “Deep strong light–matter coupling in plasmonic nanoparticle crystals”. en. In: *Nature* 583.7818 (July 2020). Publisher: Nature Publishing Group, pp. 780–784. ISSN: 1476-4687. DOI: `10.1038/s41586-020-2508-1` (cit. on p. 50).

[228] Jon Kindem. “Quantum nanophotonics with ytterbium in yttrium orthovanadate”. en. In: () (cit. on pp. 51, 116).

[229] R E Evans et al. “Photon-mediated interactions between quantum emitters in a diamond nanocavity”. en. In: (2018), p. 5 (cit. on p. 51).

[230] Andreas Reiserer and Gerhard Rempe. "Cavity-based quantum networks with single atoms and optical photons". en. In: *Reviews of Modern Physics* 87.4 (Dec. 2015), pp. 1379–1418. ISSN: 0034-6861, 1539-0756. DOI: `10.1103/RevModPhys.87.1379` (cit. on p. 51).

[231] L.-M. Duan. "Scalable Photonic Quantum Computation through Cavity-Assisted Interactions". In: *Physical Review Letters* 92.12 (2004). DOI: `10.1103/PhysRevLett.92.127902` (cit. on p. 51).

[232] Daniel Riedel et al. "Deterministic Enhancement of Coherent Photon Generation from a Nitrogen-Vacancy Center in Ultrapure Diamond". In: *Physical Review X* 7.3 (Sept. 2017). Publisher: American Physical Society, p. 031040. DOI: `10.1103/PhysRevX.7.031040` (cit. on p. 52).

[233] Kangwei Xia et al. "High-Speed Tunable Microcavities Coupled to Rare-Earth Quantum Emitters". In: *arXiv:2104.00389 [cond-mat, physics:physics, physics:quant-ph]* (Apr. 2021). arXiv: 2104.00389 (cit. on pp. 54, 61, 75).

[234] Likai Yang, Jiacheng Xie, and Hong X. Tang. "Fluorescence enabled phonon counting in an erbium-doped piezo-optomechanical microcavity". en. In: *Nanophotonics* (Jan. 2025). Publisher: De Gruyter. ISSN: 2192-8614. DOI: `10.1515/nanoph-2024-0400` (cit. on p. 58).

[235] Tian Zhong et al. "High quality factor nanophotonic resonators in bulk rare-earth doped crystals". en. In: *Optics Express* 24.1 (Jan. 2016), p. 536. ISSN: 1094-4087. DOI: `10.1364/OE.24.000536` (cit. on pp. 61, 64–66, 68, 154).

[236] Alex Abulnaga et al. "Design and fabrication of robust hybrid photonic crystal cavities". en. In: *Nanophotonics* 14.11 (June 2025). Publisher: De Gruyter, pp. 1927–1937. ISSN: 2192-8614. DOI: `10.1515/nanoph-2024-0500` (cit. on p. 61).

[237] Sebastian P. Horvath et al. *Strong Purcell enhancement of an optical magnetic dipole transition.* arXiv:2307.03022 [physics, physics:quant-ph]. July 2023 (cit. on pp. 61, 63, 68, 117).

[238] A M Dibos et al. "Supplementary Information for". en. In: () (cit. on p. 61).

[239] Alan M. Dibos. *Personal Communication.* 2025 (cit. on p. 61).

[240] Christopher M. Phenicie et al. "Narrow Optical Line Widths in Erbium Implanted in TiO2". In: *Nano Letters* 19.12 (Dec. 2019). Publisher: American Chemical Society, pp. 8928–8933. ISSN: 1530-6984. DOI: `10.1021/acs.nanolett.9b03831` (cit. on p. 63).

[241] Igal Bayn et al. "Ultra-high-Q triangular cross-section nanobeam photonic cavities in single crystal diamond". EN. In: *CLEO:2011 - Laser Applications to Photonic Applications (2011), paper CThZ7.* Optica Publishing Group, May 2011, CThZ7. DOI: `10.1364/CLEO_SI.2011.CThZ7` (cit. on p. 64).

[242] A. Sipahigil et al. "An integrated diamond nanophotonics platform for quantum-optical networks". en. In: *Science* 354.6314 (Nov. 2016), pp. 847–850. ISSN: 0036-8075, 1095-9203. DOI: `10.1126/science.aah6875` (cit. on p. 64).

[243] Sihao Wang et al. *SmartCut Er:LiNbO3 with high optical coherence enabling optical thickness control.* arXiv:2206.12645 [physics, physics:quant-ph]. June 2022 (cit. on p. 65).

[244] Tian Zhong et al. "Nanophotonic rare-earth quantum memory with optically controlled retrieval". en. In: *Science* 357.6358 (Sept. 2017). Publisher: American Association for the Advancement of Science Section: Report, pp. 1392–1395. ISSN: 0036-8075, 1095-9203. DOI: `10.1126/science.aan5959` (cit. on p. 67).

[245] Ioana Craiciu et al. "Nanophotonic Quantum Storage at Telecommunication Wavelength". en. In: *Physical Review Applied* 12.2 (Aug. 2019), p. 024062. ISSN: 2331-7019. DOI: `10.1103/PhysRevApplied.12.024062` (cit. on p. 67).

[246] Evan Miyazono et al. "Coupling erbium dopants in yttrium orthosilicate to silicon photonic resonators and waveguides". en. In: *Optics Express* 25.3 (Feb. 2017), p. 2863. ISSN: 1094-4087. DOI: `10.1364/OE.25.002863` (cit. on p. 67).

[247] Ioana Craiciu et al. "Multifunctional on-chip storage at telecommunication wavelength for quantum networks". In: *arXiv:2008.10795 [quant-ph]* (Aug. 2020). arXiv: 2008.10795 (cit. on p. 67).

[248] Chun-Ju Wu et al. *A hybrid quantum photonic interface for ^{171}Yb solid-state qubits.* arXiv:2212.01994 [physics, physics:quant-ph]. Dec. 2022. DOI: `10.48550/arXiv.2212.01994` (cit. on p. 68).

[249] Raphaël Lescanne et al. "Detecting itinerant microwave photons with engineered nonlinear dissipation". In: *Physical Review X* 10.2 (May 2020). arXiv:1902.05102 [cond-mat, physics:quant-ph], p. 021038. ISSN: 2160-3308. DOI: `10.1103/PhysRevX.10.021038` (cit. on p. 70).

[250] A. S. Dzurak. "Spin-based quantum computing in silicon CMOS-compatible platforms". In: *2016 IEEE International Electron Devices Meeting (IEDM).* Dec. 2016, pp. 13.2.1–13.2.2. DOI: `10.1109/IEDM.2016.7838407` (cit. on p. 71).

[251] D. Holmes et al. "Isotopic enrichment of silicon by high fluence 28-Si ion implantation". In: *Physical Review Materials* 5.1 (Jan. 2021). Publisher: American Physical Society, p. 014601. DOI: `10.1103/PhysRevMaterials.5.014601` (cit. on p. 71).

[252] Shao Qi Lim et al. "Silicon spin vacuum: Isotopically enriched $^{28}\mathrm{silicon-on-insulator}$ and $^{28}\mathrm{silicon}$ from ultrahigh fluence ion implantation". In: *Physical Review Materials* 9.7 (July 2025). Publisher: American Physical Society, p. 076202. DOI: `10.1103/787r-9jps` (cit. on p. 71).

[253] Ian R. Berkman et al. *Sub-megahertz homogeneous linewidth for Er in Si via in situ single photon detection.* arXiv:2108.07090 [cond-mat, physics:physics, physics:quant-ph]. Aug. 2021 (cit. on p. 71).

[254] Ian R. Berkman et al. "Long optical and electron spin coherence times for erbium ions in silicon". en. In: *npj Quantum Information* 11.1 (Apr. 2025), p. 66. ISSN: 2056-6387. DOI: `10.1038/s41534-025-01008-x` (cit. on pp. 71, 119).

[255] Alexey Lyasota et al. *Narrow magneto-optical transitions in Erbium implanted silicon carbide-on-insulator*. arXiv:2511.00400 [cond-mat]. Nov. 2025. DOI: `10.48550/arXiv.2511.00400` (cit. on p. 71).

[256] Samarth Vadia et al. "Open-Cavity in Closed-Cycle Cryostat as a Quantum Optics Platform". en. In: *PRX Quantum* 2.4 (Oct. 2021), p. 040318. ISSN: 2691-3399. DOI: `10.1103/PRXQuantum.2.040318` (cit. on p. 71).

[257] Bernardo Casabone et al. "Cavity-enhanced spectroscopy of a few-ion ensemble in Eu3+:Y2O3". en. In: *New Journal of Physics* 20.9 (Sept. 2018). Publisher: IOP Publishing, p. 095006. ISSN: 1367-2630. DOI: `10.1088/1367-2630/aadf68` (cit. on p. 72).

[258] Alexander Ulanowski et al. "Nuclear Spins in the Proximity of Individual Erbium Dopants". en. In: *Optica Quantum 2.0 Conference and Exhibition*. Denver, Colorado: Optica Publishing Group, 2023, QTh4B.3. ISBN: 978-1-957171-27-2. DOI: `10.1364/QUANTUM.2023.QTh4B.3` (cit. on p. 72).

[259] Eduardo Beattie Eizaguirre and Hugues De Riedmatten. "Single rare earth ions for quantum computing nodes". en. PhD thesis. Universitat Politècnica de Catalunya, Mar. 2025. DOI: `10.5821/dissertation-2117-430004` (cit. on pp. 72, 77).

[260] Shobhit Gupta et al. *Erbium Quantum Memory Platform with Long Optical Coherence via Back-End of Line Deposition on Foundry-Fabricated Photonics*. arXiv:2506.17557 [quant-ph]. June 2025. DOI: `10.48550/arXiv.2506.17557` (cit. on p. 72).

[261] Shobhit Gupta et al. *Dual epitaxial telecom spin-photon interfaces with correlated long-lived coherence*. arXiv:2310.07120 [quant-ph]. Oct. 2023 (cit. on p. 72).

[262] Rikuto Fukumori et al. "Subkilohertz optical homogeneous linewidth and dephasing mechanisms in Er 3 + : Y 2 O 3 ceramics". en. In: *Physical Review B* 101.21 (June 2020), p. 214202. ISSN: 2469-9950, 2469-9969. DOI: `10.1103/PhysRevB.101.214202` (cit. on p. 72).

[263] Manish Kumar Singh et al. "Epitaxial Er-doped Y $_2$ O $_3$ on silicon for quantum coherent devices". en. In: *APL Materials* 8.3 (Mar. 2020), p. 031111. ISSN: 2166-532X. DOI: `10.1063/1.5142611` (cit. on p. 72).

[264] Takehiko Tawara and Tomohiro Inaba. "Magnetically Purified Erbium-doped Oxide Crystal–Towards Creating a Quantum-information-manipulation Platform". en. In: *NTT Technical Review* 17.10 (Oct. 2019), pp. 12–17. ISSN: 2436-5327. DOI: `10.53829/ntr201910fa3` (cit. on p. 72).

[265] Neil Sinclair et al. "Spectral Multiplexing for Scalable Quantum Photonics using an Atomic Frequency Comb Quantum Memory and Feed-Forward Control". In: *Physical Review Letters* 113.5 (July 2014). Publisher: American Physical Society, p. 053603. DOI: `10.1103/PhysRevLett.113.053603` (cit. on p. 72).

[266] Xueying Zhang et al. "Telecom-band–integrated multimode photonic quantum memory". In: *Science Advances* 9.28 (July 2023). Publisher: American Association for the Advancement of Science, eadf4587. DOI: `10.1126/sciadv.adf4587` (cit. on p. 73).

[267] David Lee McAuslan. “Quantum Computing Hardware based on Rare-Earth-Ion Doped Whispering-Gallery Mode Resonators”. en. In: () (cit. on pp. 73, 174).

[268] B. D’Anjou and Guido Burkard. “Optimal dispersive readout of a spin qubit with a microwave resonator”. In: *Physical Review B* 100.24 (Dec. 2019). Publisher: American Physical Society, p. 245427. DOI: `10.1103/PhysRevB.100.245427` (cit. on p. 73).

[269] N. L. Jobbitt et al. “Prediction of optical polarization and high-field hyperfine structure via a parametrized crystal-field model for low-symmetry centers in Er 3 + -doped Y 2 SiO 5”. en. In: *Physical Review B* 104.15 (Oct. 2021), p. 155121. ISSN: 2469-9950, 2469-9969. DOI: `10.1103/PhysRevB.104.155121` (cit. on p. 75).

[270] Haitong Xu et al. *Coherent control of interacting solid-state spins below the diffraction limit.* arXiv:2508.09122 [quant-ph]. Aug. 2025. DOI: `10.48550/arXiv.2508.09122` (cit. on p. 76).

[271] Irene Fernández de Fuentes et al. “Navigating the 16-dimensional Hilbert space of a high-spin donor qudit with electric and magnetic fields”. en. In: *Nature Communications* 15.1 (Feb. 2024). Number: 1 Publisher: Nature Publishing Group, p. 1380. ISSN: 2041-1723. DOI: `10.1038/s41467-024-45368-y` (cit. on pp. 76, 179).

[272] Xi Yu et al. “Schrödinger cat states of a nuclear spin qudit in silicon”. en. In: *Nature Physics* 21.3 (Mar. 2025), pp. 362–367. ISSN: 1745-2473, 1745-2481. DOI: `10.1038/s41567-024-02745-0` (cit. on pp. 76, 179).

[273] Frank Pobell. *Matter and methods at low temperatures.* en. 3rd, rev. and expanded ed. Berlin ; New York: Springer, 2007. ISBN: 978-3-540-46356-6 (cit. on p. 79).

[274] Olli V. Lounasmaa. *Experimental principles and methods below 1K.* en. 1974. ISBN: 978-0-12-455950-9 (cit. on p. 79).

[275] Edoardo Charbon et al. “15.5 Cryo-CMOS circuits and systems for scalable quantum computing”. In: *Solid-State Circuits Conference (ISSCC), 2017 IEEE International.* IEEE, 2017, pp. 264–265 (cit. on p. 79).

[276] Attocube GmbH. *ANPx101/RES/LT - linear x-nanopositioner :: www.attocube.com* (cit. on p. 83).

[277] American Magnetics Inc. *Magnet Power Supply Systems* (cit. on p. 84).

[278] Toptica Photonics SE. *CTL.* en-US (cit. on pp. 84, 114).

[279] HighFinesse. *HighFinesse / Wavemeter* (cit. on p. 85).

[280] Boston Applied Technologies Inc. *BATi, Fast Optical Switch* (cit. on p. 86).

[281] Brimrose Corp. *Fiber-coupled Acousto-Optic Modulators.* en-US (cit. on p. 87).

[282] Fergus Ayton. “Towards Hybrid Photon Interfaces in Rare-Earth Atomic Ensembles”. en. In: () (cit. on p. 87).

[283] Agiltron. *High Speed 1x2 Fiber Optical Dual-Stage Switch: 100ns, 30dB On/Off - Agiltron Inc.* (Cit. on p. 88).

[284] Newport Photonics. *1 GHz Fiber-Optic Receiver* (cit. on p. 88).

[285] G. N. Gol'tsman et al. "Picosecond superconducting single-photon optical detector". In: *Applied Physics Letters* 79.6 (Aug. 2001), pp. 705–707. ISSN: 0003-6951. DOI: `10.1063/1.1388868` (cit. on p. 89).

[286] Chandra M Natarajan, Michael G Tanner, and Robert H Hadfield. "Superconducting nanowire single-photon detectors: physics and applications". en. In: *Superconductor Science and Technology* 25.6 (June 2012), p. 063001. ISSN: 0953-2048, 1361-6668. DOI: `10.1088/0953-2048/25/6/063001` (cit. on p. 89).

[287] I. D. Conway Lamb et al. "An FPGA-based instrumentation platform for use at deep cryogenic temperatures". en. In: *Review of Scientific Instruments* 87.1 (Jan. 2016), p. 014701. ISSN: 0034-6748, 1089-7623. DOI: `10.1063/1.4939094` (cit. on p. 90).

[288] Hans Kuzmany. *Solid-State Spectroscopy.* en. Berlin, Heidelberg: Springer Berlin Heidelberg, 2009. ISBN: 978-3-642-01478-9 978-3-642-01479-6. DOI: `10.1007/978-3-642-01479-6` (cit. on p. 93).

[289] C. Wei et al. "Raman heterodyne detected magnetic resonance: I. CW and coherent transient measurements". en. In: *Applied Magnetic Resonance* 11.3-4 (Nov. 1996), pp. 521–538. ISSN: 0937-9347, 1613-7507. DOI: `10.1007/BF03162247` (cit. on p. 94).

[290] R.M Macfarlane et al. "Spectral hole burning and optical dephasing in disordered crystals – Pr3+:LiNbO3 and Pr3+:Sr.6Ba.4Nb2O6 (SBN)". en. In: *Journal of Luminescence* 86.3-4 (Apr. 2000), pp. 311–315. ISSN: 00222313. DOI: `10.1016/S0022-2313(00)00191-5` (cit. on pp. 94, 95).

[291] Charles W. Thiel, Rufus L. Cone, and Thomas Böttger. "Laser linewidth narrowing using transient spectral hole burning". en. In: *Journal of Luminescence* 152 (Aug. 2014), pp. 84–87. ISSN: 00222313. DOI: `10.1016/j.jlumin.2013.11.038` (cit. on p. 95).

[292] Anton Mladenov et al. *Microwave cavity-free hole burning spectroscopy of Er:YSO at millikelvin temperatures.* arXiv:2206.03135 [physics, physics:quant-ph]. June 2022 (cit. on p. 95).

[293] I. D. Abella, N. A. Kurnit, and S. R. Hartmann. "Photon Echoes". In: *Physical Review* 141.1 (Jan. 1966). Publisher: American Physical Society, pp. 391–406. DOI: `10.1103/PhysRev.141.391` (cit. on p. 98).

[294] R.M. Macfarlane et al. "Nonexponential photon echo decay of Er3+ in fluorides". en. In: *Journal of Luminescence* 48-49 (Jan. 1991), pp. 313–317. ISSN: 00222313. DOI: `10.1016/0022-2313(91)90130-N` (cit. on pp. 99, 137, 141, 173).

[295] W. B. Mims. "Phase Memory in Electron Spin Echoes, Lattice Relaxation Effects in CaW O 4 : Er, Ce, Mn". en. In: *Physical Review* 168.2 (Apr. 1968), pp. 370–389. ISSN: 0031-899X. DOI: `10.1103/PhysRev.168.370` (cit. on pp. 99, 137, 146).

[296] Joseph Ganem et al. "Nonexponential photon-echo decays of paramagnetic ions in the superhyperfine limit". en. In: *Physical Review Letters* 66.6 (Feb. 1991), pp. 695–698. ISSN: 0031-9007. DOI: `10.1103/PhysRevLett.66.695` (cit. on pp. 100, 137, 173).

[297] Thomas Böttger et al. “Optical decoherence and spectral diffusion at 1.5 u m in Er 3 + : Y 2 SiO 5 versus magnetic field, temperature, and Er 3 + concentration”. en. In: *Physical Review B* 73.7 (Feb. 2006), p. 075101. ISSN: 1098-0121, 1550-235X. DOI: `10.1103/PhysRevB.73.075101` (cit. on pp. 101, 143, 144).

[298] N Kukharchyk et al. “Optical coherence of 166Er:7LiYF4 crystal below 1 K”. en. In: *New Journal of Physics* 20.2 (Feb. 2018). Publisher: IOP Publishing, p. 023044. ISSN: 1367-2630. DOI: `10.1088/1367-2630/aaa7e4` (cit. on pp. 108, 124, 173).

[299] *A Temperature Study of the EPR Spectra of CaF2:ER3+*. en. Tech. rep. Section: Technical Reports (cit. on p. 123).

[300] J.A. Capobianco et al. “Optical spectroscopy, fluorescence dynamics and crystal-field analysis of Er3+ in YVO4”. en. In: *Chemical Physics* 214.2-3 (Jan. 1997), pp. 329–340. ISSN: 03010104. DOI: `10.1016/S0301-0104(96)00318-7` (cit. on p. 124).

[301] E. Fraval, M. J. Sellars, and J. J. Longdell. “Method of Extending Hyperfine Coherence Times in P r 3 + : Y 2 S i O 5”. en. In: *Physical Review Letters* 92.7 (Feb. 2004), p. 077601. ISSN: 0031-9007, 1079-7114. DOI: `10.1103/PhysRevLett.92.077601` (cit. on p. 130).

[302] Annalise Lennon. “Identification of Resonantly Coupled Ion Pairs in Eu3+:Y2SiO5”. en. In: () (cit. on p. 134).

[303] Peter Millington-Hotze et al. “Approaching a fully-polarized state of nuclear spins in a solid”. en. In: *Nature Communications* 15.1 (Feb. 2024). Publisher: Nature Publishing Group, p. 985. ISSN: 2041-1723. DOI: `10.1038/s41467-024-45364-2` (cit. on p. 147).

[304] Luke Shaun Trainor. “Optical Parametric Frequency Generation in Whispering-Gallery Resonators”. en. In: () (cit. on pp. 152, 157, 159, 164).

[305] Florian Sedlmeir. “Crystalline whispering gallery mode resonators”. de. In: () (cit. on p. 152).

[306] S. M. Spillane et al. “Ultrahigh- Q toroidal microresonators for cavity quantum electrodynamics”. en. In: *Physical Review A* 71.1 (Jan. 2005), p. 013817. ISSN: 1050-2947, 1094-1622. DOI: `10.1103/PhysRevA.71.013817` (cit. on pp. 154, 155).

[307] D. K. Armani et al. “Ultra-high-Q toroid microcavity on a chip”. en. In: *Nature* 421.6926 (Feb. 2003), pp. 925–928. ISSN: 0028-0836, 1476-4687. DOI: `10.1038/nature01371` (cit. on pp. 154, 155).

[308] M. L. Gorodetsky and V. S. Ilchenko. “Optical microsphere resonators: optimal coupling to high-Q whispering-gallery modes”. en. In: *Journal of the Optical Society of America B* 16.1 (Jan. 1999), p. 147. ISSN: 0740-3224, 1520-8540. DOI: `10.1364/JOSAB.16.000147` (cit. on pp. 154, 155, 163).

[309] Gabriella Gardosi et al. “Discovery of parabolic SNAP microresonators produced in fibre tapering”. en. In: *Micro-Structured and Specialty Optical Fibres V*. Ed. by Christian-Alexander Bunge, Kyriacos Kalli, and Alexis Mendez. Strasbourg, France: SPIE, May 2018, p. 10. ISBN: 978-1-5106-1888-6 978-1-5106-1889-3. DOI: `10.1117/12.2307373` (cit. on p. 154).

[310] Florian Sedlmeir et al. “High-Q MgF_2 whispering gallery mode resonators for refractometric sensing in aqueous environment”. en. In: *Optics Express* 22.25 (Dec. 2014), p. 30934. ISSN: 1094-4087. DOI: `10.1364/OE.22.030934` (cit. on p. 154).

[311] M. C. Collodo et al. “Sub-kHz lasing of a CaF_2 whispering gallery mode resonator stabilized fiber ring laser”. en. In: *Optics Express* 22.16 (Aug. 2014), p. 19277. ISSN: 1094-4087. DOI: `10.1364/OE.22.019277` (cit. on p. 154).

[312] Changqing Wang and Silvia Zorzetti. *High-fidelity quantum transduction with long coherence time superconducting resonators*. en. arXiv:2204.13112 [quant-ph]. May 2022 (cit. on p. 154).

[313] Quanshen Shen et al. *Investigation of Rare-Earth Ion-Photon Interaction and Strong Coupling in Optical Microcavities*. en. Apr. 2025 (cit. on p. 154).

[314] V.B. Braginsky, M.L. Gorodetsky, and V.S. Ilchenko. “Quality-factor and nonlinear properties of optical whispering-gallery modes”. en. In: *Physics Letters A* 137.7-8 (May 1989), pp. 393–397. ISSN: 03759601. DOI: `10.1016/0375-9601(89)90912-2` (cit. on pp. 154, 155, 160).

[315] S. Schiller. “Asymptotic expansion of morphological resonance frequencies in Mie scattering”. en. In: *Applied Optics* 32.12 (Apr. 1993), p. 2181. ISSN: 0003-6935, 1539-4522. DOI: `10.1364/AO.32.002181` (cit. on p. 154).

[316] D. W. Vernooy and H. J. Kimble. “Quantum structure and dynamics for atom galleries”. en. In: *Physical Review A* 55.2 (Feb. 1997), pp. 1239–1261. ISSN: 1050-2947, 1094-1622. DOI: `10.1103/PhysRevA.55.1239` (cit. on pp. 154, 155).

[317] Ardavan F. Oskooi et al. “Meep: A flexible free-software package for electromagnetic simulations by the FDTD method”. en. In: *Computer Physics Communications* 181.3 (Mar. 2010), pp. 687–702. ISSN: 00104655. DOI: `10.1016/j.cpc.2009.11.008` (cit. on pp. 155, 156).

[318] T. J. Kippenberg, S. M. Spillane, and K. J. Vahala. “Kerr-Nonlinearity Optical Parametric Oscillation in an Ultrahigh-Q Toroid Microcavity”. In: *Physical Review Letters* 93.8 (Aug. 2004). Publisher: American Physical Society, p. 083904. DOI: `10.1103/PhysRevLett.93.083904` (cit. on p. 155).

[319] T. J. Kippenberg, S. M. Spillane, and K. J. Vahala. “Demonstration of ultra-high-Q small mode volume toroid microcavities on a chip”. In: *Applied Physics Letters* 85.25 (Dec. 2004), pp. 6113–6115. ISSN: 0003-6951. DOI: `10.1063/1.1833556` (cit. on p. 155).

[320] Justin Z Brown. *Optical Coupling to High Q/V Resonators for Erbium Quantum Technologies*. May 2022 (cit. on p. 156).

[321] *COMSOL - Software for Multiphysics Simulation* (cit. on p. 156).

[322] *Optical Simulation and Design Software | Ansys Optics* (cit. on p. 156).

[323] Ivan S. Grudinin, Andrey B. Matsko, and Lute Maleki. “On the fundamental limits of Q factor of crystalline dielectric resonators”. en. In: *Optics Express* 15.6 (2007), p. 3390. ISSN: 1094-4087. DOI: `10.1364/OE.15.003390` (cit. on p. 156).

[324] D. V. Strekalov et al. "Efficient upconversion of subterahertz radiation in a high-Q whispering gallery resonator". en. In: *Optics Letters* 34.6 (Mar. 2009), p. 713. ISSN: 0146-9592, 1539-4794. DOI: `10.1364/OL.34.000713` (cit. on p. 163).

[325] S. M. Spillane et al. "Ideality in a Fiber-Taper-Coupled Microresonator System for Application to Cavity Quantum Electrodynamics". en. In: *Physical Review Letters* 91.4 (July 2003), p. 043902. ISSN: 0031-9007, 1079-7114. DOI: `10.1103/PhysRevLett.91.043902` (cit. on p. 163).

[326] Qingxia Zhuo et al. "Angle-polished fiber-integrated submicron wall microbubble WGM resonator for pressure and temperature sensing". en. In: *Optics Express* 33.24 (Dec. 2025), p. 50007. ISSN: 1094-4087. DOI: `10.1364/OE.577921` (cit. on p. 164).

[327] N Lindenmann et al. "Photonic wire bonding: a novel concept for chip- scale interconnects". en. In: (2012), p. 11 (cit. on pp. 164, 178).

[328] Stephan Dottermusch et al. "Exposure-dependent refractive index of Nanoscribe IP-Dip photoresist layers". en. In: *Optics Letters* 44.1 (Jan. 2019), p. 29. ISSN: 0146-9592, 1539-4794. DOI: `10.1364/OL.44.000029` (cit. on p. 164).

[329] Alain Yuji Takabayashi et al. "Microresonator photonic wire bond integration for Kerr-microcomb generation". en. In: *Scientific Reports* 14.1 (Nov. 2024), p. 29054. ISSN: 2045-2322. DOI: `10.1038/s41598-024-79945-4` (cit. on pp. 164, 178).

[330] Becky Lin et al. "Cryogenic optical packaging using photonic wire bonds". In: *APL Photonics* 8.12 (Dec. 2023), p. 126109. ISSN: 2378-0967. DOI: `10.1063/5.0170974` (cit. on pp. 164, 178).

[331] Marco De Gregorio et al. "Plug-and-Play Fiber-Coupled Quantum Dot Single-Photon Source via Photonic Wire Bonding". en. In: *Advanced Quantum Technologies* n/a.n/a (). _eprint: https://onlinelibrary.wiley.com/doi/pdf/10.1002/qute.202300227, p. 2300227. ISSN: 2511-9044. DOI: `10.1002/qute.202300227` (cit. on p. 164).

[332] J.-P. Laine et al. "Silica microsphere resonator and SPARROW waveguide coupler structures". EN. In: *Integrated Photonics Research (2000), paper IFC4*. Optica Publishing Group, July 2000, IFC4. DOI: `10.1364/IPR.2000.IFC4` (cit. on p. 164).

[333] Yuyang Zhuang et al. "Coupling of a whispering gallery mode to a silicon chip with photonic crystal". en. In: *Optics Letters* 44.23 (Dec. 2019), p. 5731. ISSN: 0146-9592, 1539-4794. DOI: `10.1364/OL.44.005731` (cit. on p. 164).

[334] Noel Lito B. Sayson et al. "Octave-spanning tunable parametric oscillation in crystalline Kerr microresonators". en. In: *Nature Photonics* 13.10 (Oct. 2019). Publisher: Nature Publishing Group, pp. 701–706. ISSN: 1749-4893. DOI: `10.1038/s41566-019-0485-4` (cit. on p. 164).

[335] Mohammad Soltani, Siva Yegnanarayanan, and Ali Adibi. "Ultra-high Q planar silicon microdisk resonators for chip-scale silicon photonics". en. In: (2007), p. 11 (cit. on p. 165).

[336] Omar Nagib, M. Saffman, and K. Mølmer. "Efficient Preparation of Entangled States in Cavity QED with Grover's Algorithm". In: *Physical Review Letters* 135.5 (July

2025). Publisher: American Physical Society, p. 050601. DOI: `10.1103/3fzf-wsr2` (cit. on p. 170).

[337] Stephan Welte et al. “Cavity Carving of Atomic Bell States”. In: *Physical Review Letters* 118.21 (May 2017). Publisher: American Physical Society, p. 210503. DOI: `10.1103/PhysRevLett.118.210503` (cit. on p. 170).

[338] Li Ma et al. “Optically detected magnetic resonance to characterize atomlike microwave-optical transducers”. en. In: *Physical Review A* 107.5 (May 2023), p. 053514. ISSN: 2469-9926, 2469-9934. DOI: `10.1103/PhysRevA.107.053514` (cit. on p. 178).

[339] B. E. Little et al. “Pedestal antiresonant reflecting waveguides for robust coupling to microsphere resonators and for microphotonic circuits”. EN. In: *Optics Letters* 25.1 (Jan. 2000). Publisher: Optica Publishing Group, pp. 73–75. ISSN: 1539-4794. DOI: `10.1364/OL.25.000073` (cit. on p. 178).

[340] Ian Reynaldo Berkman. “Optical and spin properties of Er3+ sites in Si”. en. In: () (cit. on p. 178).

[341] H. Bernien et al. “Heralded entanglement between solid-state qubits separated by three metres”. en. In: *Nature* 497.7447 (May 2013), pp. 86–90. ISSN: 0028-0836, 1476-4687. DOI: `10.1038/nature12016` (cit. on p. 178).

[342] Nicholas F. Chilton. “Ab initio electronic structure calculations of lanthanide single-molecule magnets; a practical guide”. en. In: *Chemical Society Reviews* (2025). Publisher: Royal Society of Chemistry. DOI: `10.1039/D5CS00493D` (cit. on p. 179).

[343] Maxime Grasser. “Ab initio calculations of chiroptical properties for lanthanide complexes”. Issue: 2023URENS078. Theses. Université de Rennes, Oct. 2023 (cit. on p. 179).

[344] Rizwan Nabi et al. “Accurate and Efficient Spin–Phonon Coupling and Spin Dynamics Calculations for Molecular Solids”. In: *Journal of the American Chemical Society* 145.45 (Nov. 2023). Publisher: American Chemical Society, pp. 24558–24567. ISSN: 0002-7863. DOI: `10.1021/jacs.3c06015` (cit. on p. 179).

[345] Alexander M. Jakob et al. “Deterministic Shallow Dopant Implantation in Silicon with Detection Confidence Upper-Bound to 99.85% by Ion–Solid Interactions”. In: *Advanced Materials (Deerfield Beach, Fla.)* 34.3 (Jan. 2022), p. 2103235. ISSN: 0935-9648. DOI: `10.1002/adma.202103235` (cit. on p. 179).

[346] Jason Pitters et al. “Atomically Precise Manufacturing of Silicon Electronics”. In: *ACS Nano* 18.9 (Mar. 2024). Publisher: American Chemical Society, pp. 6766–6816. ISSN: 1936-0851. DOI: `10.1021/acsnano.3c10412` (cit. on p. 179).

[347] Diana Serrano et al. “Ultra-narrow optical linewidths in rare-earth molecular crystals”. en. In: *Nature* 603.7900 (Mar. 2022), pp. 241–246. ISSN: 0028-0836, 1476-4687. DOI: `10.1038/s41586-021-04316-2` (cit. on p. 180).

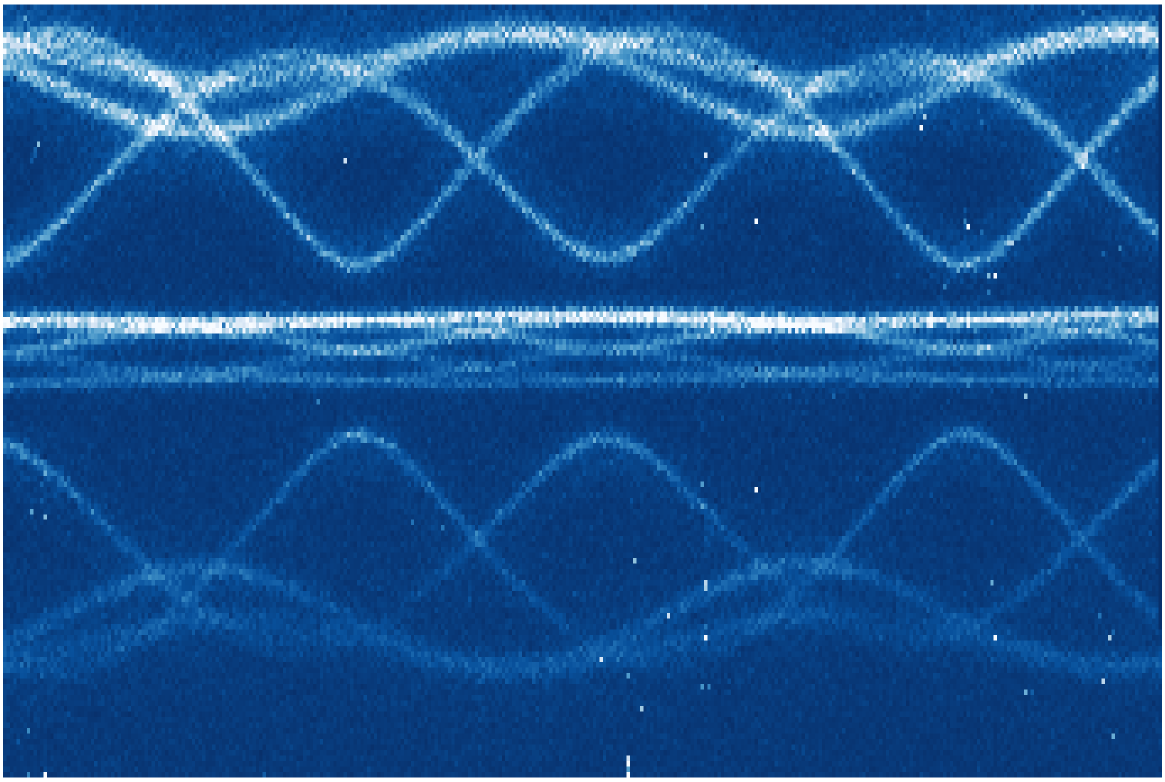

Two roads diverged in a yellow wood,
And sorry I could not travel both
And be one traveler, long I stood
And looked down one as far as I could
To where it bent in the undergrowth;

Then took the other, as just as fair,
And having perhaps the better claim,
Because it was grassy and wanted wear;
Though as for that the passing there
Had worn them really about the same,

And both that morning equally lay
In leaves no step had trodden black.
Oh, I kept the first for another day!
Yet knowing how way leads on to way,
I doubted if I should ever come back.

I shall be telling this with a sigh
Somewhere ages and ages hence:
Two roads diverged in a wood, and I—
I took the one less traveled by,
And that has made all the difference.

— Robert Frost